Structural dynamics and spectroscopic studies of human cytochrome *c*: Linking dynamics and disease

Oliver Mario Deacon

A Thesis submitted for the degree of Doctor of Philosophy – Biochemistry

School of Biological Sciences
University of Essex

June 2018

Abstract

"Life is pleasant. Death is peaceful. It's the transition that's troublesome"

Isaac Asimov (1920 – 1992)

Mitochondrial cytochrome *c* (C*c*) is a small haem protein, primarily involved in electron transfer, but is an example of an extreme multifunctional protein with roles in several stages of apoptosis through interaction with phospholipids and Apaf-1. The switch in function is associated with an interaction with cardiolipin (CL) and gain of peroxidase activity. Mutations in the C*c* gene lead to Thrombocytopenia 4, a disease associated with enhanced apoptotic activity. The Y48H variant is found in the 40-57 Ω-loop, the lowest free-energy foldon. A 1.36 Å resolution X-ray structure of the Y48H variant reveals minimal structural changes to that of the wild-type protein and G41S variant (also associated with Thrombocytopenia 4). Despite this, the intrinsic peroxidase activity is enhanced, implying that a penta-coordinate haem species is more prevalent in the Y48H variant, corroborated through determination of a Met80 off-rate of > 125 s^{-1} compared with ~ 6 s^{-1} for the wild-type protein. Heteronuclear NMR experiments with the ferric Y48H variant have revealed heighted dynamics relative to the WT protein in the 40-57 and 71-85 Ω-loops, the latter being the loop containing the Met80 ligand, suggesting communication between these two substructures. When these results are considered in relation to the G41S variant, a dynamic picture emerges in which heightened dynamics in key substructures of the C*c* fold facilitate an increased population of a penta-coordinate, peroxidase active species of the order wild-type < G41S < Y48H. Studying the alkaline transition through pH jump stopped-flow

spectroscopy has revealed that not only is the pK_{695} is reduced by ~ 1 pH unit compared to that of the wild-type protein, but also the pK of the trigger is lowered. In contrast, variants in the 71-85 Ω-loop do not alter the pK of the trigger but are nevertheless associated with enhanced peroxidase activity relative to the wild-type protein, due to enhanced local dynamics within the haem crevice.

Acknowledgments

Firstly, I wish to thank my Supervisor Dr Jonathan Worrall. Thank you for providing me with the opportunity to study for a PhD within your Research Group. Thank you for introducing me to the exciting field of haem-protein biochemistry, for your guidance, motivation and support during my PhD.

Special thanks must go to the one and only Professor Mike Wilson, for his unconditional support and truly ***incredible*** patience whilst teaching me Mathematics (or arithmetic as he would say!) and Kinetics … Mike, your immense generosity and efforts with myself, and all others whom you have worked with, are forever appreciated. Our conversations over the years, covering a broad range of topics, have quite literally been one of the highlights of my PhD and it has always been a true pleasure and a privilege learning from you. Your ability to make me sweat on a cold winters day will always be unrivalled!

I also thank our collaborators at the University of East Anglia, Professor Geoff Moore and Drs Colin Macdonald and Tharin Blumenschien for their efforts on this PhD project. Geoff, it has been an absolute pleasure working with yourself and Mike and I have many fond memories indeed of our stopped-flow experiments and our discussions on the *medicinal* properties of alcoholic beverages!

I would like to acknowledge Dr Sara Whittaker for her assistance with the acquisition of the Relaxation Dispersion NMR data, furthermore, the Welcome Trust funded HWB-NMR facility for providing open access.

I also must thank Dr Dmitri Svistunenko for his assistance with EPR spectroscopy during the latter stages of my PhD research. Furthermore, thank you Dima for always being a happy and calming influence!

Special thanks must also go out to my laboratory mentor, and NMR guru, Dr Andreas Ioannis Karsisiotis, for teaching me good (and efficient!) laboratory practices, and ultimately making me a better Scientist. I will always look back on our work together, especially our numerous NMR adventures, with great fondness. Most of all, I would like to thank you for introducing me (somewhat forcibly …) to electronic music! I wish you the greatest of success in your future teaching career.

I also wish to thank all laboratory 5.08 members, both past and present, for their friendship, encouragement, and support during both my undergraduate research project, and my PhD. The greatest pleasure of my PhD experience, has without doubt, been the people I have been fortunate enough to have worked with. To that end, I wish to thank Dr Mila Pavlova specially, for her tremendous friendship and support, through both the high points, and low point, of my PhD (and no Mila, I haven't forgotten my promise to take you for a ride on the motorbike!). I also wish to thank Mr (soon to be Dr!) Tadeo Moreno-Chicano for his assistance with the Y48H crystallography and for our many enjoyable MotoGP discussions over coffee, even though Márquez won last year's championship, not Viñales!).

Great appreciation also goes out to technician's Dr Victoria Allen-Baume, Miss Hannah Dundon (née Adams), Miss Amanda Clements and Mrs Anna Freeman for ensuring that our lab has been well maintained, well stocked, and for ensuring that our research has always been possible. Appreciation also goes out to Mrs Jackie Maidwell, for her many years of service in the departmental stores. Special thanks also go to our Postgraduate Administrator, Mrs Emma Revill, for always being tremendously helpful,

reminding us all of deadlines etc, but most of all, for being a very happy and warming presence in the Department.

I also wish to thank Sharon at the Campus Kitchen, for keeping me caffeinated throughout my studies at the University of Essex. I would also like to thank Mrs Kath Birks and Dr Paul Irvine for keeping me going through my PhD research. Furthermore, I wish to thank Snr Sister Kate Williams for being a tremendous friend to my family and I.

This PhD research would not have been possible without the financial contribution of The Leverhulme Trust (project grants RPG-2013-164 and EM-2014-088), therefore, I wish to express formally on behalf of all grant members, our appreciation.

I also wish to thank the University of Essex for my higher education. I have received an excellent education at this University, both at Undergraduate and Doctoral research levels, and wish the University a successful and prosperous future.

Finally, I must thank my family, particularly my parents, Donna and Richard Deacon, for their unconditional love and support throughout my education, and life thus far. You have made many sacrifices for me, and the fact of the matter is simple, if it were not for the education I received, and if I did not have you as parents, I would never have been in a position to succeed at University, let alone complete a PhD … This PhD has, and always will be, one of my life's significant experiences, and whatever my future holds, I owe it all to you.

Contents

Figures

Figure 5.3: Far-UV CD spectra of the WT protein and the 81 and the 71-85 Ω-loop variants in the ferric form.

Figure 5.4: Equilibrium unfolding by GuHCl of the WT protein and the 71-85 Ω-loop variants in the ferric form.

Figure 5.5: Stopped-flow kinetics of N_3^- binding to ferric WT hC*c* and the 81 and 83 variants. (**A**) Amplitudes of the time-courses as a function of $[N_3^-]$. (**B**) The rate constant (k_{obs}) determined for N_3^- binding.

Figure 5.6: (A) Peroxidase activity of the WT protein and 71-85 Ω-loop variants. **(B)** The pH dependence of the 695 nm band.

Figure 5.7: (A) Spectral transition observed through stopped-flow spectroscopy when mixing WT hC*c* (pH 7) with equal volume pH 10 buffer. **(B)** $Logk_{obs1}$ (slow phase) of the alkaline transition of the WT human and equine protein, the disease variants G41S and Y48H and the 81 and 83 variants.

Figure 5.8: pH jump kinetics of the fast phase observed in the Y48H variant at pH > 10.5.

Figure 5.9: The pH dependence of k_{obs2} for the WT proteins and disease variants (**A**) and WT hC*c* and the 71-85 Ω-loop variants (**B**).

Figure 5.10: EPR spectra generated when pH jumping the Y48H variant from pH 7 to 11 by slow freezing and Rapid-Freeze-Quench.

Figure 5.11: The mechanistic pathways linking the de-protonation and conformational changes in hC*c*.

Abbreviations

γ = Gyromagnetic ratio

$(Fe(CN)_6]^{4-}$ - Ferrocyanide

$[Fe(CN)_6]^{3-}$ - Ferricyanide

1D – 1-Dimensional

2D – 2-Dimensional

3D – 3-Dimensional

Å – Ångström

ABTS – 2,2-azinobis (3-ethylbenthiazoloine-6-sulfonic acid)

AGE – Agarose Gel Electrophoresis

ALA – 5-aminolaevulinic acid

Ala – Alanine

Amp – Ampicillin

Apaf-1 – Apoptosis protein activating factor-1

APS – Ammonium persulfate

Arg – Arginine

Asn – Asparagine

Asp – Aspartic acid

ATP – Adenosine Triphosphate

B_0 = External magnetic field

Bax – Bcl-2-like protein 4

Bcl-2 – B-cell lymphoma-2

BH – Bcl-2 homology domain

Bid – BH3 interacting domain

BIM – Bcl-2-like protein 11

BMRB – Biological Magnetic Resonance Bank

BNC – Binuclear centre

Ca^{2+} - Calcium

CAPS – 3-(Cyclohexylamino)-1-propanesulfonic acid

C*c* – Cytochrome *c*

C*c*O – Cytochrome *c* Oxidase

CD – Circular Dichroism

Ced – Cell death abnormal

CL – Cardiolipin

Cm – Centimetre

Cm – Chloramphenicol

CO – Carbon monoxide

Cu – Copper

Cys – Cysteine

D_2O – Deuterium chloride

$_{D6}$DMSO – Deuterated DMSO

Da – Daltons

dATP – Deoxyadenosine triphosphate

dd – Double distilled

DFT – Density Functional Theory

DISC – Death inducing signalling complex

DMSO – Dimethyl sulfoxide

DNA – Deoxyribonucleic acid

dNaOH – Sodium deuteroxide

dNTP – Deoxyribonucleotide triphosphate

DOPC – 1, 2-dioleoyl-*sn*-glycero-3-phosphocholine

dTFA – Trifluroacetic acid-d

eC*c* – Equine C*c*

EDTA – Ethylenediaminetetraacetic acid

$E_{m,7}$ – Redox potential under standard conditions at pH 7

EPR – Electron Paramagnetic Resonance

EtBr – Ethidium Bromide

ETC – Electron Transfer Chain

eV – Electron volts

FID – Free Induction Decay

FRET – Fluorescence Resonance Energy Transfer

FT – Fourier Transform

FT-IR – Fourier Transform-Infrared

Gln – Glutamine

Glu – Glutamic acid

Gly – Glycine

H/D – Hydrogen/Deuterium

H_2O – Water

H_2O_2 – Hydrogen peroxide

hC*c* – Human Cytochrome *c*

HCl – Hydrochloric acid

His – Histidine

His – Histidine

HSQC – Heteronuclear Single Quantum Correlation

I = Nuclear Spin

IAP – Inhibitor of Apoptosis Proteins

Ile – Isoleucine

INEPT – Insensitive Nuclei Enhanced by Polarisation Transfer

$InsP_3R$ – Inositol-1,4,5-triphosphate receptor

IPTG – Isopropyl β-D-1-thigalactopyranoside

K – Kelvin

K_d – Dissociation constant

K_m – Michaelis constant

KPi – Potassium Phosphate

LB – Lysogeny Broth

Leu – Leucine

LMCT – Ligand to Metal Charge Transfer

Lys – Lysine

MAS-SS-NMR – Magic Angle Spinning SS-NMR

MES – 2-(*N*-morpholino)ethansulfonic acid

Met – Methionine

MIM – Mitochondrial Inner Membrane

MIS (Mitochondrial Inter-membrane Space)

mm – Millimetre

MOM – Mitochondrial Outer Membrane

MOMP – Mitochondrial Outer Membrane Permeabilisation

MRE – Mean Residue Ellipticity

mV – Millivolts

NaCl – Sodium chloride

NaOH – Sodium hydroxide

NaPi – Sodium Phosphate

NH – Amide

NMR – Nuclear Magnetic Resonance

ns – Nanosecond

O_2 – Oxygen

OH – Hydroxide

OH – Hydroxyl group

PCR – Polymerase Chain Reaction

PDB – Protein Data Bank

PEG – Polyethylene glycol

PF – Potassium fluoride

PhD – Doctor of Philosophy

Phe – Phenylalanine

pK_{695} – pK of the alkaline transition

pK_a – Acid dissociation constant

PLS – Proton Loading Site

Pro – Proline

PS – Phosphatidylserine

ps – Picosecond

RO – Reverse Osmosis

ROS – Reactive Oxygen Species

SDS-PAGE – Sodium Dodecyl Sulphate Polyacrylamide Gel Electrophoresis

Ser – Serine

SHE – Standard Hydrogen Electrode

SMAC/DIABLO – Second Mitochondria-derived Activator of Caspases/Diablo homolog

SP – Sulfopropyl

SS-NMR – Solid-State NMR

t-Bid – Truncated Bid

TB – Terrific Broth

TEMED – Tetramethylethylenediamine

TFA – Trifluroacetic acid

THC-4 – Thrombocytopenia 4

Thr – Threonine

TOCL – 1, 1', 2, 2'-tetraoleoyl cardiolipin

Trp – Tryptophan

Tyr – Tyrosine

UV – Ultra Violet

V – Volts

Val – Valine

Zn^{2+} – Zinc

$\Delta\psi_m$ – Membrane potential

ε - Extinction Coefficient

μM – Micrometre

Chapter 1

General introduction on the properties and the physiological/pathophysiological roles of cytochrome *c*

1.1 Cytochrome *c* classes

Cytochromes *c* belong to one of four subclasses based on their structural and physicochemical properties (Ambler, 1991).

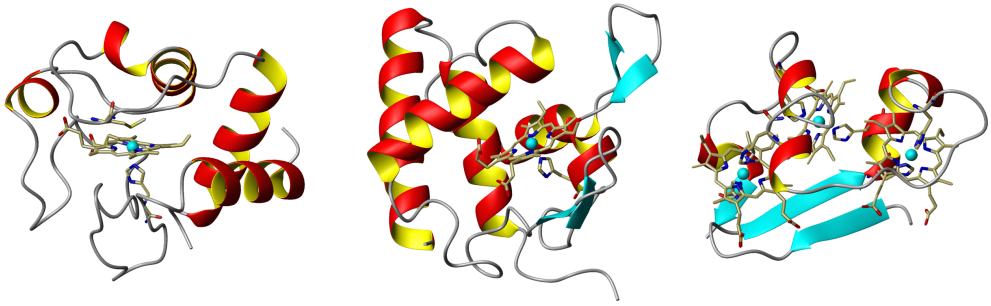

Figure 1.1 X – ray crystal structures of the class I human cytochrome *c* (left), the class II cytochrome *c*' (middle) and the class III cytochrome c_7 (right) (Rajagopal et al., 2013, Enguita et al., 2006, Czjzek et al., 2001).

Class I cytochromes consist of the soluble mitochondrial and bacterial cytochromes *c* (Ambler, 1991). They are characterised by the low spin state of the six coordinate haem iron and in the axial haem ligands whereby the haem iron is coordinated towards the N-terminus by a proximal histidine and at the C-terminal end by a distal methionine ligand (Ambler, 1991). Ambler (1991) recognised a further five subclasses of Class I cytochromes, Classes Ia-e. Class Ia include the "long" Cc_2 and Cc_{-550} from *Rhodospirillum rubrum* and *Aquaspirillum itersonii* respectively (Ambler, 1991). Class Ib consist of both eukaryotic mitochondrial cytochrome *c* (C*c*) (Figure 1.1, left) and the prokaryotic "short" Cc_2 of *Rhodopila globiformis* (Ambler, 1991). The Class Ic cytochromes possess a 'split alpha band' or widened alpha band in the UV-visible spectra and display lower absorptivity, with this sub class consisting of the dihaem Cc_4, monohaem Cc_6 and Cc_{-554} (Ambler, 1991). Class Id only consist of bacterial cytochromes such as Cc_{-551} of the *Pseudomonas spp.*, Cc_{-552} of *Hydrogenobacter thermophiles* and Cc_{-553} of *Rhodocyclus tenuis* (Ambler, 1991).

Ambler (1991) noted that Class Id cytochromes possess several proline residues around the methionine ligand and a highly conserved tryptophan residue around the C-termini of the proteins.

Class II cytochromes *c* primarily include the high spin C*c'* (Figure 1, middle) but also low-spin cytochromes such as C*c*$_{-556}$ (Ambler, 1991). Characteristically, the haem attachment site is located towards the C-terminus of the proteins (Ambler, 1991), but C*c'* are also able to bind carbon monoxide, nitric oxide and cyanide, with significantly lower rate and equilibrium constants (100 – 1,000,000 fold lower) than other high-spin haemproteins, such as myoglobin (Kassner, 1991). Based on these properties, Moore and Pettigrew (1991) suggested that C*c'* functions as an electron transfer protein rather than a terminal oxidase.

Class III cytochromes *c* comprise the multi-haem cytochromes with low redox potentials such as the trihaem C*c*$_7$ (Figure 1.1, right), tetrahaem C*c*$_3$ and the hexadecahaem high molecular weight C*c* (Coutinho and Xavier, 1994). All of the class III cytochromes *c* have approximately 30-40 residues per haem group and all haems are bis-histidinyl coordinated (Coutinho and Xavier, 1994). These cytochromes are therefore non-equivalent, both structurally and functionally and possess ranges in redox potential from 0 to -400 mV versus the Standard Hydrogen Electrode (Coutinho and Xavier, 1994). All of the class III cytochromes c consist of 4-5 α-helices and 2 β-sheets surrounding 4 non-parallel haems thus conferring high solvent exposure, and overall the structural properties of these cytochromes are highly conserved (Coutinho and Xavier, 1994).

Class IV cytochromes *c* consist of complex proteins which do not contain *c*-type haems, but instead contain other prosthetic groups, examples include flavocytochromes *c* and cytochromes *cd* (Ambler, 1991).

1.2 Mitochondrial cytochromes c

Mitochondrial cytochromes *c* (C*c*) are a family of small (104 ± 10 amino acids), globular, water soluble, haem proteins that primarily function as electron carriers in the electron transfer chain (ETC) (Pettigrew, 1987). The haem is attached covalently via two thioether bonds between two cysteines and two haem vinyl groups, as part of a penta-peptide motif of CXXCH with the histidine acting as the proximal ligand (Pettigrew, 1987). A second axial ligand to the haem by way of a methionine residue is also present (Battistuzzi et al., 2001). In its role as a redox protein C*c* can alternate between two oxidation states, the ferrous Fe(II) diamagnetic state and the ferric Fe(III) paramagnetic state (Moore and Pettigrew, 1991). Thus, the haem confers the electron transfer ability to the holoenzyme and the polypeptide is responsible for the redox potential of the iron and correct subcellular localisation and subsequent docking with redox partners (Baxter and Fetrow, 1999).

1.3 Cytochrome c: Interactions with cytochrome bc_1

Cytochrome bc_1, also known as Cytochrome *c* Reductase (C*c*R), is a homodimeric multisubunit integral membrane protein complex (Trumpower, 1990a). The catalytic core of C*c*R is composed of cytochrome *b* (C*b*) with two non-covalently attached haem *b* groups, a Rieske centre composed of an iron-sulphur protein (ISP) with a 2Fs-2S cluster, and cytochrome c_1 with a covalently attached haem *c* prosthetic group (Alvarez-Paggi et al., 2017). C*c*R's primary enzymatic role is in the catalysis of electron transfer from ubiquinol (QH_2) to C*c*:

$$QH_2 + 2Cc^{+3} + 2H^+in \rightarrow Q + 2Cc^{+2} + 4H^+out$$

The above reaction summarises what is known as the Q-cycle, which couples electron transfer to proton translocation across the inner mitochondrial membrane, thereby

contributing to the generation of the proton gradient (Trumpower, 1990b, Trumpower and Gennis, 1994). This process proceeds as follows, an ISP accepts one electron from quinol in the Qo site of C*b* followed by dissociation from C*b* and subsequent conformational change prior to docking with Cc_1 and resulting electron transfer (Alvarez-Paggi et al., 2017). An electron transfer reaction then proceeds from Cc_1 to C*c*, which can then shuttle an electron to cytochrome *c* oxidase (C*c*O) (Alvarez-Paggi et al., 2017).

Elucidation of the interaction site between C*c*R and C*c* has been problematic due to discrepancy between mutational and functional studies and the more recently obtained X-ray crystal structures (Alvarez-Paggi et al., 2017). Seminal mutational studies conducted on mammalian C*c* suggested that part of the Lys patch (Lys8, 13, 27, 72, 86 and 87) are key members of the binding process, with Lys73 and 79 also playing a minor role (Speck et al., 1979, Smith et al., 1981, Ahmed et al., 1978, Konig et al., 1980, Rieder and Bosshard, 1980). Hunte and colleagues have, to date, provided the only X-ray crystal structures of the C*c*R/C*c* complex, using iso-1-C*c* of *S. cerevisiae* and have provided contradictory information to the previous mutational studies (Lange and Hunte, 2002, Solmaz and Hunte, 2008, Hunte et al., 2002, Nyola and Hunte, 2008).

Through analysis of the contact interface, Hunte and colleagues have demonstrated that the interaction site is not formed from modules of closely interacting residues, but instead through individual contacts that are dispersed over the small interface (Alvarez-Paggi et al., 2017). The C*c*R/C*c* complex consists of a small hydrophobic channel surrounded by a half ring of charged residues and proceeds via an apparent two-step process, in which an encounter complex first forms proceeded by an electron transfer competent reorganisation (Alvarez-Paggi et al., 2017). Hunte and

colleagues suggest that Lys16, 91 and 92 (iso-1-C*c* numbering) are the unspecific electrostatic contacts which drive complex formation through establishing long-range interactions with negatively charged Asp and Glu residues in the c_1 subunit of C*c*R. As the distances involved are from 5-9 Å none form salt bridges or intermolecular H-bonds. Conversely, specific hydrophobic contacts are established by Ala86, Val33 and Thr17, and a cation-π interaction between a Phe and an Arg are observed. The complex is further stabilised by a number of H_2O molecules situated between C*c*R and C*c*, however, the water molecules do not mediate H-bonds between protein surfaces in the X-ray crystal structure. Interestingly, the redox state of C*c*R does not affect the complex bound state (Nyola and Hunte, 2008).

Surprisingly, Hunte and colleagues found that despite the highest binding affinity was observed at low ionic strength (< 160 mM), a bell-shaped dependence in enzymatic activity was observed (Hunte et al., 2002). The authors attribute the low enzymatic activity observed at low ionic strength to stronger electrostatic stabilisation between C*c*R and C*c* thereby inhibiting electron transfer. Furthermore, intermediate ionic strength may weaken the electrostatic interactions in which complex rearrangement to a more electron transfer competent structure is facilitated. Conversely, high ionic strength would destabilise the electrostatic contacts inhibiting complex formation.

EPR spectroscopy has provided an alternative interpretation to the relationship between C*c*R/C*c* enzymatic activity and complex binding affinity through the interrogation of short-lived complexes (Sarewicz et al., 2008). It has been demonstrated that at low ionic strength the electron transfer is fast, but the turnover rate is hindered by complex dissociation. By increasing the ionic strength, the complex dissociation rate is increased until an optimal concentration is reached. As ionic

strength increases further, well-oriented complex formation is rate limiting because the electrostatic attraction between C*c*R and C*c* is lost. The premise of this interpretation is based on diffusion-coupled reactions between soluble electron carriers and membrane complexes and could therefore be applicable to other protein complexes (Hackenbrock et al., 1986, Gupte et al., 1984). The C*c*R crystal structure displays only a single C*c* molecule bound to monomer B of the homodimer, conferring a structure in which haem's *c* and c_1 are in close proximity (Fe-Fe distance of 17.4 Å, haem-haem distance of 9 Å and a 1000 $Å^2$ interaction surface) (Alvarez-Paggi et al., 2017). The interaction surface is smaller than the average protein-protein interface, but consistent with other transient electron transfer complexes (Lo Conte et al., 1999). Interestingly, the observation that only one C*c* binds to only one C*c*R monomer is not attributed to an artefact of crystallisation. This assertion arises from the differences in the ubiquitinone reduction site, despite both C*c*R monomers being conformationally identical (Solmaz and Hunte, 2008). These differences mainly involve the head domain of the ISP and the QCR6p subunit of each monomer (Solmaz and Hunte, 2008). The QCR6p subunit is highly acidic and has therefore been proposed to guide C*c* docking to Cc_1 (Bogan and Thorn, 1998). The ISP has been suggested to play a regulatory role in the mechanistic alternating site model in which only one C*c*R monomer is active at a time, the ISP physically cross-links the two functional units of the intertwined dimer (Wenz et al., 2007). Hunte and colleagues have suggested that the structural differences suggest coordinated binding of both electron acceptors for quinol oxidations, perhaps in order to circumvent the production of toxic intermediates or catalytic side products. In order for such a coordinated model to be employed, there must be long-range communication within C*c*R, which would be achieved through redox-induced conformational change, changes in protonation state of interior residue

side chains or long range electrostatic interactions (Lange and Hunte, 2002). The validity of this model has been challenged on the basis of the complex lifetimes, which appear to be far shorter than those required for such rearrangements to take place (Sarewicz et al., 2008).

Rather surprisingly, the crystallographic structure demonstrates that the conserved lysine residues that were previously shown to be involved in C*c* binding do not participate in short-range interactions, but instead they may play a role in C*c* orientation on the surface of Cc_1 or in the formation of transient complexes involved in binding/unbinding, or finally that the interactions are exclusively long-range and do not participate in H-bonds or the formation of salt bridges (Lange and Hunte, 2002, Nyola and Hunte, 2008). These proposed roles of the conserved lysine residues are not consistent with the previously reported equilibrium studies (Ahmed et al., 1978, Rieder and Bosshard, 1980) and the X-ray crystal structure reveals no steric constraints that would prevent side-chain reorganisation leading to the formation of H-bonds and/or salt bridges. MD simulations with the C*c*R/C*c* complex highlight the significance of dynamics, as the residues involved are highly mobile and do take place in short-range interactions (Kokhan et al., 2010). The authors speculate there is potential for crosstalk between both Cc_1 monomers involving finger-like β-strands, the result of which could alter the affinity of one monomer following subsequent binding of the other monomer by altering the position of the acidic residues involved in binding. This would therefore provide a mechanism for the one C*c* per dimer binding scenario (Alvarez-Paggi et al., 2017).

Schulten and colleagues have recently published a MD study that yields new insights into the Cbc_1/Cc_2 complex from *Rhodobacter sphaeroides*, with binding information expected to be extrapolated to mammals and bacteria (Moser and Dutton,

1988). Their calculations demonstrate that an ensemble of near identical, yet conformationally slightly disordered complexes is formed with a short haem edge-haem edge distance (8.5 Å) thereby contradicting the crystallographic structures of a single structurally well-resolved docking complex. As a result of these findings, the scenario is compatible with a dynamic docking mechanism for the electron transfer reaction (Alvarez-Paggi et al., 2017). The authors suggest that complex formation involves the complementary charged residues within the peripheral half ring structure that encloses the polar and hydrophobic core, thus allowing close inter-haem proximity and direct electron transfer (Alvarez-Paggi et al., 2017). Consistent with the crystallographic information, the distances between electrostatically interacting residues does not allow for direct short-range interactions, instead, dynamic long-range interactions occur. The binding interface is stabilised by H_2O molecules that mediate the majority of interactions yet are excluded from the space separating the haem cofactors. The authors suggest that these interactions occur concomitantly with C*c* conformational change that are associated with the loss of several internal H-bonds that are reasonable for maintaining the native fold of C*c*. However, loss of these H-bonds does not result in protein unfolding or denaturation. Schulten and colleagues state that protein fluctuations resulting in a loss of electrostatic interactions play a crucial role in complex dissociation following electron transfer. Following from the loss of electrostatic contacts, the H_2O exposed surfaces force the hydrophobic residues to bury themselves within the surface of the respective protein matrix, the result of which is a loosening of the interface and subsequent complex disruption thus preventing back electron transfer (Alvarez-Paggi et al., 2017).

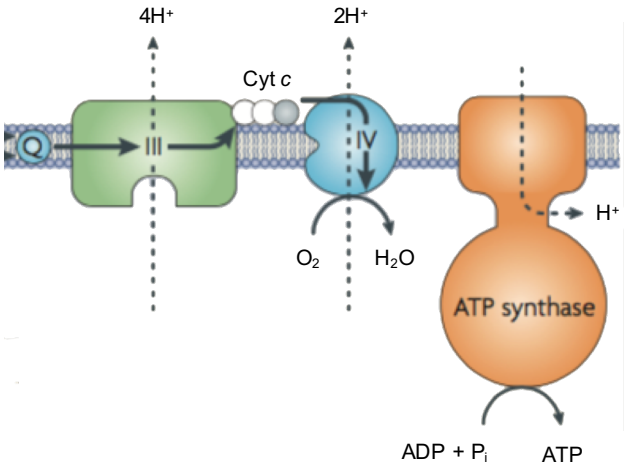

Figure 1.2 Schematic depiction of the latter half of the ETC. The ETC is comprised of 4 membrane bound complexes (I-IV, with complexes III and IV shown), in which the flow of electrons (black arrows) is facilitated with a number of electron carriers; ubiquinone (coenzyme Q), C*c* (grey circle) and iron-sulphur proteins. The shuttling of electrons yields an exergonic reaction in which protons are pumped from the mitochondrial matrix across the inner membrane. The result of the proton pumping is the generation of the membrane potential ($\Delta\psi_m$) and electrochemical energy in the form of a proton-motive force. The proton gradient is dissipated through a proton pore complexed to an ATP synthase (F_1 F_0 ATP synthase). Adapted from (Ow et al., 2008).

1.4 Cytochrome c: Interactions with cytochrome c oxidase

Cytochrome *c* Oxidase (C*c*O) is the terminal electron acceptor in the mitochondrial respiratory chain (Yoshikawa and Shimada, 2015). C*c*O pumps four protons from the mitochondrial matrix into the intermembrane space using four electron supplied from C*c*, the result of which is the generation of the electrochemical gradient used to produce ATP via the F_1F_0 ATP-synthetase complex (Figure 1.2) (Alvarez-Paggi et al., 2017). The respiratory chain concludes with the electrons finally transferred to molecular O_2 to form H_2O:

$$4Cc^{2+} + 8H^{+}in + O_2 \rightarrow 4Cc^{3+} + 2H_2O + 4H^{+}out$$

Mammalian C*c*O is a large dimeric macromolecular complex with each monomer composed of 14 subunits and several redox centres, namely: two haem cofactors, a Cu_A site and a Cu_B site (Ramirez et al., 1995). Electron flow within C*c*O commences when C*c* docks near the Cu_A site, which functions as the primary electron acceptor. The electron is subsequently transferred to a species-specific haem cofactor and then transferred on to a binuclear centre that is formed from haem a_3. The binuclear centre is the site at which reduction of molecular O_2 to H_2O takes place.

Since the late 1970's many groups have contributed to the elucidation of the binding interface between C*c* and C*c*O, using techniques such as chemical modification of surface lysine residues (on C*c*) (Ferguson-Miller et al., 1978, Smith et al., 1977) and chemical modification/protection and monoclonal antibody studies on C*c*O (Millett et al., 1982, Millett et al., 1983, Taha and Ferguson-Miller, 1992) provided a range of residues potentially involved in complex formation. The following residues were identified: Lys8, 13, 72, 86 and 87 of C*c* and Asp112, Glu114 and 198 within the soluble domain of C*c*O subunit II (Alvarez-Paggi et al., 2017). The C*c*O/C*c* complex structure, as determined by X-ray crystallography, has recently been reported (Shimada

et al., 2017). Despite this, due to the large size of eukaryotic C*c*O and the transient nature of the interaction with C*c*, more detailed and dynamically relevant structural information has been hindered. This issue has been, to some extent, circumvented by structural and spectroscopic studies on bacterial and eukaryotic variants. The aa_3-type C*c*O from *Paracoccus denitrificans* (*Pd*) has been studied extensively and is composed of only four heterogenous subunits (Alvarez-Paggi et al., 2017). Subunits I, II and III are the largest and possesses high homology to the mitochondrion-encoded components of eukaryotes that form the enzyme's catalytic core, thus the bacterial complex serves as a suitable model system in the context of complex formation processes (Richter and Ludwig, 2003). The model system also consists of the redox partner Cc_{552}, a membrane-anchored protein that can be expressed as a 100 residue soluble fragment (Alvarez-Paggi et al., 2017). Studies have been employed using this model system, consisting of biochemical, kinetic, mutational and spectroscopic methodologies (Maneg et al., 2004). Ludwig and colleagues demonstrated that the glutamates and aspartates within subunits I and II of C*c*O mediate the binding of *Pd*-C*c*O to eC*c* (Witt et al., 1998a). Furthermore, Ludwig's study found evidence of the contribution of hydrophobic residues to the interaction, of which Trp121 (*Pd* numbering) acts as the electron entry site (Witt et al., 1998b).

Bertini and colleagues found through combining NMR data and docking calculations (Bertini et al., 2005) that there are multiple possible complex structures related through rotations of Cc_{552} round the intermolecular axis defined by two docked structures, thus suggesting considerable dynamics are involved in scanning for optimal orientation. Furthermore, the authors found that the binding interface includes a region of hydrophobic residues involving Phe120, Trp121, Tyr122 and Leu137 on C*c*O and residues Ala16, Val26, Ala79, Phe80 and Ala81 on Cc_{552}. Acidic residues surround

the hydrophobic core of C*c*O forming salt bridges with Lys residues, whereas the exposed haem edge of Cc_{552} is in close proximity to the indole ring of Trp121 of C*c*O when in the proposed electron transfer active conformation. Electrostatic interactions are intermittently formed whilst C*c* scans the surface of C*c*O, thus preserving the transient complex. Furthermore, the authors suggest that C*c* forms electrostatic interactions with subunit I of C*c*O, in addition to subunit II. Thus these findings are consistent with the two-step docking mechanism first proposed by Ludwig and co-workers (Witt et al., 1998b), in which the protein encounter is mediated by long-range electrostatic interactions followed by a second "fine" rearrangement that is mediated through hydrophobic interactions that maximise the electronic coupling H_{DA} and therefore consistent with a Gated Docking (GD) scenario (Alvarez-Paggi et al., 2017). Ludwig however, suggests from EPR experiments that a dynamic ensemble of protein-protein distances is compatible with either a GD or Dynamic Docking (DD) scenario (Lyubenova et al., 2007). A GD scenario is consistent with the low electron transfer rate from C*c* to C*c*O (10 – 100 s^{-1}).

Ishimori and colleagues have recently investigated the nature of the gating/binding process in C*c*O/C*c* complex formation, through the use of spectroscopic and functional studies (Sakamoto et al., 2011, Sato et al., 2016). The authors found that the negatively charged residues and the Lys residues are involved in complex formation, the result of which is a weakening of the overall electrostatic contribution (Sakamoto et al., 2011). Furthermore, the authors demonstrated that the hydrophobic cluster of C*c*O, comprising Trp104, Tyr105, 121 and Phe206, surrounding the Cu_A site participates in the dominant interaction for redox centre positioning. Through the combined use of steady-state kinetics, docking and MMPBSA calculations, the authors estimated the different contributions to ΔG for the binding process (ΔG_{bind}) (Alvarez-

Paggi et al., 2017). By determining the K_m values, the authors were able to group residue mutations, such as Lys to Leu and Ile to Ala, based on their observed effect. The authors demonstrated that the largest impact on K_m was observed by substitution of Lys13, 86 and 87, a moderate effect is observed by substitution of Lys7, 8, 72 and 79, and no effect was observed by substitution of Ile9, 11, 81 or Lys39.

Molecular Mechanics combined with Poisson-Boltzmann Surface Area (MMPBSA) calculations suggest the overall electrostatic component of the binding between C*c*O and C*c* is destabilising, as the favourable electrostatic interactions between charged residues, such as the Lys from C*c* and the carboxylic acids on C*c*O, are overcompensated by the large destabilisation involved in desolvation (Alvarez-Paggi et al., 2017). Despite this, the Coulombic interaction is dominant in determining the differences in ΔG between mutants, therefore rationalising the increase in K_m for the various Lys mutants. Furthermore, the authors suggests that the predominant stabilising interactions mediated by Lys13 and 86 are due to van der Waals and non-polar interactions, the former of which mediated by hydrophobic residues are dominant contributors to complex stabilisation, electrostatic contributions on the other hand contribute to the binding orientation of C*c* to C*c*O (Alvarez-Paggi et al., 2017). This interpretation of C*c* binding to C*c*O is supported by their rapid co-evolution in early anthropoid primates (Pierron et al., 2011, Schmidt et al., 2005, Pierron et al., 2012). It has been proposed that a reduction in the number of electrostatic interactions between C*c*O and C*c* increases respiratory efficiency (Pierron et al., 2011, Schmidt et al., 2005, Pierron et al., 2012). This has been surmised due to the substitution of charged residues within half of the amino acids on C*c*O that are involved with C*c* interaction (Pierron et al., 2011, Schmidt et al., 2005, Pierron et al., 2012). Ishimori and colleagues obtained the chemical shift perturbations upon binding of oxidised and reduced C*c* to C*c*O and

in doing so were able to speculate on the nature of the electron transfer gating step (Sakamoto et al., 2011, Sato et al., 2016). The authors propose that despite being of similar magnitude, the binding of ferrous C*c* to C*c*O is of higher affinity than ferric C*c*. They demonstrate that the binding of ferrous C*c* induces structural changes in both the N- and C-terminal helices different to those which take place when binding ferric C*c*, which the authors ascribe to suggesting that protein rearrangement takes place primarily at the N-terminal helix and therefore constituting a possible gating step (Alvarez-Paggi et al., 2017). Interestingly, the strong interactions between the C-terminal helix and the C*c*O are still present in the ferric form following the redox reaction, thus it is possible that the ferric C*c*/C*c*O complex could supress the binding of ferrous C*c* in which the respiratory rate is regulated. The authors suggest that Lys13 could play a regulatory role in preventing back electron transfer through redox-linked structural rearrangements, the ε-amino group could move towards the haem *c* iron resulting in a decrease of electron affinity of the oxidised haem *c*. Furthermore, the authors suggest that as Lys13 is located at the centre of the C*c*/C*c*O interaction site, in which the side chain is buried within the protein interior, this would preclude protonation of the ε-amino group (Alvarez-Paggi et al., 2017). Instead, they suggest that the nitrogen atom is negatively polarised, therefore following complex formation, the ε-amino group could move toward the haem *c* iron, in which there is a decrease of electron affinity of ferric haem *c* thus preventing back electron transfer.

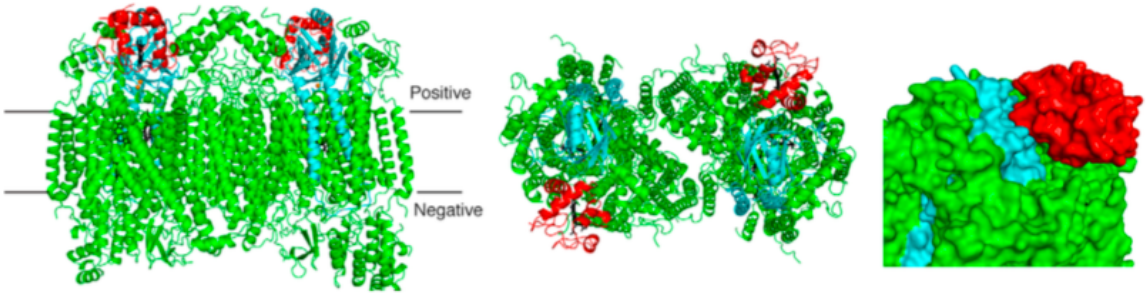

Figure 1.3 X-ray crystal structure of the mammalian C*c*/C*c*O complex, viewed from the trans-membrane surface (left) and the positive side (middle). The right panel shows an expanded view of the binding interface between C*c* and C*c*O subunit II. Figure taken from (Shimada et al., 2017).

A 2 Å X-ray crystal structure of the mammalian C*c*O/C*c* complex has recently been reported (Shimada et al., 2017) (Figure 1.3) and is in agreement with the previously determined key residue; namely Lys8, 13 and 87 and Gln12, and in agreement with recent kinetic studies (Sato et al., 2016). The authors suggest that the key residues are functionally relevant and not only involved in a redox-inactive encounter complex. The predicted electron transfer pathways that arise from the crystal structure do not involve a tryptophan residue in C*c*O, instead, it is suggested that the dominant pathway involves haem *c*, Cys14 and Lys13 from C*c*. This is followed by a through-space jump to Tyr105 of C*c*O that is in close proximity to Met207 (the axial ligand of the Cu_A site) (Alvarez-Paggi et al., 2017). The authors describe a novel scheme for the interaction between C*c* and C*c*O, coined "soft and specific" (Figure 1.4). This docking scheme is characterised by "a few "long arms" of hydrophilic residues, a small contact interface, a long span between the proteins, the presence of three solvent layers in the interface that form a H-bond network between both proteins

and a fluctuating C*c* that uses the interacting residues with C*c*O as a fulcrum" (Alvarez-Paggi et al., 2017).

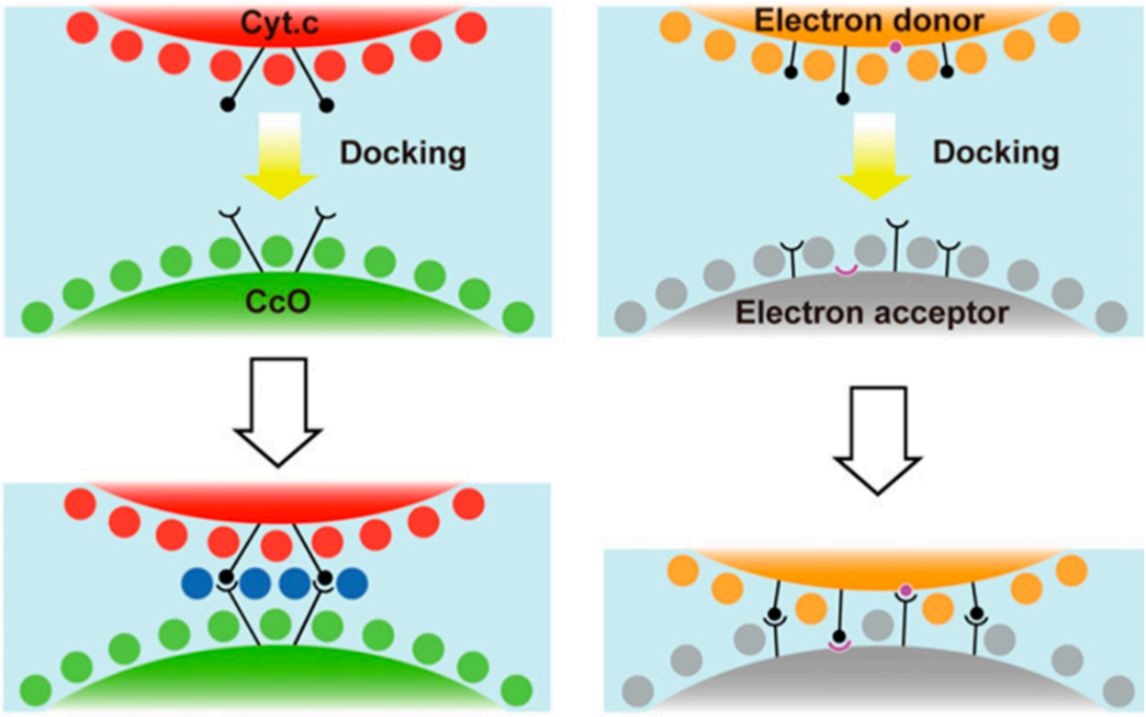

Figure 1.4 (Left) During interaction between C*c* and C*c*O, three layers of H_2O molecules are formed due to preservation of surface H_2O molecules being preserved on each respective protein during the encounter phase. C*c* and C*c*O interact specifically via the long sidechains arms of hydrophilic residues. H_2O molecules on the surface of each respective protein are represented by the red and green circles, blue circles represent the non-interacting H_2O molecules. The sidechains of residues involved in protein-protein interactions are represented by the black circles and semicircles.
(Right) Traditionally in other electron transfer systems, the complex forms by excluding H_2O molecules on the surface of each protein. Surface H_2O molecules are represented by orange and grey circles of their respective proteins colour. The main chains of residues involved in protein-protein interactions are represented by magenta circles and semicircles. Sidechains of residues involved in protein-protein interactions are represented by the black circles and semicircles. Figure taken from (Shimada et al., 2017).

Finally, there are two competing models which describe the dynamics of association between C*c* and C*c*O. The diffusion of C*c* within the intermembrane space may be governed by 3D Brownian motion in the bulk solvent, in which the motion is only affected by electrostatic interactions between the two respective proteins (Spaar et al., 2009, Gupte and Hackenbrock, 1988). Alternatively, there may be 2D diffusion along the membrane surface (Spaar et al., 2009, Gupte and Hackenbrock, 1988). Despite there being no clear evidence in favour of either model, it is likely that at physiologically relevant ionic strengths the 3D Brownian diffusion scenario is most probable (Gupte and Hackenbrock, 1988).

1.5 Cytochrome c and apoptosis

Apoptosis, a form of programmed cell death, has been appreciated for its physiological significance since the latter part of the 20st Century (Kerr et al., 1972, Liu et al., 1996, Kluck et al., 1997, Newmeyer et al., 1994, Paweletz, 2001, Kerr, 2002). Apoptosis displays a wide array of unique morphological features that are unique to programmed cell death (cell shrinkage, plasma membrane blebbing, chromatin condensation, nuclear membrane breakdown and formation of apoptotic bodies) and are distinguishable from cells undergoing senescence or necrosis (Kerr et al., 1972, Horvitz, 1999). Physiologically apoptosis serves to prevent an inflammatory response, as cells which have undergone apoptosis are rapidly cleared by phagocytes, apoptosis also contributes to the development of multicellular organisms, the prevention of cancers, immunological function, remodelling in the adult (such as mammary changes during pregnancy) and wound healing (Nijhawan et al., 2000, Opferman and Korsmeyer, 2003, Greenhalgh, 1998, Osborne, 1996, Tilly et al., 1991, Lund et al., 1996). It is of the utmost importance that apoptosis is tightly controlled for the

aforementioned reasons, particularly when one considers estimates that in an adult human ~ 10 billion cells are made every 24 hours to compensate for the apoptotic losses (Renehan et al., 2001). The molecular basis of apoptosis was elucidated during the 1990s by Horvitz and co-workers, who elegantly showed that in *Caenorhabditis elegans* there is intrinsic control of cell death in neuronal cells during development (Horvitz et al., 1994). In subsequent years, it was established that in *C. elegans* there are both positive and negative regulators of programmed cell death (Hengartner, 1999, Liu and Hengartner, 1999, Horvitz, 1999). Egl-1 initiates the apoptotic pathway by antagonising the negative regulator cell death abnormal (Ced)-9, facilitating release of Ced-4 which is subsequently able to recruit Ced-3 (Hengartner and Horvitz, 1994). Ced-3 is a cysteine protease and plays a pivotal, orchestrating role in apoptosis of *C. elegans* (Hengartner and Horvitz, 1994).

Subsequent research has shown that there are many human homologues of the pro- and anti-apoptotic proteins in *C. elegans*, highlighting that in both worms and mammals, apoptotic control is highly conserved (Hengartner and Horvitz, 1994, Zou et al., 1997, Hengartner et al., 1992, Vaux et al., 1992, Yuan et al., 1993, Yuan and Horvitz, 1992). Specifically, Ced-9 is homologous to the human oncogene product B-cell lymphoma-2 (Bcl-2) (Hengartner and Horvitz, 1994). Bcl-2 is associated in B-cell lymphoma following translocation and overexpression, as Bcl-2 negatively regulates apoptosis (Tsujimoto et al., 1985b, Tsujimoto et al., 1985a, Cleary et al., 1986, Graninger et al., 1987, Raffeld et al., 1987, Vaux et al., 1988, Hockenbery et al., 1990). This information highlighted how fundamentally linked apoptosis and oncogenesis are, as cancer can develop not only as a result of cell over-proliferation, but also through inhibition of apoptosis (Jiang and Wang, 2004). In addition to Ced-9 and the Bcl-2 proteins, the mammalian homologue of Ced-3 are the cysteine proteases known as

caspases (Thornberry and Lazebnik, 1998, Budihardjo et al., 1999). Under normal physiological conditions caspases are inactive in their zymogen form, however, prior to apoptosis procaspases are proteolytically cleaved to create a small and large subunit within the protein. This allows for two cleaved procaspases to interact and form a heterotetramer, at which point the substantial conformation change reveals the catalytic pocket and therefore activates the enzyme (Jiang and Wang, 2004, Walker et al., 1994, Wilson et al., 1994, Rotonda et al., 1996, Blanchard et al., 1999, Watt et al., 1999). Certain caspases can self-activate through autocatalysis, and these are known as initiator caspases, whilst others require activation though an upstream caspase (Thornberry and Lazebnik, 1998, Budihardjo et al., 1999, Jiang and Wang, 2004). An initiator caspase, once self-activated, triggers a cascade resulting in the activation of executioner caspases that abolish normal physiological cellular functions and activate other pro-apoptotic factors that result in programmed cell death (Thornberry and Lazebnik, 1998, Budihardjo et al., 1999).

C*c* plays a crucial role in apoptosis. Further research discovered that dATP, Apoptotic protein activating factor-1 (Apaf-1), Caspase-9 and C*c* must be present to activate caspase-3 (Zou et al., 1997, Li et al., 1997, Liu et al., 1996). Bcl-2 inhibits apoptosis by its ability to inhibit C*c* release from the mitochondrion (Yang et al., 1997). C*c* binds to Apaf-1 in a dATP/ATP dependent manner to form the apoptosome, the major caspase activating octomeric complex in mammalian cells (Zou et al., 1999). Proper regulation of apoptosis is vital for mammalian development and in the protection against cancers (Yoshida et al., 1998, Cecconi et al., 1998, Hakem et al., 1998, Kuida et al., 1998, Li et al., 2000, Soengas et al., 1999, Wang, 2001, Soengas et al., 2001).

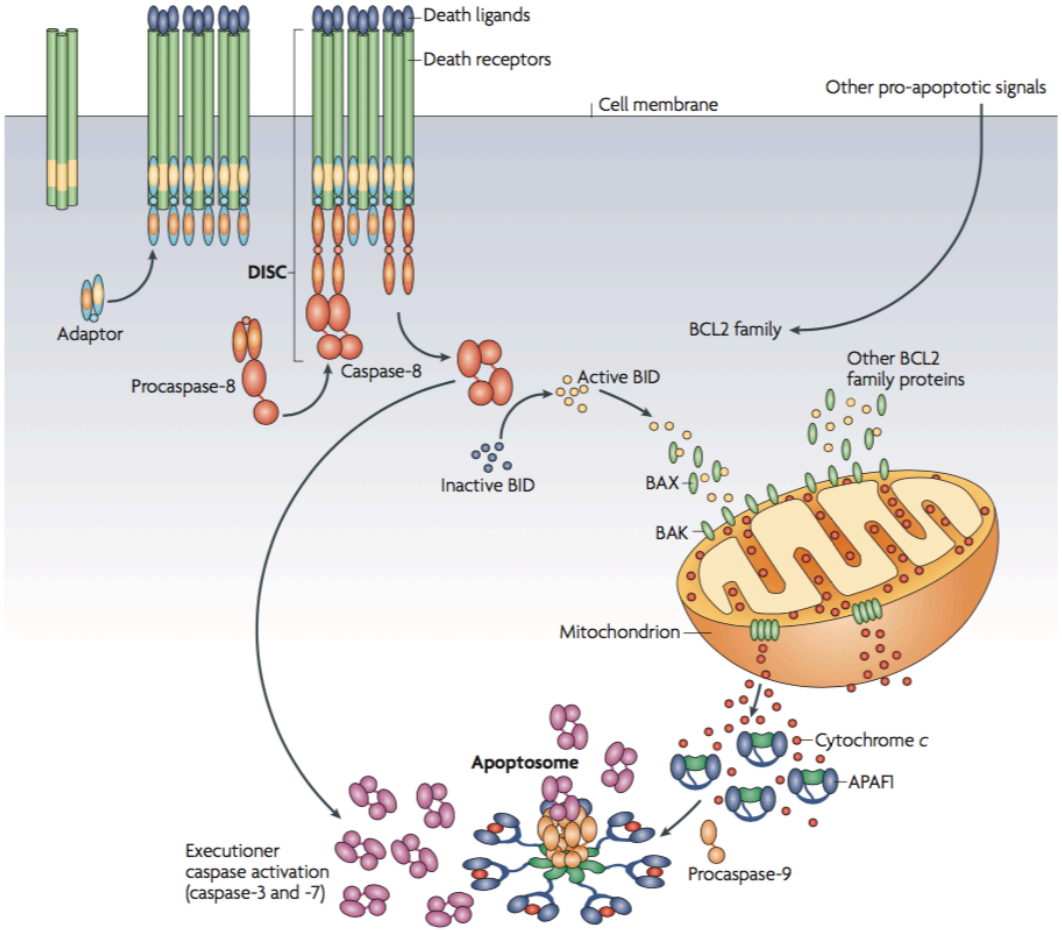

Figure 1.5 Schematic overview of extrinsic and intrinsic apoptosis pathways. The extrinsic pathway is initiated by a transmembrane death receptor upon binding a death ligand, for example FAS and FASL respectively. The result of this interaction is the formation of the death-inducing signalling complex (DISC), which facilitates the auto-activation of various caspases. In contrast, the intrinsic "mitochondrial" pathway is activated by various stimuli in which the outer mitochondrial membrane becomes permeabilised enabling the release of intermembrane space proteins into the cytosol. C*c* is a critical component of apoptosis due to its caspase activating role when associated with Apaf-1 in the apoptosome. Taken from (Ow et al., 2008).

The C*c* mediated, type 2 intrinsic (Figure 1.5) apoptotic pathway is significant, as can serve to amplify caspase activation occurring though alternative pro-apoptotic routes, such as the death receptor pathway and the cytotoxic T-lymphocyte-mediated pathways (Budihardjo et al., 1999, Luo et al., 1998, Lord et al., 2003, Li et al., 1998, Barry et al., 2000). This occurs as a result that, in these pathways, despite downstream executioner caspases being activated by the upstream proteases caspases-8 and -10, and Granzyme B for the death receptor and cytotoxic T-lymphocyte pathways respectively, these upstream caspases can both cleave and activate the pro-death member of the Bcl-2 family, Bid (Jiang and Wang, 2004, Luo et al., 1998). Truncated Bid (t-Bid), localises to the mitochondrion and induces C*c* release (Luo et al., 1998). The support provided by the C*c* mediated apoptotic pathway to other pro-apoptotic pathways is of paramount importance in Type 2 cells, as in these cells death receptor-mediated apoptosis is regulated by the C*c*/mitochondrial pathway, and the consequence of this is that it can be blocked by Bcl-2 anti-apoptotic members (Scaffidi et al., 1998). The mechanism by which this occurs is that the death-receptor pathway can be inhibited by Inhibitor of Apoptosis Proteins (IAPs), which serve to inhibit caspase activity, and to counter this inhibition the mitochondrial proteins SMAC/DIABLO must be released into the cytosol to antagonise the IAPs (Srinivasula et al., 2000, Sun et al., 2002). C*c*'s role in the amplification of the death-receptor mediated apoptosis pathway has profound implications with regard to therapeutics, both current and future, as chemotherapeutic drugs targeted to multiple pro-apoptotic pathways have, when combined, a synergistic effect that might overcome poor efficacy with an individual drug (Jiang and Wang, 2004). One would assume this cocktail approach would be of particular benefit to cancers of Type 2 cell origin (Jiang and Wang, 2004).

Ca^{2+} ion fluctuations also play a role in the release of C*c*, as apoptosis that occurs as a result of Ca^{2+} ionophores is dependent on the Bcl-2-like protein 11 (BIM) (Bouillet et al., 1999). Elevation in intracellular Ca^{2+} induces a permeability transition resulting in a positive feedback loop increasing the concentration of both C*c* and Ca^{2+} in the cytosol (Kroemer et al., 2007, Grimm and Brdiczka, 2007). In the early stages of apoptosis, low levels of C*c* are released from the mitochondrion, in which they interact with inositol-1,4,5-triphosphate receptors ($InsP_3R$) (Kroemer et al., 2007). Ca^{2+} interacts with $InsP_3R$, and in doing so functions as an inhibitor, the binding of C*c* to $InsP_3R$ relieves the inhibition, thus resulting in Ca^{2+} ion release from the endoplasmic reticulum and further C*c* release (Kroemer et al., 2007, Mootha et al., 2001, Wei et al., 2001).

1.6 Cytochrome c: The mitochondrion and interactions with cardiolipin

It is known that the proteins Bak and Bcl-2-like protein 4 (Bax), members of the pro-apoptotic group of Bcl-2 family proteins, function as the final gateway to C*c* release from the mitochondrion (Gross et al., 1999, Adams and Cory, 2001). However, it is also known that Bak and Bax function is regulated by the mitochondrial specific phospholipid, cardiolipin (CL) (Lutter et al., 2000, Kuwana et al., 2002).

The release of C*c* into the cytosol occurs via two phases, mobilisation followed by translocation through the outer mitochondrial membrane (OMM) (Ow et al., 2008). It has been suggested that mobilisation occurs through cristae remodelling, in which fusion of individual cristae and subsequent opening of junctions between cristae and the intermembrane space is required (Pellegrini and Scorrano, 2007). Kalanxhi and Wallace (2007) suggest that there is a significant proportion of C*c* associated with CL,

and that for C*c* to be effectively released from the inner mitochondrial membrane (IMM) the C*c*/CL complex must first be dissociated.

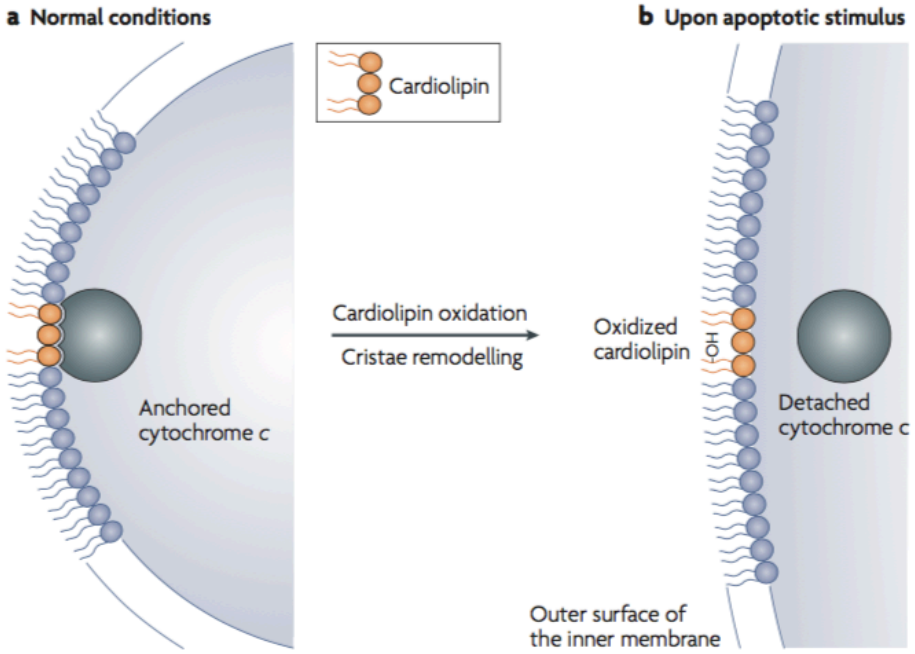

Figure 1.6 A model for C*c* release in which there is first mobilisation followed by translocation through the outer mitochondrial membrane, as a result of cristae remodelling followed by the opening of junctions between cristae and the intermembrane space (Pellegrini and Scorrano, 2007). Gonzalvez and Gottlieb have stated that a substantial fraction of C*c* is associated to the anionic phospholipid cardiolipin and it has been suggested that there is a high thermodynamic barrier to breaking the C*c*/CL complex (**a**) (Gonzalvez and Gottlieb, 2007, Kalanxhi and Wallace, 2007). (**b**) The oxidation of cardiolipin which occurs through a number of process, one of which is the CL/Cyt *c* complex, following the breaking of the complex there is an immediate increase in ROS through ETC dysfunction (Mootha et al., 2001, Zhao et al., 2003). As ROS can oxidise CL, the result is a positive amplification loop. Taken from (Ow et al., 2008).

Several works have demonstrated that the electrostatic interaction between basic C*c* and acidic phospholipid exist in rapid equilibrium under low ionic strength conditions (Nantes et al., 2001, Rytomaa and Kinnunen, 1994, Rytomaa et al., 1992). The lipid anchorage between C*c* and CL can be considered a rate-limiting step in the overall strong binding interaction between C*c* and the phospholipid membranes (Kalanxhi and Wallace, 2007). The reason for the rate limitation, is that there is likely to be a particularly high thermodynamic barrier associated with the passage of an anionic CL acyl chain, through the polar surface of the lipid bilayer (Kalanxhi and Wallace, 2007). This thermodynamic barrier can be overcome by CL oxidation, in which the affinity for C*c* is decreased (Figure 1.6) (Ow et al., 2008). There are four known oxidising agents of CL, phospholipase A_2, reactive oxygen species (ROS), an increased intracellular Ca^{2+} concentration and rather significantly, the C*c*/CL complex (Ow et al., 2008). It has been proposed that during pro-apoptotic events, there is a positive-feedback mechanism, of sorts, within the mitochondrion, in which following permanent C*c* detachment from the IMM, there is a rapid increase in the concentration of ROS due to ETC dysfunction, thereby providing a powerful stimulus for the further release of C*c* (Mootha et al., 2001, Zhao et al., 2003).

The electrostatic interaction between C*c* and CL is benign in relation to apoptosis, it is instead the far less frequent hydrophobic interaction (i.e. insertion of an acyl chain into the C*c* molecule) (Figure 1.7) which confers the peroxidase activity in C*c* (Kagan et al., 2005, Belikova et al., 2007). The peroxidase active C*c* can then oxidise the CL, breaking the protein-lipid complex, and allowing the CL to translocate to the OMM, whereby it can relieve the inhibition on the Bak and Bax proteins resulting in Mitochondrial Outer Membrane Permeabilisation (MOMP) and C*c* release into the cytosol (Kagan et al., 2005, Belikova et al., 2007).

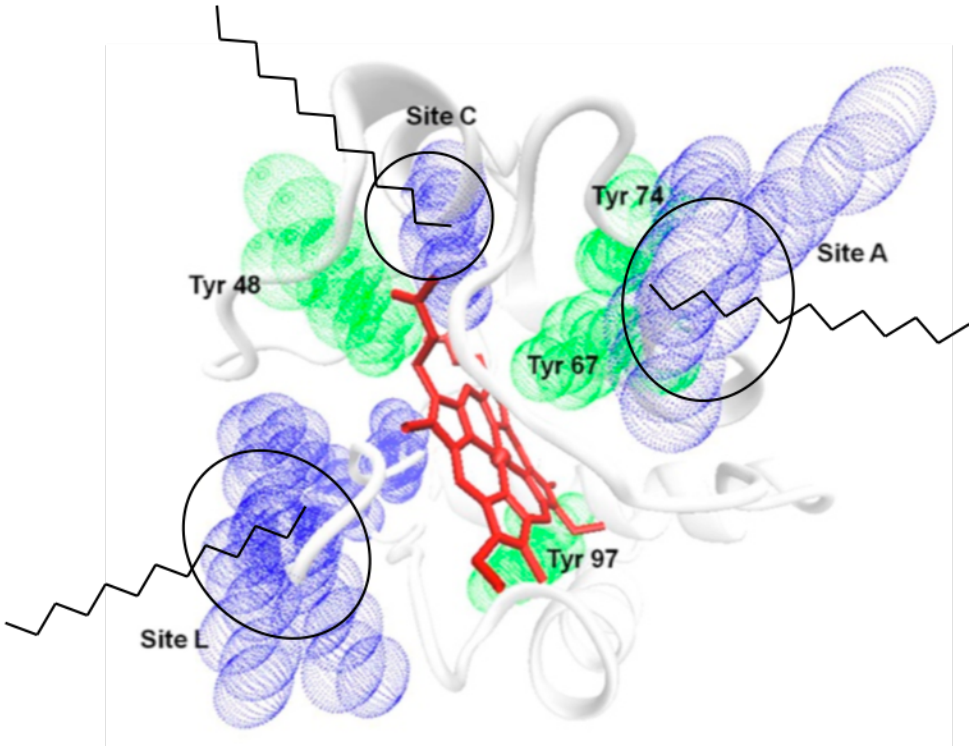

Figure 1.7 Schematic illustration of three of the proposed cardiolipin acyl chain insertion sites (Sites A, C and L) mapped onto the X-ray crystal structure of C*c*. It is not known whether one, or two cardiolipin acyl chains are inserted into the hydrophobic interior of C*c*. Adapted from (Alvarez-Paggi et al., 2017).

In multiple cell types, C*c* release causing apoptosis is a rapid, complete and ultimately irreversible process (Goldstein et al., 2000). Apoptosis is likely the most significant decision a cell makes, and therefore this process is regulated by multiple layers of control with much degeneracy/redundancy (Ow et al., 2008). The apoptosis antagonists of the Bcl-2 family function to prevent MOMP, by directly interacting with Bak and Bax thus inhibiting their oligomerisation, or by interacting with BH (Bcl-2 homology) 3-only proteins and disrupting their function (Youle and Strasser, 2008).

The BH3-only proteins BID and BIM are known to be the primary activators of Bax and Bak (Green, 2006). tBID (the truncated "active" form of BID) induces the oligomerisation of Bax and Bak thereby regulating the pore formation in the OMM

which allows for the release of Inter Membrane Space (IMS) pro-apoptotic factors into the cytosol (Wei et al., 2001, Eskes et al., 2000, Desagher et al., 1999, Kluck et al., 1999). An additional function of tBID is how it causes the cristae remodelling, when complexed with CL, that promotes C*c* mobilisation (Balakrishnan et al., 2007, Kim et al., 2004). It is known that the addition of tBID to cells having undergone MOMP results in a reduction in the concentration of CL, probably because of CL hydrolysis (Basanez et al., 2002, Giordano et al., 2005). It has been suggested that there is a temporal separation between BID and C*c* during their interactions with CL, in order to circumvent C*c* and BIDs conflicting pro-apoptotic activity, as it is known that tBID completely sequesters the peroxidase activity of the C*c*/CL complex (Tyurin et al., 2007).

1.7 Cytochrome c, cardiolipin and the extended lipid anchorage model

The C*c* mediated apoptosis pathway is well established, with its physiological and pathological significance clearly defined by research at the biochemical, genetic and cellular levels (Jiang and Wang, 2004). However, despite this, there are still fundamental questions that have yet to be conclusively answered, ranging from tissue specific regulation of these pathways and how this relates to development, to how these pathways are regulated in cells undergoing oncogenesis. One such question that remains unanswered is: what is the precise molecular mechanism by which C*c* undergoes a switch in function that results in transformation from electron shuttle into a powerful pro-apoptotic effector?

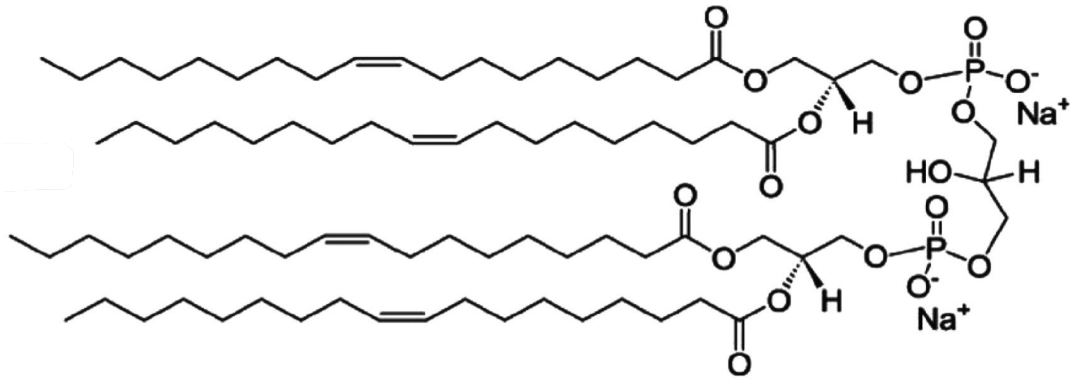

Figure 1.8 Chemical structure of Cardiolipin (diphosphatidylglycerol), with oxidisable acyl chains shown. Figure adapted from (Rajagopal et al., 2013).

CL (Figure 1.8) was first isolated by Pangborn (1942), the origin of the name stems from the fact that it was isolated from beef heart. However, it was Nicholls (1974) who conducted research into membrane interactions involving C*c*, which ultimately stimulated research into the C*c*/CL interactions. Cells experiencing normal physiological conditions contain CL exclusively located within the mitochondrion, and this is essential in the proper function of several enzymes required for energy metabolism (Hasan et al., 2011). CL may behave as a molecular chaperone in the sense that is able to bind with high affinity, and non-covalently, with a wide number of proteins such as Complexes I, III, IV and V of the respiratory chain including C*c* and creatine kinase (Schlame et al., 2000). Successful crystallographic studies have yielded insights about the potential binding site and biological function of CL in the C*c*R and C*c*O complexes (Shinzawa-Itoh et al., 2007) and have identified hydrogen bonding between the phosphate groups of CL and van der Waals interactions with the fatty acid acyl chains of CL (Lange et al., 2001).

To date there is no conclusive atomic resolution structural information on the C*c*/CL interaction. As CL contains two negatively charged phosphate head groups, and as C*c* bears a strong net positive charge at physiological pH, it is inevitable that electrostatic interactions will play a significant role in complex formation. Some study utilising model lipid bilayers has suggested that there is a strong electrostatic interaction between the negatively charged phospholipid and the positively charged C*c* which results in partial unfolding (Kagan et al., 2009b). These electrostatic interactions revolve around two sites, the A-site, (residues Lys72, Lys73, Lys86 and Lys87), and the L-site, (residues Lys22, Lys25, His26, Lys27 and His33) (Figure 1.7) (O'Brien et al., 2015) and it has been shown that these sites can be attenuated through salt titration (Kagan et al., 2009b). There is a third suggested interaction site, termed the C-site (Figure 1.7), incorporating a H-bonding interaction between Asn52 and a protonated CL head group (Rytomaa and Kinnunen, 1994). In addition, and perhaps surprisingly, it has become apparent that hydrophobic interactions are essential in the switch of C*c* function (Kalanxhi and Wallace, 2007).

Kinnunen and colleagues suggested a model for the interaction, in which a phospholipid acyl chain could enter the hydrophobic interior of C*c* (Kinnunen, 1992, Kinnunen et al., 1994, Rytomaa and Kinnunen, 1995). A similar model was suggested by Stewart et al. (2000), who observed a spin-state change in the haem iron, and suggested that acyl chain insertion causes dissociation of the distal Met80 haem ligand. Tuominen et al. (2002) were the first to provide experimental support via a spectroscopic

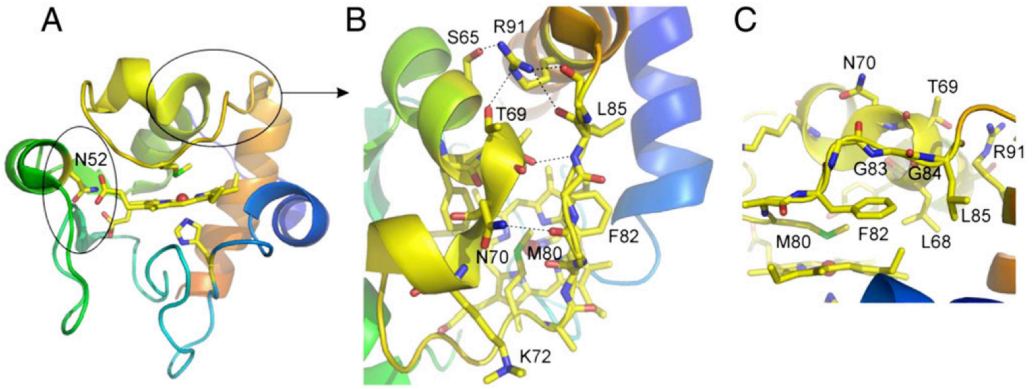

Figure 1.9 X-ray crystal structure of yeast cytochrome *c* (pdb entry 1YCC). **A** Circled regions highlight the proposed CL interaction sites based on the extended lipid anchorage model. The haem and both axial ligands are shown in stick form with the Asn52 highlighted. **B** provides a more detailed view of all residues involved in the cleft capable of accommodating a single CL acyl chain. The H-bonds which stabilise the cleft are shown as dashed lines. **C** provides a view of the putative hydrophobic channel situated bellow the cleft that functions to stabilise the CL acyl chain. Taken from Rajagopal *et al*. 2012).

investigation involving dibrominated CL and Zn^{2+} substituted C*c*, this model became known as the 'extended lipid anchorage' model. Although this model was used to describe the interaction with ferrous (Fe^{2+}) C*c*, it is also likely to account for the ferric (Fe^{3+}) form by unlocking the haem peroxidase potential (Kapralov et al., 2007, Kapetanaki et al., 2009). Despite the initial belief that the double bonds in the acyl chains were required to induce peroxidase activity (Belikova et al., 2006, Kagan et al., 2005), more recent research (Abe et al., 2011) has shown that these double bonds are not required. Early solid-state NMR (SS-NMR) studies (Spooner and Watts, 1991) suggested that the intercalation of an acyl chain in the hydrophobic interior of the protein causes partial unfolding driving the dissociation of the Met80 distal ligand.

The nature and location of the entry site(s) for acyl chain insertion are not unequivocally determined, however, there are two proposed sites that both rely on

surface openings which form hydrophobic channels that direct the acyl chain to the Met80 ligand (Figure 1.9A) (Rajagopal et al., 2012, Sinibaldi et al., 2010, Kalanxhi and Wallace, 2007). Studies with yeast ferrocytochrome *c* and CL found changes in binding strength between protein and liposomes were dependent on alterations in the electrostatic surface potential in localised areas (Stewart et al., 2000, Kalanxhi and Wallace, 2007). It was determined, based on the charge location on the surface of C*c*, that two parallel polypeptide strands corresponding to residues 67-71 and 82-85 formed clefts amenable to acyl chain insertion (Kalanxhi and Wallace, 2007). These chains form a hydrophobic channel situated to one side of the Met80 ligand, and thus could stabilise the interaction with a CL acyl chain (Stewart et al., 2000, Kalanxhi and Wallace, 2007).

Located at the top of the cleft lies the invariant Arg91 which participates in H-bonds particularly with the side chain OH group of Ser65 in yeast C*c* (Figure 1.9B) (Rajagopal et al., 2012). The invariant Asn70 forms a H-bond to the backbone carbonyl of Phe82, whilst the backbone carbonyl of Leu68 forms a H-bond to the backbone NH of the residue at position 84 (Figure 1.9B) (Rajagopal et al., 2012). Kalanxhi and Wallace (2007) suggested that Lys72 and 73, which are situated at the bottom of the cleft, facilitate an electrostatic interaction with the negatively charged head group of CL, serving two purposes, firstly, aiding stability of the complex, and secondly, facilitating the acyl chain to move through the cleft and into the hydrophobic channel. It has also been suggested that the neighbouring Lys86 and 87 form part of the binding surface (Kawai et al., 2005, Kostrzewa et al., 2000).

Studies on ferricytochrome *c* have identified the binding process to consist of two steps (Sinibaldi et al., 2008, Sinibaldi et al., 2010). The first of these requires binding to an electrostatic "A-site", a high affinity interaction, and secondly a lower

affinity hydrophobic interaction at the "C-site" (Figure 1.7) (Sinibaldi et al., 2008). The aforementioned A-site is suggested to be located near to Lys72 and 73 and the C-site near the invariant Asn52 (Sinibaldi et al., 2010). Sinibaldi and colleagues perturbed the second binding transition to CL through mutagenesis of the Asn52 to an Ile, and in doing so demonstrated the C-sites significance (Figure 1.7) (Sinibaldi et al., 2010). This is believed to suggest that the second insertion site for an acyl chain for an individual CL is localised around Asn52, whilst the first site is localised to the cleft at residues 67-71 and 82-85, obtained from studies involving ferrocytochrome *c* (Sinibaldi et al., 2008, Sinibaldi et al., 2010, Kalanxhi and Wallace, 2007).

A hydrophobic interaction is also required in activating the peroxidase activity in the C*c*/CL complex (Basova et al., 2007), which arises through the dissociation of the distal haem iron Met80 ligand, resulting in a penta-coordinate haem. The newly acquired peroxidase activity allows C*c* to carry out the oxidation of a single fatty acid chain in the CL molecule (Kagan et al., 2005). The oxidised CL results in dissociation of the C*c*/CL complex, with the oxidised CL then acquiring the function of a downstream effector in the apoptosis signalling pathway (Kagan et al., 2005). Under apoptotic conditions the OMM has high concentrations of CL due to migration from the IMM (Kagan et al., 2005), resulting in MOMP and the release of pro-apoptotic factors, including C*c* into the cytoplasm, although the exact mechanisms of pore opening are yet to be fully elucidated (Ow et al., 2008). Bergstrom and colleagues have provided insight into C*c*/CL mediated MOMP, by describing a direct visualisation of fluorescent C*c* crossing synthetic CL-containing membranes in the absence of other proteins (Bergstrom et al., 2013). Bergstrom and colleagues presented a model for C*c* leakage through the permeabilised OMM, where the formation of toroidal lipid pores is driven by initial C*c*-induced negative spontaneous membrane curvature and

subsequent protein unfolding interactions (Bergstrom et al., 2013). Ultimately, their work demonstrated how the C*c*/CL interaction is sufficient to enable C*c* escape from the mitochondrion, demonstrating that C*c* contributes to its own release during apoptosis (Bergstrom et al., 2013).

C*c* also binds to phosphatidylserine (PS), a plasma membrane anchored phospholipid which is also able to induce peroxidase activity in C*c* (Kagan et al., 2000). The C*c*/PS interaction plays a significant role in the cell death process, as it has been demonstrated that externalization of PS facilitates macrophage clearing of apoptotic cells (Kagan et al., 2002). Jiang et al. (2004) showed that C*c* functions as a catalyst to selectively oxidize PS. C*c* therefore not only carries out an essential respiratory function, but also crucial activities at the initial and end stages of apoptosis.

1.8 Structural studies of the Cc/CL interaction

The current evidence of the C*c*/CL interaction, the method of interaction and crucially its relation to apoptosis presents a paradox; how is it that this mechanism does not constantly result in a significant fraction of partially unfolded, peroxidase active C*c* *in vivo*? The result of which would be both a vastly diminished capacity to shuttle electrons in the ETC, and abhorrent apoptotic signalling. It has been proposed that partitioning of CL away from C*c* in the IMM contributes to regulating this process, however, this does not have definitive experimental support (Kagan et al., 2009a), particularly when considering that CL associates specifically with complex III and complex IV (Bazan et al., 2013) and that this interaction is essential for the proper formation of super-complexes containing complexes III and IV (Bazan et al., 2013, Pfeiffer et al., 2003). For C*c* to perform its primary biological role, CL must bind to each of these complexes.

The majority of approaches to characterise the interaction between C*c* and CL have essentially relied on either planar or positively curved lipid bilayers (O'Brien et al., 2015). However, the micro-environment of the IMM is quite different, as the cristae form extensive invaginations that result in high negative curvature, and therefore impose significant confinement (O'Brien et al., 2015). To obtain information of greater ecological validity on the C*c*/CL interaction, Wand and co-workers utilised the interior water core of a reverse micelle to solubilise C*c*, and then relied on the exterior surfactant shell as a host for CL to great effect (O'Brien et al., 2015, Nucci et al., 2014). Under suitable conditions, it is possible to not only encapsulate proteins within micelles, but when used with solvents of sufficiently low viscosity high resolution NMR data can be obtained enabling full structural characterisation of not only the protein, but also the interaction with ligands embedded in the surfactant wall, or dissolved in the aqueous core (Nucci et al., 2014, Wand et al., 1998, Babu et al., 2001, Valentine et al., 2010, O'Brien et al., 2015). The result of Wand and colleagues work supported for the electrostatic interactions at the A- and L-sites, however, they both elucidated a previously unidentified binding site encompassing residues Phe36, Gly37, Thr58, Trp59 and Lys60, and found no evidence of local unfolding, but instead found the tertiary structure of C*c* to remain fully intact (O'Brien et al., 2015).

Techniques involving SS-NMR spectroscopy have been used to shed further light on the interactions between C*c* and CL. Previous studies have demonstrated that the interaction with C*c* and CL results in partial unfolding of the protein, as a precursor to the apoptotic response (Spooner and Watts, 1991, Kagan et al., 2009b, Muenzner et al., 2013), however, a limitation of previous studies is not only a lack of site resolution, but also a lack of membrane curvature thus not reflecting the micro-environment within the mitochondrion (O'Brien et al., 2015). Further support for the interaction between

C*c* and CL without the induction of unfolding comes from the work of van der Wel and colleagues who used Magic Angle Spinning NMR (MAS-SS-NMR) spectroscopy to identify the site specific conformational changes that occur in both the ferric and ferrous forms of ^{15}N, ^{13}C uniformly labelled equine C*c* (eC*c*) when bound to CL bilayers (Mandal et al., 2015). The use of MAS-SS-NMR and Fourier Transform infrared spectroscopy (FT-IR) revealed that CL membrane bound C*c* displays significant dynamics, yet maintains its secondary structure (Mandal et al., 2015). Furthermore, in both two and three dimensional MAS-SS-NMR spectra they report that the CL bound C*c* displays a spectral resolution characteristic of a folded protein, and therefore exhibits structural homogeneity that is fundamentally inconsistent with the extensive membrane-induced unfolding previously reported (Mandal et al., 2015). They conclude that C*c* interacts with the CL membrane interface without significantly perturbing the lipid bilayer, and therefore despite membrane binding resulting in the C*c* pro-apoptotic peroxidase gain of function, they do not observe evidence of large scale unfolding events or penetration into the membrane core (Mandal et al., 2015). Thus, these two recent manuscripts oppose the long-held view that the C*c*/CL complex is a highly heterogeneous ensemble, whereby there is no "static" interaction between protein and lipid. Instead, the long-held view has been that the hydrophobic C*c*/CL interaction results in considerable disruption of the native compact protein structure resulting in intermediate conformations (Kagan et al., 2009b). These intermediate conformations would lie somewhere between the fully folded and unfolded tertiary structural states, known as a "molten globule", defined as a compact conformation possessing a secondary structure comparable to that of the native state, but with greater tertiary structural fluctuation as a result of enhanced intramolecular motions (Pinheiro and Watts, 1994, Pinheiro et al., 1997, Muga et al., 1991, Spooner and Watts, 1992).

1.9 Human cytochrome c and thrombocytopenia 4

Knock-in mice with a mutant C*c* having a disrupted intrinsic apoptosis signalling pathway, so that C*c* is unable to activate Apaf-1, but still retain the ETC activity display enlarged brains and abnormal lymphocyte homeostasis (Hao et al., 2005). Despite these drastic developmental and physiological abnormalities other tissues display minimal phenotypic abnormalities (Hao et al., 2005). This information raises the question; is mitochondrial C*c*-induced caspase activation rate limiting in apoptosis (Ekert and Vaux, 2005). As the knock-in mice seldom survive it was previously not possible to evaluate the role of C*c* in apoptosis after birth (Ekert and Vaux, 2005).

However, Morison and colleagues studied a large New Zealand family with a 6-generation pedigree of mild autosomal dominant thrombocytopenia, thrombocytopenia-4 (THC-4) (Morison et al., 2008). The average platelet count of the 29 family members was 109 x 10^9/l (healthy range 150 – 450 x 10^9/l), however the platelet morphology and volume were normal, in addition to other peripheral blood counts (Morison et al., 2008). Interestingly, the clinical observations of thrombocytopenia were either mild or absent, individuals displayed normal longevity, fertility and fitness, additionally there was no evidence of neurodegenerative, muscular, eye, renal diseases or diabetes (Morison et al., 2008).

Morrison and colleagues identified a G-to-A substitution at nucleotide 132 of exon 2 in the CYCS gene on chromosome 7p15.2, the result of which is a protein level substation at residue 41 in C*c* (G41S) (Morison et al., 2008). C*c* is highly conserved, and Gly41 is invariant in 113 eukaryotic species (Banci et al., 1999). A total of 26 family members were found to be heterozygous for the G41S mutation, with a WT/G41S ratio of 2:1 (Morison et al., 2008). Platelets form in the bone marrow, where

megakaryocytes undergo a compartmentalised activation involving the intrinsic apoptosis pathway, but without nuclear DNA fragmentation (De Botton et al., 2002). The protoplatelets circulate for 10 days before undergoing apoptosis and subsequent phagocyte clearing (Mason et al., 2007). Thrombocytopenia results from either inefficiency in platelet formation, or their premature death. However, in the case of the G41S variant phenotypes, it is a reduction in platelet formation resulting from increased apoptosis which is responsible (Morison et al., 2008).

The G41S mutation is located near to Lys39, a residue known to be involved in the interaction between hC*c* and Apaf-1, and it was shown that the G41S variant of hC*c* results in significantly greater cleavage of the caspae-3 substrate DEVD-AMC (Morison et al., 2008, Olteanu et al., 2003, Yu et al., 2001). G41S was the first variant of hC*c* know to increase cellular apoptotic activity, indeed, engineered mutations previously studied either had no effect, or decreased apoptotic activity (Morison et al., 2008, Olteanu et al., 2003, Sharonov et al., 2005).

In 2013, De Rocco and colleagues reported on the second novel mutation of the CYCS gene (Y48H), present in a small Italian family with 4 individuals affected by THC-4 (De Rocco et al., 2014). As in the case of the G41S variant, individuals carrying the Y48H variant have platelets that are both of normal size and morphology and only partially reduced in number (De Rocco et al., 2014). The measured platelet count in individuals expressing the Y48H phenotype was comparable to that of the G41S carriers, with a range of 73 – 135 x 10^9/L, however, interestingly, the respiratory competency of both G41S and Y48H were shown to be lower than that of the WT protein by some 30 % in mammalian cell experiments, with G41S conferring the greatest loss of respiratory efficiency (De Rocco et al., 2014).

Johnson and colleagues have recently published their genomics work using next-generation sequencing to study the exomes of 55 patients consisting of 37 index cases and 18 additional family members (Johnson et al., 2016). Their work has highlighted a number of genes that display pathogenic, or likely pathogenic variation at the protein level associated with Thrombocytopenia (Johnson et al., 2016). Interestingly, they identify the third novel missense mutation in the CYCS gene, coding for A51V, and designate the mutation as "likely pathogenic" (Johnson et al., 2016). As the A51V mutation is in the 40-57 Ω-loop, as is the case with both G41S and Y48H, one speculates that the A51V mutation is also pathogenic to a comparable extent to that of the G41S and Y48H variants. Unfortunately, there is extremely limited clinical information on the A51V variant, and yet to be biochemical or biophysical investigation into the proteins structural dynamics or spectroscopic features.

1.10 Peroxidase activity

As in the case of classical peroxidases (Veitch, 2004, Volkov et al., 2011), C*c* follows a mechanism in which H_2O_2 reacts with the Fe(III) resting state producing "Compound I", with a Fe(IV)=O haem and an adjacent radical (Yin et al., 2017). The resting state is regenerated by the subsequent abstraction of H from organic substrates (Lawrence et al., 2003), and reactions between the newly formed radicals and O_2 yield the stable oxidation products (Xu and Chance, 2007, von Sonntag and Schuchmann, 1991). In contrast to C*c*, classical peroxidases possess a penta-coordinate haem, in which the distal (hexa-coordinate) site is either vacant or loosely occupied by a bound H_2O (Veitch, 2004, Volkov et al., 2011). The penta-coordinate haem enables Fe/H_2O_2 interactions that are essential for initiating the catalytic cycle (Godoy et al., 2009, Bren and Raven, 2017, Abe et al., 2011, McClelland et al., 2014, Diederix et al., 2002, Wang

et al., 2007). It is therefore paradoxical that C*c* can be peroxidase active given its hexa-coordinate haem (Bushnell et al., 1990). A likely explanation lies in the transient formation of a penta-coordinate species (Hannibal et al., 2016, Nold et al., 2017, Milazzo et al., 2017, Amacher et al., 2015, Karsisiotis et al., 2016, Diederix et al., 2002, Sutin and Yandell, 1972, Xu et al., 1998, Garcia-Heredia et al., 2010). It is known that rupture of the Met80-Fe bond through protein unfolding (Bren and Raven, 2017, Diederix et al., 2002), chemical (Hannibal et al., 2016, Capdevila et al., 2015, Chen et al., 2002, Amacher et al., 2015, Wang et al., 2014, Abriata et al., 2009), or mutational modification (Godoy et al., 2009, McClelland et al., 2014, Wang et al., 2007, Moreno-Beltran et al., 2017, Karsisiotis et al., 2016, Wang et al., 2014, Josephs et al., 2014, Tognaccini et al., 2016) enhance C*c* peroxidase activity.

The proximal His18-Fe ligand is robust in C*c*, whereas the distal Met80 ligand is located within a flexible 71-85 Ω-loop (Xu et al., 1998) and allows for non-native ligands (Hannibal et al., 2016, Gu et al., 2017). Alkaline solution conditions result in "alkaline conformers" in which the Met80 is replaced by either Lys72, 73 or 79 as the hexa-coordinate distal haem ligand (Nold et al., 2017, Garcia-Heredia et al., 2010, Abriata et al., 2009, Assfalg et al., 2003, Döpner et al., 1998). The displacement of Met80 can occur in neutral pH ranges through a variety of means (Hannibal et al., 2016, Amacher et al., 2015, Abriata et al., 2009, Gu et al., 2017, Garcia-Heredia et al., 2011), including Tyr67 modification (Tognaccini et al., 2016, Gu et al., 2017, Ying et al., 2009). It is also known that C*c*/CL binding (Abe et al., 2011, Kagan et al., 2009b, Serpas et al., 2016) can cause the displacement of Met80 by a Lys or His (Bradley et al., 2011, Milazzo et al., 2017, Yanamala et al., 2014).

Interestingly, and counterintuitively, the non-native alkaline conformers of C*c* display enhanced peroxidase activity to that of the native protein, despite their hexa-

coordinate haem ligation (Godoy et al., 2009, Abe et al., 2011, Hersleth et al., 2006, Diederix et al., 2002, Wang et al., 2007, Amacher et al., 2015, Abriata et al., 2009, Garcia-Heredia et al., 2011, Belikova et al., 2006), and due to the Lys-Fe bond being more stable than the Met80-Fe bond (Kitt et al., 2017, Amacher et al., 2015, Abriata et al., 2009, Garcia-Heredia et al., 2011, Belikova et al., 2006, Capdevila et al., 2015). This further suggests that the transient population of a penta-coordinate haem species facilitates catalysis (Hannibal et al., 2016, Nold et al., 2017, Milazzo et al., 2017, Amacher et al., 2015, Karsisiotis et al., 2016, Diederix et al., 2002, Sutin and Yandell, 1972, Xu et al., 1998, Garcia-Heredia et al., 2010).

Certain catalysed reactions display an initial lag-phase, from a variety of mechanistic origins, though the behaviour is often interpreted to reflect the *in-situ* activation of a pre-catalyst species (Widegren et al., 2003, Haw et al., 2003, Wunder et al., 2011). Native C*c* peroxidase assays display an initial lag phase (McClelland et al., 2014, Garcia-Heredia et al., 2010, Radi et al., 1991, Karsisiotis et al., 2016), Yin and co-workers have considered this lag phase and provided further mechanistic insights into the structural modifications that result in C*c* peroxidase activity using mass spectrometry (Yin et al., 2017).

Yin and co-workers were able to demonstrate the occurrence of C*c* self-oxidation in the presence of H_2O_2, in which the generation of oxidised proteoforms possess enhanced peroxidase activity (Yin et al., 2017). Their work demonstrates that H_2O_2-induced modifications proceed initially with oxidation of Tyr67, followed by the permanent displacement of the hexa-coordinate Met80 (Yin et al., 2017). They propose that the actual peroxidase activation step corresponds to side chain carbonylation, which they speculate likely occurs at Lys72/73 (Yin et al., 2017). Ultimately, they demonstrate that the Tyr67-oxidised/carbonylated form, with penta-coordinate haem,

is in fact the true peroxidase-active structure of C*c* (Yin et al., 2017). This work has provided insight into the structure-function mismatch of hexa-coordinate haem resulting in peroxidase activity in native C*c*.

It has been known for some time that the loss of axial coordination of Met80, driven by CL binding, causes an open haem structure which facilitates the haems peroxidase potential, in which the porphyrin molecule of the haem functions as a source of electrons (Diederix et al., 2002). However, Josephs et al. (2014) have found that mutations at residue 41 in both human and mouse C*c* can enable peroxidase activity without prior loss of Met80 haem coordination and protein unfolding. They also found that the effects of CL binding and residue 41 mutation did not result in cumulative peroxidase enhancement, suggesting that CL binding confers peroxidase activity in the protein through the same mechanism as residue 41 mutation, which they suggest is due to disruption of the 40-57 Ω-loop and the resulting H-bonds which bind to haem ring A, ultimately facilitating H_2O_2 access to the haem (Josephs et al., 2014). The work by Josephs and colleagues is however, conflicting with peroxidase activity assays by Rajagopoal and co-workers, and the data presented in Chapter 4 (Rajagopal et al., 2013, Karsisiotis et al., 2016).

The Pletneva group have utilised Dansyl variants of eC*c* to probe the steps in this functional structural transformation. 5(DimethylAmino)Napthalene-1-Sulfonyl chloride (Danysl chloride) is a highly sensitive fluorescent reagent used in Fluorescence Resonance Energy Transfer (FRET) experiments to study protein folding and dynamics (Gray, 1967). Muenzner and co-workers were able to show the occurrence of four discrete steps involving rapid protein/liposome binding, rearrangement of substructures with small unfolding energies, partial insertion of protein into the lipid bilayer and lastly extensive restructuring resulting in an open

conformation ensemble (Muenzner et al., 2013). Pletneva and colleagues found that the open conformation also serves to free the C-terminal helix to facilitate C*c* translocation through CL membranes (Muenzner et al., 2013). Previous studies by Pletneva and co-workers have used time-resolved FRET (TR-FRET), fluorescence correlation spectroscopy and biolayer interferometry to measure the interconversion between the open and closed conformation states and found that C*c*/CL binding is a peripheral binding event rather than deep protein insertion into the membrane. Hanske and colleagues conducted a TR-FRET investigation measuring four Dansyl labelled variants of C*c* and found that a fraction of the C*c*/CL ensemble is substantially denatured resembling the Guanidine hydrochloride unfolded state (Hanske et al., 2012). Their findings support previous works showing that electrostatic interactions particularly in the C-terminus of the protein are involved in CL induced unfolding.

1.11 Scope of this Thesis

The work reported in this thesis aims to meet two main goals, the first being to develop a solution-based NMR spectroscopy technique based on previously established Hydrogen-Deuterium (H/D) Exchange methodologies, that would provide a platform to study soluble protein/phospholipid interactions. This H/D exchange methodology would, in principle, provide salient structural information on the hC*c*/CL interaction, yielding much needed structural insights at the single amino acid residue resolution.

The second goal of this PhD project is to further our insights into the mechanism(s) behind hC*c*'s switch from the primary, life sustaining respiratory role, to that of a powerful peroxidase active pro-apoptotic effector. Reported in this Thesis is a range of biochemical and biophysical techniques, which one hopes, provide a coherent and consistent picture behind hC*c*'s disease mechanism.

In addition to studying the disease variants G41S and Y48H in the 40-57 Ω-loop of hC*c*, other variants in the 71-85 Ω-loop I81A, V83G and a double mutant I81A/V83G were also constructed and studied in addition to the WT protein. Specifically, this Thesis uses 1-, 2- and 3-dimensional solution NMR spectroscopy to obtain structural and dynamic information on the disease variants of hC*c*, in addition to that of the WT protein. Circular Dichroism spectroscopy has been used to report on both the secondary structural content of the aforementioned proteins, but also to determine their chemical stability through GuHCl denaturation titrations. The X-ray crystal structure of the Y48H variant has been determined, providing direct comparisons with the previously determined WT hC*c* and G41S variant X-ray crystal structures (Rajagopal et al., 2013). UV-visible spectroscopy has been used to characterise the optical spectra of the variant proteins and stopped-flow spectroscopy has been used extensively to determine the mechanism behind hC*c*'s peroxidase activity, further probing the properties of the aforementioned variants. Finally, Electron Paramagnetic Resonance (EPR) spectroscopy has been used to determine the properties of a high-spin intermediate species, observed during pH-jump stopped-flow experiments.

Chapter 2

Backbone resonance assignments of ferric human cytochrome *c* under native aqueous conditions and acid-denatured in dimethylsulfoxide

---

Results from this Chapter has been published in:

Karsisiotis, A.I., Deacon, O.M., Rajagopal, B.S., Macdonald, C., Blumenschein, T.M.A., Moore, G.R., Worrall, J.A.R. "Backbone resonance assignments of ferric human cytochrome *c* and the pro-apoptotic G41S mutant in the ferric and ferrous states" (2015) *Biomol. NMR Assign.*, **9**, 415-419.

Karsisiotis, A.I., Deacon, O.M., Macdonald, C., Blumenschein, T.M.A., Moore, G.R., Worrall, J.A.R. "Near-complete backbone resonance assignments of acid-denatured human cytochrome *c* in dimethylsulfoxide: A prelude to studying interactions with phospholipids" (2017) *Biomol. NMR Assign.*, **11**, 165-168.

2.1 Introduction

2.1.1 NMR spectroscopy

Nuclear Magnetic Resonance (NMR) is a physical phenomenon in which certain atomic nuclei absorb and re-emit electromagnetic radiation. Select elemental nuclei possess a variety of characteristic spins (I), a quantum phenomenon that exists as either an integral value $I = 1, 2, 3\ldots$, a fractional spin whereby $I = ½, 3/2, 5/2\ldots$ or no spin $I = 0$ (Keeler, 2010). The most useful nuclei for NMR spectroscopic purposes are the $I = ½$ nuclei (^{1}H, ^{15}N, ^{13}C, ^{19}F and ^{31}P). Such nuclei, when in the presence of an external magnetic field (B_0) display two precisely opposing spin states, either the ground state ($I = + ½$), or a higher energy level state ($I = – ½$) (Figure 2.1). These are respectively known as the "up and down" spin states as the magnetic moment of $I = + ½$ spin is pointing along the north pole of B_0, whereas the higher energy level $I = – ½$ spin is pointing towards the south pole of B_0 (Figure 2.1). The nuclear spin vectors do not align perfectly with or against B_0, thus a permanent torque is applied on the magnetic moment (μ_N) (Campbell, 1984). NMR active nuclei also possess the property of angular momentum as a result of their nuclear spin. The net result of angular momentum and torque is precession, the frequency of which is defined as $\omega_0 = \gamma B_0$, where γ is the unique proportionality constant of a given nuclei and ω_0 is the Larmor frequency (Campbell, 1984). Figure 2.2 illustrates how in the absence of an external magnetic field, the energy separation between the two quantum spin states of a nuclei is 0, and that upon increasing field strength, this energy separation is increased.

$I = > ½$ nuclei are also able to interact with magnetic fields, however, they have an additional property known as a nuclear quadrupole moment (Q). A Q allows the nuclei to interact with the electric fields that are produced by neighbouring electrons

and nuclei, and these interactions leads to significant spectral modifications that complicate NMR spectroscopy.

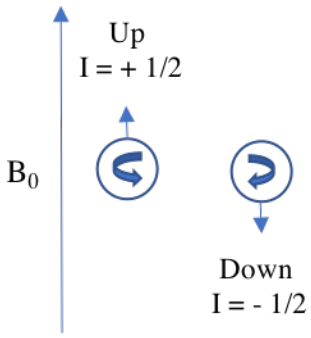

Figure 2.1 Schematic depiction of the opposing spin states of I = ½ nuclei in an external magnetic field (B_0).

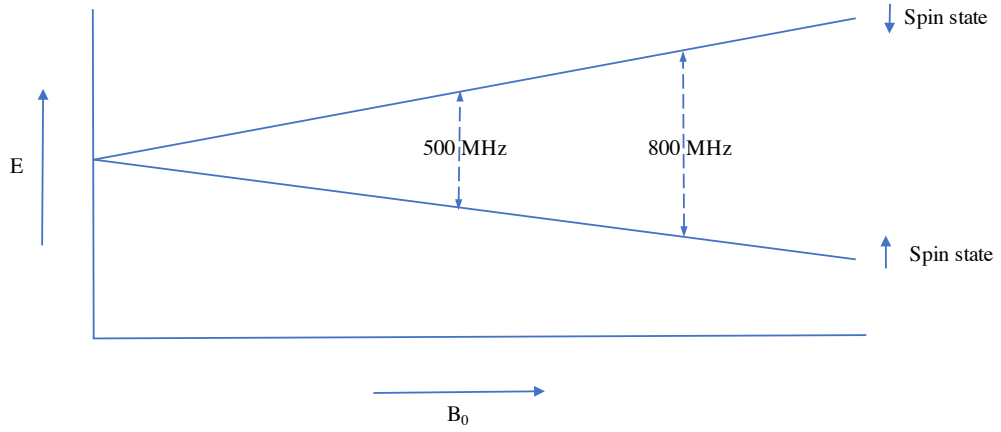

Figure 2.2 Schematic representation of the increasing energy separation between nuclei with spins of I = ½ in an increasing external magnetic field (B_0). The "down" spin state (southward facing arrow) is at a higher energy level, then that of the "upward" spin state (north facing arrow).

2.1.2 Magnetisation

As samples used in NMR spectroscopy have a large number of spins, classical physics can be used to describe the properties of nuclear magnetisation, defined as the magnetic moment per unit volume of sample (Campbell, 1984). The magnetisation is a vector, the specific components of interest in NMR spectroscopy are the M_z (defined along the B_0 direction) and the M_x and M_y components (defined at right angles to B_0) (Figure 2.3) (Campbell, 1984). The M_z component depends on the population difference between the up and down spins with respect to B_0, namely the N_1 and N_2 spins respectively (Campbell, 1984).

$$M_Z = \gamma h\ (N_1 - N_2)$$

The M_{xy} components arise because the spins do not align perfectly along B_0. In an NMR sample, each individual spin is precessing about B_0 and so it is convenient to bring all of the spins to a common origin, as shown in Figure 2.3. Under equilibrium conditions the spins are randomly distributed in which there is no net M_{xy} component ($M_{xy} = 0$) (Campbell, 1984). On application of a rotating radiofrequency (RF) field that precisely matches the frequency of precession ($\omega_0 = \gamma B_0$), the spins resonate and the random distribution changes to a coherent one in which there is net a M_{xy} component (Figure 2.3). Such spin systems are said to be phase coherent, due to their net M_{xy} component (Campbell, 1984).

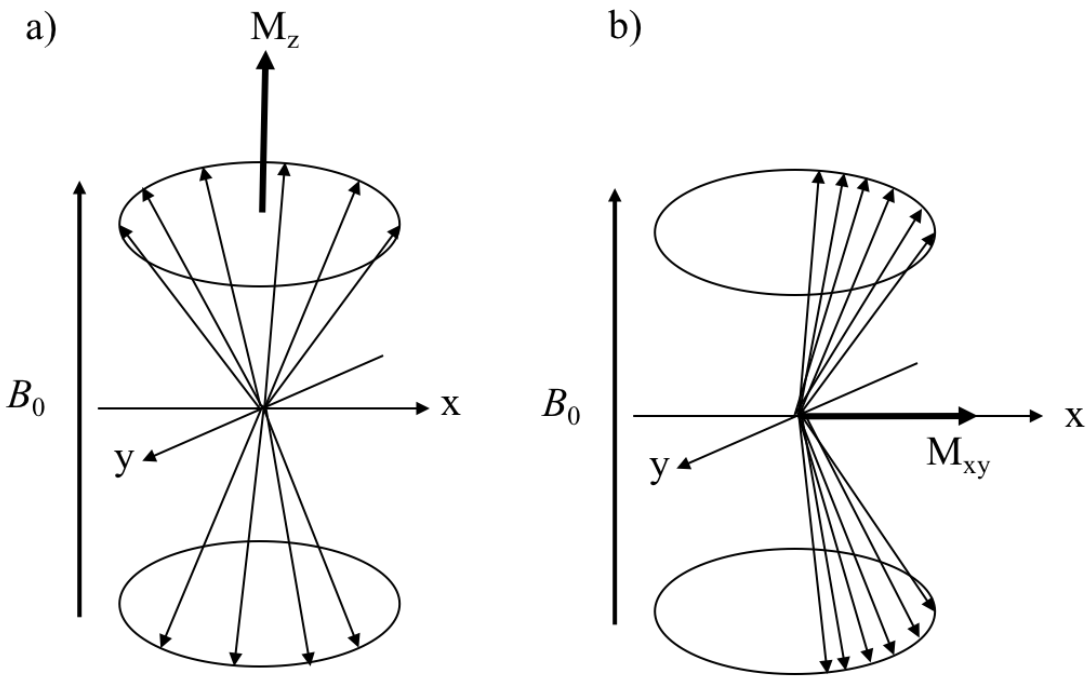

Figure 2.3 The numerous individually precessing spins in an NMR sample have a common origin. In a) there are a greater number of spins oriented along the B_0 direction (+ z). The result of which is a net M_z vector with no phase coherence in which M_{xy} = 0.

2.1.3 Data acquisition

Usually in spectroscopy a spectrum is measured by sweeping the applied radiation frequency. An alternative approach is the transient-response method, which forms the basis of modern NMR spectroscopy (Campbell, 1984). The transient in NMR spectroscopy, known as the Free Induction Decay (FID), is a complex sinusoidal signal that contains all of the samples frequencies. In order to interpret the FID, so that the individual frequencies may be resolved, a Fourier Transform must be carried out.

A typical NMR experimental setup is as follows: A large B_0 field, typically 2 – 21 T is applied to the sample. In order to increase the B_0 field homogeneity, the sample is spun about its vertical axis. In order to generate phase coherence amongst the nuclear spins, a rotating magnetic field is applied at right angles to the B_0 field (B_1). The result of the B_1 field are net M_{xy} components that precess at frequency ω_0 (Campbell, 1984). Phase coherence is lost via Relaxation processes, with equilibrium reached ($M_{xy} = 0$) after longer timescales. This relaxation process typically results in an exponential decay of M_{xy} with time constant T_2. The result of which is a transient signal with frequency ω_0 and decay rate $1/T_2$ (Campbell, 1984). The FID is complex as contains many signals with different frequencies (ω_0) and decay rates ($1/T_2$). However, as mentioned previously the FID's time and frequency domains are linked by FT, and in carrying out a FT on the FID generates the NMR spectrum (Figure 2.4).

The signal-to-noise ratio from a single NMR experiment is usually very poor, so it is possible to conduct multiple scans which use time averaging to improve the signal. After N number of scans the protein signal will be N times greater, however, as the noise is random it increases at the square root of N, hence it is routinely possible to vastly improve the spectral quality through multiple scans (Keeler, 2010). The

intensity of an NMR signal can be increased through higher field strength spectrometers, which increase the equilibrium magnetisation by increasing the energy separation between the opposing spin states (Figure 2.2) (Keeler, 2010). However, NMR signal intensity is also dependent on the gyromagnetic ratio (γ) of the detected nuclei (Keeler, 2010). For example, ^{1}H nuclei have a γ of 267.513 10^{6} rad s^{-1} T^{-1}, whereas ^{13}C and ^{15}N nuclei have a γ of 67.262 and -27.116 10^{6} rad s^{-1} T^{-1}, respectively. This variation in nuclei sensitivity is exploited in an Insensitive Nuclei Enhanced by Polarisation Transfer (INEPT) experiment, whereby weaker signals from lower sensitivity nuclei can be enhanced through the transfer of equilibrium magnetisation from a higher sensitivity nuclei (Keeler, 2010). This is fundamental in the context of multi-dimensional NMR spectroscopy, such as the 2D Heteronuclear Single Quantum Correlation (HSQC) which correlates the single bond proton coupling to either the ^{13}C or ^{15}N nuclei and reports on the NH groups of a protein.

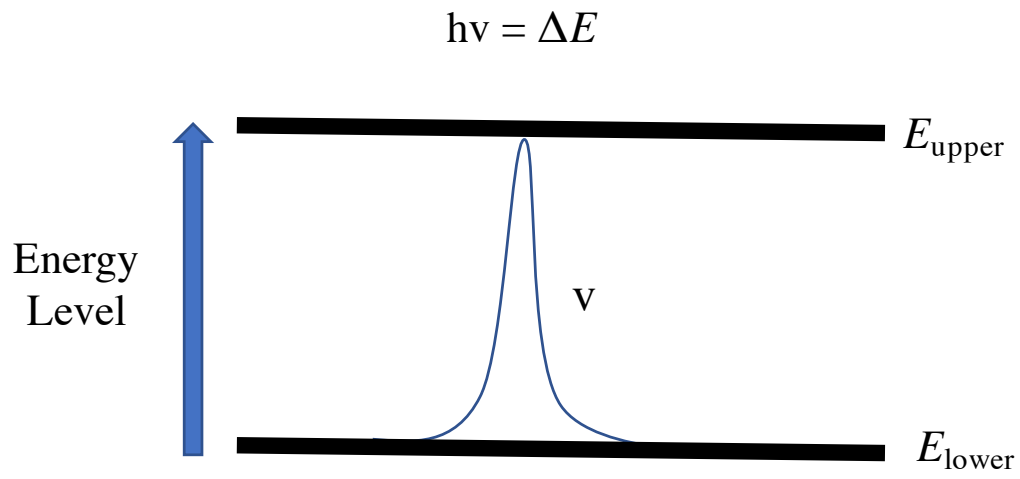

Figure 2.4 Schematic representation of the basic description of all spectroscopies, whereby a photon is absorbed so long as its energy (hv) matches the difference in energy between the two energy levels ($E_{upper} - E_{lower}$). This gives rise to an absorbance signal in the resulting spectrum at frequency v. Adapted from Keeler (2010).

The applied pulse B_1 can be defined in terms of angles. Precession can be extended to the rotating B_1 field by the expedient of using a rotating reference frame that matches the frequency of B_1. Figure 2.5 displays the instant at which B_1 is applied, with B_1 along the rotating x' axis and the equilibrium magnetisation along the z axis. The M_0 component precesses around B_1, with the frequency of precession defined as $\omega_1 = \gamma B_1$ (Campbell, 1984). ω is an angular frequency and therefore the M_0 angle of rotation is $\theta = \gamma B_1 t$, where t is the duration of the B_1 pulse. Following a 90 ° pulse, $M_{xy} = M_0$, whereas following a 180 ° pulse, $M_z = -M_0$ and $M_{xy} = 0$ (Campbell, 1984).

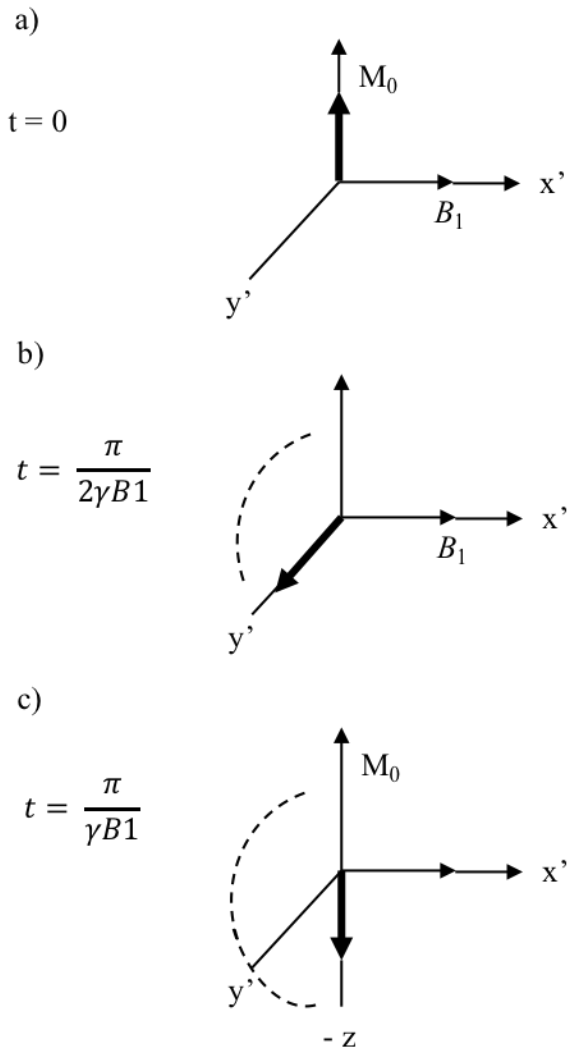

Figure 2.5 The effect upon application of a rotating B_1 field on the magnetisation M_0. x' and y' are rotating reference frames of equal frequency to B_1. b) and c) correlate to 90 ° and 180 ° pulses, respectively. Adapted from (Campbell, 1984).

2.1.4 NMR spectral parameters

There are four phenomena that constitute an NMR spectrum of a particular group: The intensity/area (I); the chemical shift (δ) that defines the position on a frequency scale; the multiplet structure which relates to the J-constant and finally the T_2 relaxation time that influences linewidth (Campbell, 1984). A fifth phenomenon is the T_1 relaxation time, though this relates to the lifetime of a spin within an energy level.

2.1.5 Chemical Shift

Atomic nuclei are shielded from the B_0 field due to the presence of the surrounding electrons. The B_0 field induces currents within the electron clouds that reduce the effective field experienced by the nucleus, as the electrons typically oppose B_0. These induced fields are directly proportional to B_0 and can be written as

$$B_{\text{eff}} = B_0(1 - \sigma)$$

where σ is a shielding constant dependent on the nature of the surrounding electrons (Campbell, 1984). Thus, different nuclei within a sample experience different magnetic fields depending on their local chemical environment. The chemical shift scale is a normalised frequency scale with units in parts per million (ppm) and is advantageous due to its B_0 field strength independence. The chemical shift is defined as

$$\delta = 10^6 \left(\frac{\delta_{ref} - \delta_{obs}}{\delta_{ref}} \right)$$

where δ_{ref} is the position observed for a reference compound measured in hertz and δ_{obs} is the position of the signal of interest (Campbell, 1984).

There are two classes of chemical shift; an intrinsic or primary shift that is diagnostic of a specific chemical group, and an induced or secondary chemical shift that arise from the influence of neighbouring magnetic centres, either through bond and/or through space couplings. The intrinsic shifts vary considerably between different groups and nuclei and are sensitive to ionisation state. Secondary shifts play an important role in defining the spectrum of macromolecules, the spectrum of a folded globular protein is completely different to its respective unfolded spectrum. This spectral variation arises from the small but significant contribution of secondary shifts, as in a folded protein spectrum each chemical group is in a well-defined environment.

It is possible to quantify some secondary shifts, particularly in the case of aromatic rings and paramagnetic ions. Aromatic rings confer ring-current effects due to the electron delocalisation. When B_0 is applied perpendicular to the plane of the aromatic ring, the delocalised electrons generate a field that opposes B_0 (Campbell, 1984). The field generated is a diploe μ of magnitude $B_0 e_2 a^2 / 4m$, in which e is the charge of an electron, a the aromatic ring radius and m the electron mass (Campbell, 1984). The field and induced dipole are averaged due to molecular tumbling in solution.

2.1.6 Spin-Spin coupling and multiplet structure

NMR spectra display a multiplet structure that arises from weak interactions between magnetic nuclei. These interactions arise from the electrons involved in bonding and the size of the interaction is known as the spin-spin coupling constant (J) and is expressed in hertz (Campbell, 1984).

In the case of two bonded nuclei, each respective nucleus can be oriented in two ways (spin up or down) (Figure 2.1). The effect of these two orientations is minor

variation in electron distribution causing minor chemical shifts, the result of which is a splitting of the two individual resonances into a pair of doublets (Figure 2.6). A nucleus coupled to two equivalent nuclei yields a triplet spectrum, with ratio of intensities 1:2:1 as a result of the following nuclear spin orientations:

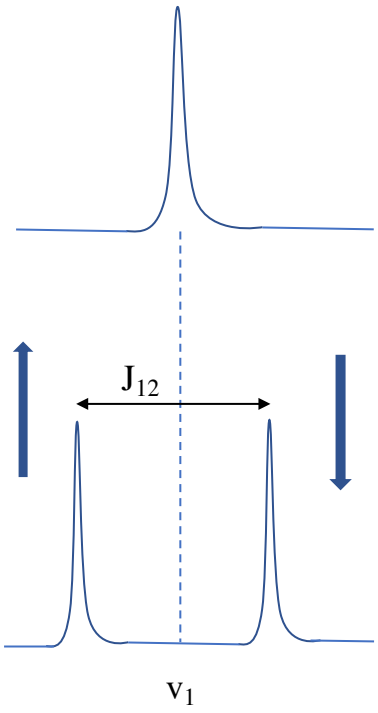

Figure 2.6 Illustration of *J*-coupling between nuclei, in spectrum (**A**) there is a single peak present from two different spin systems at a frequency v_1. If however there is a *J*-coupling in this spin system, then the individual peak splits symmetrically into a doublet as shown in the lower spectrum (**B**). The splitting within each doublet is the coupling constant labelled J_{12}. It is possible to interpret each respective peak within a doublet as representing the "up" and "down" spin states of each coupled spin, as seen by the adjacent blue arrows. Adapted from Keeler (2010).

↑↑, ↓↑, ↑↓, ↓↓ in which pair two and three are equivalent. This phenomena is extended to three equivalent nuclei that yield a quartet of intensity ratios 1:2:2:1 (Campbell, 1984).

The relative magnitudes of δ and *J* also influence the appearance of a multiplet. If the ratio of $\delta/J >> 1$ then a pair of doublets is observed. However, with decreasing δ/J ratios quantum mechanics dictates the probabilities of the outer peaks on a multiplet spectrum decrease with respect to the inner peaks, to the point where when $\delta = 0$ the nuclei are equivalent and so no multiplet structure is observed. As multiplet structures arise from through-bond interactions, the magnitude of *J* is affected by the type and number of bonds involved (Campbell, 1984).

Spin-coupling multiplets can be removed by chemical exchange, in which the relative orientation of coupled nuclei changes rapidly with respect to $1/J$. This rapid reorientation can arise form a number of means, firstly if the relaxation time of one nuclei is very short, and secondly is by selective irradiation of a group by a radiofrequency pulse (B_2) (Campbell, 1984). Use of a radiofrequency pulse in such a way is known as double resonance and the phenomena by which there is collapse of the nuclear spin multiplets is known as decoupling (Campbell, 1984).

2.1.7 T_2 relaxation time and linewidth

The T_2 relaxation time is defined as the time constant of the decay of the M_{xy} components. The T_2 time is related to linewidth by the relationship:

$$\Delta\nu_{1/2} = \frac{1}{\pi T_2}$$

Inhomogeneity affects NMR spectral linewidths and FID decay due to the fact that a range of field strengths yields a range of frequencies (Campbell, 1984). Despite this, there are methods to reduce the effect of field inhomogeneities allowing a T_2 value to

be determined. One such example is a 90 ° - τ – 180 ° – τ pulse sequence, which generates an echo at time 2τ. The decay of this echo is rather insensitive to inhomogeneous field effects (Campbell, 1984).

2.1.8 T_1 relaxation time

The T_1 relaxation time is defined as the time constant of the recovery of M_z after perturbation. M_z can be perturbed in multiple ways, for example, if B_1 is applied for long duration than the population difference between the energy levels is destroyed (M_z = 0), a process known as saturation (Campbell, 1984). Another, more practical way in which M_z can be perturbed is through the use of a 180 ° and 90 ° B_1 pulse. When M_z is perturbed by a 180 ° - τ – 90 ° pulse sequence, the 180 ° pulse inverts the nuclear spin populations in which M_0 = - M_0. The recovery of M_0 along the z-axis occurs with a rate constant of $1/T_1$. Therefore, M_z as a function of time is

$$M_z(t) = M_0\left(1 - 2e^{-\frac{t}{T1}}\right)$$

It is not possible to directly observe the recovery as it takes place along the z-axis, in which there is no M_{xy} components and thus no phase coherence. To overcome this, 90 ° pulses are applied at intervals to flip the magnetisation into the xy-plane so that the recovery may be observed (Campbell, 1984).

2.1.9 Causes of T_1 relaxation

$1/T_1$ defines the rate at which a Boltzmann distribution of populations is setup amongst the energy levels. Spontaneous emission is negligible in the context of NMR spectroscopy; therefore, all NMR transitions are caused by fluctuations in magnetic fields at frequencies related to ω_0 (Campbell, 1984). The Boltzmann distribution is setup due to thermal motion of the molecules within the sample, that in turn causes

fluctuating local fields at the nuclei of interest. As these molecular motions also have an energy distribution, the probability of inducing upward and downward transitions is not equal, such that there is a minor increase in the population within the lower energy level (Campbell, 1984).

There are numerous sources of fluctuating magnetic fields caused by molecular motion, however, in the context of $I = ½$ nuclei the most significant is typically dipole-dipole interactions. The field exerted by one magnetic moment on another is $(3 \cos^2\theta - 1) / r^3$ (Campbell, 1984). If the magnetic moments μ_1 and μ_2 are part of the same molecule, then their separation (r) is fixed and as the molecule tumbles in solution the spins maintain their orientation within the field. Therefore, θ varies randomly due to Brownian motion whereas μ_1 produces a fluctuating field at μ_2 and vice versa (Campbell, 1984).

The time scale of the random motion is defined by the function $g(\tau)$. This function is often exponential and can therefore be expressed as $\exp(-t/\tau_c)$. τ_c is the correlation time, in which the probability of there being a correlation between the vector orientation and a defined direction exponentially decreases with time constant τ_c (Campbell, 1984).

The probability of a field fluctuation to induce a transition between energy levels depends on there being a component of the correct frequency, but also the amplitude of said fluctuation. The amplitude of a dipole-dipole interaction is given by $\mu_0\mu_1\mu_2 / 4\pi r^3$. The magnitude of a nuclear magnetic moment is given by $\gamma\hbar I$ with the transition probability dependent on the amplitude squared (Campbell, 1984). When two spins with equal T_1 and $\gamma_1 = \gamma_2$, T_1 is fully expressed by

$$\frac{1}{T_1} = \frac{3\pi 0^2 \gamma 1^4 \hbar^2}{160\pi^2 r^6}\left\{\frac{\tau_c}{1+\omega^2\tau^2 c} + \frac{4\tau_c}{1+4\omega^2\tau^2 c}\right\}$$

As both ω and 2ω cause transitions, there are separate terms for $J(\omega)$ and $J(2\omega)$ (Campbell, 1984).

2.1.10 T_2 relaxation processes

As mentioned previously, a 90 ° RF pulse causes M_0 to flip into the *xy*-plane resulting in $M_z = 0$. However, there are additional ways in which M_{xy} components are lost. For example, if there are a range of ω_0 values due to local field effects within the NMR sample, or alternatively as a result of chemical exchange, then T_2 can be decreased. Therefore, the general scheme is that $T_2 < T_1$. In the case of dipolar interactions, the equation for T_2 is given by: (Campbell, 1984)

$$\frac{1}{T_2} = \frac{3\pi 0^2 \gamma^4 \hbar^2}{320\pi^2 r^6}\left(3\tau_c + \frac{5\tau_c}{1+\omega^2\tau c^2} + \frac{2\tau_c}{1+4\omega^2\tau c^2}\right)$$

2.1.11 The Nuclear Overhauser Effect

The Nuclear Overhauser Effect (NOE) is the transfer of nuclear spin polarisation from one spin system to another via cross-relaxation, a through space effect (Campbell, 1984). As mentioned previously, the primary way in which $I = ½$ nuclei relax arises from dipole-dipole interactions. The double-resonance that results causes intensity changes in other spin systems through irradiation with a B_2 field. This is due to the irradiation of one pair of spins influencing the T_1 relaxation. In the case of two nuclear-spin dipoles termed *I* and *S*, by saturating the *S*-resonance ($M_z = 0$) through B_2 irradiation causes a NOE that is described by

$$\eta = \frac{R_c}{R_I + R_x}\frac{\gamma_S}{\gamma_I}$$

in which η is the fractional change in intensity of resonance I, γ_S and γ_I are the gyromagnetic ratios of the I and S nuclei, R_I is the dipolar relaxation rate due to S, R_x is the relaxation rate from all other sources than I, and R_c is the cross-relaxation rate between I and S. $R_c = R_I/2$ when $\omega\tau_c = << 1$and $R_c = -R_I$ when $\omega\tau_c = >> 1$ (Campbell, 1984).

The following section describes, in brief, the NMR experiments used for the work presented in this Thesis, particularly but not exclusively with regard to resonance assignments of native WT hC*c* in aqueous solution conditions and acid-denatured in dimethylsulfoxide (DMSO).

2.1.12 Heteronuclear Single Quantum Correlation

A HSQC is a type of 2D NMR experiment in which magnetisation is first transferred from the ^{1}H to the covalently bound ^{15}N of the amide, due to the *J*-coupling, the chemical shift is evolved to the lone ^{15}N and then subsequently transferred back to the ^{1}H for detection (Bodenhausen and Ruben, 1980) (Figure 2.7). The HSQC experiment is therefore able to show all amide (NH) connections in a protein, which primarily correspond to the backbone NH group of the polypeptide, however tryptophan side chains (Nε-Hε groups) and asparagine and glutamine side chain Nδ-Hδ/Nε-Hε groups

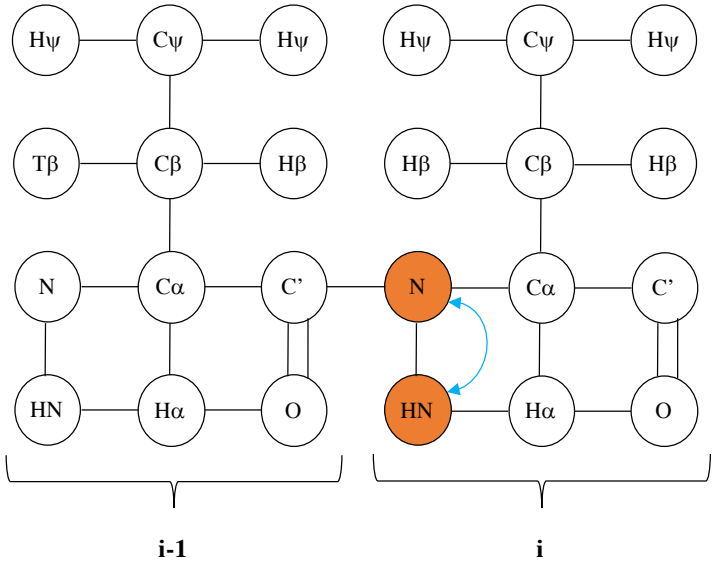

Figure 2.7 Schematic representation of magnetisation transfer in a HSQC pulse sequence. Orange atoms are observed in the spectrum with the blue arrow showing the path that magnetisation evolves during the experiment. Adapted from (Higman, 2012, Cavanagh, 2006).

are also observed (Bodenhausen and Ruben, 1980). Under low pH conditions the arginine Nη-Hη and lysine Nζ-Hζ groups can also be visible (Bodenhausen and Ruben, 1980).

2.1.13 HNCO

A HNCO is a 3D experiment in which magnetisation is transferred from the ^{1}H to the ^{15}N nuclei and then to the carbonyl group ^{13}C via the single bond *J*-coupling of $^{15}N^{H}$-^{13}CO, the magnetisation is then transferred back to the ^{1}H from the ^{15}N to enable detection (Figure 2.8). As the chemical shift is evolved on all three of the nuclei, a highly sensitive 3D spectrum is obtained (Kay et al., 1990a). The HNCO correlates not only the backbone CO-N-HN, but also asparagine and glutamine side chain peaks are visible, which in sequential assignment therefore provides a link to the carbonyl of the *i-1* residue in a given NH strip (Kay et al., 1990a).

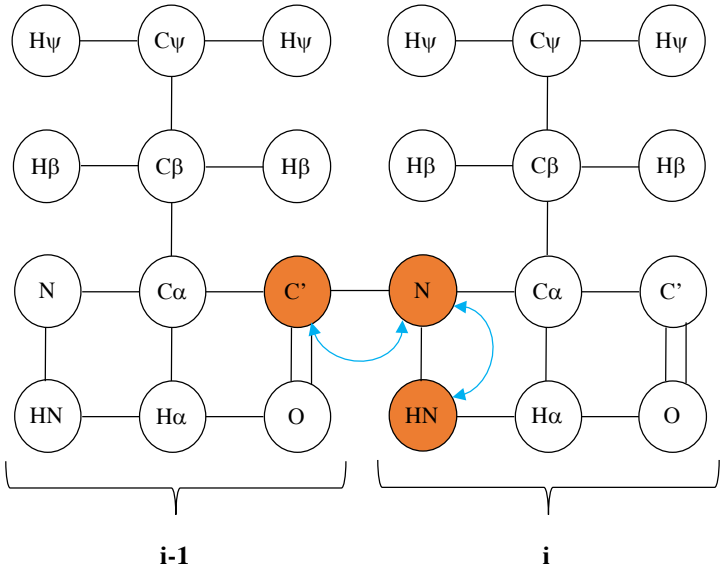

Figure 2.8 Schematic representation of magnetisation transfer in a HNCO pulse sequence. Orange atoms are observed in the spectrum with the blue arrows showing the path that magnetisation evolves during the experiment (Kay et al., 1990b, Grzesiek and Bax, 1992c, Muhandiram and Kay, 1994). Adapted from (Higman, 2012).

2.1.14 HN(CA)CO

In a HN(CA)CO experiment the magnetisation is transferred from the ^{1}H to the ^{15}N and then through the *J*-coupling to the $^{13}C\alpha$. The magnetisation then transfers to the ^{13}CO through the $^{13}C\alpha$-^{13}CO *J*-coupling, however the magnetisation is transferred back through the same pathway before being detected (Clubb et al., 1992) (Figure 2.9). As the NH group nitrogen is bonded both to the Cα residue *i* and to the *i-1* residue, the magnetisation transfer occurs in both residues and therefore for a given amide NH group two CO groups are observed in the spectra, although that of the *i-1* residue is weaker due to the weaker coupling to the nitrogen (Clubb et al., 1992). The HN(CA)CO experiment can be used in conjunction with the HNCO experiment in backbone sequential assignment strategies.

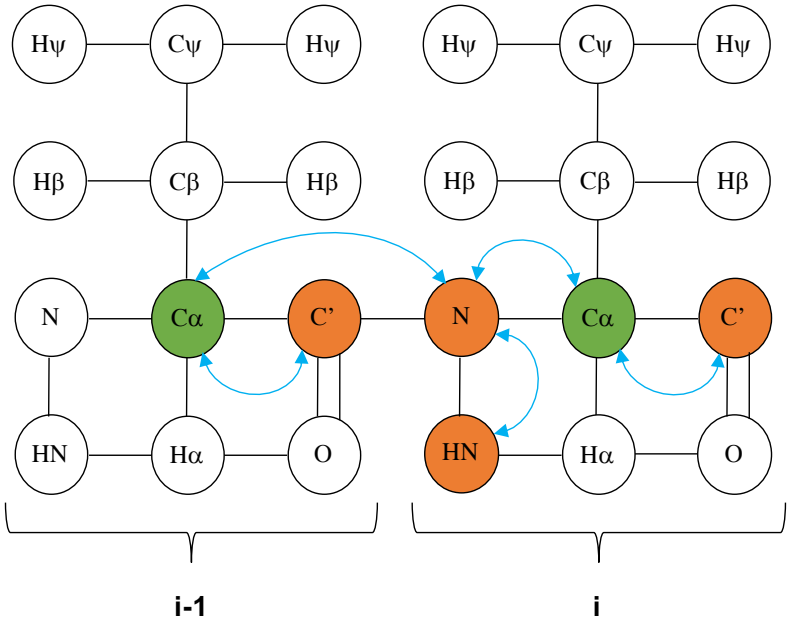

Figure 2.9 Schematic representation of magnetisation transfer in a HN(CA)CO pulse sequence. Orange atoms are observed in the spectrum with the blue arrows showing the path that magnetisation evolves during the experiment (Clubb et al., 1992). Adapted from (Higman, 2012).

2.1.15 CBCA(CO)NH

In a CBCA(CO)NH experiment magnetisation is first transferred from the $^{1}H\alpha$ and $^{1}H\beta$ to the $^{13}C\alpha$ and $^{13}C\beta$ respectively, before transferring from the $^{13}C\beta$ to the $^{13}C\alpha$. Next the magnetisation is transferred to the ^{13}CO and then to the $^{15}N^{H}$ before reaching the $^{1}H^{N}$ for detection (Figure 2.10). Due to the chemical shift evolution occurring simultaneously in the $^{13}C\alpha$ $^{13}C\beta$, these peaks appear in one dimension and the $^{15}N^{H}$ and $^{1}H^{N}$ in the other two dimensions (Grzesiek and Bax, 1992a). For most residues, two peaks are observed corresponding to the Cα and Cβ of the *i-1* residue.

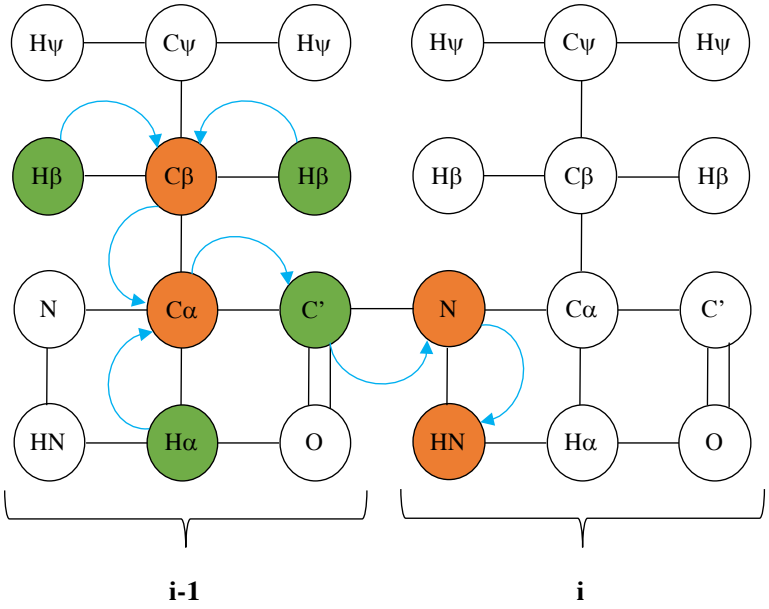

Figure 2.10 Schematic representation of magnetisation transfer in a CBCA(CO)NH pulse sequence. Orange atoms are observed in the spectrum with the blue arrows showing the path that magnetisation evolves during the experiment (Grzesiek and Bax, 1992a). Adapted from (Higman, 2012).

2.1.16 HNCACB

In a HNCACB experiment magnetisation is first transferred from the $^{1}H\alpha$ and $^{1}H\beta$ to the respective $^{13}C\alpha$ and $^{13}C\beta$, then the magnetisation is transferred from the $^{13}C\beta$ to the $^{13}C\alpha$. The magnetisation is then transferred to the $^{15}N^{H}$ and then finally the $^{1}H^{N}$ for detection (Figure 2.11). However, the magnetisation from the $^{13}C\alpha$ of residue *i* and *i-1* is transferred to the ^{15}N of residue *i*, therefore for each respective NH group two Cα and Cβ peaks are visible. As the chemical shift is evolved simultaneously on the $^{13}C\alpha$ and $^{13}C\beta$ the peaks appear in one dimension, the other two dimensions occupy the chemical shifts of the $^{15}N^{H}$ and $^{1}H^{N}$ (Grzesiek and Bax, 1992b). The HNCACB can be used in conjunction with a CBCA(CO)NH as an experiential pair in backbone sequential assignment strategies.

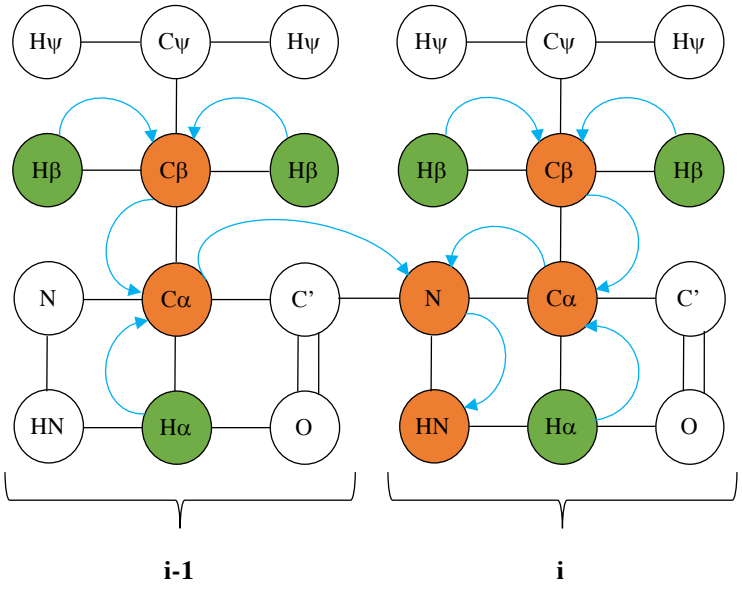

Figure 2.11 Schematic representation of magnetisation transfer in a HNCACB pulse sequence. Orange atoms are observed in the spectrum with the blue arrows showing the path that magnetisation evolves during the experiment (Grzesiek and Bax, 1992b). Adapted from (Higman, 2012).

2.1.17 HNN

In a HNN experiment, magnetisation is transferred from the ^{1}H of the NH then to the covalently bound ^{15}N of residue *i* (Panchal et al., 2001). From this ^{15}N, the magnetisation is evolved to the Cα of the *i-1* residue, then transferred to the covalently bound ^{15}N and ^{1}H (Panchal et al., 2001). This therefore confers *i* and *i-1* residue connectivity, however, unlike the above experiments, magnetisation is also evolved from the covalently bound ^{15}N of residue *i* to the Cα of *i* and then evolved to the covalently bound ^{15}N and ^{1}H of the *i+1* residue (Panchal et al., 2001) (Figure 2.12). In doing so the HNN provides *i*, *i-1* and *i+1* connectivity, and is therefore a very powerful tool in unfolded protein sequential assignment strategies. This is due to not only the three connections provided, but largely because the HNN exploits the ^{15}N chemical shift dispersion, rather than ^{1}H dispersion which is typically very poor in disordered or unfolded proteins (Panchal et al., 2001).

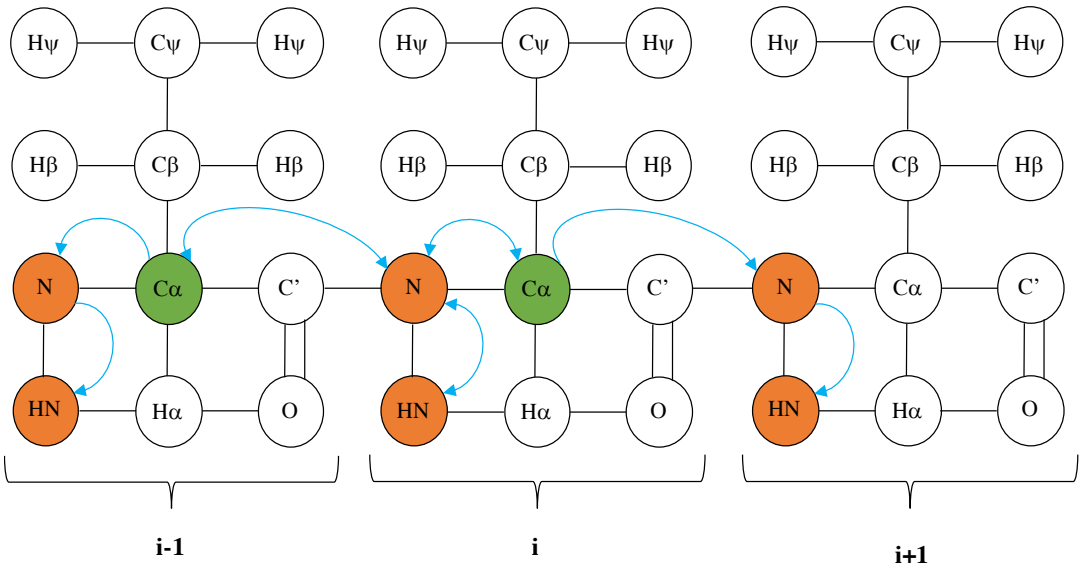

Figure 2.12 Schematic representation of magnetisation transfer in a HNN pulse sequence. Orange atoms are observed in the spectrum with the blue arrow showing the path that magnetisation evolves during the experiment (Panchal et al., 2001). Adapted from (Higman, 2012).

2.1.18 Scope of chapter

This Chapter reports on the backbone sequential assignment strategies for ferric WT hC*c* in both native aqueous conditions and acid-denatured in the aprotic solvent DMSO. The obtained assignments have been used in studies that address the role of hC*c* in complex with the mitochondrial phospholipid CL and to assess the role of dynamics in its apoptotic function.

2.2 Materials and methods

2.2.1 Isotopic labelling and purification of human cytochrome c in Escherichia coli

A co-expression system consisting of the DNA inserts to encode for WT hC*c* and the yeast haem lyase in a $pUC19^{Amp}$ vector was used to over-express the mature hC*c* (Rajagopal et al., 2013). This vector was transformed into *Escherichia coli* BL21 (DE3) RIL cells (Invitrogen) and overnight transformants were used to inoculate 3 ml Terrific Broth (Melford Chemicals) starter cultures grown at 37 ºC, 220 rpm for ~ 4 h. Once starter cultures showed signs of turbidity, ~ 3 ml of culture was added to ~ 330 ml of minimal media in 2 L Erlenmeyer flasks. The minimal media consisted of autoclaved M9 salts supplemented with 0.8 g/L $^{15}NH_4Cl$, 5 g/L $^{13}C_6$-glucose, 5 g/L thiamine and 1 mM final concentrations of the antibiotics Chloramphenicol and Ampicillin (Cai et al., 1998). To further aid haem biosynthesis, the first committed precursor, 5-aminolevulnic acid, is added to a final concentration of 0.1 mM. The cultures are then incubated at 37 ºC with shaking at 250 rpm until the point of induction (OD_{600} 0.6 – 0.8), usually occurring after ~ 6 h of growth, protein expression is induced through the addition of Isopropyl-β-D1-thioglactopryanoside (IPTG) (Melford Chemicals) at a final concentration of 1 mM.

Cells were harvested after ~ 16 h by centrifugation with a Sorvall SLC-6000 rotor at 3325 RCF for 20 min, 4 ^{o}C (Pollock et al., 1998, Rajagopal et al., 2013). Following centrifugation, the cells were re-suspended in a lysis buffer consisting of 50 mM Tris/HCl, 100 mM NaCl, 1 mM EDTA, 50 mM $MgCl_2$ pH 8.0 and lysed using a C3 Emulsiflex (Avestein). The protein/cell debris solution was then centrifuged with a Sorvall SS-34 rotor at 38724 g for 20 min to isolate the protein solution within the supernatant. The protein solution was stirred continuously at 4 ^{o}C and $(NH_4)_2SO_4$ (Fischer Scientific) added gradually over the course of 15 min to a final concentration of 164 g/L and incubated for a further 45 min. As C*c* is highly water soluble, it remains in solution with 164 g/L of $(NH_4)_2SO_4$, less soluble proteins are precipitated and therefore following centrifugation at 38724 *g* for 20 min, the C*c* can be recovered in the aqueous phase whilst the precipitate is discarded. Due to the high salt content of protein solution, the protein is dialysed overnight against 4 L of 20 mM NaPi, pH 7 in a 3,500 Da MW cut-off (MWC) dialysis membrane (Fischer Scientific). The following morning the dialysis buffer was replaced with a fresh buffer and dialysed further to remove additional salt. Following dialysis, the protein solution was centrifuged at 38724 *g* and diluted ~ 100 % v/v with 20 mM NaPi, pH 7 (Buffer A). An XK-26 column containing SP-Sepharose resin (GE-Healthcare) was equilibrated with Buffer A and the protein solution loaded using a peristaltic pump. Once loaded the column is attached to an ÄKTA purification system and the hC*c* eluted by a salt gradient against 20 mM NaPi, 1 M NaCl, pH 7 (Buffer B) over the course of 70 min with a 3 ml/min flow rate, yielding fractions from ~ 65 – 90 ml. These fractions were collected, pooled and concentrated in 5,000 Da MWC concentrators (Fischer Scientific) to a final volume of < 2 ml, so that the protein can be loaded to an XK-16 column containing G75 sephadex resin (GE-Healthcare) equilibrated with 20 mM NaPi, 150 mM NaCl, pH 7.

The protein eluted at ~ 95 – 105 ml and the resulting fractions collected, pooled, concentrated and buffer exchanged to a working buffer via a PD10 de-salting column (GE Healthcare). Samples were aliquoted and frozen at -20 ^{o}C until required.

2.2.2 Sample preparation

Ferric hC*c* was oxidised through the addition of a 2-fold excess of $K_3[Fe(CN)_6]$ (Sigma) with the subsequent excess of $K_3[Fe(CN)_6]$ and $K_4[Fe(CN)_6]$ removed and exchanged into 20 mM NaPi, 50 mM NaCl, pH 6.8 using a PD-10 desalting column (GE-Healthcare). All hC*c* samples were between 1 – 1.8 mM in concentration. Protein concentrations were determined spectrophotometrically using a Cary 60 UV-Visible spectrophotometer. Samples were reduced through addition of excess ascorbic acid and the absorbance at 550 nm was recorded and concentration determined using an extinction coefficient (ε) of 27500 $M^{-1}cm^{-1}$. All NMR samples were lyophilised prior to acquisition of NMR spectra. For acid-denatured samples, hC*c* was oxidised, buffer exchanged and concentrated in the same method as previously described, however, the protein was exchanged into 20 mM NaPi, pH 7 and acid-quenched with 0.3 % v/v Trifluroacetic acid (TFA) (Acros Chemicals) prior to lyophilising at a working volume of 500 µl.

2.2.3 NMR spectroscopy

All NMR spectra were acquired on a Bruker 800 MHz spectrometer equipped with a 5 mm HCN inverse triple resonance z-axis gradient probe. For the acquisition of NMR assignment spectra of doubly labelled ^{13}C,^{15}N oxidised hC*c* under aqueous conditions, samples were re-suspended on the day with deionised MilliQ H_2O and 8 % D_2O (Sigma), for the spectrometer lock, to a final volume of 500 µl. A set of 2D [^{1}H,

^{15}N]-HSQC and 3D HNCACB and CBCA(CO)NH spectra were recorded at 293 K. For acquisition of assignment spectra in DMSO ^{13}C,^{15}N oxidised hC*c* samples were resuspended in 100 % DMSO (Sigma) and supplemented with a small amount of D_2O for lock and 0.2 % v/v TFA to maintain protein solubility to a final volume of 500 µl. A set of HSQCs and the triple resonance CACB pair experiments HNCACB and CBCACONH were recorded at 308 K. All spectra were processed using TopSpin (Bruker BioSpin) and assignments determined using the graphical NMR assignment programs CCPN Analysis (Vranken et al., 2005) and Sparky (Goddard, 2008, Lee, 2015).

2.3 Results and Discussion

2.3.1 Assignment strategy and backbone resonance assignments for human cytochrome c under aqueous conditions

For native oxidised WT hC*c* in aqueous solution conditions, the assignment strategy consisted of the conventional CACB pair, CBCA(CO)NH and HNCACB experiments, being used to sequentially assign the backbone NH groups observed in the [^{1}H, ^{15}N]-HSQC spectra. These CACB pair spectra are displayed with the ^{1}H and ^{13}C dimensions on the x and y axis respectively, whilst the ^{15}N dimension is represented along the z axis. The HNCACB typically displays 4 peaks of two differing intensities on a given strip, correlating to the Cα and Cβ resonances of residue *i* and *i-1* (Figures 2.11 and 2.13). In the case of the CBCACONH experiment, only two peaks are typically observed correlating the Cα and Cβ resonances of residue *i-1* (Figures 2.10 and 2.13). These CACB pair spectra were used in conjunction to assign the [^{1}H, ^{15}N]-HSQC NH peaks in the following way. Firstly, a non-side chain peak is selected from the HSQC and used to navigate to the respective triple resonance strip in the CACB

pair experiments. The experiments are "linked" in the sense that the [^{1}H, ^{15}N]-HSQC pulse sequence form the base for the triple resonance experiments and therefore the ^{1}H and ^{15}N dimensions correlate with residue *i* between experiments. The intra-residue connections are based on the ^{13}C dimension and due to the distinct Cα and Cβ chemical shift patterns of certain residues (Thr, Ser, Ala and Gly) it is possible to tentatively assign sequential stretches of the protein. The assignment procedure relies on taking precise note of the ^{13}C chemical shift of a given residue and then searching for two differing intensity peaks that precisely match the "marked" chemical shift, but crucially, on a different ^{15}N plane. Figure 2.13 illustrates how this assignments procedure works on a five residue sequentially connected strip within the CACB pair experiments. It is clear how the CBCACONH *i-1* peaks are used to support *i-1* assignments in the HNCACB spectrum (which can, at times, be somewhat ambiguous). It should also be clear how these experiments are used in conjunction to sequentially connect stretches of the protein, working either towards the N- or C-termini.

The triple resonance experiments allowed for the assignment of corresponding Cα and Cβ carbons, and in the case of the WT protein enabled for all but two NH resonance assignments of the 99 non-proline residues to be assigned, with the exceptions being Glu21 and Thr28 as resonances were simply not observed (Figure 2.14). It is noted that there is a strongly upfield shifted NH resonance at 4.29 ppm ^{1}H and 104.25 ppm ^{15}N in the WT protein. This has also been noted in the ferric G41S variant of hC*c* (Karsisiotis et al., 2015) and has been assigned to Gly84 based on the original identification in heart eC*c*, whereby the extreme shift is attributed to the proximity of the Phe82 phenol ring, which would subsequently impose a strong ring-current effect (Volkov et al., 2012). A similar case can be made for WT hC*c* due to the X-ray crystal structure displaying a similar orientation of the Phe82 side chain

(Rajagopal et al., 2013). It is also worth noting that the spectral dispersion observed in the aqueous WT HSQC is very good, which facilitated the assignment process of the triple resonance datasets in the conventional way (Figure 2.14).

Backbone (HN, Cα and Cβ) resonance assignments for ferric WT hC*c* have been deposited in the Biological Magnetic Resonance Data Bank (BMRB) database under the accession number 25,418 and reported in Appendix A.

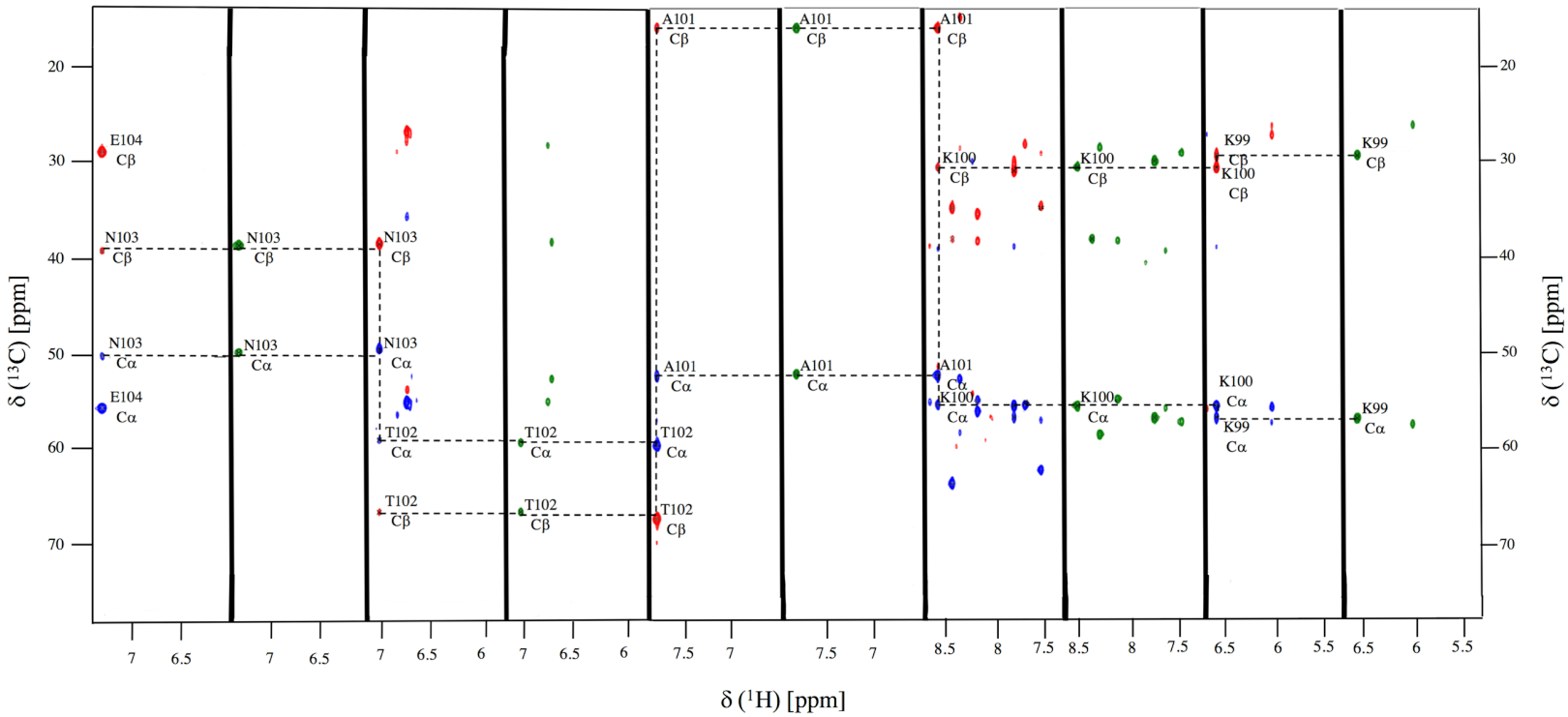

Figure 2.13 Strips illustrating the sequential Cα and Cβ resonance assignments from the spin system of E104 to the spin system of K100 in WT hC*c* under aqueous conditions (20 mM NaPi, 50 mM NaCl, pH 6.8). The standard CACB pair experiments are displayed (HNCACB and CBCACONH), positive peaks are represented by the colours red and green in the HNCACB and CBCACONH respectively, whilst negative peaks are represented by the colour blue in the HNCACB. The HNCACB spectra typically display 4 peaks on a given strip, two with greater intensity, corresponding to the "i" spin system and the weaker peaks corresponding to the spin system of *i-1*. The corresponding CBCACONH spectra is displayed adjacent to the HNCACB and typically only show 2 peaks on a given strip corresponding to the preceding *i-1* residue. Used in conjunction, it is possible to sequentially navigate through the protein either towards the N-termini (as illustrated), or towards the C-termini. Horizontal lines are used to illustrate the precise overlap in ^{13}C chemical shift, between the connected residues, thus allowing for sequential connections to be made.

2.3.2 Assignment strategy and backbone resonance assignments for acid-denatured human cytochrome c in DMSO

For an interrupted H/D exchange NMR method to be developed, which would in theory provide insights into the structural interaction(s) between hC*c* and the mitochondrial phospholipid CL (Chapter 3), NH assignments of acid-denatured hC*c* in an aprotic solvent are required. Samples must be acidified in aqueous conditions through the addition of Trifluroacetic acid (TFA). TFA then functions as a counter ion to solubilise the freeze-quenched protein when re-suspended, post freeze drying, in high concentration solutions of the aprotic organic solvent DMSO. The result of this acidic pH, is that the ^{1}H chemical shift dispersion is extremely narrow due to the protein being extensively denatured. The spectral overlap therefore severely affects the traditional CACB pair experiments as seen in Figure 2.15 and as a result, assignment progress was impossible using these conventional experiments as illustrated in Figure. 2.13. Therefore, in addition to the CACB pair, triple resonance experiments that confer CO connections (HN(CA)CO and HNCO) were acquired. However, it was apparent that although somewhat improved, spectral overlap was still a significant problem, which meant that the HN(CA)CO and HNCO experiments were used to further corroborate assignments rather than be used as the main assignment tool.

The main experiment used in the DMSO assignment protocol was the HNN, which confers *i-1*, *i* and *i+1* connections and is extremely useful in unfolded proteins as it takes advantage of the ^{15}N chemical shift dispersion which is significantly less affected from overlap (Panchal et al., 2001). On any given ^{1}H-^{15}N plane the NH group of residue *i* is connected to both the preceding and proceeding NH groups (Figure 2.16). The sign of these triplet peak strips is dependent on the type of adjacent residue in the sequence, particularly with respect to Gly and Pro residues (Panchal et al., 2001).

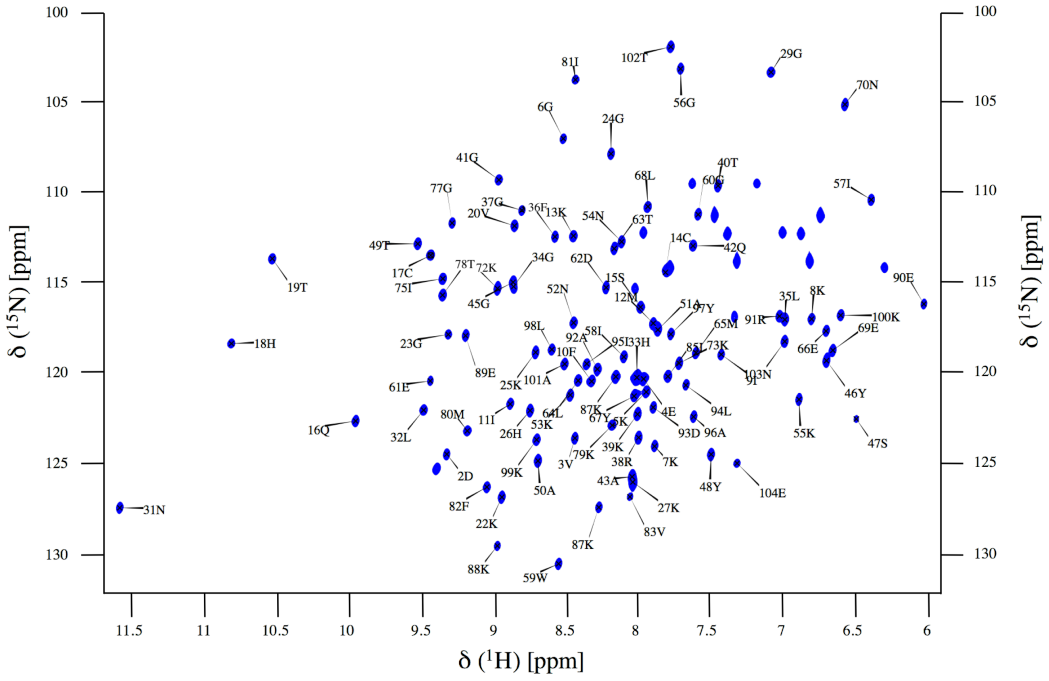

Figure 2.14 [^{1}H, ^{15}N]-HSQC spectra of WT hC*c* at 293 K in 20 mM NaPi, 50 mM NaCl, pH 6.8. The backbone NH resonance assignments are presented.

Despite the utility of the HNN experiment, this was still susceptible to spectral overlap on certain residues, thus the assignment protocol relied on the combination of these five triple resonance experiments in conjunction to assign most of the NH resonances (85 % of the non-proline residues) (Figure 2.17). It was however, impossible to assign the following residues under the experimental conditions employed: Lys7, Cys17, Thr19, Glu66, Tyr67, Leu68, Glu69, Tyr74, Ile75, Met80, Lys87, Lys88, Glu89, Glu90 and Lys100. This was due to either the residues simply not being observed, or due to consistent spectral overlap in all triple resonance experiments. It was possible to tentatively assign certain residues in two stretches of the protein, corresponding to region 66-69 and 87-90, however, as these were ambiguous these have been excluded from the deposited assignments. Backbone (H^N, N, $C\alpha$, $C\beta$ and CO) resonance assignments have been deposited in the BMRB database under the accession number 26973 and are reported in Appendix A.

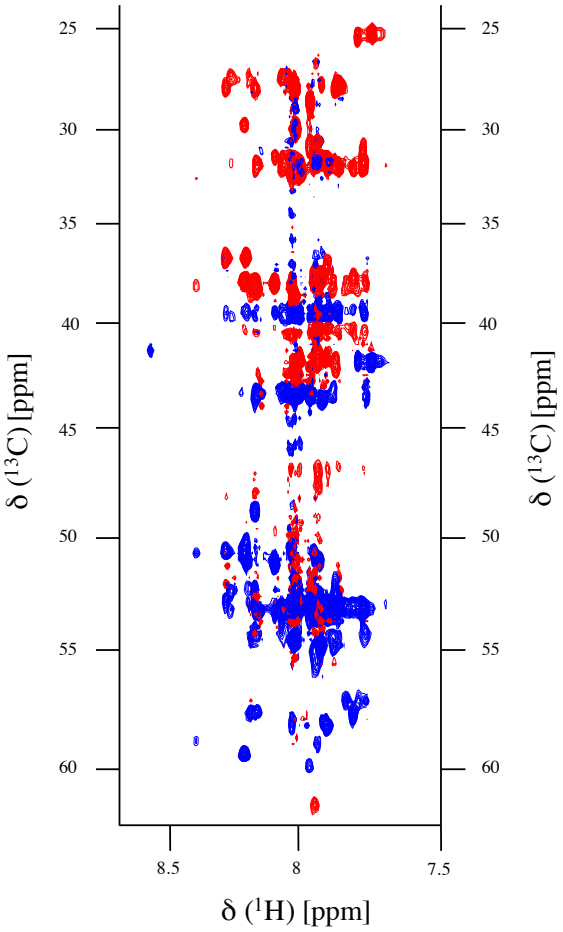

Figure 2.15 An example of a typical ^{15}N plane within an HNCACB spectrum of acid-denatured WT hC*c* in the aprotic solvent DMSO at 308 K. Positive Cα peaks are displayed in blue, whilst negative Cβ peaks are displayed in red. Note the narrow spectral dispersion in the ^{1}H dimension, leading to extensively overlapped datasets.

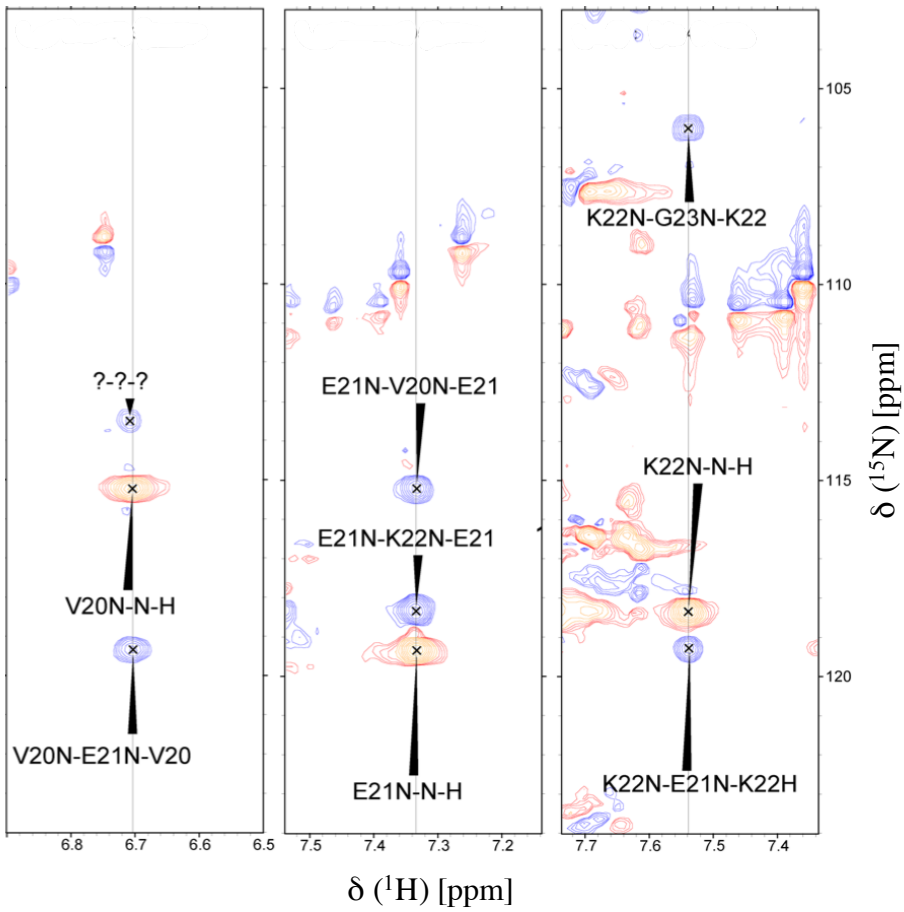

Figure 2.16 Strips of the HNN experiments used primarily, but in conjunction with several other triple resonance experiments to assign WT hC*c* in an acid-denatured state in DMSO. Displayed are three sequential spin systems ranging from Val20 to Lys22. On any given strip, there are typically three peaks observed, the positive peak (orange) relates to the spin system of residue *i*, whilst the other two negative peaks (blue) represent sequentially connected preceding residue *i-1* and the proceeding *i+1* residue. Adapted from Karsisiotis et al. (2017).

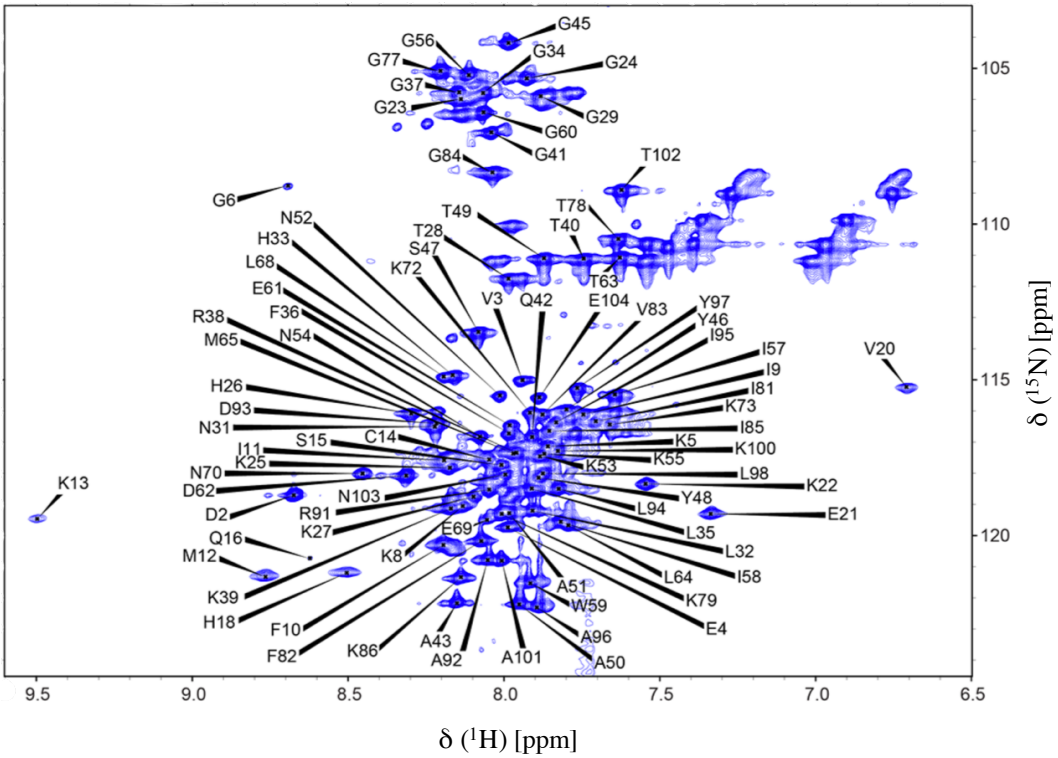

Figure 2.17 [^{1}H, ^{15}N]-HSQC spectrum of acid-denatured WT hC*c* at 308 K in the aprotic, organic solvent, DMSO. The backbone NH resonance assignments are included. Adapted from Karsisiotis et al. (2017).

2.4 Conclusions

In summary, to assign acid-denatured hC*c* in DMSO is more challenging than in aqueous conditions and requires a comprehensive assignment strategy utilising several different triple resonance experiments. The extremely narrow ^{1}H dispersion which leads to heavily overlapped triple resonance datasets making sequential assignment difficult was somewhat overcome through the use of the HNN experiment, which not only provides three sequential residue connections, but crucially exploits the ^{15}N dispersion which is significantly less effected in disordered or denatured proteins (Panchal et al., 2001). The successful assignments of oxidised hC*c* in aqueous and DMSO conditions now enables for the backbone NH assignments to be used in further studies reported in the proceeding Chapters of this thesis.

Chapter 3

Interrupted H/D exchange: A new approach to study protein/lipid interactions?

Analysis of iH/D exchange experiments lead by Dr Andreas Ioannis Karsisiotis

3.1 Introduction

3.1.1 Conventional H/D exchange

Hydrogen-Deuterium (H/D) Exchange methodologies are based on the fact that the proton of a protein backbone amide (NH) group is chemically labile and therefore constantly in exchange with solvent protons. Secondly, as protons and deuterons are highly NMR active and inactive nuclei, respectively, it is possible to exploit this exchange property and follow the continual reduction in both the number of NH groups and their respective peak intensities by conventional solution NMR spectroscopy using the HSQC (or variations of) experiment (Figure 3.1A). H/D exchange was first conceptualised and developed by the works of Kaj Ulrik Linderstrøm Lang and co-workers over 60 years ago (Linderstrøm-Lang, 1955a, Linderstrøm-Lang, 1955b, Linderstrøm-Lang, 1958, Linderstrøm-Lang, 1959). Since then, H/D exchange methodologies have been used to provide structurally related dynamic information on proteins within a single reside resolution (Bai et al., 1994, Bai et al., 1993, Bedard et al., 2008, Dyson et al., 2008, Nishimura et al., 2005, Alexandrescu, 2013). The primary H/D exchange methodology used is conventional H/D (cH/D) exchange, which has provided insights into protein folding and dynamics studies, as demonstrated by the pioneering work of Englander and colleagues (Bai et al., 1995a, Bai and Englander, 1996, Bai and Englander, 1994, Bai et al., 1994, Bai et al., 1993, Bai et al., 1995b, Connelly et al., 1993, Calhoun and Englander, 1985, Houry et al., 1998, Englander and Kallenbach, 1983, Zhang et al., 1995).

3.1.2 Concepts and theories of H/D exchange

H/D exchange methodologies work because the rate at which the proton of a given amino acid NH group exchanges with solvent protons/deuterons varies significantly by a number of key factors. These are namely the residue type, temperature, solvent conditions, pH (as both acids and bases can catalyse the exchange reaction), however crucially, in the context of structural biology and protein dynamics, the presence of higher order structures i.e. protein secondary structure, or structural elements. In order for the exchange reaction to occur, the NH group must be freely exposed to the solvent, and therefore the presence of hydrogen bonding (H-bonding) provides considerable protection from exchange.

$$k_{int} = k_w + k_{acid}[H^+] + k_{base}[OH^-] \qquad [3.1]$$

Equation 3.1 represents the intrinsic exchange rate constant of a hydrogen atom in a freely exposed amide (Hoshino et al., 2007). k_{int} represents the observed exchange rate constant, k_w represents the spontaneous rate constant for water, $k_{acid}[H^+]$ and $k_{base}[OH^-]$ are the second order rate constants for the acid and base catalysed reactions respectively (Hoshino et al., 2007). Bai and colleagues demonstrated that the k_{int} value of a given amino acid is highly dependent on pH producing "V-shaped" curves whereby minimal exchange occurs at approximately pH 3 in an aqueous environment (Bai et al., 1993). The exchange rates vary by one order of magnitude between a single pH unit shift and can be significantly reduced by bulky neighbouring residues due to steric blocking, or facilitated by inductive affects from polar residues (Bai et al., 1993). Bai and colleagues have determined the k_{int} values for every amino acid in a sequence using dipeptide models, furthermore, their work demonstrated both the inductive and

steric blocking effects of neighbouring residues using oligo- and polypeptide models, demonstrating approximately one order of magnitude variability (Bai et al., 1993).

As mentioned above, the H/D exchange rates of folded proteins are also further reduced by the formation of H-bonds which form between the hydroxyl and carbonyl groups. Additionally, hydrophobic protection of protons located within the hydrophobic core of a folded protein also provides significant exchange protection (Hoshino et al., 2007). The observed reduction in exchange rate of folded proteins directly correlates to the formation of higher order structures and therefore the ratio between the observed and intrinsic exchange rates of freely exposed sites is a significant value, known as the protection factor (P), first defined by (Houry et al., 1998). The P is the temperature corrected value used to report on all H/D exchange data and is defined as in equation 3.2.

$$P = k_{int} / k_{ex} \qquad [3.2]$$

In this equation k_{int} is the intrinsic exchange rate constant under reaction conditions considering the effects of amino acid sequence, pH and temperature by calculating these factors as a function and k_{ex} is simply the observed experimental exchange rate (Hoshino et al., 2007). As mentioned earlier the intrinsic exchange rate varies by an order of magnitude depending on the local amino acid environment, therefore, the observed exchange rate is dependent on the term defining the structural stability of the protein and the local amino acid sequence effects (from neighbouring residue steric blocking and facilitating polar residues), therefore, the conversion process from the obtained exchange rate to the protection factor serves to rectify this problem and in doing so provides thermodynamic stability of specific sites when the EX2 exchange conditions are satisfied (Hoshino et al., 2007). Protection in the native

state of globular proteins show very high protection patterns usually in the region of 10^4-10^6 s^{-1}.

3.1.3 Exchange Mechanisms

In order for a hydrogen atom in an NH group that forms a stable H-bond or that is located in the hydrophobic core to undergo exchange, the hydrogen must be in an exchange competent state. This can be achieved by either small-scale local structural fluctuations (local unfolding, known as "breathing") or by complete, transient, unfolding (global unfolding) (scheme 3.1) (Englander and Kallenbach, 1983). NH_c and

$$NH_c \underset{k_c}{\overset{k_o}{\rightleftharpoons}} NH_o \xrightarrow{k_{int}} ND \qquad \text{[Scheme 3.1]}$$

NH_o represent, respectively, the closed and open conformations under local unfolding conditions and the folded and unfolded conformations under global unfolding conditions (Hoshino et al., 2007).

$$k_{ex} = \frac{k_o k_{int}}{k_o + k_c + k_{int}} \qquad [3.3]$$

ND represents the deuterium exchanged amide, k_o and k_c are the opening *i.e.* unfolding and closing *i.e.* folding rate constants respectively, k_{int} is the intrinsic exchange rate constant for an unprotected state (Hoshino et al., 2007). In this schematic, backward exchange from ND to NH_o is not required due to massive excess of the solvent D_2O in respect to the concentration of protein. Therefore, the exchange rate constant when under steady-state conditions is expressed by equation 3.3. However, most H/D exchange experimental conditions significantly favour the folded condition therefore $k_c >> k_o$. This allows equation 3.3 to be approximated as equation 3.4.

$$k_{ex} = \frac{k_o k_{int}}{k_c + k_{int}} \qquad [3.4]$$

Crucially, there are two limits to the above equation 3.4. Firstly, when $k_c >> k_{int}$, a scenario associated with low pH and temperature, the subsequent exchange rate becomes equation 3.5.

$$k_{ex} = \frac{k_o k_{int}}{k_c} = K_o k_{int} \qquad [3.5]$$

Where by $K_o = k_o/k_c$ represents the equilibrium constant between the unfolded and folded conformations. This scenario is known as the bimolecular exchange (EX2) limit, where the H/D exchange rate expressed by the P states the thermodynamic site stability as equation 3.6.

$$\Delta G_{ex} = -RT\ln K_o = -RT\ln\frac{k_{ex}}{k_{int}} = RT\ln P \qquad [3.6]$$

Where ΔG_{ex} is the Gibbs free energy of unfolding at the NH site, R is the gas constant, and T is absolute temperature. However, there is another limit to equation 3.3, known as the monomolecular (EX1) exchange limit, a condition usually considered at high pH and temperature (Hoshino et al., 2007). Under EX1 conditions $k_c << k_{int}$ and therefore the exchange reaction is limited by the unfolding event at the particular NH site, the result of which is that equation 3.3 is simplified to equation 3.7 (Hoshino et al., 2007).

$$k_{ex} = k_o \qquad [3.7]$$

The EX1 condition exchange rate constant is the unfolding kinetic constant and therefore conversion to a protection factor is unnecessary. The pH dependence of the exchange rate allows identification of whether the reaction is controlled by the EX1 or EX2 limit, if EX2, the exchange rate is proportional to the intrinsic exchange rate and is highly dependent on pH (Hoshino et al., 2007). Whereas the EX1 limit displays a near pH-independent observed exchange rate (Hoshino et al., 2007).

3.1.4 Interrupted H/D exchange in dimethylsulfoxide

The aprotic solvent DMSO can be used in a relatively new type of H/D exchange methodology, interrupted H/D exchange (iH/D exchange). iH/D exchange is not like cH/D exchange, which is based on one live sample that evolves over time (Figure 3.1A), instead, a number of separate samples have the exchange reaction quenched. This can be achieved either by flash freezing or pH drop (through addition of trifluroacetic acid (TFA)) or both and then freeze dried and resuspended in DMSO in order to prevent any further exchange occurring (Figure 3.1B) (Zhang et al., 1995, Hoshino et al., 2007).

Zhang and colleagues investigated the exchange rate constant of a model peptide in DMSO and found an approximate 100-fold decrease in H/D exchange rate when in 90-95% DMSO compared to that of aqueous solvents (Zhang et al., 1995). Their work also found differences in the pH dependence of the rate constant when compared to an aqueous solvent and that the characteristic minimal exchange rate associated with aqueous conditions at pH 3 was increased by 2 pH units to an approximate observed pH of 5 in 95 % DMSO. It was reasoned that the differences in exchange rate are caused by the transient formation of deprotonated NH groups which are required for the base catalysed exchange reaction and subsequently become

increasingly unfavourable in high concentrations of aprotic organic solvents such as DMSO (Scheme 3.2) (Zhang et al., 1995).

$$NH + D_2O \rightleftharpoons [NH\cdot\cdot\cdot OD^- + D^+ \rightleftharpoons N\cdot\cdot\cdot HOD + D^+] \rightleftharpoons ND + HOD$$ [Scheme 3.2]

Roder and co-workers have demonstrated that iH/D exchange experiments can provide insight into local structural dynamics on the sub-millisecond timescale (Fazelinia et al., 2013). This was achieved through the development of an ultra-rapid microfluidic mixing device able to extend the temporal resolution of cH/D exchange experiments down to 60 μs (Fazelinia et al., 2013). They successfully demonstrated that during the first 140 μs of refolding in ferric eC*c*, three helical regions form in the 60s, 70s and C-terminal helices of the native protein structure, but no secondary structure formation in the N-terminal half of the protein (Fazelinia et al., 2013). By allowing the protein to refold under refolding conditions of a given time and then rapidly quenching the exchange reaction with an acidic quenching buffer, the number of visible backbone amid peaks in a 2D [^{1}H-^{15}N] HSQC experiment vary. Extrapolation of exchange rate constants show local, residue specific secondary structural information. The more uniformly exposed a protein is to the solvent, the greater the exchange rate, therefore, regions which fold are protected from exchange and thus in turn highlight regions that have adopted ordered structural features.

iH/D exchange has been used to study several protein systems such as GroES, amylin and melittin (Chandak et al., 2013, Alexandrescu, 2013, Zhang et al., 1995). In particular, iH/D exchange has been used to great effect within the mammalian cochaperone Aha1 system, whereby Dyson and co-workers were able to define the interaction sites with the middle domain of the chaperone Hsp90 (Dyson et al., 2008). Not only were their findings consistent with the X-ray crystal structural data obtained

from the homologous yeast complex, but they also were able to identify a secondary interaction site within this protein complex (Dyson et al., 2008).

3.1.5 iH/D exchange to study lipid binding sites?

iH/D exchange has not been used previously to study a holo-haem protein, and so during the course of this PhD research, the primary initial goal was to develop an iH/D exchange methodology that would provide salient structural information on soluble protein/phospholipid interactions. Protein/lipid interactions are not amenable to X-ray crystallography due to the heterogeneity of the subsequent solutions, and lipids are too large for conventional solution NMR spectroscopy. Solid State NMR (SS-NMR) traditionally has also not been appropriate for these systems as a protein precipitate will not be representative of the dynamics present with the lipid under aqueous conditions. However, recently the technology and methodologies have advanced sufficiently to provide structural information on such systems as described below.

Alternative solution NMR techniques have been used recently by Wand and co-workers to study the C*c*/CL interaction through the use of reverse micelle encapsulation (O'Brien et al., 2015). Previous studies have demonstrated that the interaction with C*c* and CL results in partial unfolding of the protein, as a precursor to the apoptotic response, however, a limitation of previous studies is not only a lack of site resolution, but also a lack of membrane curvature thus not reflecting the micro-environment within the mitochondrion (O'Brien et al., 2015). Wand and co-workers used reverse micelle encapsulation to mimic the effects of confinement on the interaction between C*c* and CL using ferric eC*c* and reverse micelles prepared in pentane (O'Brien et al., 2015). The results of their investigation supported the previously defined electrostatic A-

(Lys72, Lys73, Lys86 and Lys87) and L- (Lys22, Lys25, His26, Lys27 and His33) sites, but also identified a new binding site incorporating residues Phe36, Gly37, Thr58, Trp59 and Lys60 (O'Brien et al., 2015). The work of Wand and co-workers also found no evidence of local C*c* unfolding, instead they found the tertiary structure to remain fully intact upon interaction with CL (O'Brien et al., 2015). Such a finding contradicts many previous studies (*vide infra*).

Further support for the interaction between C*c* and CL without unfolding comes from the work of van der Wel and colleagues who used Magic Angle Spinning Solid-State NMR spectroscopy (MAS-SS-NMR) to identify the site specific conformational changes that occur in both the ferric and ferrous forms of ^{15}N, ^{13}C uniformly labelled eC*c* when bound to CL bilayers (Mandal et al., 2015). The use of MAS-SS-NMR and Fourier Transform infrared spectroscopy (FT-IR) revealed that CL membrane bound C*c* displays significant dynamics, yet maintains its secondary structure (Mandal et al., 2015). Additionally, in both two and three dimensional MAS-SS-NMR spectra they report that the CL bound C*c* displays a spectral resolution characteristic of a protein exhibiting structural homogeneity, a result that is therefore, fundamentally inconsistent with the extensive membrane-induced unfolding previously reported (Mandal et al., 2015). They conclude that C*c* interacts with the CL membrane interface without significantly perturbing the lipid bilayer, and therefore despite membrane binding resulting in the C*c* pro-apoptotic peroxidase gain-of-function, they do not observe evidence of large scale unfolding events or penetration into the membrane core (Mandal et al., 2015).

Despite the complications of studying such a system, preliminary work prior to this PhD Thesis in the Worrall Group has revealed that the addition of TFA to WT hC*c*/CL solutions causes dissociation of CL. This therefore means that if the

protein/lipid complex were allowed to exchange for discrete time durations, then the addition of TFA would not only separate the lipid and simultaneously quench the exchange reaction, but it would also

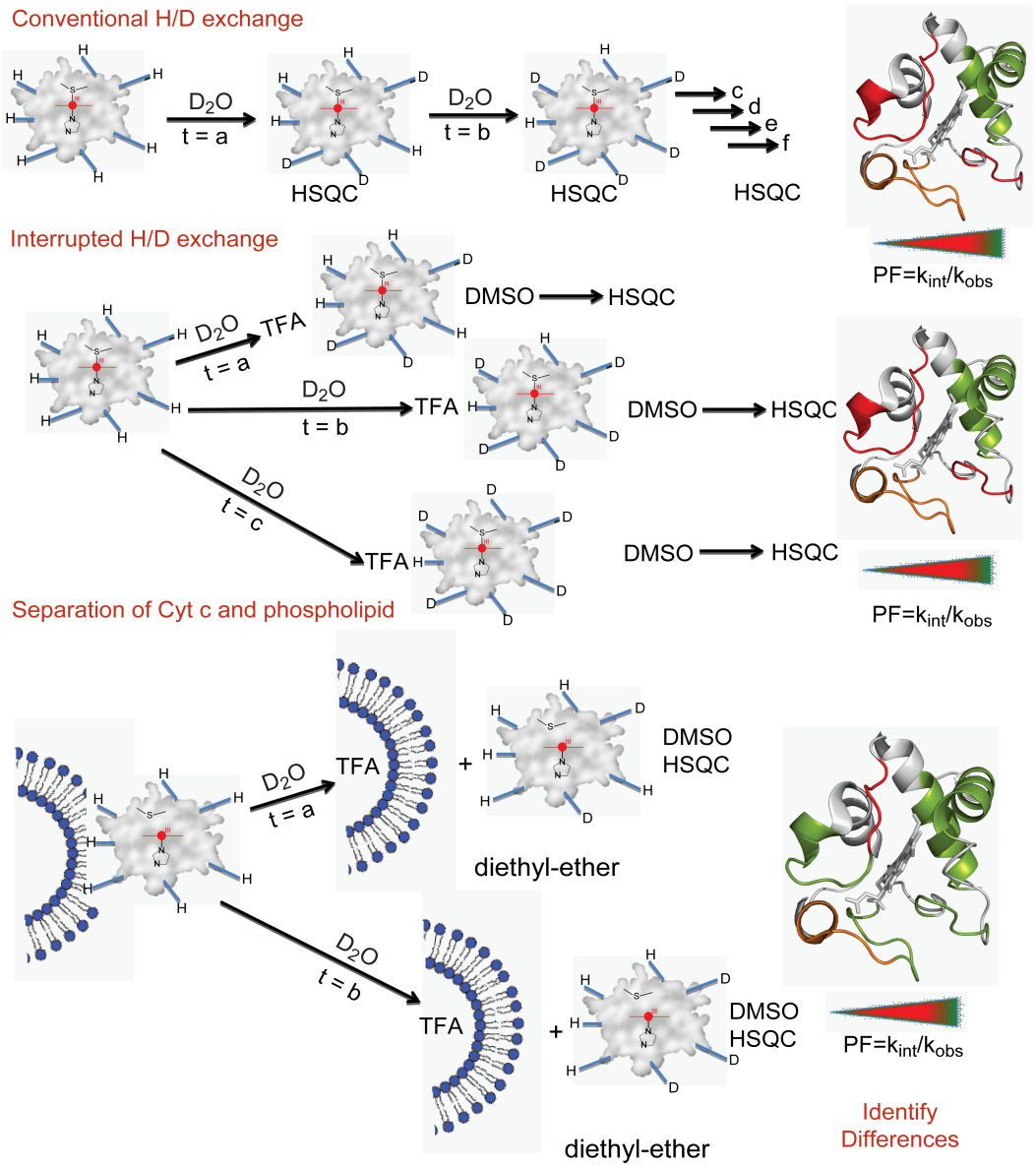

Figure 3.1 Schematic illustration of Traditional (conventional) H/D exchange (upper inset) and the established interrupted H/D exchange methodologies (middle inset). The lower inset illustrates how interrupted H/D exchange theoretically can be utilised to resolve lipid binding site information on a per residue resolution, through the use of acid quenching (with TFA) and the aprotic organic solvent DMSO.

allow for the isolation of the aqueous protein components from the mixture via the addition of diethyl-ether (DEE) (Figures 3.1 lower and 3.8). It would then be possible to carry out the iH/D exchange methodology using DMSO and acquire HSQC experiments (Figure 3.1C). Theoretically, there would be a specific iH/D exchange profile displayed in the absence of lipid, which differs from that of a lipid bound dataset, in which there might be a few residues that display increased H/D exchange protection, i.e. slower experimental exchange rates that one would attribute directly to the physical protection conferred by the lipid (through H-bonding) (Figure 3.1 lower).

This chapter documents the research into both iH/D exchange of holo-WT hC*c*, and the integration of the hC*c*/CL interaction into said iH/D exchange methodology with the aim of extracting information as to which structural regions of hC*c* are interacting with CL.

3.2 Materials and Methods

3.2.1 Over-expression and purification of WT human cytochrome c

The over-expression and purification of hC*c* were as reported in Chapter 2.

3.2.2 Protein preparation

All WT hC*c* preparations were oxidised to the ferric haem state and equilibrated in 20 mM sodium phosphate, pH 7 as described in Chapter 2.

3.2.3 NMR spectroscopy

Full details of NMR sample preparations, experimental conditions and assignment procedures are described in Chapter 2.

3.2.4. Cardiolipin-liposome preparation

Cardiolipin liposomes consisting of a 1:1 molar ratio of TOCL (1, 1', 2, 2'-tetraoleoyl CL) and DOPC (1, 2-dioleoyl-*sn*-glycero-3-phosphocholine) (Avanti Polar Lipids) were used for the NMR experiments reported in this chapter and in the ABTS peroxidase activity assays reported in Chapters 4 and 5. Lipid stocks stored in chloroform were aspirated in an atmosphere of argon (BOC) to prevent oxidation. During aspiration, the lipid solution is kept in continual motion to produce a uniformly thin and dry film at the base of the glassware prior to sealing with Parafilm. The lipids were re-suspended in 20 mM sodium phosphate, pH 6.5 by vortexing for ~ 10 min yielding a 2.5 mM stock. Once a homogenous, cloudy solution is achieved, liposomes were made of uniform size by sonication at 4℃ for ~ 15 min, or until a clear solution was achieved. Liposome solutions were used within 24 hours of preparation.

3.3 Results and Discussion

3.3.1 Initial attempts of observing iH/D exchange in DMSO

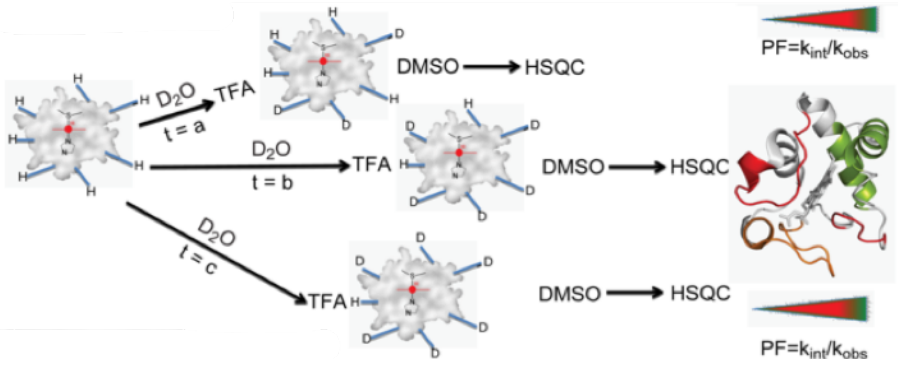

Figure 3.2 Schematic illustration of the iH/D exchange methodology. Multiple protein samples are used, that in theory represent a discrete exchange time-point. hC*c* is resuspended in 100 % D_2O and the exchange reaction allowed to proceed for a predetermined time. At a desired time, the exchange reaction is quenched in the aqueous phase through the addition of TFA. The protein solution is lyophilised and then resuspended in a high concentration DMSO solution at the time of measurement.

iH/D exchange is visualised in DMSO, where theoretically different exchange profiles are present based on exchange duration.

Initial attempts to observe iH/D exchange in DMSO were setup in accordance with the relatively few protocols described in the literature (Dyson et al., 2008, Chandak et al., 2013, Alexandrescu, 2013, Fazelinia et al., 2013). A set of iH/D exchange ^{15}N WT hC*c* samples (250 μM, 20 mM sodium phosphate, 50 mM NaCl) were quenched with an optimised amount of TFA (1.8 % v/v) (Figure 3.2) that conferred excellent protein solubility once redissolved in a DMSO/D_2O mixture (99.6 %, 0.4 %, respectively) post lyophilising (Figure 3.2). The following exchange time points were used; 0.169, 1.027, 3.085, 7.717, 24.018 and 48.028 h. [^{1}H-^{15}N] HSQC spectra were acquired on the Bruker 500 MHz spectrometer (Chapter 2 materials and methods). Analysis of each respective sample did not indicate iH/D exchange, furthermore, significant and non-uniform spectral shifts were observed with respect to the triple resonance assignment spectra, which one may attribute to more acidic solution conditions and increased salt content.

3.3.2 Varying TFA concentration

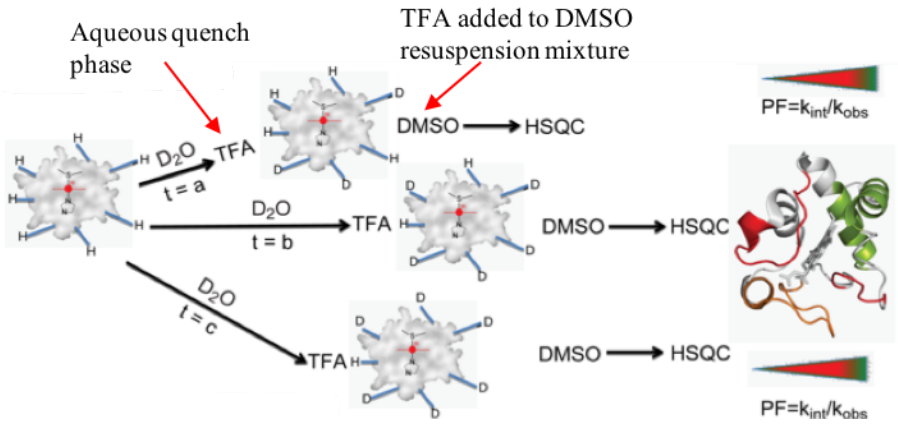

Figure 3.3 Schematic illustration of the iH/D exchange methodology. Annotated red arrows highlight the two experiential stages in which TFA is used. The "aqueous quench phase" represents the point at which the exchange reaction is first suppressed. "TFA added to DMSO resuspension mixture" represents the second experimental stage in which TFA is added to the protein solution, in order to solubilise the hC*c* in DMSO.

Further work demonstrated that additional TFA was a necessity in the DMSO resuspension mixtures (Figure 3.3), as an inadequate TFA concentration correlated with considerable, or total protein precipitation. In contrast, an excessive TFA concentration led to protein denaturation, loss of haem coordination and poor NMR spectral quality. Unfortunately, an ideal TFA concentration, with respect to protein solubility, in the DMSO resuspension mixture, or an excess of TFA added at the aqueous quench phase (Figure 3.3) correlated with no observable iH/D exchange. These negative results are most likely attributed to an inappropriate quench pH in the "aqueous quench phase" and/or from an inappropriate "apparent" pD in DMSO (Figure 3.3). It was discovered that there are two crucial factors in maintaining the H/D exchange status, namely the aqueous solution pH at the "aqueous quench phase" (Figure 3.3), in which the addition of 1.8 % v/v TFA was inappropriate, but also the

apparent pD in the redissolved $_{d6}$-DMSO/D_2O/TFA mixtures, which literature explains by preventing back exchange (Hoshino et al., 2007).

Attempts to prevent back exchange involved experiments using four samples (a no exchange control, 10 min exchange, 3 h exchange and 24 h exchange) with the low salt 20 mM sodium phosphate, pH 6.5 buffer, with 0.2 % v/v TFA used to quench the exchange reaction, followed by sample resuspension in DMSO/D_2O/TFA mixtures of 95 %, 5 % and 0.1 % v/v respectively (Figure 3.3). It was determined that the use of 0.1 % v/v TFA in DMSO is appropriate for protein solubility only if used with a pre-mixed resuspension solution (if added separately 0.2 % v/v TFA is required). Unfortunately, these experiments showed no indication of iH/D exchange and demonstrated that with increased D_2O content higher TFA concentrations are required in the DMSO resuspension solution, in order to maintain protein solubility.

3.3.3 Evidence of iH/D exchange in water

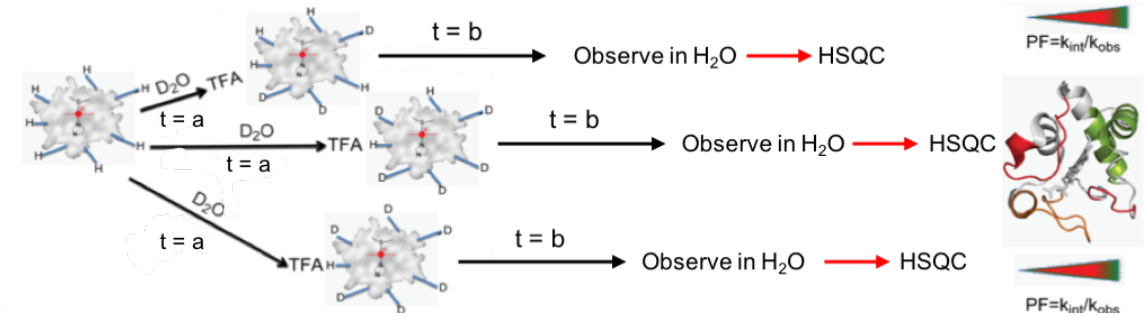

Figure 3.4 Schematic illustration of the experiment described in section 3.3.3. Samples were allowed an initial exchange period (8 h "t = a") in D_2O, at which point the reaction was quenched with varying amounts of TFA to access performance. Following the quench, samples were allowed an additional longer time interval (16 h "t = b"), in order that any samples which were not successfully quenched through the addition of TFA would continue to exchange. Samples were then flash frozen, lyophilised and resuspended in H_2O at the time of measurement.

In order to obtain evidence as to whether iH/D exchange is possible for the hC*c* system, an experiment was designed in which the two respective stages (quenching in water and resuspending in DMSO) were separated. The data reported in this sub-section (3.3.3) arise from measuring iH/D exchange samples in water, in order to access the efficacy of quenching the exchange reaction in aqueous conditions (Figure 3.4).

The experimental design was as follows; samples were allowed an initial exchange period of 8 h in D_2O, samples were then quenched with varying TFA concentrations (0.15, 0.1, 0.075, 0.05, 0.025 % v/v) and allowed a second longer exchange period of 16 h before being flash frozen in liquid N_2 and lyophilised. The purpose of the second exchange

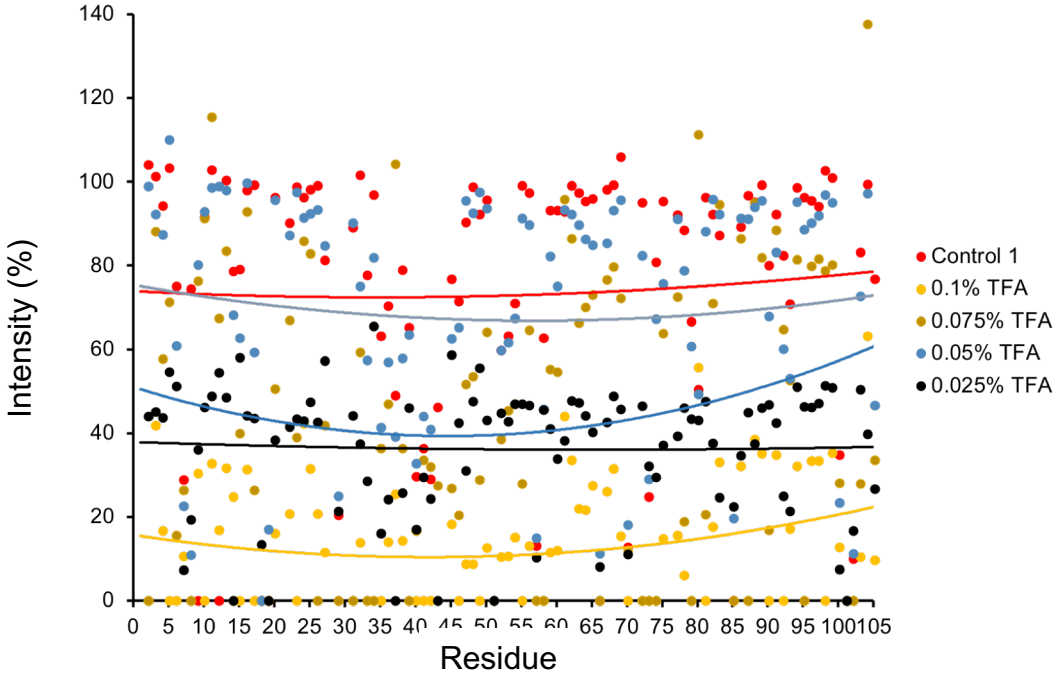

Figure 3.5 Individual residue peak height intensity of all experimental samples and the no-exchange control (Control 1), plotted as a percentage of Control 2, the control sample that only experiences the initial deuteration period (Figure 3.4). As explained in section 3.3.3 NMR HSQC spectra have been acquired in H_2O buffer conditions. Individual data points are fitted to a simple polynomial function to observe general trends in the data sets.

interval following the addition of TFA, was in order to allow any non-quenched samples to further exchange. Samples containing 250 μM hC*c* in 20 mM sodium phosphate, pH 6.5 were produced and by varying the quench TFA concentration and therefore, the corresponding pH values, a range of conditions was sampled. Two controls were used, the first (Control 1) a no deuterium exchanged sample and the second (Control 2) a sample only allowed the initial exchange period. Both controls received the addition of 0.05 % v/v TFA.

Samples were re-suspended in water and observed by acquisition of HSQC spectra in H_2O buffer conditions. The decision to acquire the NMR spectra in H_2O was made with the two following considerations:

a) That the relatively short interval in H_2O between sample resuspension and data acquisition is negligible in terms of re-protonation when compared to the far longer deuteration exchange period.
b) Detection in aqueous conditions allows for the use of the full set of resonance assignments as used in the cH/D exchange experiments, in contrast to the limited subset of assignments obtained in DMSO.

This experiment enabled both the visualisation of iH/D exchange information and allowed one to identify more suitable quenching conditions in H_2O (0.05 % v/v TFA). These conclusions were determined from comparison of polynomial fits to the experimental datasets vs the no-exchange control (Control 1) (Figure 3.5). In Figure 3.5 the intensity of each residue is plotted for all samples as a percentage of Control 2, the control sample that received only the initial exchange period. As the experimental sample quenched with 0.05 % v/v TFA shows the greatest intensity of all experiential samples, and therefore the highest protonation state, it can be concluded that during the second exchange interval following the aqueous quench phase, that this experimental

sample has "evolved" the least, i.e. not significantly exchanged further. This conclusion is valid when the previously stated assumption is made that the re-protonation in H_2O (at the time of measurement) is insignificant when compared with the timescales involved for deuteration.

Following from the success of the aqueous quench optimisation experiment, a repeat experiment was conducted in order to further refine aqueous conditions as much as practically possible. Eight samples were produced, quenched with 0.07, 0.065, 0.06, 0.055, 0.05 % v/v TFA respectively. Two control samples were used as per the previously described experiment that received the addition of 0.05 % TFA. Analysis of this follow up optimisation experiment revealed that the optimal quench conditions in H_2O had been further refined, with 0.065 % v/v TFA providing the best quality preservation of H/D exchange data (Figure 3.6).

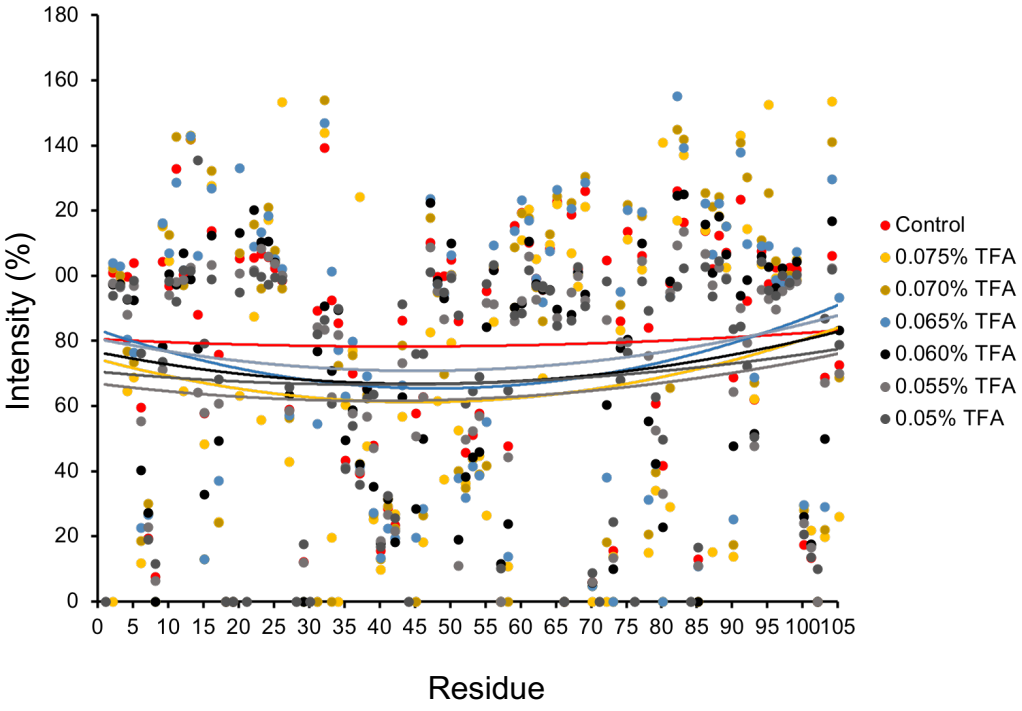

Figure 3.6 Individual residue peak height intensity of all experimental samples and the no-exchange control (Control), plotted as a percentage of Control 2, the control sample that only experiences the initial deuteration period (Figure 3.4). As explained in section 3.3.3 NMR HSQC spectra have been acquired in H_2O buffer conditions. Individual data points are fitted to a simple polynomial function to observe general trends in the data sets.

3.3.4 Attempts to observe iH/D exchange in DMSO

In order to address the issue of maintaining the quenched H/D exchange reaction in DMSO, a number of samples were produced so that systematic variation of $_{d6}$-DMSO/D_2O/TFA ratios in the resuspension solution (Figure 3.3) could be explored. The aim of this systematic variation was to determine an optimal apparent pD in DMSO between ~ pD 3.5 – 5.5 based on literature for minimising back exchange (i.e. D > H exchange) (Alexandrescu, 2013, Dyson et al., 2008, Hoshino et al., 2007, Fazelinia et al., 2013). Samples consisted of TFA ranges as follows; 0.1, 0.15, 0.175, 0.2, 0.21, 0.225, 0.25, 0.3, and 0.4 % v/v. The control had no exposure to deuterium but was quenched with 0.065 % v/v TFA, then following lyophilisation the control was redissolved with 0.25 % v/v TFA in $_{d6}$-DMSO. The data showed that resuspending in DMSO with 0.25 % v/v TFA, resulting in an apparent pD ~ 4 yields the best-preserved H/D exchange profile, whilst the extremes of the dataset (0.1 and 0.4 % v/v respectively) resulted in the worst exchange profiles, due to an inappropriate pD of 7.4 and 3.44 respectively in DMSO.

Despite these optimisations, it was still not possible to obtain quantitatively useful exchange state information in DMSO.

3.3.5 Using FAST-HSQC to monitor sample evolution in DMSO

It became apparent that the use of a single high-quality HSQC spectrum obtained over ~ 45 min – 1 h was not sufficient to observe iH/D exchange, due to the limited observation window. All previously documented attempts at observing iH/D exchange had been conducted on the Bruker 500 MHz spectrometer (Chapter 2 materials and methods) as the 800 MHz spectrometer had been off-line for a considerable duration for extensive repair work. The use of the 800 MHz spectrometer enabled the FAST-HSQC pulse sequence to be used on all subsequent iH/D exchange samples, with a series of consecutive HSQC spectra acquired for each respective time point. As the acquisition time with the FAST-HSQC pulse sequence was ~ 5 min, the acquisition of multiple spectra enabled the theoretical zero time point to be determined, through back extrapolation of fits to the HSQC data obtained over multiple time points after protein dissolution. The use of multiple FAST-HSQC spectra for each sample, followed by back extrapolation, is an approach used by Wright and colleagues to great effect on apomyoglobin (Nishimura et al., 2005).

By switching from a single high-resolution HSQC spectrum for each respective time point, to a series of consecutive FAST-HSQC spectra using the optimised DMSO conditions allows the H/D exchange reaction to be followed once the samples are reconstituted in DMSO. Experiments conducted using the FAST-HSQC approach illustrated the efficiency of following the H/D exchange process and therefore sample evolution over time. Residues which display different types of H/D exchange profile (based on the cH/D exchange experiments) can be followed in real time in terms of their respective NMR peak intensities, which can be predicted to some extent. It is inevitable that the chosen quench and solution conditions could be improved further,

but it is clear that the exchange reaction is sufficiently quenched in order to monitor the intensities in real time, in which it is possible to back extrapolate to time zero.

Through a detailed attempt at observing iH/D exchange in DMSO a wide variety of exchange time points were used (8, 24, 48, 72, 96 and 168 h) in conjunction with consecutive HSQC spectra using the FAST-HSQC pulse sequence with detection in DMSO (0.25 % $_{d}$-TFA, 99 % $_{d6}$-DMSO, 1 % D_2O). Differences were observed between the fast and slow exchanging residues (categorised by the cH/D exchange experiments for WT hC*c*). However, it is only for the very slow exchanging residues in which differentiation in the exchange profiles are observed (Figures 3.7 – 3.10).

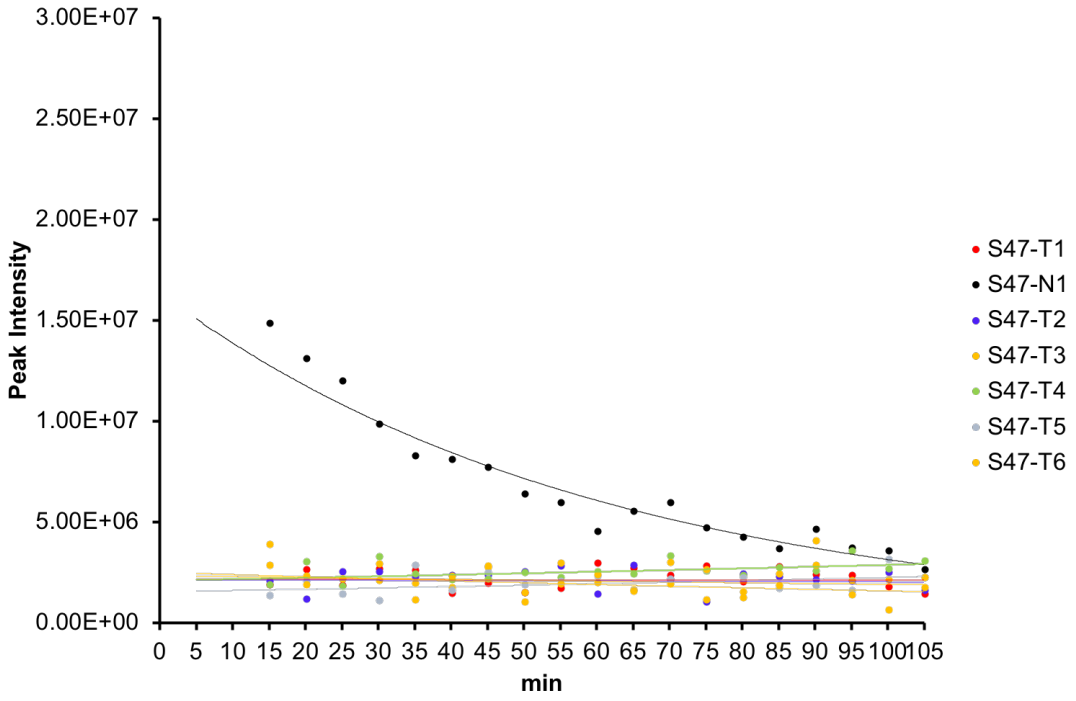

Figure 3.7 Plot of intensity as a function of time (min) for Ser47 using the FAST-HSQC pulse sequence with data fitted to a polynomial equation. The following exchange time points were used; 8 h (T1), 24 h (T2), 48 h (T3), 72 h (T4), 96 h (T5) and 168 h (T6), with a no exchange control (N1).

Approximately a third of the residues exchange within the first 10 min, though their peak intensities increase throughout data acquisition as a result of re-protonation. Theoretically time zero intensity should be near zero, however, NMR detection is not sufficiently fast to provide information before the re-protonation of these initially fully exchanged residues occurs. As a result, it is only for the very slow exchanging residues in which differences between time points could be extrapolated, but for all other suitable residues (based on the cH/D exchange experiments), it is not possible to discern differences between time points. Due to this result, the realisation is that quantitative characterisation of an iH/D exchange dataset for WT hC*c* is certainly of extreme technical difficulty, or perhaps impossible with current methods. However, qualitative characterisation could be possible for this system, in the sense that one might be able to discern whether the H/D exchange profile of a particular residue, or group of residues, is altered upon interaction with CL liposomes through comparisons between the lipid unbound and lipid bound iH/D exchange datasets.

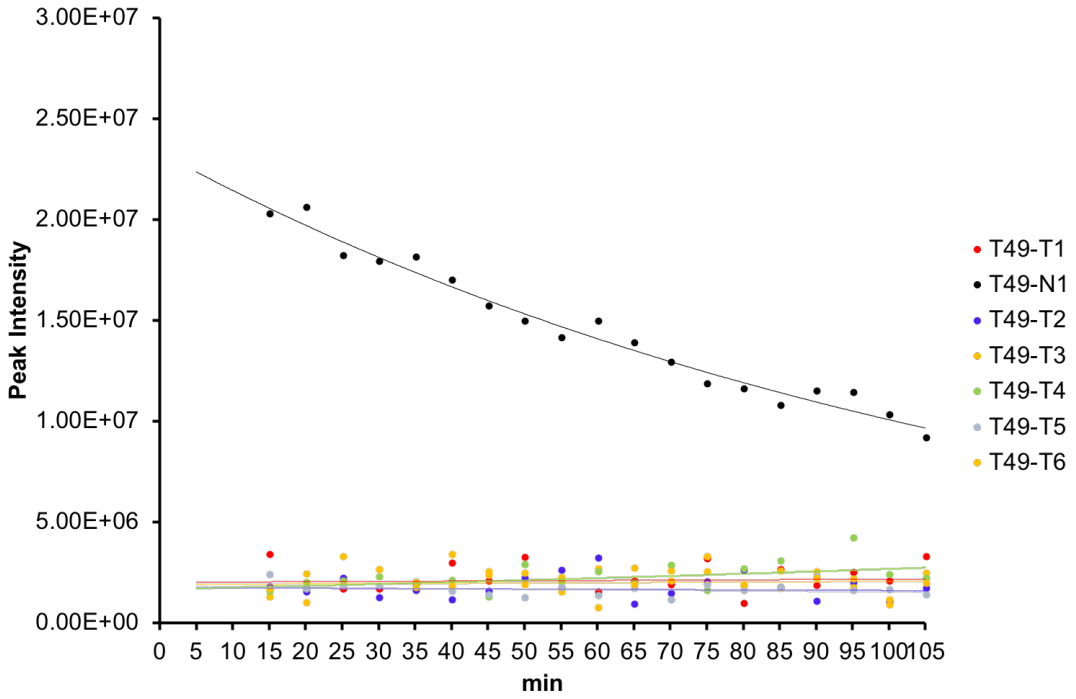

Figure 3.8 Plot of intensity as a function of time (min) for Thr49 using the FAST-HSQC pulse sequence with data fitted to a polynomial equation. The following exchange time points were used; 8 h (T1), 24 h (T2), 48 h (T3), 72 h (T4), 96 h (T5) and 168 h (T6), with a no exchange control (N1).

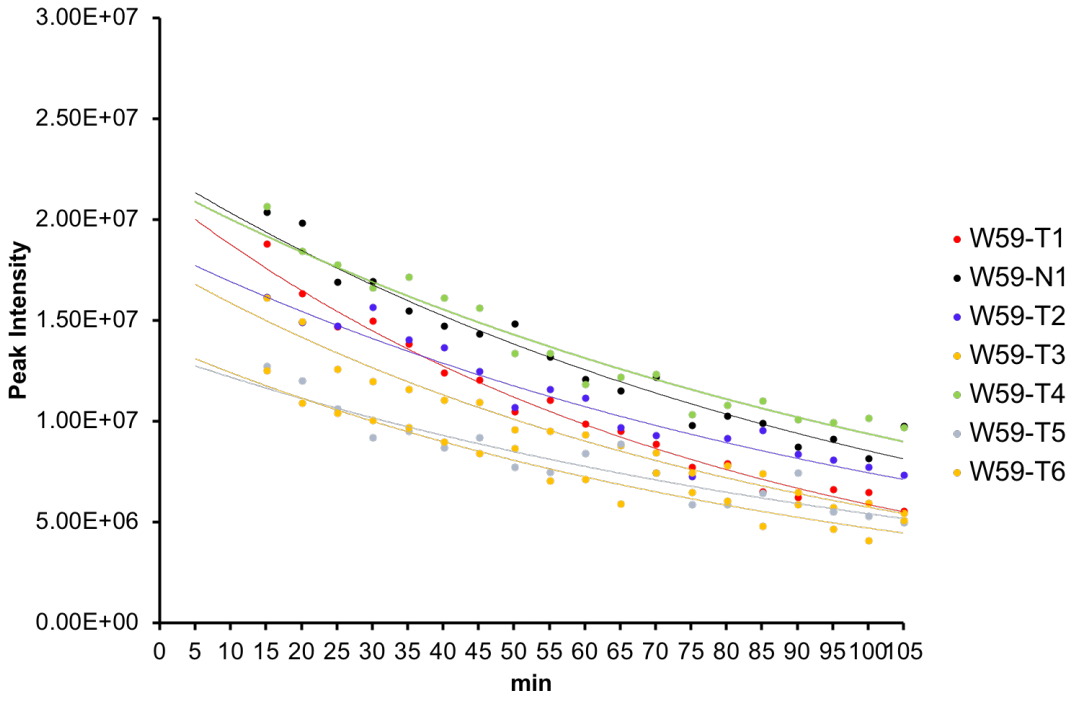

Figure 3.9 Plot of intensity as a function of time (min) for Trp59 using the FAST-HSQC pulse sequence with data fitted to a polynomial equation. The following exchange time points were used; 8 h (T1), 24 h (T2), 48 h (T3), 72 h (T4), 96 h (T5) and 168 h (T6), with a no exchange control (N1).

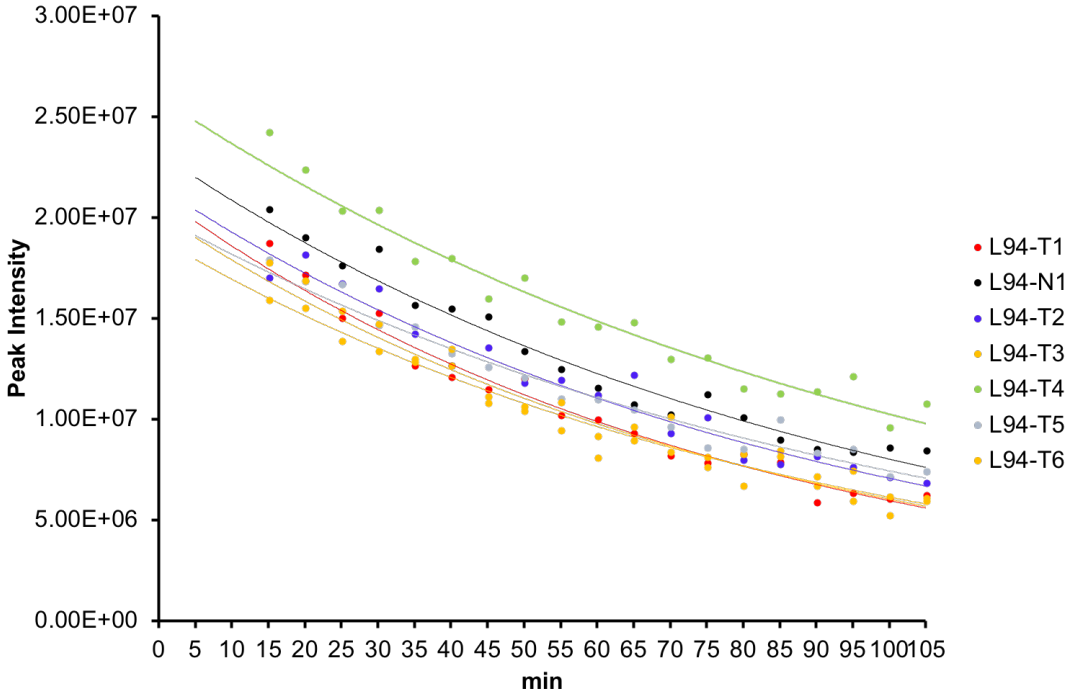

Figure 3.10 Plot of intensity as a function of time (min) for Leu94 using the FAST-HSQC pulse sequence with data fitted to a polynomial equation. The following exchange time points were used; 8 h (T1), 24 h (T2), 48 h (T3), 72 h (T4), 96 h (T5) and 168 h (T6), with a no exchange control (N1).

3.3.6 iH/D exchange conclusions from WT hCc

From experiments conducted it has been possible to conclude that evidence of iH/D exchange is possible in water (section 3.3.3). Furthermore, the solution conditions are optimised to the practical limit, in water and DMSO. Despite these optimisations, it has been demonstrated that in it is only for the very slow exchanging residues in which differences in the H/D exchange profile may be determined, an observation fundamentally inconsistent with the exchange information determined by the cH/D exchange methodology.

An advantage was gained using the 800 MHz spectrometer, enabling the acquisition of multiple sequential HSQC spectra using the FAST-HSQC pulse sequence. The benefit of acquiring consecutive HSQC's over ~ 1 h duration, is that it enables the sample evolution (variation in protonation state) within DMSO to be followed. Using the protocol described by Nishimura and colleagues, it was possible to back extrapolate to a theoretical time-zero from exponential fits to the datasets (Nishimura et al., 2005).

3.3.7 Attempts of integrating CL liposomes into the iH/D exchange methodology

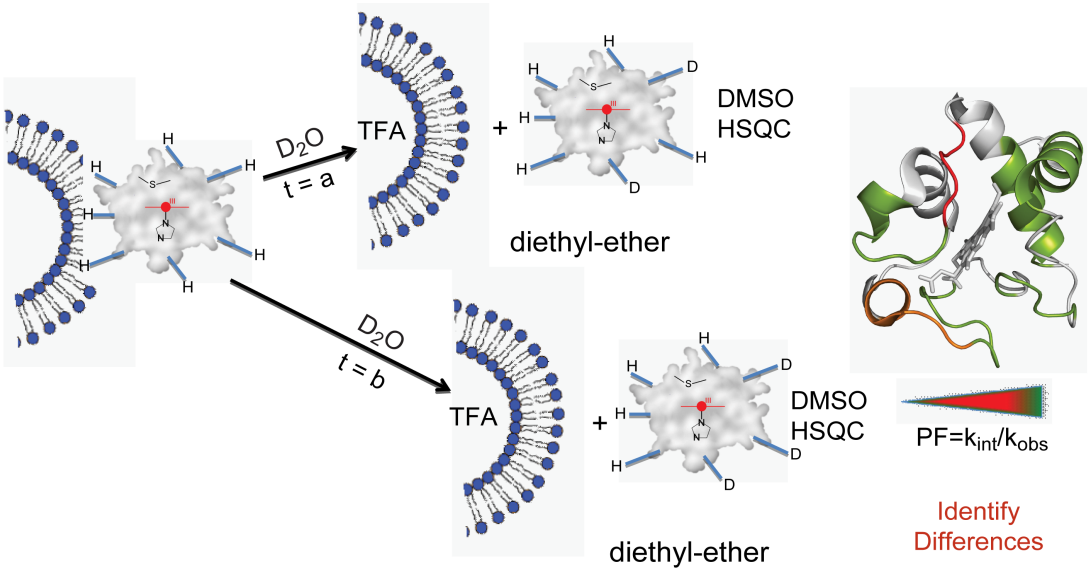

Figure 3.11 Schematic illustration of an iH/D exchange methodology that incorporates soluble protein/phospholipid complexes. The general scheme is as follows, a fully protonated hC*c*/CL complex is allowed to exchange in D_2O for discrete durations, as per an iH/D exchange protocol. At pre-determined time points, the exchange reaction is quenched, the complex disrupted, and the soluble protein isolated through the addition of diethyl-ether (Figure 3.12). The recovered protein is then lyophilised and resuspended in high concertation DMSO solutions at the time of NMR data acquisition. In theory, such a technique would allow for either quantitative and/or qualitative comparisons to be made between a lipid unbound and bound dataset, thus providing direct evidence of the binding interface.

As a result of the difficulties in optimising the conditions necessary to truly preserve the exchange data from the WT hC*c* iH/D exchange data sets, it was decided that the scope of the methodology should be expanded to include iH/D exchange samples with CL liposome complexes. Preparations of DOPC-TOCL liposomes, in addition to TOCL only were incorporated into the experimental routine, with protein/lipid complex formation, viability and long-term stability assessed through guaiacol and ABTS peroxidase activity assays. As introduced in Chapter 1 (reported in Chapters 4 and 5), hC*c*/CL complex formation results in enhanced peroxidase

activity. Variations in the protein/liposome ratio were explored and correlated with long term complex stability. Following from this preliminary work, it was determined that a 1:5 protein to lipid molar ratio is optimal, as any further increase in lipid concentration results in decreased complex stability, increased solution heterogeneity and no additional increase in peroxidase activity.

In order to develop the iH/D exchange protocol for use with protein/liposome complex samples also required the optimisation of the diethyl-ether (DEE) separation protocol. This necessary organic phase separation is carried out following the H/D exchange quench process with TFA, so that the protein/lipid complex is dissociated, but also crucially that the exchange reaction is quenched. Through gentle but thorough mixing, it is possible to form a lipid emulsion layer between the organic phase (top) and the aqueous phase (bottom) (Figure 3.12).

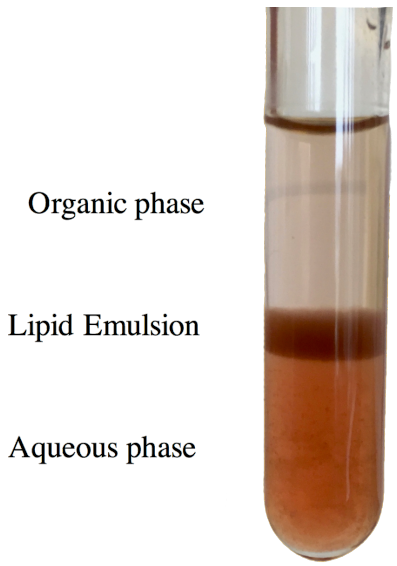

Figure 3.12 Organic and aqueous phase separation following addition of Diethyl ether and mixing. The lipid emulsion forms between the organic and aqueous phases, however, unusually the organic phase lies on top of the aqueous phase.

Unbound hC*c* exists in the aqueous phase and can be extracted through the organic and lipid emulsion phases using a Hamilton syringe (Figure 3.12).

3.3.8 Attempts of observing iH/D exchange with hCc/CL separated samples in DMSO

Initial attempts of observing iH/D exchange with the dissociated WT hC*c*/CL complexed samples led to a new set of technical problems. The most significant issue is how to deuterate the complex, as despite the hC*c*/CL complex formation occurring rapidly, approximately a third of all residues will exchange with equal speed or significantly faster. As a result, it is essential that the hC*c*/CL complex is formed prior to exposure of D_2O. Unfortunately, the protein/lipid complex is not sufficiently robust to survive lyophilising, as determined from ABTS peroxidase activity assays. Therefore, it is not possible to simply remove all H_2O by lyophilisation and then resuspend the complex in D_2O (the conventional approach with un-complexed samples).

There are two main approaches which could achieve complex deuteration, the first is dilution in D_2O followed by concentration of the complex, the second approach is to expose the complex to D_2O through a PD10 desalting column pre-equilibrated in deuterated buffer (20 mM NaPi, pH 6.5). The first iH/D exchange experiment with lipid complex data comprised the dilution/concentration approach, specifically, four samples were constructed as follows; a no H/D exchange and no lipid control (C1N), a no H/D exchange with lipid control, a H/D exchange no lipid control (C3X) and an experimental sample with H/D exchange and lipid (L4X). The DMSO resuspension solution consisted of 0.25 % TFA, 98.75 % $_{d6}$-DMSO and 1 % D_2O. Whilst analysis of the data demonstrated differences between the lipid complexed control and experimental samples (L2N and L4X samples, respectively), ultimately it was apparent

that the optimised quench TFA concentration of 0.065 % v/v and/or resuspension with 0.25 % v/v TFA in the DMSO mixture is not correct for use with lipid complexed samples. This is due to fact that iH/D exchange methodologies are system specific and therefore the integration with lipid solutions represents and significant departure from the previously refined experimental conditions.

3.3.9 Efforts to develop the hCc/CL complex deuteration protocol and subsequent attempts of observing iH/D exchange with hCc/CL separated samples in water

Due to the technical difficulties of observing iH/D exchange in DMSO and the additional complications of integrating liposomes into the methodology, the decision was made to again evaluate the iH/D exchange data in water. As mentioned in section 3.3.3, by acquiring the HSQC datasets in water allows for the full set of resonance assignments to be used, but also provides superior spectral quality.

Of the two complex deuteration techniques stated in 3.3.6 (dilution concentration and the PD10 approaches), the latter PD10 approach proved the most promising technique, as this is both gentle to the complex (supported by good quality NMR spectra) and allows for the majority of the H_2O to pass through the column, allowing for a conservative < 5 % H_2O presence in the final D_2O exchanging sample. It is also possible to maintain reproducibility through identical sample treatment. The alternative dilution/concentration method is less successful both in terms of the resulting NMR spectral quality, but also the residual H_2O content which is between 5-10 % depending whether a 1:20 or 1:10 D_2O dilution is used, respectively.

In order to assess the success of the PD10 approach, dual samples were used reflecting the pre- and post-DEE separation in both D_2O and H_2O conditions. Despite a prominent lipid layer forming following addition of DEE, there was no other sign of

complex formation, specifically no line broadening in NMR spectra prior to lipid separation. These NMR spectra also showed signs of hC*c* auto-reduction suggesting that the PD10 approach required further optimisation.

Despite conventional solution NMR spectroscopy not being amenable to study complexes such as hC*c*/CL, titrations of WT hC*c* with both TOCL and DOPC/TOCL liposomes were performed. The purpose of this was to quantify the timeframe required for complex formation. However, it was again the case that no line broadening was observed suggesting that what is in fact observed during a lipid titration is an ever-diminishing fraction of free (unbound) protein. The reduction in concentration of free C*c* was the result of both lipid binding, but also proportional to the increase in protein/lipid precipitate, particularly at higher lipid concentration. At the end of the titration no NMR signals were observable due to complete protein/lipid complex formation and high levels of precipitation. An interesting observation from titrating both TOCL and DOPC/TOCL liposomes, is that the binding of lipids proceeds differently for the two liposomes. Changes with TOCL liposomes occurs earlier in the titration, starting between 1 and 2 equivalents but also at a later point between 4 and 5 equivalents. Changes with DOPC/TOCL liposomes occur later in the titration, largely between 2 and 3 equivalents.

Both the PD10 and dilution/concentration approaches were evaluated in terms of complex stability using ABTS peroxidase activity assays. Upon dilution and concentration, a significant amount of the hC*c*/CL complex is lost, however, it is not the dilution which breaks the complex, but rather the subsequent concentration using spin concentrators. Despite this, it is known that the hC*c*/CL complex precipitates in low ionic strength solutions, due to the formation of orderly nanospheres surrounding C*c* in what is essentially a hydrophobic CL monolayer (Vikulina et al., 2015). It is

plausible that the high centrifugal forces used in concentrators irreparably disrupt this arrangement in a proportion of the protein/lipid complex.

An interesting observation with the PD10 approach, was the necessity of NaCl in order to elute the complex. The low salt buffer (20 mM NaPi, pH 6.5, in D_2O) used throughout the work reported in this Thesis failed to elute the majority of the protein/lipid complex with resulting fractions displaying varying degrees of peroxidase activity. Despite trialling a variety of NaCl concentrations, it was only when eluting with molar concentrations of salt (20 mM NaPi, 1 M NaCl, pH 7, in D_2O) that the hC*c*/CL complex could be reliably eluted, as confirmed by ABTS peroxidase activity assays. Unfortunately, the consequence of this is a further dilution step in order that the samples have a suitable salt content for NMR spectroscopy (max ~ 150 mM NaCl). As low salt fractions contained the majority of the protein content which existed as free protein, the final protocol for complex deuteration was elution with a single high salt fraction in order to maximise the resulting protein concentration post separation at the spectrometer for NMR detection.

A significant drawback to the PD10 approach for complex deuteration is two-fold: Firstly, the technique requires significant amounts of D_2O, but secondly, the PD10 approach is very sensitive to high concentrations of hC*c*/CL complex and as a result, upscaling the deuteration process with higher protein concentrations is not feasible, as the result is a significantly higher probability of precipitate and thus loss of sample. This is therefore a contributor to the high D_2O cost of the technique.

Furthermore, when using the PD10 approach it is likely that during deuteration there is a significant fraction of the protein population which is "free" protein, the precise quantity is difficult to quantify, but it is likely proportional to the loss in peroxidase activity. This results in a significant technical issue, in that during the

exchange intervals there will be two exchange profiles occurring, one for the protein/liposome complex and the other for the free protein. The result of this, is that the exchange information for the lipid-protected dataset is corrupted to a varying extent by the presence of the free protein H/D exchange profile.

Complicating matters further is the quench TFA concentration and corresponding pH value. Unfortunately, the concentration of TFA required for free hC*c* (0.065 % v/v TFA) proved inappropriate for use with the hC*c*/CL complex. An iH/D exchange experiment in which all previously optimised conditions (for PD10 and dilution/concentration approaches) failed to show any indication of lipid protected and persevered exchange information, furthermore, the overwhelming majority of residues showed relatively unchanged NMR signal intensities throughout the detection regardless of the H/D exchange duration.

3.3.10 Reverse D/H exchange measured in water; a possible way forward?

Most of the technical issues encountered revolve around an appropriate way to expose the hC*c*/CL complex to deuterium. It is a lack of control over the deuteration process which has proved difficult, if not impossible to overcome. A simple method which helps solve some of these issues is to proceed with the H/D exchange reaction in reverse, starting with fully deuterated protein and CL liposomes prepared in D_2O. Solution volumes (in D_2O) can be kept to a minimum as the concentration of hC*c* in D_2O can be kept high and simple dilution in H_2O is sufficient to allow for protonation. An additional benefit of this approach is that it is more cost effective due to the lower consumption of D_2O.

As per the previous experimental efforts described in sections 3.3.3 and 3.3.7, the decision was made to observe the following iH/D exchange datasets in water. The

purpose of this was to not introduce further complications until the methodology was robust enough, but also due to measuring the protonation states in real time using the FAST-HSQC pulse sequence means that time-zero intensities can be determined. Furthermore, as explained in section 3.3.3, an additional benefit of measuring in aqueous buffer conditions is that it is possible to follow a greater number of residues, due to the complete NH resonance assignment set obtained for the WT hC*c*. A final benefit of observing iH/D exchange data in aqueous buffer conditions is that it allows for direct comparison with the detailed cH/D exchange dataset obtained for WT hC*c*, facilitated by the fact that D/H and H/D exchange rates are comparable.

In order to determine a more appropriate TFA quench concentration for use with lipid bound samples, a repeat experiment was designed as per the H_2O quench optimisation experiments previously described in section 3.3.3. However, the exchange reaction would occur in

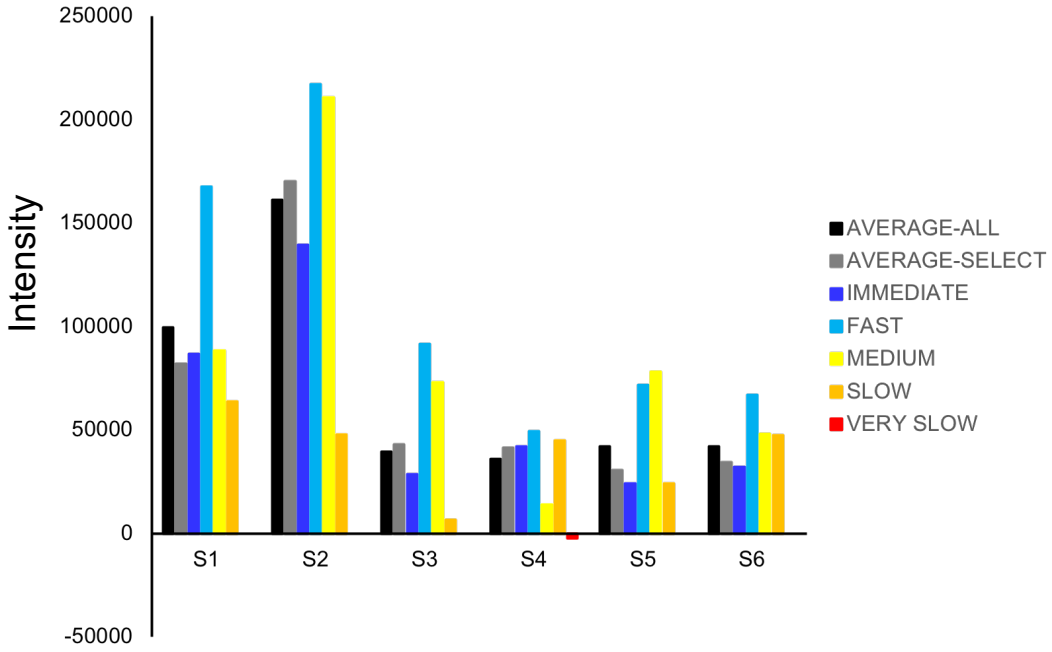

Figure 3.13 Average residue peak intensities obtained from iH/D exchange experiments using the FAST-HSQC pulse sequence, measured in water. Average "quenched" peak height intensity of entire protein (black), select residues (grey) and based on the cH/D exchange profile of WT hC*c* (Karsisiotis et al., 2016) immediately exchanged residues (blue), fast exchanging residues (aqua), medium exchanging residues (yellow), slow exchanging residues (orange) and very slow exchanging residues (red). Sample TFA quench concentrations are as follows; 0.065 %, 0.075 %, 0.085 %, 0.100 %, 0.115 % and 0.130 % v/v for samples S1 – S6 respectively.

reverse, starting from a fully deuterated sample, which is subsequently allowed to exchange in H_2O. Six samples (S1 – S6 Figure 3.13) quenched with 0.065 %, 0.075 %, 0.085 %, 0.100 %, 0.115 % and 0.130 % v/v d-TFA respectively, were produced. Samples S1 (0.065 % v/v TFA) and S2 (0.075 % v/v TFA) resulted in a solution pH of 5.04 and 5.16 respectively and showed a complete inability to arrest exchange (Figure 3.13). Analysis of the four remaining samples, ranging from 0.085 – 0.13 % v/v d-

TFA, yielding pH values < pH 3.6 revealed low exchange rates, with 0.1 % identified as the optimal condition (S4 Figure 3.13). 0.1 % v/v TFA was determined to be optimal, as it can be seen from Figure 3.13 that "overall" there is the lowest intensity across all residues based on the exchange rate framework (very fast, fast, medium, slow and very slow exchange groupings), as determined by the cH/D exchange experiment for WT hC*c*.

3.3.11 "Dry" DMSO

A final avenue of iH/D exchange exploration reported in this Chapter is the use of "dry" DMSO using molecular sieves (Dr Joseph Wright's Group, University of East Anglia). An experiment was designed in which iD/H exchange samples would be resuspended in "dry" DMSO with all sample preparation conducted under anaerobic conditions (anaerobic chamber and sealable NMR tubes), prior to measuring. A preliminary 1D ^{1}H NMR experiment comparing the H_2O contamination within "dry" DMSO obtained through molecular sieves vs the $_{d6}$-DMSO in sealed ampules (as used for the majority of experiments documented in this chapter) revealed that there was significantly less H_2O content in the previously used $_{d6}$-DMSO ampules than in the "dry" DMSO.

3.3.12 Conclusions and summary of methodology achievements

Ultimately the aforementioned attempts at optimising conditions in order to preserve and observe iH/D exchange data for WT hC*c* has proved unsuccessful. The issue of preserving exchange state data in DMSO has been a constant challenge throughout the method development. It is possible to preserve exchange information for a variety of residues in water, however, in DMSO it is only possible to extract

exchange information for the very slow exchanging residues. Due to the difficulties encountered with DMSO, qualitative data analysis has been more feasible than quantitative.

Integration of liposome preparations into the iH/D exchange methodology, including characterisation of the hC*c*/CL complex, both in terms of stability and the necessary conditions needed for post quench separation using an organic phase has been achieved. Detailed work has determined the most suitable approach for deuterating the protein/lipid complex and highlighted the shortcomings of the PD10 column and dilution/concentration approaches. Other issues such as the appropriate quench pH with lipids, the impact of each treatment to the stability of the hC*c*/CL complex and the optimisation of every sub-step of the process has been investigated in the context of all previous observations. Finally, the re-protonation (D/H exchange) approach is essentially the most promising way to observe iH/D exchange of the hC*c*/CL complex, both in terms of practical feasibility but also in terms of control over each individual step in the technically challenging process, without compromising complex stability. Summaries of the iH/D exchange methodology development and various exchange protocols used with the protein/lipid complex are provided in Appendix C.

Chapter 4

Dynamics of G41S and Y48H variants of human cytochrome *c* regulate an apoptotic role

---

Results from this Chapter have been published in:

Karsisiotis, A.I., Deacon, O.M., Wilson, M.T., Macdonald, C., Blumenschein, T.M.A., Moore, G.R., Worrall, J.A.R. "Increased dynamics in the 40-57 W-loop of the G41S variant of human cytochrome *c* promote its pro-apoptotic conformation" (2016) *Sci. Rep.* **6**, 30447.

Deacon, O.M., Karsisiotis, A.I., Moreno-Chicano, T., Hough, M.A., Macdonald, C., Blumenschein, T.M.A., Wilson, M.T., Moore, G.R., Worrall, J.A.R. "Heightened Dynamics of the Oxidised Y48H Variant of Human Cytochrome *c* Increases Its Peroxidatic Activity" (2017) *Biochemistry* **56**, 6111-6124.

4.1 Introduction

hC*c* is a well-known multifunctional haem protein that functions as an electron carrier in the electron transfer chain between the cytochrome bc_1 and C*c*O aa_3 complexes (Ferguson-Miller and Babcock, 1996). More recently hC*c* has been shown to play two crucial roles in apoptosis (Ow et al., 2008, Huttemann et al., 2011); one function is a lipid peroxidase in the early stages of the intrinsic apoptosis pathway, as part of the process of creating a pore in the OMM (Kagan et al., 2005), and the second set of roles is as a structural component of multi-protein complexes, including: the apoptosome (Wang, 2001), heat shock protein 27 (Bruey et al., 2000) and inositol triphosphate receptors of the endoplasmic reticulum (Boehning et al., 2003). hC*c* also plays a functional role as an inhibitor of a histone chaperone activity in the nucleus following DNA damage by binding to a nucleosome assembly protein (González-Arzola et al., 2015) and as an extracellular ligand to serum leucine-rich alpha-2-glycoprotein-1 (Cummings et al., 2006), an important interaction aiding lymphocytes survival from the toxicity resulting from hC*c* release in apoptosed cells.

C*c* has also been shown to function as a signalling molecule regulating the activity of the nuclear oncoprotein complex SET/template-activating factor-Iβ (SET/TAF- Iβ) (Li et al., 1997, Kagan et al., 2005, Huttemann et al., 2011, González-Arzola et al., 2015). Under physiological conditions hC*c* has a hexa-coordinate haem iron, in which the proximal and distal axial ligands are His18 and Met80 respectively. The haem is buried within the hydrophobic core of the protein, an environment formed by 5 α-helices and 3 Ω-loops. Under native physiological conditions oxidised hC*c* possesses a low level of intrinsic peroxidase activity, which has been shown to facilitate the regulation of ROS (Diederix et al., 2002). The peroxidase activity arises from an equilibrium in oxidised C*c* between a hexa-

coordinate haem form and a penta-coordinate form, with the latter arising from dissociation of the Met80 ligand (Sutin and Yandell, 1972). Prior to mitochondrial degradation and subsequent release of hC*c* into the cytosol, hC*c* forms a complex with CL, a phospholipid localised to the IMM (Kagan et al., 2005). The hC*c*/CL complex causes dissociation of the Met80 haem ligand yielding the peroxidase active penta-coordinate haem form and this complex greatly boosts peroxidase activity (Vladimirov et al., 2013). Under alkaline conditions, oxidised hC*c* has access to a conformation in which the Met80 ligand is replaced by a Lys (either Lys73 or Lys79) within the 71-85 Ω-loop (Rosell et al., 1998). This alkaline isomerisation, known as the "alkaline transition" occurs in C*c* with an apparent $pK_a \sim 9$ which is dependent on the ionic strength and temperature (Wilson and Greenwood, 1996). Ferric hC*c* therefore has a variety of energetically accessible conformational states that confer very different properties than that of the native form (Karsisiotis et al., 2016).

Autosomal dominant Thrombocytopenia 4 (THC4; OMIM 612004) is an inherited disease which arises from mutations in the hC*c* gene *CYCS* and results in enhanced mitochondrial apoptotic activity (Morison et al., 2008). To date, there have been three mutations in the *CYCS* gene which yield the protein variants G41S, Y48H and A51V (Morison et al., 2008, De Rocco et al., 2014, Johnson et al., 2016). All mutations reside in the 40-57 Ω-loop (Hunte et al., 2000, Lange and Hunte, 2002, Sakamoto et al., 2011, Volkov et al., 2011), which Englander and co-workers found to be the foldon (a cooperative folding/unfolding unit within the polypeptide) with lowest free energy of the five foldons identified (Krishna et al., 2003a, Krishna et al., 2006). In the absence of CL, the oxidised G41S variant displays greater peroxidase activity than that of the WT protein (Rajagopal et al., 2012, Josephs et al., 2014). High resolution X-ray structures have been determined for WT and the G41S variant of hC*c*

and have shown minimal structural changes, but with perturbations near the mutation sites that influence the H-bonding arrangements with haem propionate-7 (HP-7) (Liptak et al., 2011, Rajagopal et al., 2013). These altered interactions with the haem propionates, as seen in the G41S variant, may well be of significance as it is known that the electronic properties of haem propionates impact haem reactivity (Moore and Pettigrew, 1990). The G41S variant haem environment displays greater polarity as a result of rotation of the Arg38 sidechain and the presence of additional H_2O molecules which might also contribute to H_2O_2 access to the haem, thus directly impacting peroxidase activity (Josephs et al., 2014, Josephs et al., 2013). Despite small conformational differences between the WT and G41S proteins, there is a substantial difference in global stability where the free energy of denaturation for WT being 10.5 kcal mol^{-1}, representing a 2.6 kcal mol^{-1} greater stability than that of the G41S variant (Rajagopal et al., 2013).

As both the WT and G41S variant of hC*c* are able to access non-native conformations, it was postulated that the G41S variant would perturb the energy landscape of the ferric protein, thus changing the relative populations and kinetics of conversion between the native state and non-native conformer and therefore help to explain the pro-apoptotic behaviour of the G41S variant (Karsisiotis et al., 2016). To support this hypothesis, it has been demonstrated that the 40-57 Ω-loop, the lowest free energy foldon as determined by Englander and co-workers (Hoang et al., 2003, Maity et al., 2004, Maity et al., 2005), along with the Ω-loops 71-85 and 19-35 display increased dynamics in the G41S variant as determined by HDX and ^{15}N relaxation experiments (Karsisiotis et al., 2016).

This chapter describes stopped-flow kinetics of azide binding to the WT protein, G41S and Y48H variants, peroxidase activity assays, as well as the dynamics

of the Y48H variant as determined through heteronuclear H/D-exchange and relaxation measurements. This enables for a comparison to be made between the WT protein and the two pro-apoptotic variants in terms of their dynamics in the haem environment and their main-chain dynamics. A direct conformational link between the 40-57 Ω-loop and the dynamical properties of the axial Met80 ligand is found and placed in the context of small fluctuations in the energy landscape that leads to an increased population of the penta-coordinate peroxidase active form.

4.2 Materials and Methods

4.2.1 Site-directed mutagenesis

The Y48H variant was produced using the Quickchange mutagenesis protocol (Stratagene). The following forward and reverse mutagenic primers were used: 5'-GCCCCTGGATACTCTCATACAGCCGCCAATAAGAAC-3' and 5'-GTT CTTATTGGCGGCTGTATGAGAGTATCCAGGGGC-3', respectively. A PCR reaction mixture consisting of primers (75 ng/μl), WT template (15 ng/μl), 10 mM dNTPs (Fermentas), Pfu Turbo polymerase (Stratagene), 10 x Pfu Buffer (Agilent) and deionised H_2O to yield a final volume of 50 μl was used. This reaction mixture was subjected to the following PCR protocol; 95 °C – 3 min, (95 °C – 1 min, 65 °C – 1 min, 72 °C – 6 min) x 18 cycles, 72 °C – 10 min. PCR products were digested with DpnI (Fermentas) and transformed into DH5α *Escherichia coli* cells. Isolated clones were DNA sequenced to corroborate the presence of the expected nucleotide change.

4.2.2 Over-expression and purification of the G41S and Y48H variants

The over-expression and purification protocols for Y48H and G41S hC*c* variants were identical to that of the WT protein reported in detail in Chapter 2.

4.2.3 Protein preparation

All proteins were oxidised to the ferric haem state through addition of a 2-fold excess of $K_3[Fe(CN)_6]$, followed by removal of $K_3[Fe(CN)_6]$ and $K_4[Fe(CN)_6]$ and exchanged into the desired buffer using a PD-10 desalting column (GE Healthcare). Protein concentrations were determined with a Cary 60 spectrophotometer (Agilent) and a molar extinction coefficient of $\varepsilon = 106\ mM^{-1}\ cm^{-1}$ at 409 nm. The ferrous proteins were formed through addition of a 2-fold excess of sodium ascorbate (Sigma). Excess sodium ascorbate was removed, and the protein exchanged into the desired buffer using a PD-10 desalting column (GE Healthcare) and protein concertation determined using the absorbance at 550 nm with an $\varepsilon = 27.5\ mM^{-1}\ cm^{-1}$.

4.2.4 NMR spectroscopy

All NMR data were collected with a Bruker 500 MHz (H/D exchange) or 800 MHz (1D, ^{15}N relaxation and sequence specific resonance assignments) spectrometer, both equipped with 5 mm HCN inverse triple-resonance z-axis gradient probes. Samples for 1D ^1H NMR were oxidised and buffer exchanged in 20 mM sodium phosphate (pH 6.5) as described previously (Chapter 2) and lyophilised. Samples were redissolved in 500 μL of 99.9 % D_2O (Sigma) and allowed to deuterate at room temperature for ~ 72 h. 4,4-Dimethyl-4-silapentane-1-sulfonic acid (DSS) (Sigma) (final concentration of 200 μM) and $K_3[Fe(CN)_6]$ (final concentration of 100 μM, to maintain an oxidising environment) were added to each sample and 1D ^1H spectra recorded at temperatures ranging from 288 K to 313 K using presaturation to supress the solvent signal, with spectral widths of 20 and 80 ppm. TopSpin (Bruker BioSpin) was used for spectral processing.

Singly (^{15}N) and doubly (^{15}N and ^{13}C) labelled samples of the Y48H variant were prepared as previously described (Chapter 2). NMR samples of ferric Y48H hC*c* were prepared in 20 mM sodium phosphate (pH 6.5) and contained 1 mM protein with 10 % D_2O (Sigma) for the spectrometer lock. A set of 2D ^{1}H-^{15}N HSQC and 3D HNCACB and CBCA(CO)NH spectra were acquired at 288 K, with TopSpin (Bruker BioSpin) again used for spectral processing. Sequence specific resonance assignments were obtained using both the CCPN Analysis and Sparky applications (Vranken et al., 2005, Goddard, 2008, Lee, 2015).

H/D exchange NMR data were acquired at 288 K. Lyophilised samples of the ferric Y48H variant (1 mM) were redissolved in 20 mM sodium phosphate (pH 6.5) and 50 mM NaCl premade in 99.9 % D_2O (Sigma). Spectra were recorded as matrices of 1024 x 64 complex data points with four scans and spectral widths of 15 (^{1}H) and 42 (^{15}N) ppm centred at 4.7 and 118.6 ppm, respectively. The acquisition of consecutive ^{1}H-^{15}N HSQC spectra started ~ 5 min after sample resuspension with an acquisition time of ~ 5 min per spectra. A total of 191 experiments were acquired, the first 100 with 10 s delays between each experiment to ensure maximum resolution of the fast-exchanging residues, with the following 74 experiments at 45 min intervals, followed by 17 experiments at 4 h intervals. H/D exchange analysis was conducted in the CCPN Analysis application, where peak volumes were fitted as a function of time to a two-parameter single exponential decay function (Vranken et al., 2005). Protection Factors (PF) were determined from these extracted exchange rates following the protocol of Bai *et al.* and Hoshino *et al*. as described in Chapter 3 (Bai et al., 1993, Hoshino et al., 2007). The prerequisite intrinsic exchange rate constants were determined as described in Bai *et al*. whilst ΔG_{ex} values were obtained from the

equitation $\Delta G_{ex} = -RT\ln(PF)$ from Hoshino *et al*. where R is the gas constant and T is the temperature in Kelvin (Bai et al., 1993, Hoshino et al., 2007).

^{15}N T_1, T_2 and [^1H]-^{15}N NOE data were acquired at 800 MHz as matrices of 1024 x 256 complex data points, with 8 scans for T_1 and T_2 data, and 64 scans for [^1H]-^{15}N NOE experiments. Spectral widths of 15 (^1H) and 39.3 (^{15}N) ppm centred at 4.7 and 118.6 ppm respectively were used. T_1 experiments were acquired with the following relaxation delays, 10, 50, 80, 200, 500, 750, 2000 and 3500 ms with duplicates of 10, 200 and 500 ms. T_2 experiments were acquired with the following relaxation delays, 16.96, 33.92, 50.88, 67.84, 101.76, 135.68, 203.52 and 254.4 ms, with duplicates at 16.96, 50.88 and 101.76 ms. Both experiments used a 5 ms recycle delay. The repeated relaxation delays were used to settle peak height uncertainties as documented in (Palmer et al., 1991), whilst the first T_1 delay of 20 ms was set due to limitations in the pulse sequence (Karsisiotis et al., 2016). To reduce sample heating, T_1 and T_2 experiments were acquired with interleaved delay values. To determine T_1 and T_2 values, peak heights were fitted as a function of the relaxation delay to a two-parameter single exponential decay function using the "follow intensity changes" function within CCPN Analysis (Karsisiotis et al., 2016). T_1 and T_2 rates were converted to the relaxation rates R_1 and R_2 with $R_1 = 1/T_1$ and $R_2 = 1/T_2$ (Karsisiotis et al., 2016). Fit errors for T_1 and T_2 were converted to their corresponding R_1 and R_2 errors through the equality of the T_1/T_2 and R_1/R_2 errors (Karsisiotis et al., 2016). The heteronuclear [^1H]-^{15}N NOE experiments were acquired with a ^1H saturation duration of 5 s, interleaved saturated and unsaturated experiments were acquired in triplicate so that experimental error could be determined as the standard deviation from the average NOE value (Karsisiotis et al., 2016). The NOE values were determined by taking the ratio of peak height with and without ^1H saturation.

4.2.5 Stopped-flow spectroscopy

All kinetic experiments were conducted with an Applied Photophysics (Leatherhead UK) SX20 stopped-flow spectrophotometer equipped with both photomultiplier and photodiode array detection systems, thermostatted at 25 °C. Various stocks of buffer consisting of 2 M sodium azide (N_3^-), 50 mM sodium phosphate and 50 mM MES, pH 7, were diluted to desired N_3^- concentrations with identical buffer except with 2 M N_3^- substituted for 2 M NaCl to maintain equal ionic strength (Karsisiotis et al., 2016). Reaction time-courses are recorded at 420 nm with known N_3^- concentration, ranging from 0.08 – 2 M prior to mixing, and 10 μM protein also prior to mixing. Traces were fitted to a single exponential function giving pseudo first-order rate constants and amplitudes, with all reported errors being standard errors (Karsisiotis et al., 2016).

4.2.6 Peroxidase assays

Phospholipid liposomes consisting of a 1:1 ratio of TOCL (1, 1', 2, 2'-tetraoleoyl CL) and DOPC (1, 2-dioleoyl-*sn*-glycero-3-phosphocholine) (Avanti Polar Lipids) were used. Lipids stored in chloroform were aspirated in an atmosphere of argon (BOC) to prevent oxidation. During aspiration, the lipid solution is kept in continual motion to produce a uniformly thin and dry film at the base of the glassware prior to sealing with Parafilm. The lipids were re-suspended in 20 mM sodium phosphate, pH 6.5 by vortexing for ~ 10 min yielding a 2.5 mM stock. Once a homogenous, cloudy solution is achieved, liposomes were made of uniform size by sonication in a high-power sonicating water bath at 4℃ for ~ 15 min, or until a clear solution was achieved. All peroxidase assays were carried out on a Hewlett-Packard 8453 photodiode-array spectrophotometer scanning from 190 – 730 nm, thermostatted

at 20 °C. Assay conditions consisted of 5 μM protein, 200 μM 2,2-Azinobis(3-ethylbenthiazoline-6-sulfonic acid) (ABTS), 1 mM H_2O_2 (Sigma) with and without 25 μM TOCL-DOPC liposomes. Assay volumes were set at 3 ml with a 1 cm path length, as this volume facilitated mixing with H_2O_2 during the initial phase of the assay. To maintain a consistent start-point for the assays, H_2O_2 was added at ~ 40 s after scanning commenced and then proceed to run for 1000 s. The absorbance changes were monitored at 730 nm, with a single reference wavelength of 475 nm. The maximum rate of absorbance change was taken from the initial slope after the addition of H_2O_2, which in the absence of lipid for WT hC*c* occurred after a short initial lag phase. The slope of each trace was determined from the first linear portion of the traces post-lag phase, thus providing rates in AU/s. To convert rates from AU/s to μM/s, the rates are divided by the extinction coefficient of oxidised ABTS at 730 nm (14 mM^{-1} cm^{-1}). Assays were repeated in triplicates, so the average of the three rates obtained for each protein under both conditions are plotted with the error reported as standard deviation.

4.2.7 Circular Dichroism spectroscopy

Circular Dichroism (CD) spectra were recorded from 190 – 250 nm with an Applied Photophysics Chirascan CD spectrophotometer (Leatherhead, UK), thermostatted at 15℃. Sample conditions consisted of 20 μM protein, 10 mM potassium phosphate pH 7, 50 mM KF in a final volume of 200 μl in a 0.1 cm path length cuvette. The raw data was converted from millidegrees to Mean Residue Ellipticity (MRE) using equation 4.1, where θ is the circular dichroism, 0.1 refers to the cuvette path length in cm, 20 $x10^{-6}$ is the protein concentration (M) and 104 is the number of residues in hC*c*.

$$MRE = (\theta / 10 \times 0.1 \times (20 \times 10^{-6}) \times 104) \quad [4.1]$$

Chemical denaturation studies were carried out using Guanidinium hydrochloride (GuHCl; Fluka) using CD spectroscopy at 15 °C through monitoring the change in ellipticity at 222 nm. The proteins were equilibrated in 20 mM sodium

$$\text{observable} = \frac{(\alpha_N + \beta_N[\text{GuHCl}]) + (\alpha_D + \beta_D[\text{GuHCl}])\exp\left(\frac{-\Delta G_{D-N}^{H_2O} + m[\text{GuHCl}]}{RT}\right)}{1 + \exp\left(\frac{-\Delta G_{D-N}^{H_2O} + m[\text{GuHCl}]}{RT}\right)} \quad [4.2]$$

phosphate, 50 mM NaCl pH 6.5 to a starting working volume of 1 ml and 20 μM protein. A 3 ml cuvette with 1 cm path length was used for the titration, in which various additions of a stock 6 M GuHCl solution in 20 mM NaPi, 50 mM NaCl pH 6.5 were added to the cuvette so that each point in the titration reflected a 0.1 M increase in GuHCl. Measurements in triplicates of each protein were carried out and raw data in millidegrees converted to Fraction Denatured (FD) using equation 4.2, where α_N and β_N represent the respective values for the lowest and highest values of the slope in the folded state during the titration and the α_D and β_D represent the highest and lowest values of the slope in the unfolded state during the titration and R is the gas constant (J/mol). ΔG, C_m and "m" values are ultimately determined from fits to equation 4.3, following an initial fit to the raw data using equation 4.2.

$$F_D = \frac{\theta_{222nm} - (\alpha_N + \beta_N[\text{GuHCl}])}{(\alpha_D + \beta_D[\text{GuHCl}]) - (\alpha_N + \beta_N[\text{GuHCl}])} \quad [4.3]$$

4.2.8 Static pK_a titrations

All static pK_a titrations have been carried out at room temperature up to three times and in different batches for each respective protein. Buffer conditions consisted of 20 mM sodium phosphate, pH 6 and 100 μM protein concentration in a quartz cuvette (Hellma). Additions of 0.3 μl – 1 μl of 1 M NaOH were used to gradually increase pH to a final concentration of ~ pH 11, with pH measurements taken using a semi-micro glass pH electrode (Corning) in the cuvette prior to scanning. The absorbance changes were monitored at the 695 nm band and data plotted after baseline subtracting the absorbance at 800 nm to account for any baseline shifts that occurred during the titrations. The data is fitted to a one-proton ionisation equilibrium equation, y = P1+((P2*(10^(x-P3)))/(1+10^(x-P3)))), yielding the apparent pK_a of the 695 nm band.

4.2.9 Y48H crystallisation and structure determination

Crystals were grown using the sitting-drop vapour diffusion method at 18 °C. A 0.2 μl solution containing 56 mg/ml of the ferric Y48H hC*c* variant in 20 mM sodium phosphate pH 6.5 was used to screen for crystallisation conditions using an ARI Gryphon crystallisation robot (Art Robbins Instruments). A successful crystal hit was found in conditions of 33 % PEG 6000, 100 mM Tris/HCl pH 7.5. Single crystals were transferred to a cryoprotectant solution containing the reservoir solution and 15 % glycerol, prior to flash cooling in liquid nitrogen. Crystallographic data were measured at the Swiss Light Source (SLS, Villigen, Switzerland) at beamline X10SA with a wavelength of 1 Å using a Pilatus 6M-F detector (Dectris). The collected data were indexed, integrated and merged using XDS (Kabsch, 2010) and Aimless (Evans and Murshudov, 2013) in the CCP4 suite with the CCP4i2 graphical user interface. The

Y48H structure was solved by molecular replacement within Phaser using the structure of WT hC*c* (3zcf) as a template, as previously reported (Kabsch, 2010, Evans, 2006, Rajagopal et al., 2013). Structural refinement and model building cycles were conducted in Refmac5 and Coot, respectively. Riding hydrogen atoms were added after the protein refinement had converged with final structure validation through the MolProbity server (Murshudov et al., 1997, Emsley and Cowtan, 2004, Davis et al., 2007).

4.3 Results

4.3.1 UV-Visible and far UV CD spectroscopy

The optical absorbance of the WT protein and Y48H variant of hC*c* in the oxidised and reduced forms are indistinguishable and shown in Figure 4.1. The far-UV CD spectra of the WT protein G41S and Y48H variants display two negative

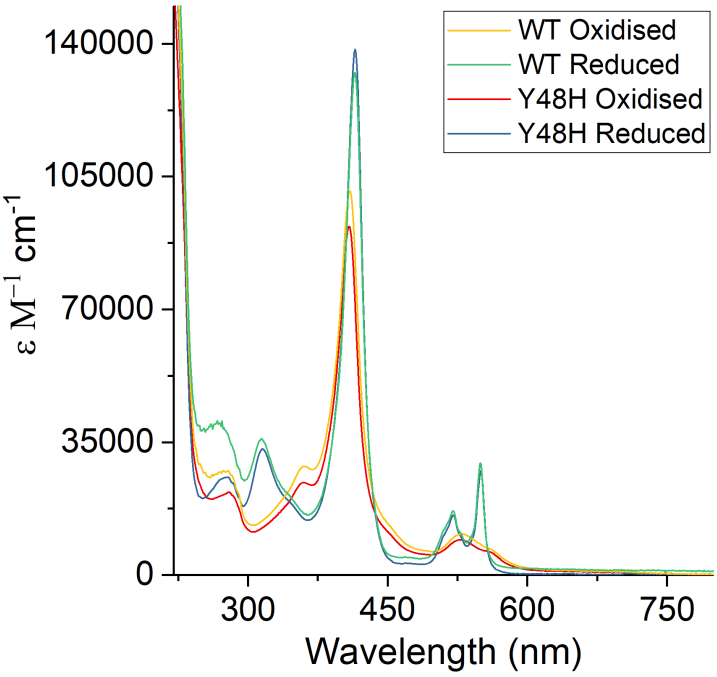

Figure 4.1 UV visible spectra of the WT protein and Y48H variant of hC*c* in both the ferric and ferrous forms at pH 6.5 (20 mM NaPi) and at room temperature.

minima at 208 and 222 nm indicating significant α-helical content and is a good indication that all proteins are folded (Figure 4.2). Furthermore, both variants appear to have a higher helicity than the WT protein.

Determination of the ΔG_{unf}

Far-UV CD spectroscopy was used to assess the stability of the WT protein and the G41S and Y48H variants by means of chemical denaturation through addition of increasing concentrations of GuHCl. It is known that chemical denaturation is superior to thermal melts in the context of determining C*c* thermodynamic stability parameters, as it has been extensively reported in literature that for Cytochromes *c* thermally induced denaturation of the protein is not an entirely reversible process, therefore

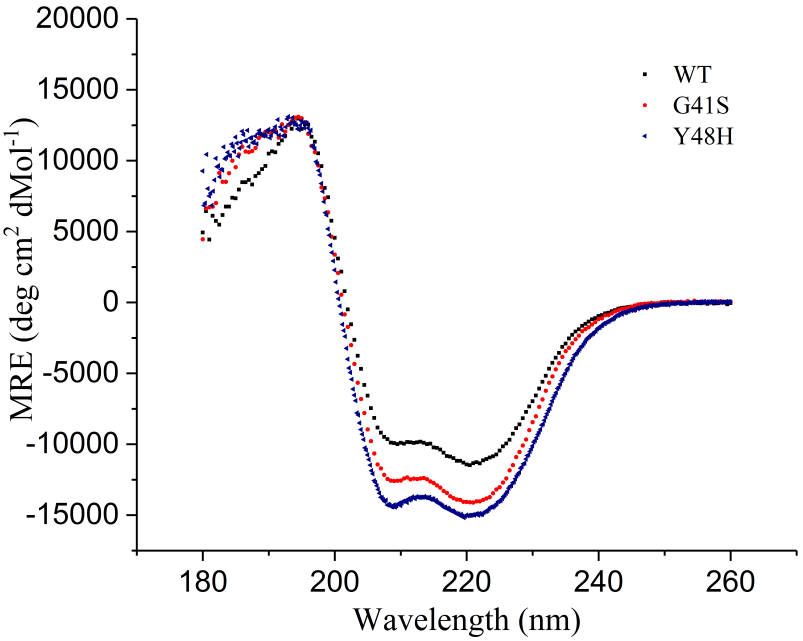

Figure 4.2 Far-UV CD spectra of ferric WT, G41S and Y48H hC*c* at pH 7.0 and 15℃.

opposing the assumptions made by the model used to determine said thermodynamic stability parameters. Figure 4.3 displays typical denaturation profiles for the three proteins with fits to equation 4.3 yielding the thermodynamic unfolding parameters

reported in Table 4.1. The data show that there is a progressive decrease in the cooperativity of unfolding (WT > G41S > Y48H), with the Y48H variant having the lowest global stability (ΔG_{unf}, Table 4.1). The *m*-value (Table 4.1) quantifies a measure of the change in hydrophobic surface area that has become desolvated upon denaturation, also decreases in the order of WT > G41S > Y48H, suggesting that the disease variants of hC*c* have an increasingly more compact denatured state relative to the WT protein (Shortle, 1995). The K54H variant of *S. cerevisiae* iso-1 C*c* stabilises the denatured state through a His-haem loop which results in a decreased *m*-value in relation to the WT protein (Hammack et al., 2001). Two possible interpretations of this in relation to the Y48H variant, are either that a similar effect occurs, or, that the Y48H variant is simply partially unfolded in solution (Godbole et al., 1997, Hammack et al., 2001). The latter is perhaps more likely, as it is supported by the NMR data presented in Figure 4.13.

Table 4.1 Summary of the thermodynamic and kinetic parameters for the Y48H variant, in comparison with that of the G41S variant and WT proteins.

	GuHCl denaturation				Azide binding		
Protein	ΔG_{unf} (kcal mol^{-1})	C_m (M)	*m* (kcal mol^{-1} Mol^{-1})	pK_{695}	K_{app} (M)	k_1 (s^{-1})	k_{-2} (s^{-1})
WT	10.65 ± 0.55	2.6 ± 0.05	4.10 ± 0.25	9.3 ± 0.2	0.31 ± 0.03	5.77 ± 1.5	3.5 ± 0.44
G41S	6.75 ± 0.10	2.25 ± 0.05	3.00 ± 0.10	8.5 ± 0.2	0.11 ± 0.01	45 ± 18	8.9 ± 0.3
Y48H	5.09 ± 0.16	1.98 ± 0.05	2.57 ± 0.10	8.4 ± 0.1	0.07 ± 0.01	> 125	12.1 ± 1.1

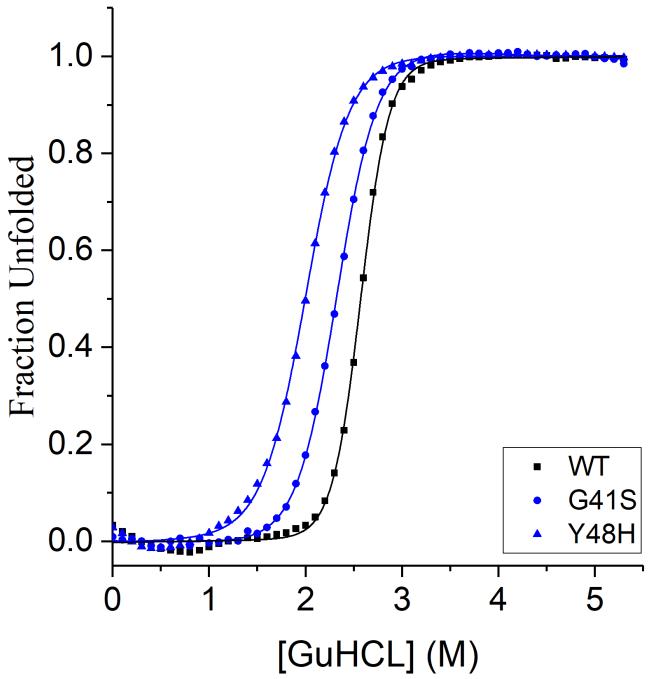

Figure 4.3 Equilibrium unfolding by GdnHCl of the WT protein, and the G41S and Y48H variants of hC*c* at pH 7 and 15℃.

4.3.2 The pH dependence of the 695 nm absorption band

The UV-visible spectrum of ferric hC*c* is pH dependent. Below the pK_a of the optical transition hC*c* primarily populates the hexa-coordinate "acid" form of the protein, in which the proximal and distal field haem ligands are His18 and Met80 respectively. During a pH titration, in which the pH of the protein solution is gradually increased, spectral changes occur as a result of haem ligation changes, namely Met80 is replaced by a Lys (Lys73 or Ly79) resulting in a low-spin hexa-coordinate haem species, lacking the 695 nm band (Figure 4.4). This phenomenon is known as the "alkaline transition" of C*c*, and the point at which the protein occupies an equal distribution of both acid and alkaline forms is the pK_a of the 695 nm band.

$$\begin{array}{c} Ka \quad H \quad Kc \\ CH \leftrightarrow C \leftrightarrow C^{*} \\ +695 \ +695 \ -695 \end{array}$$ [Scheme 4.2]

It is generally regarded that the pK_{695} is composed of two components, a de-protonation event in a "trigger" group and a conformational change resulting in the bleached 695 nm band. In the case of hC*c*, when going from acidic to more alkaline pH, it is the de-protonation of the trigger group which precedes the conformational change, in which the haem goes from His18 and Met80 coordination to His18 and Lys (either Lys73 or Lys79) coordination. Scheme 4.2 depicts this, whereby K_a is the equilibrium constant of the acid, protonated Met80 conformer (CH), this conformation possesses the 695 nm band (+ 695). An equilibrium then exists between the de-protonated (H^+), acid form of the protein with Met80 bound (C) and the 695 nm band still present. Following this de-protonation event, there is an equilibrium which forms from a conformational change in the protein whereby the Met80 ligand is replaced with a Lys (either Lys73 or Lys79), this haem conformation does not produce the 695 nm band (- 695).

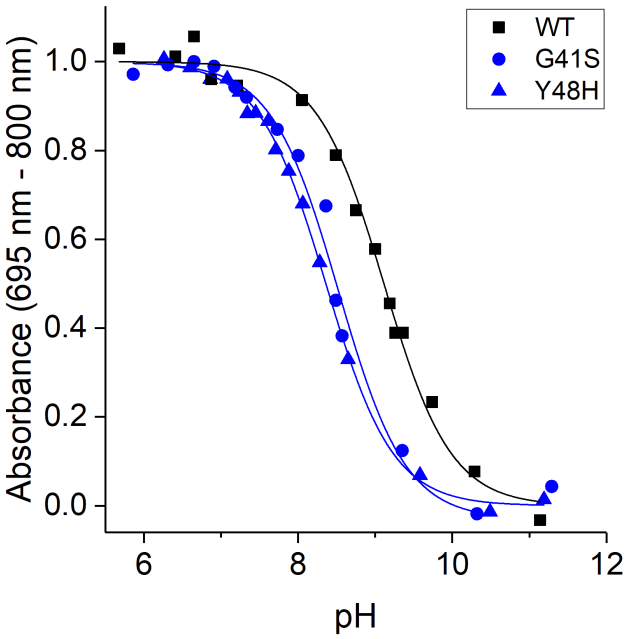

Figure 4.4 The pH dependence of the 695 nm band for WT, G41S and Y48H hC*c* fitted to a one-proton equilibrium equation. The p*K*a$_{695}$ values are reported in Table 4.1.

The alkaline transition therefore reports on the lability of the Met80-Fe(III) bond, as a C*c* variant with a more labile haem ligand will exhibit a lower pK_a. Both G41S and Y48H variants have pK_{695} values more than one pH unit lower than that of WT hC*c* (Table 4.1), suggesting that both protein variants possess a more labile Fe(III)-S(Met80) bond.

4.3.3 X-ray crystal structure of the Y48H human cytochrome c variant

The X-ray crystal structure of the Y48H variant of hC*c* was resolved to 1.36 Å (Figure 4.5), with the asymmetric crystallographic unit composed of two protein molecules in the $P2_1$ space group, contrasting the reported X-ray structures of the WT protein (Rajagopal et al., 2013) and G41S variant (Liptak et al., 2011), both of which had four hC*c* molecules in the P_1 space group.

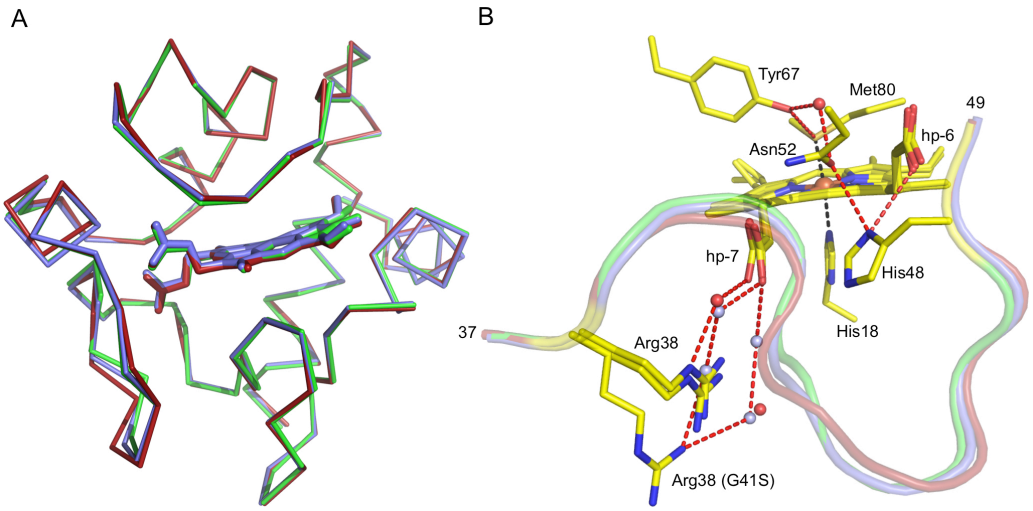

Figure 4.5 X-ray crystal structure of the Y48H variant of hCc. **A)** Ribbon representations of a Cα superposition of the Y48H variant (green; pdb 5O10) with the G41S variant (red; pdb 3nwv) and WT protein (blue; pdb 3zcf). The haem groups are shown in sticks. **B)** A cartoon and stick representation of the region between residues 37 and 49 of the WT protein (blue), the Y48H (green) and G41S (red) variants. The coordinate bonds (black dashes) of the axial His18 and Met80 ligands to the haem iron in the Y48H variant are indicated and H-bonding is represented as red dashes. The side chain position of His48, Asn52 and Tyr67 in the Y48H variant are shown together with the side chain position of Arg38 in all three structures. Water molecules are shown in red spheres for the WT and Y48H structures and in grey for the G41S variant. Figure taken from (Deacon et al., 2017).

Despite crystallization solutions containing ferric Y48H, it is likely that the X-ray beam intensity from the synchrotron would have reduced the protein into the ferrous state

during data acquisition, as the 2.54 MGy diffraction-weighted dose (Zeldin et al., 2013) incurred during data acquisition greatly exceeds that required to fully reduce ferric haem proteins to the ferrous form (typically tens to hundreds of kGy) (Beitlich et al., 2007, Kekilli et al., 2017). Thus, in light of the extensive previous studies measuring the typical radiation doses required for ferric to ferrous haem protein reduction, one may conclude that the Y48H structure is predominantly that of the ferrous state. Despite this, the crystal structure is likely to reflect that of the ferric protein, with electron density around the haem diagnostic of a hexa-coordinate ligand coordination between the Nε2 atom of His18 and the Sδ atom of Met80. To this effect, it is important to note that in the case of tuna C*c* (Takano and Dickerson, 1981) and *Saccharomyces cerevisiae* iso-1 C*c* (Brayer and Murphy, 1996) with significantly lower X-ray doses than used for the Y48H dataset, showed that the protein conformation is largely independent of the haem oxidation state. Each molecule of Y48H displays the same overall fold within the asymmetric unit to that of both the WT and G41S variant of hC*c,* with Cα positions varying by a RMS deviation of 0.18 Å between the three respective proteins (Table 4.2, Figure 4.5A). It is noted that between residues 37 and 61, the Cα deviation increases to 0.27 Å. The apparent effects on protein structure by replacing Tyr48 with a His residue in the Y48H variant appears to alter the H-bonding arrangement with the haem propionates (Figure 4.5). There are differences and similarities in this respect between all three proteins, in the case of the WT protein, the sidechain OH group of Tyr48 is involved in a H-bond of 2.57 Å to the O1A atom of Haem Propionate-7 (HP-7) (Rajagopal et al., 2013). In contrast, this polar interaction is not present in the Y48H variant, which instead displays the Nδ1 atom from the His48 sidechain favourably oriented to from a medium length polar interaction with the O2D atom of Haem Propionate-6 (HP-6) (3.19 Å) (Figure 4.5B). The OD2 atom of HP-6 is

therefore involved in a greater number (two rather than one, as in the WT protein) of H-bonds, with the second H-bond involving the backbone NH of Thr49. A second polar interaction of medium length (3.19 Å) is noted between the Nδ1 atom of His48 and the OD1 atom of Asn52. This interaction confers communication between His48 and the distal Met80 ligand through a H-bond (involving an H_2O molecule) network extending from Asn52 to Tyr67 (Figure 4.5B). An interesting similarity between the Y48H variant and WT protein is that the sidechain of Arg38 is orientated in the same position to that of the WT protein, where the ε-amido group is coupled to HP-7 via a single H_2O molecule (Figure 4.5B). In contrast, the G41S variant Arg38 sidechain is positioned away from HP-7 enabling the presence of an additional two H_2O molecules (Figure 4.1B). The result of this positioning in G41S, is that the ε-amido group of Arg38 remains coupled to HP-7 via a "forked" H-bond network (Figure 4.1B). The X-ray crystal structures of WT, G41S and Y48H hC*c* show no other discernible differences and thus display remarkable overall similarity (Figure 4.5).

Table 4.2 Crystallographic data processing and refinement statistics for the Y48H variant of hC*c*. Values in parenthesis refer to the outermost resolution shell 1.36 – 1.39 Å.

Parameter	Y48H hC*c*
Space group	$P2_1$
Unit cell	a = 56.9, b = 36.5, c = 60.7 Å, β = 116.7°
Resolution (Å)	1.36
R_{merge}	0.072 (1.115)
Unique reflections	45812 (2124)

Mn (I/SD)	13.3 (1.4)
$CC_{1/2}$	0.998 (0.512)
Completeness (%)	95.3 (90.2)
Redundancy	6.2 (5.4)
R_{cryst}	0.144
R_{free}	0.175
RMS dev. bond lengths (Å)	0.015
RMS dev. bond angles (°)	2.18
Ramachandran favoured (%)	97.0
Accumulated dose (MGy)	2.54
PDB accession code	5O10

4.3.4 N_3^- binding kinetics

Exogenous ligand binding to ferric hC*c*, monitored by stopped-flow spectroscopy, was used to further probe the Fe(III)-S(Met80) bond lability. Upon mixing N_3^- with ferric hC*c* an optical transition is observed, characterised as the dissociation of Met80 from the haem and subsequent association of N_3^- in its place.

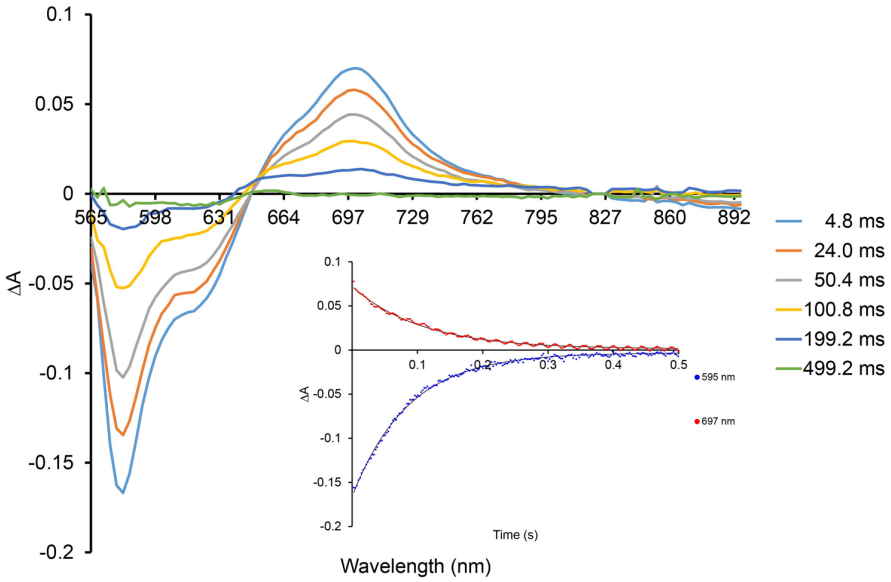

Figure 4.6 N^{3-} binding to ferric G41S hC*c* variant at 25 °C, pH 7.0. 425 µM protein and 0.5 M N_3^- (both after mixing) were mixed and the difference spectra recorded from 565 – 895 nm. The bleaching of the 695 nm band is observed and the inset depicts the time courses and their respective fits to a single exponential at 697 nm (descending) and 595 nm (ascending). Adapted from (Karsisiotis et al., 2016).

Support for this characterisation comes from additional experiments at higher protein concentration, which allowed for the 695 nm band to be assessed (Figure 4.6). For WT, G41S and Y48H hC*c,* interaction with N_3^- results in a quenching of the 695 nm band, diagnostic for the loss of Met80 haem coordination. The reaction time-course of this transition conformed to a simple exponential at all wavelengths, with no detectable intermediates observed (Karsisiotis et al., 2016, Deacon et al., 2017). Normalised

amplitudes of the corresponding reaction time courses, observed over a wide range of N_3^- concentrations, fit consistently to a simple hyperbolic function yielding the apparent equilibrium dissociation constants (K_{app}) reported in Table 4.1 (Figure 4.7A). The observed rate constant (k_{obs}) for N_3^- binding in all three proteins was determined from the measurable range of N_3^- concentration, which appear almost linear (Figure 4.7B).

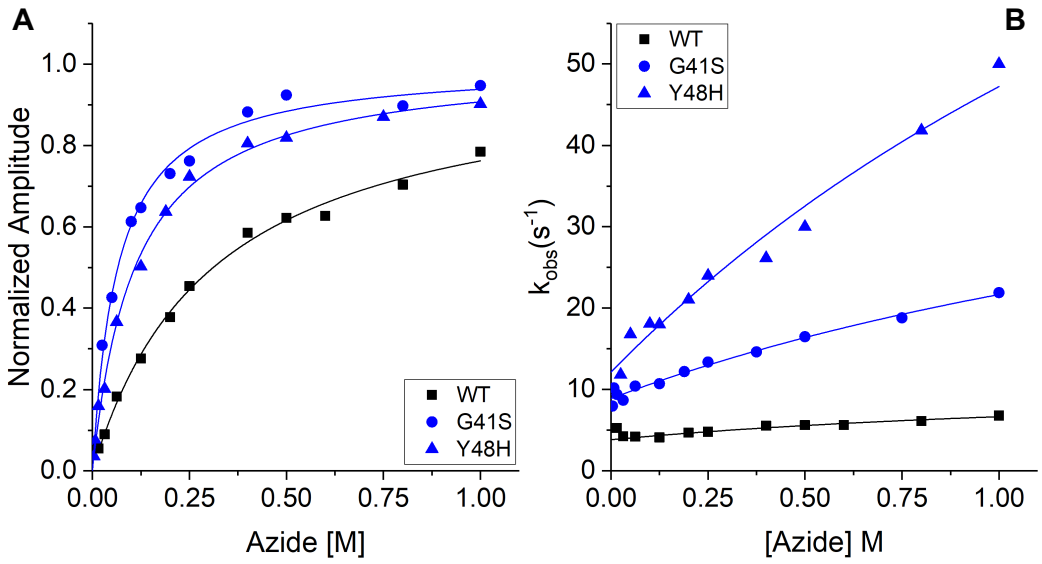

Figure 4.7 Stopped-flow kinetics of N_3^- binding to ferric hC*c* at 25 °C, pH 7.0. **A**) Normalised amplitudes of the time courses recorded at 420 nm plotted as a function of N_3^- concentration. The subsequent binding curves are fitted to a hyperbolic equation (equation 4.4) yielding the K_{app} values reported in Table 4.1. **B**) The rate constant (k_{obs}) determined for N_3^- binding fitted to equation 4.5 yielding k_1 and k_2 values reported in both the main text and Table 4.1 where k_1 and k_2 refer to the Met80 and N_3^- dissociation rate constants, respectively.

Due to the pK_{695} for the WT protein being approximately a pH unit higher than that of the G41S and Y48H variants (Table 4.1), N_3^- binding experiments were also conducted using stopped-flow spectroscopy at higher pH values for WT and G41S hC*c*

(Figure 4.8), in which the fraction of the alkaline conformer is/are increased thus allowing one to determine whether or not the presence of any fraction of the alkaline conformer would have on N_3^- binding. The optical transitions observed upon mixing ferric hC*c* with N_3^- revealed that the alkaline form(s) react far more slowly than that of the native, acid form. Furthermore, pH-jump experiments revealed that the rate constant for binding to the alkaline form was very close in value to that of the conversion rate between the Lys-bound ferric hC*c* to the native Met80-bound form. For example, Figure 4.8 displays the optical transition observed when ferric G41S (pH 9) binds to 1 M N_3^-. The optical transition was characterised by a small fast phase followed by a large slow phase, with rate constants of 19 s^{-1} and 0.086 s^{-1} respectively. The amplitudes of these phases revealed that their respective proportions conformed to

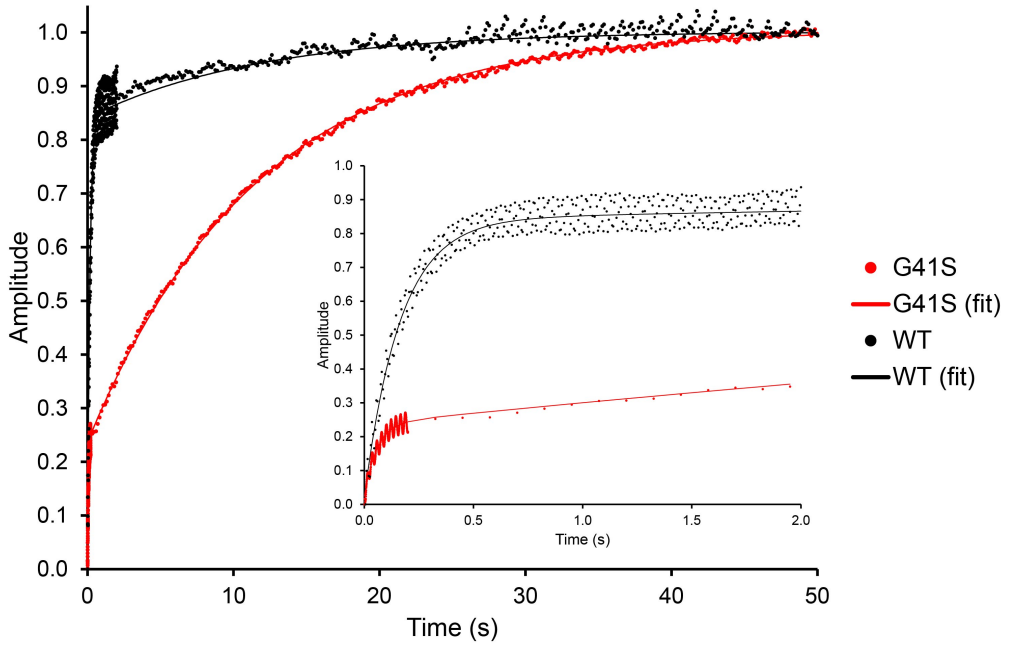

Figure 4.8 N_3^- binding to the ferric WT protein and the G41S variant at pH 9.0, 25 °C. hC*c* at a concentration of 5 µM after mixing was mixed with 1 M N_3^- (after mixing) and the time courses recorded at 416 nm. The inset shows an expanded view of the initial two seconds of the time courses. Adapted from (Karsisiotis et al., 2016) SI.

expectations for binding to the neutral and alkaline forms respectively. The rate constant for the fast phase displayed N_3^- dependence, whereas the slow phase rate constant did not. A consistent pattern of results was obtained from the WT ferric protein, in which the rate constants were 6.1 s^{-1} and 0.085 s^{-1} respectively.

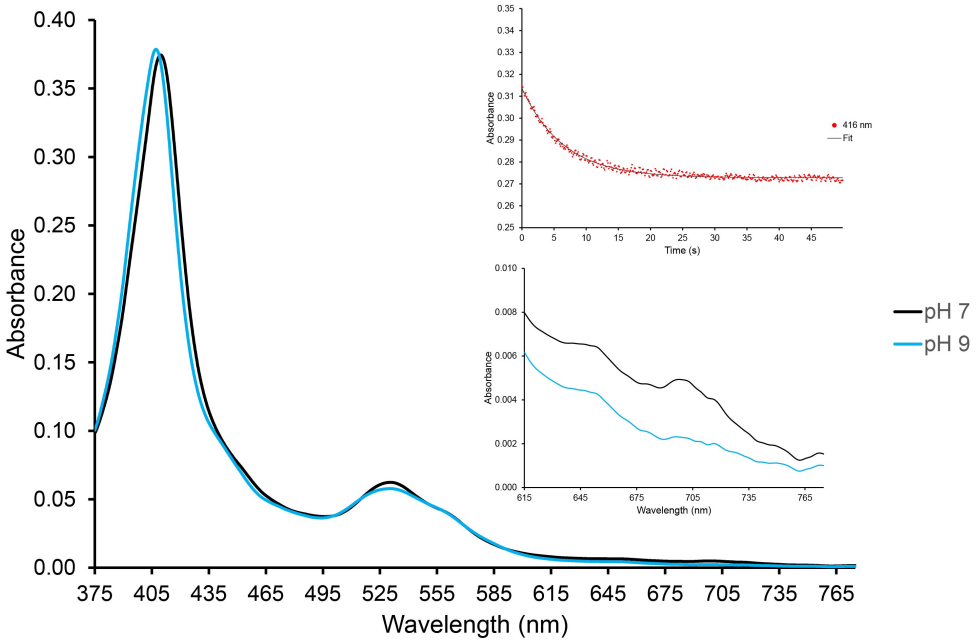

Figure 4.9 Stopped flow analysis of a pH jump experiment from pH 7 to pH 9 with ferric WT hCyt *c* at 25 °C. The displayed spectra are generated from global analysis of the full data set and depict the initial spectrum at pH 7 (black) and the final spectrum at pH 9 (blue). Inset (upper) illustrates a time course at 416 nm, fitted to a single exponential. Inset (lower) shows the bleaching of the 695 nm band at pH 9 through an expanded spectrum. The ferric WT hCyt *c* (10 μM) was prepared in 2 mM sodium phosphate, pH 7 and mixed with equal volume 20 mM borate, 100 mM NaCl yielding a final solution pH of pH 9.

The interconversion rate of conformers within the G41S variant were investigated further through a pH jump experiment, in which the pH of a solution was rapidly changed from ~ pH 7 to pH 9. The optical transition observed (Figure 4.9) was consistent with that of a Met80 to Lys haem ligation change. This transition comprised a single exponential with rate constant of 0.167 s^{-1}, and therefore close to that of the

value obtained from N_3^- binding to the alkaline form of 0.085 s^{-1}. The reason for the slight discrepancy in rate is due to a small term involving the back reaction at this pH (Davis et al., 1974), as the rates of the reactions involving the alkaline conformers are so slow, and due to their N_3^- concentration independence, one may conclude that these are not significant in the binding of N_3^- at pH 7 as reported in Table 4.1. These higher pH experiments revealed that the variation in pK_{695} values between the three proteins is insignificant in the context of N_3^- binding at pH 7.0.

Exogenous ligand binding to ferric C*c* is widely regarded to occur via an SN1 mechanism (Figure 4.10), in which the hexa-coordinate haem exists in equilibrium with a penta-coordinate form characterised by a lack of Met80 coordination. The hexa-coordinate form is the most populated with the equilibrium lying strongly in its favor. N_3^- binds to the penta-coordinate form yielding a characteristic low-spin, hexa-

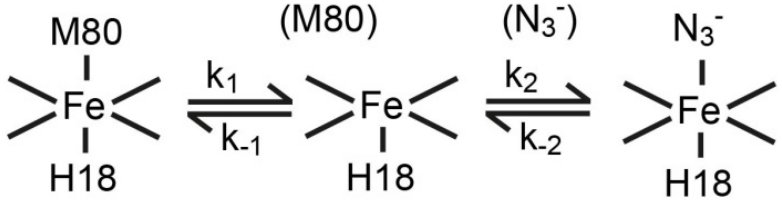

Figure 4.10 Schematic representation of the SN1 reaction of hC*c* binding N^{3-}. k_1 and k_{-1} are the Met80 dissociation and association rate constants respectively, whilst k_2 and k_{-2} are the N^{3-} association and dissociation rate constants, respectively. Adapted from (Karsisiotis et al., 2016).

coordinate N_3^- adduct. This SN1 reaction is amenable to kinetic analysis, however, the process is greatly simplified with the following assumptions, firstly, that the minor population of penta-coordinate species is in steady-state throughout the reaction (Rafferty et al., 1996) and, secondly, that the reaction can be considered pseudo-first order due to the large excess of N_3^- in relation to hC*c* (Rafferty et al., 1996).

$$K_{app} = K_D\left(\frac{K+1}{K}\right) \qquad (4.4)$$

$$k_{obs} = \frac{(k_1 - k_{-2})[N_3^-]}{\left(\frac{k1+k_{-1}}{k'}\right)+[N_3^-]} + k_{-2} \qquad (4.5)$$

As a result of these simplifying kinetic assumptions, it is possible to derive equations 4.4 and 4.5 which describe both K_{app} and k_{obs} respectively, as a function of N_3^-. $K = k_1/k_{-1}$, with k_1 and k_{-1} being the respective rate constants for Met80 dissociation and association, respectively. $K_D = k_{-2}/k_2$, where k_2 is the pseudo-first order rate constant for N_3^- binding (i.e. $k_2 = k'[N_3^-]$, where k' is the second-order rate constant and k_{obs} is ~ k_1 at high N_3^- concentration. It is possible to predict from equation 4.5 that plots of k_{obs} vs $[N_3^-]$ (Figure 4.7B) follow hyperbola that intercept the k_{obs} axis at the value of k_{-2} (N_3^- dissociation rate constant) and plateau at k_1, the Met80 dissociation rate constant. Fits of the normalised amplitude data are satisfactory and yield the values of K_{app} reported in Table 4.1.

When k_{obs} data are plotted as a function of N_3^-, a hyperbolic trend is followed that intercepts the k_{obs} axis at k_{-2} (the N_3^- dissociation rate constant) and plateau at k_1 (the Met80 dissociation rate constant). When data displayed in Figure 4.7B is fitted to equation 4.5, the following k_{-2} values reported in Table 4.1 are determined. Unfortunately, due to experimental limitations of N_3^- concentration, the predicted hyperbola are not discerned for the Y48H variant, thus resulting in a somewhat unreliable Met80 dissociation constant (k_1). However, it is entirely possible to predict a minimal value of k_1 (125 s^{-1}), reported without error in Table 4.1, that is both consistent with equation 4.5 and produces, subjectively, good quality fits to the data. Despite this limitation, it is apparent that the Y48H variant has a Met80 off-rate (k_1)

significantly higher than that of the WT protein and G41S variant. Furthermore, equation 4.4 shows that K_{app} is ~ K_D/K when $K < 1$, as is the case under these experimental conditions due to the concentration of the penta-coordinate species being low, in which $K_{app} \sim K_D/K$. From the assumption that distant mutations in the protein do not directly influence the binding of N_3^- to penta-coordinate haem, then K_D will be similar for WT, G41S and Y48H, with ratio of K_{app} ($^{WT}K_{app}/^{G41S\ or\ Y48H}K_{app}$) reflecting the ratio of K values ($^{G41S\ or\ Y48H}K/^{WT}K$). On this basis, as can been seen in Table 4.1, $^{Y48H}K > {}^{G41S}K > {}^{WT}K$, one may conclude that the penta-coordinate form is more populated in the Y48H variant than in both the WT protein and G41S variant.

The k_1 values determined for WT hC*c* are comparable to that of eC*c* (11-16 s^{-1}) derived from non-linear curve fitting to data using N_3^- as a competitor ligand (Sutin and Yandell, 1972). Bowler and colleagues suggest that due to the sequence difference between eC*c* and hC*c* at residue 83, there are effects on dynamics due to sequence variation within the 71-85 Ω-loop (McClelland et al., 2014). Despite G41S and Y48H mutations occurring within the 40-57 Ω-loop, due to the substantially higher k_1 rates observed in both proteins, one may conclude that there is a larger proportion of penta-coordinate haem in both the G41S and Y48H variants than that of the WT protein, suggesting that these variants possess a more flexible and labile haem crevice.

4.3.5 Peroxidase Assays

Peroxidase activity of WT, G41S and Y48H hC*c* was directly measured by monitoring ABTS oxidation in the presence of H_2O_2. Preliminary tests with various excess of lipid to protein (2.5-fold to 10-fold) showed no additional gain in peroxidase activity beyond a five-fold excess and afforded good solution stability, thus all assays recorded with lipid were at a five-fold excess. Figure 4.11A shows the average of three

traces for each respective protein under the experimental conditions employed. From the reaction time-courses of the WT protein, there is a gradual increase in basal peroxidase activity throughout the experimental time course following an initial lag phase (~ 160 s). However, when complexed with CL liposomes, there is not only a substantial increase in the rate of peroxidase activity, but also, the initial lag phase is abolished (Figure 4.11A). In contrast, both the G41S and Y48H variants do not exhibit this initial lag phase, instead, peroxidase activity commences immediately after addition of H_2O_2 (Figure 4.11A). The G41S and Y48H variants also exhibit greater peroxidase activity than that of the WT protein, both in the absence and presence of lipid, however, to a lesser extent in the G41S variant than that of the Y48H variant (Figure 4.11B). The progressive increase in peroxidase activity correlates with an increase in the level of cooperative global unfolding (Figure 4.3). No change in peroxidase activity is observed for the Y48H variant in the presence of CL liposomes, in contrast to both the WT protein and G41S variant (Figure 4.11B). The secondary increase displayed in the WT and G41S proteins when in the presence of CL, suggests that the hC*c*/CL complex pushes the equilibrium between hexa- and penta-coordinate haem state towards the latter. This finding further conforms to the interpretation from the N_3^- binding kinetics, that in the case of the Y48H variant, the penta-coordinate form of the oxidised protein is energetically more favourable than it is in the G41S variant and WT protein (Deacon et al., 2017). That being said, an alternative interpretation that is still theoretically possible, is that it is not the penta-coordinate form which is more energetically favourable, but instead the hexa-coordinate form is less favourable in the disease variants than in the WT protein.

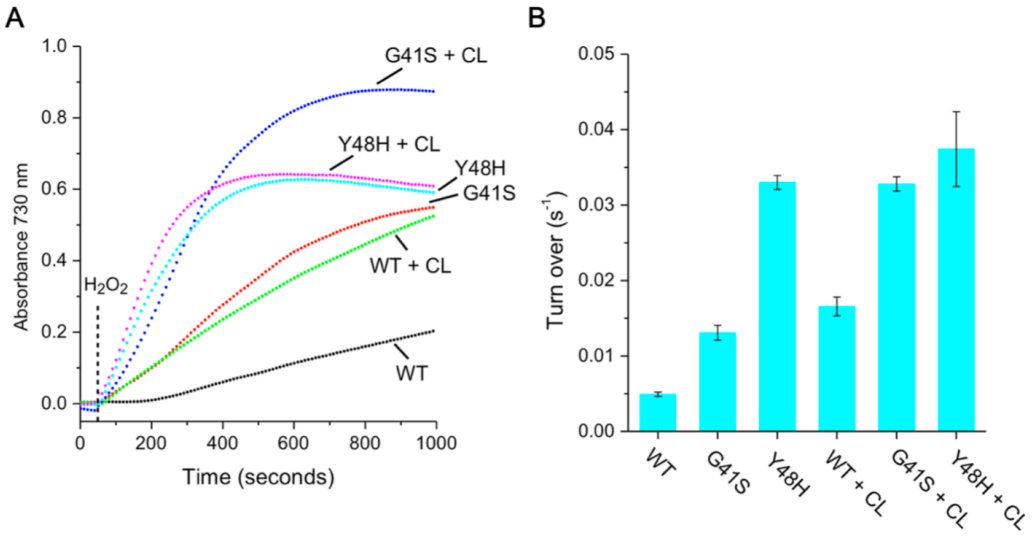

Figure 4.11 **A)** Absorbance changes monitored at 730 nm on a photodiode-array spectrophotometer, thermostatted at 20℃ of WT, G41S and Y48H hCyt *c* both in the absence and presence of CL liposomes. The absorbance changes refelect the oxidation of ABTS in the presence of H_2O_2. **B)** Histogram of the average turnover rates for each of the above-mentioned proteins with standard errors reflecting the experimental error. Figure taken from (Deacon et al., 2017).

4.3.6 1D ^{1}H NMR spectroscopy of WT human cytochrome c and the disease variants G41S and Y48H

The 1D ^{1}H NMR spectrum of ferric C*c* displays numerous peaks that can be either upfield or downfield shifted. This is due to the nuclei experiencing a hyperfine interaction from the unpaired electron on the haem iron (Wüthrich, 1969). These signals arise from paramagnetism and can yield insights into both the electronic structure of the haem group and provide valuable information into haem-ligand dynamics and non-native haem ligation states (Ubbink et al., 2002). Figure 4.12A displays the 1D ^{1}H NMR spectrum of WT hC*c* with several resonances of known assignment labelled (Santos and Turner, 1987, Feng et al., 1990). In the case of the WT and G41S proteins, the traditional pattern of haem-methyl signals 8 > 3 > 5 > 1 is followed and thus consistent with expectations (Senn and Wuthrich, 1985). The

hyperfine chemical shift for both the 8- and 3-methyl groups, and the upfield hyperfine resonances of the protons from the axial His18 and Met80 field ligands of the WT protein and G41S variant follow a Currie-type dependence upon increasing temperature (from 283 to 313 K) (Figure 4.12B and C), whereas the 5-methyl group displays an anti-Curie temperature dependence. In contrast to both WT and G41S hC*c*, the Y48H variant displays significant spectral changes in both upfield and downfield shifted regions (Figure 4.12B and C), for example, at 283 K the hyperfine peak found at ~ 36 ppm is split (Figure 4.12B). The 3-methyl peak displays excess line broadening in comparison to other haem methyl groups in both the WT protein and G41S variant consistent with expectations from other mitochondrial ferric C*c*, such as eC*c* (Burns and La Mar, 1979, Burns and La Mar, 1981). It is reported that a splitting of the 3-methyl peak into two components is observed at low temperatures (266 to 278 K), this activity is consistent with exchange induced line broadening from the very fast interconversion between heterogeneous protein environments surrounding the 3-methyl group (Burns and La Mar, 1981, Burns and La Mar, 1979).

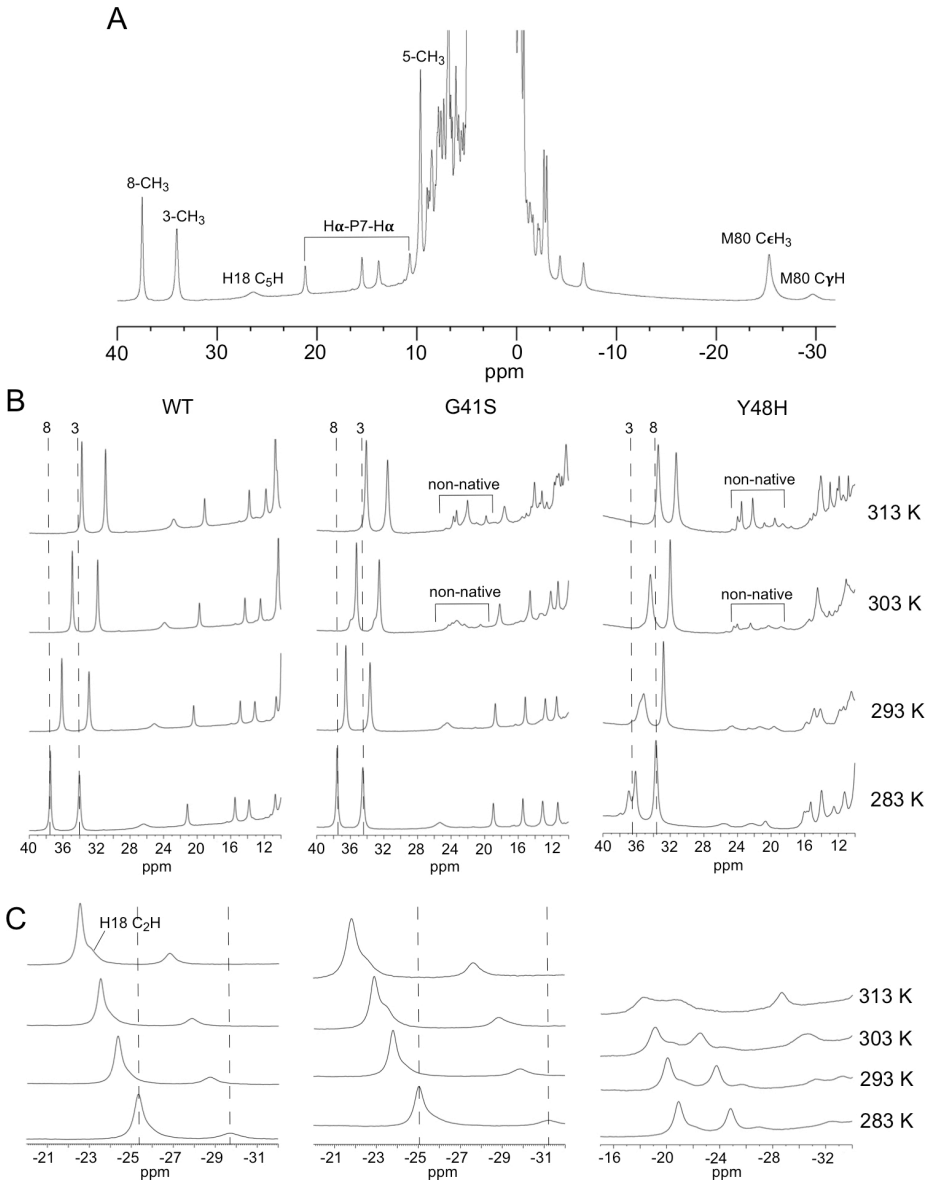

Figure 4.12 A) 1D ^{1}H NMR spectra of WT hC*c* with almost all backbone NH groups deuterated and haem-methyl resonances of known assignment labelled. **B)** The downfield region of WT, G41S and Y48H hCyt *c* at a temperature range of 283 to 313 K. **C**) The upfield region of WT, G41S and Y48H hCyt *c*. Figure taken from (Deacon et al., 2017).

As a result of this behaviour in the 3-methyl of other ferric C*c*, the split peak observed at ~ 36 ppm in the Y48H variant is therefore consistent with the 3-methyl group (Figure 4.12B). As the temperature is raised, the interconversion rate between these two species is increased to a rate beyond that of the experimental pulse sequence and thus the two individual components are dynamically averaged yielding a single broadened peak (Figure 4.12B). It is therefore clear that the factors at play which result in conformational heterogeneity affecting the 3-methyl group are perturbed in the Y48H variant, resulting in a reduction in the interconversion rate thus enabling the two species to be resolved under far more moderate temperatures. It has been demonstrated at 298 K, pH 5.8 that the rate of exchange in oxidised eC*c* was ~ 10^3 s^{-1} (Burns and La Mar, 1981). A similar rate is obtained for the Y48H variant at 283 K, pH 6.5, through the chemical shift difference between the 3-methyl resonances in the two respective environments (Figure 4.12B). This rate is therefore considerably faster than the rate (k_1) determined for the Fe(III)-Met80 bond dissociation (Table 4.1), suggesting that the atypical dynamic behaviour observed for the 3-methyl group of the Y48H variant is not directly related to the formation of the penta-coordinate species. Another significant change observed in the Y48H spectrum, is that the pattern of haem-methyl chemical shifts is altered, displaying a 3 > 8 > 5 > 1 pattern. This pattern of haem-methyl chemical shifts has not been previously reported in either mitochondrial or bacterial ferric C*c*, which so far have only displayed the following 8 > 3 > 5 > 1 or 5 > 8 > 1 > 3 whereby the 8-methyl is always ahead of the 3-methyl and the 5-methyl is always ahead of the 1-methyl in all S = ½ ferric C*c* (Zhong et al., 2004). These haem-methyl patterns are limited due to the orientation of haem axial ligands and the orientation of the Met80 side chain through the possible inversion of the Met thioether sulphur bond (Senn and Wuthrich, 1985). The peaks associated to the protons of the

His18 and Met80 sidechains are observed in the upfield region in both the WT and G41S proteins, however, in the Y48H variant there are substantial changes (Figure 4.12C). One possible interpretation of this atypical haem-methyl peak pattern in the upfield region of the Y48H variant, is an alternate orientation of the axial haem ligands that would result in a change in the electronic structure of the haem. Fluxional solution behaviour of the Met80 haem ligand was shown by Bren *et al*. to be a regular occurrence in C*c*'s (Zhong et al., 2004), and so in the context of the Y48H variant, altered fluxional behaviour results in a change in the magnetic susceptibility axes thus perturbing the 3- and 8-methyl chemical shifts respectively. A final observation is that in the case of the disease variants G41S and Y48H, both proteins display non-native hyperfine signals in the downfield region between 18 to 26 ppm at temperatures of 303 K and above (Ångström et al., 1982) (Figure 4.12B). These hyperfine features may therefore be attributed to a change in the ligation of the haem axial field ligands from His18 and Met80 to His and Lys coordination in accordance with the non-native hexa-coordinate haem species observed in ferric eC*c* at temperatures of 315 K or greater (Ångström et al., 1982). This ligation change is observed only in the G41S and Y48H variants at higher temperatures, therefore, it is proposed that these mutations shift the equilibrium between the hexa- and penta-coordinate haem species towards the latter. It is important to note that the N_3^- binding study with the ferric G41S variant showed that under the same experimental conditions used for these NMR measurements the fraction of the alkaline form(s) was not significantly populated (Karsisiotis et al., 2016). When considering both the higher protein concentrations and longer experimental acquisition times required for NMR data acquisition, it is readily apparent that at elevated temperatures the alkaline conformer(s) become populated. These

findings are consistent with expectations as it is apparent that these pro-apoptotic disease variants possess a more labile Fe(III)-Met80 ligand.

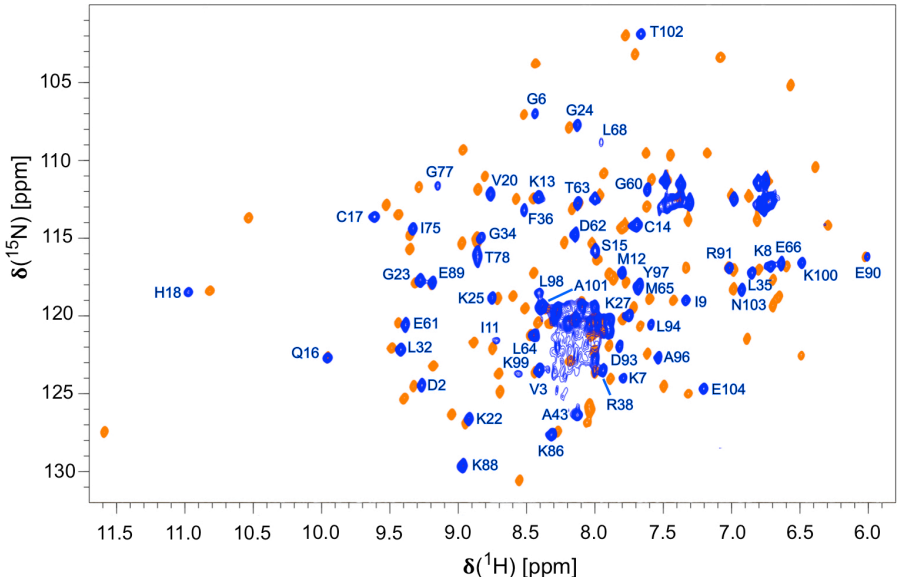

Figure 4.13 An overlay of the 800 MHz [^{1}H, ^{15}N]-HSQC spectrum of the Y48H variant (blue), with most backbone NH resonances assigned (blue), and the WT protein spectrum (orange) at 288 K overlaid.

4.3.7 Backbone resonance assignments of the ferric Y48H human cytochrome c variant

There are clear differences in the [^{1}H, ^{15}N]-HSQC spectrum of the Y48H variant in relation to that of the WT protein as can be seen in Figure 4.13, where the two respective spectra are overlaid. The most significant observation is the substantial number of backbone amide resonances absent from the Y48H spectrum in relation to that of the WT protein, 64 vs 97 out of the 99 non-proline resonances respectively (for resonance assignments, see Appendix A). The majority of the missing resonances are found within the 40-57 Ω-loop encompassing helix-II and the 71-85 Ω-loop. Interestingly, no new peaks are observed in the [^{1}H, ^{15}N]-HSQC spectrum at lower magnetic field strength (500 MHz), which when considered with the increased line

widths of the backbone amide resonances observed at 800 MHz is indicative of the Y48H variant having significantly greater conformational heterogeneity compared to that of the WT protein (Karsisiotis et al., 2016, Karsisiotis et al., 2015).

4.3.8 Hydrogen Deuterium exchange of the Y48H variant of human cytochrome c

In order to explore the dynamics of the ferric Y48H variant of hC*c* so that a comparison can be made with the WT protein and G41S variant, ^{15}N backbone amide H/D exchange experiments using NMR spectroscopy were conducted. The H/D exchange profile of the ferric Y48H variant of hC*c* was monitored and the backbone amide PFs (the defined ratio between the observed experimental and intrinsic exchange rates (k_{ex}/k_{int}) determined (Bai et al., 1993) (see Chapter 3, for PFs see Appendix B). As the exchange rates of the backbone amide groups are influenced by H-bonding, particularly pertaining to protein secondary structure and subsequent solvent accessibility, they report on protein dynamics on an individual residue resolution (Englander and Kallenbach, 1983). The backbone amide H/D exchange profile for the Y48H variant is extreme, with 32 of the 64 assigned residues exchanged within the first 10 min, and therefore leaving only 32 residues for which H/D exchange behaviour could be analysed (Figure 4.14). Of these 32 residues, PFs could be calculated for only 29 residues as 3 residues simply exchanged too slowly to calculate a PF within the experimental timeframe (Figure 4.14). Figure 4.14 shows the sequence dependence of the rapid H/D exchange profile and subsequent 28 missing backbone amide resonances observed in the ferric Y48H variant of hC*c*. It can be seen that only the interlocking helices-I and –V, in addition to small portions of helix-III and the 32-36 turn which exhibit various levels of protection, thus suggesting that the remainder of the protein is likely to be undergoing extensive dynamic fluctuations.

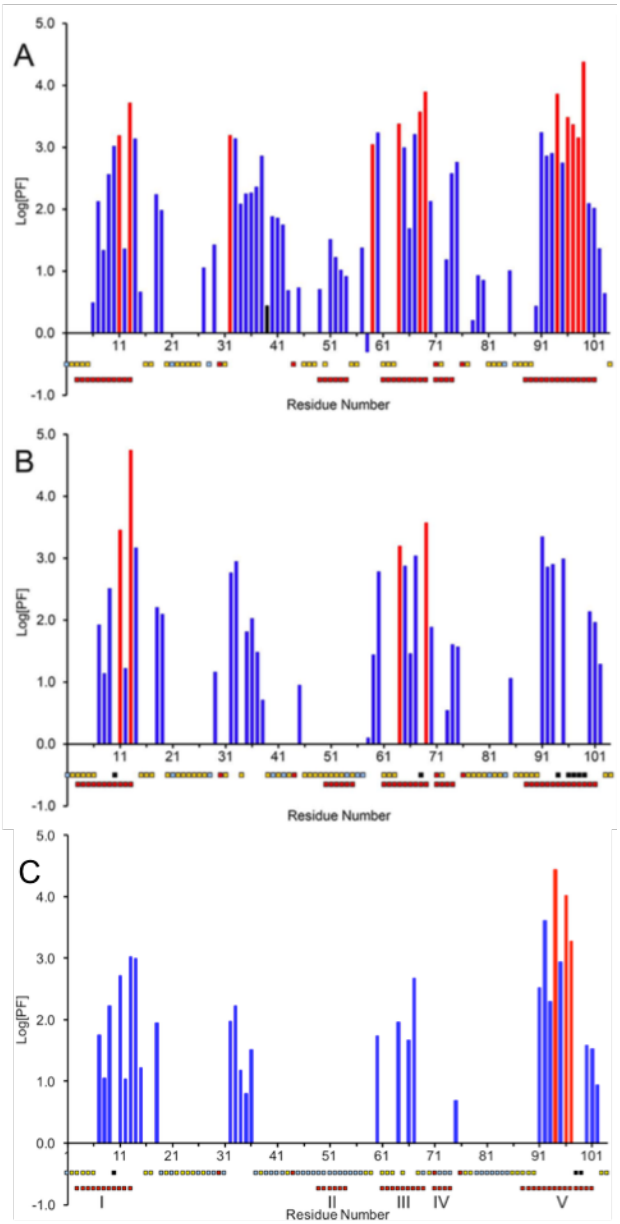

Figure 4.14 Protection Factors (PFs) determined for WT hC*c* (A) and the disease variants G41S (B) and Y48H (C) plotted against residue number. For the residues in which PFs could be determined, 3 residues underwent fast-exchange (logPF $\leq$ 1), 13 medium exchange (1 $\leq$ logPF $\leq$ 2), 10 slow (2 $\leq$ logPF) and 3 extremely slow exchange whereby the residues proton occupancy > 80 % after ~ 134 h and thus corresponding to exchange rates < 0.003 h^{-1} which prove unable to mathematically fit (shown in red). The 5 α-helices comprising hC*c* secondary structure is indicated by the I-V numbered red squares, whereas the isolated red squares above indicate Pro residues. Unassigned and very fast exchanging residues are indicated in blue and yellow squares respectively. The 3 residues that were not amenable to PF calculation are indicated by black squares. Figure adapted from (Deacon et al., 2017, Karsisiotis et al., 2016).

4.3.9 ^{15}N Relaxation

For the Y48H variant of hC*c* the ^{15}N relaxation parameters T_1, T_2, and NOE were acquired for 55 residues. Figure 4.15 shows plots of these parameters vs residue number. The average relaxation rates obtained were $R_1 = 1.08 \pm 0.03$ s^{-1} and $R_2 = 14.99 \pm 0.72$ s^{-1} with an average NOE = 0.84 ± 0.06. These values are comparable to that of the WT protein (R_1 = 0.99, R_2 = 14.23 and NOE = 0.84) and the G41S variant (R_1 = 1.07, R_2 = 14.48 and NOE = 0.84) (Karsisiotis et al., 2016). The T_1 values, which report on ns-ps motions are relatively constant throughout the Y48H protein sequence, however, there are two exceptions, His18 and Ile75 (Figure 4.15A). In contrast, the T_2 plot (Figure 4.15B) reveals significant changes to that of the WT and G41S proteins with multiple residues falling below the average, and thus reflecting contributions from slower conformational exchange equilibria (Deacon et al., 2017). By plotting the R_2/R_1 ratio it is possible to visualise residues that experience chemical exchange (Figure 4.15C). Despite the relaxation dataset of Y48H being considerably smaller than that obtained for the G41S variant (55 vs 92 residues, respectively), a similar pattern of residues that experience slow conformational exchange (15-36, 40-57 and 71-85 Ω-loops) emerges and is also consistent with regions which experience rapid H/D exchange (Figure 4.14).

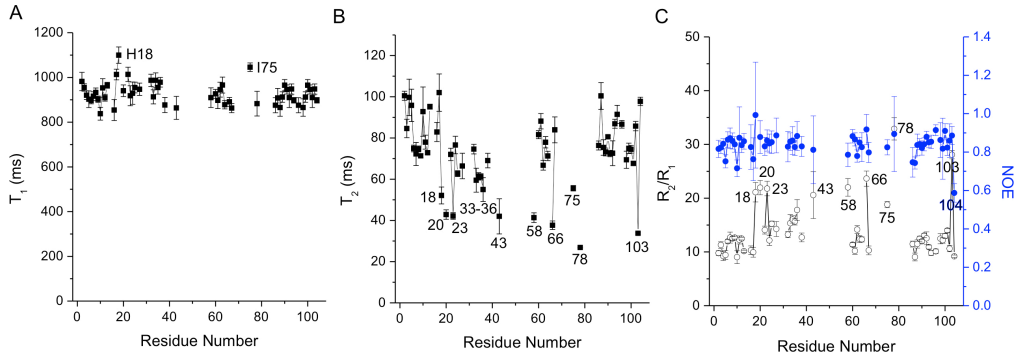

Figure 4.15 ^{15}N relaxation parameters for the Y48H variant of hC*c* acquired at 800 MHz and 288 K. Insets A and B display T_1 and T_2 times plotted against their respective residue number. Black open circles from inset C shows the R_2/R_1 ratio whilst the blue circles represent the [^{1}H]-^{15}N NOE, again plotted against the respective residue number. Figure taken from (Deacon et al., 2017).

4.4 Discussion

For hC*c* to gain peroxidase activity, access to an alternative structural state, or conformer, is required. This peroxidase active form could arise due to the hC*c*/CL interaction resulting in a conformational change, in which a peroxidatic state is created, or, because the ground state structure is in equilibrium with one or more higher-energy forms of different structure. The CL interaction with the latter scheme would displace the equilibrium by binding preferentially to a higher energy state. It has been shown previously that the pro-apoptotic G41S variant, the first variant of hC*c* responsible for the disease Thrombocytopenia 4, that enhanced conformational dynamics within the 40-57 Ω-loop exists (Karsisiotis et al., 2016). This increase in conformational dynamics is directly linked to the dissociation of the Met80 haem Fe(III) ligand, through communication between the 40-57 and 71-85 Ω-loops and results in an increased population of a penta-coordinate species (Karsisiotis et al., 2016). This penta-coordinate form of hC*c* is peroxidatic, and under healthy physiological

conditions is one of the mechanisms by which the cell regulates levels of ROS (Bayir et al., 2006). However, during the initial stages of apoptosis, the inner mitochondrial membrane lipid CL is peroxidated, and once hC*c* is released from the mitochondrion, it has been shown to carry out the peroxidation of the plasma membrane lipid phosphatidylserine (Bayir et al., 2006).

More recently, a second mutation in hC*c* was discovered, which also causes Thrombocytopenia 4 (De Rocco et al., 2014). Interestingly, this mutation (Y48H), is also located within the 40-57 Ω-loop. The 40-57 Ω-loop is of significant importance, as this loop is not only the least conserved region in C*c* evolution, but also possesses the lowest free energy of the five cooperative folding/unfolding units, termed "foldons" by Englander and co-workers (Krishna et al., 2003b, Krishna et al., 2006). As a result, and consistent with expectation, the Y48H variant displays both enhanced mobility and dynamics. However, it is consistently apparent that both the local and global dynamics of the Y48H variant are further enhanced than that of the G41S variant. Evidence from the global perspective, is initially shown from the ~ 35 % loss of observed NH resonance peaks within a [^{1}H-^{15}N]-HSQC spectrum. In contrast, the WT protein and G41S variant have only 2 and 6 % missing assignments respectively, under the same conditions. With the exception of Ala43, the 40-57 Ω-loop is missing in its entirety, along with the second half of the 71-85 Ω-loop, corresponding to residues 79-85, the second least stable foldon that contains the Met80 haem Fe(III) ligand (Krishna et al., 2006). It is likely that these unobserved resonances in the Y48H variant, are as a result of a decreased T_2 relaxation time, due to exchange between different conformations. Unfortunately, it is not possible to show unequivocally that the Y48H variant displays enhanced dynamics on the μs-ms timescale from direct NMR measurements, by compute R_{ex} terms. However, for the resonances that allow for an NH H/D exchange

PF to be calculated, which encompasses residues within the N- and C- terminal helices, the end of the 14-36 Ω-loop and parts of helix-III, it is possible to say that these are generally smaller for the Y48H variant than for the G41S variant and WT proteins (Karsisiotis et al., 2016). One can appreciate the increase in dynamics going from WT < G41S < Y48H from Figure 4.16A, in which the H/D exchange NH PF's obtained from the three proteins are mapped onto their respective X-ray crystal structures (Karsisiotis et al., 2016). It is apparent that in the case of the WT protein and disease variants G41S and Y48H, that in helices I, III and V, similar H/D exchange profiles are maintained, but with mutations resulting in more rapid exchange and thus enhanced dynamics (WT < G41S < Y48H) in the 40 – 57 and 71-85 Ω-loops, in addition to helix II (Figure 4.16A).

Englander and co-workers elegantly revealed how C*c* folds, by uncovering its foldon substructure (Krishna et al., 2003b, Krishna et al., 2006). Of the five foldon units identified, the two with the lowest free energy are the 40-57 and 71-85 Ω-loops (Maity et al., 2005, Hu et al., 2016). From the data reported in this Chapter, it is readily apparent that the dynamics of the 40-57 Ω-loop is directly linked to the dissociation of the Met80 ligand and the formation of the penta-coordinate form, which is in turn governed by the dynamics of the 71-85 Ω-loop.

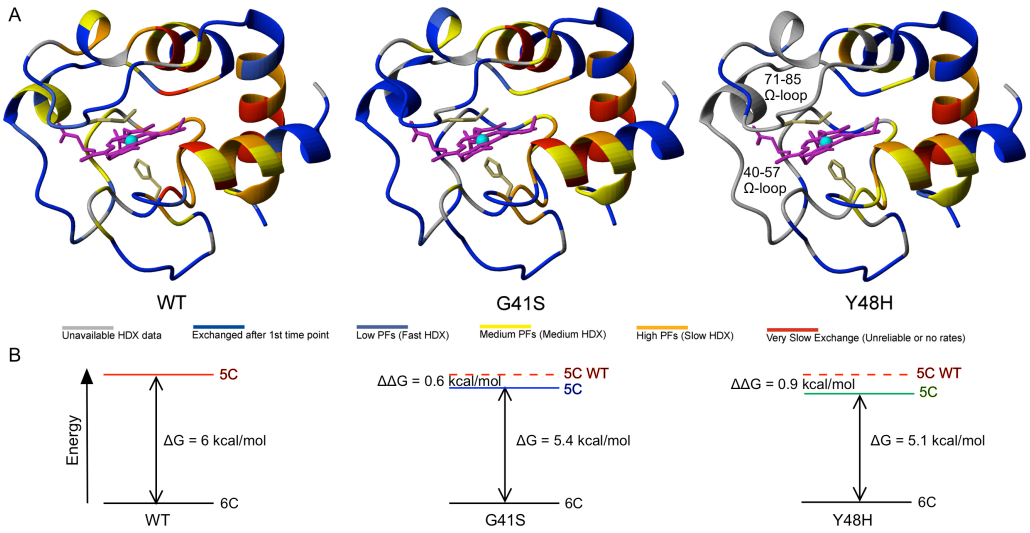

Figure 4.16 Comparative dynamics of the thrombocytopenia 4 causing mutants of hC*c* Y48H and G41S compared to that of the WT protein. Inset A shows the Protection Factors (PFs) obtained from all three hC*c* proteins mapped onto their respective X-ray crystal structures, with PFs colour coded as indicated. Data for the WT and G41S proteins was taken from (Karsisiotis et al., 2016), whilst data for the Y48H variant is taken from Figure 4.14. The haem and its axial ligands are displayed as sticks. Inset B shows schematic energy diagrams illustrating the calculated differences in free energy (ΔΔG) between the penta-coordinate and hexa-coordinate forms in the various protein species. This data is derived from $\Delta G = -RT\ln({}^{WT}K_{app}/{}^{variant}K_{app})$ from stopped flow N_3^- binding kinetics. Figure taken from (Deacon et al., 2017).

There is indeed a striking correlation between the conformational dynamics linking the G41S and Y48H variants with the displacement of the Met80 ligand and the energetic impact on their respective foldon substructures. If the following assumptions are made, that the penta-coordinate form of ferric C*c* is equivalent to the partially unfolded form of the two lowest energy foldon units, in which the penta-coordinate state represents a 6 kcal/mol increase in free energy above that of the ground state structure, in accordance with the analyses of Hu and colleagues (Hu et al., 2016). Furthermore,

when also assuming the energetics of eC*c* are the same as those of hC*c*, then using the equation $\Delta G = -RT\ln({}^{WT}K_{app}/{}^{Y48H}K_{app})$, obtained from the interpretation of the N_3^- binding kinetics, it is possible to determine the $\Delta\Delta G$ of the penta-coordinate state for WT, G41S and Y48H hC*c* (as illustrated, by the schematic energy level diagram in Figure 4.16B). As described in the results of the N_3^- binding kinetics, the ratio of ${}^{WT}K_{app}/{}^{Y48H}K_{app}$ reflects the ratio of equilibrium constants for dissociation and re-association of the Met80 haem ligand (${}^{Y48H}K/{}^{WT}K$), in which the assumption is that the free energy of the ground state structure is equivalent for the disease variants G41S and Y48H, to that of the WT protein. Figure 4.16B illustrates how the penta-coordinate form of G41S and Y48H are 0.6 and 0.9 kcal/mol, respectively, lower in energy than that of the WT protein. For every kcal/mol change in free energy, there is a 5-fold change in the equilibrium constant that governs the distribution of the hexa- and penta-coordinate species. As the minor fraction, in this case the penta-coordinate form, plays a significant mechanistic role in this enzyme, then a single kcal/mol change in stability represents a 5-fold increase in the concentration of the penta-coordinate form. The suggestion that the G41S and Y48H variants cause small changes in the oxidised C*c* energy landscape should be considered with regard to the recent finding that the Fe(III)-S(Met80) bond is weak and therefore requires constraints from the protein structure, such as extensive H-bonding between neighbouring residues maintained under physiological conditions (Kroll et al., 2014, Mara et al., 2017). The process in which the protein structure stabilises a weak bond is an example of entasis, a concept originally proposed to account for some of the unusual properties of metalloproteins by suggesting that the metal centre "constituted an energetically poised domain" (Vallee and Williams, 1968). Mara and colleagues have determined that the protein entatic contribution to the Fe(III)-S(Met80) bond is ~ 4 kcal/mol (Mara et al., 2017).

Therefore, it is clear that relatively minor changes within the energy landscape of a protein, can have significant mechanistic effects.

A noteworthy finding from the peroxidase activity assays is that the turnover of H_2O_2 by the Y48H variant is not enhanced in the presence of CL liposomes, as in the case of the WT protein and G41S variant (Figure 4.11B). An absence of the CL rate enhancement for G41S has been reported by others (Josephs et al., 2014), which therefore contradicts the previous works from the Worrall group using Amplex red assays (Rajagopal et al., 2013) and the ABTS assay data presented in this Chapter. The findings that there is an enhancement in peroxidase activity in the G41S variant is entirely consistent with the dynamic appraisal of the disease variants G41S and Y48H presented in this Thesis. The Y48H variant is more dynamic than the G41S variant, which in the case of the peroxidase activity assays, reveal how in the case of the Y48H variant, the equilibrium between the hexa- and penta-coordinate forms is no longer rate limiting in the turnover of H_2O_2, as the peroxidase activity of Y48H is not increased in the presence of CL liposomes, unlike the WT protein and G41S variant (Figure 4.16B).

There are two potential explanations for this, firstly, that the concentration of the peroxidase active penta-coordinate form is increased, as seen in Figure 4.16B, but another reason could be that the access of H_2O_2 to the haem Fe(III) is facilitated. Arg38 has been proposed to function as a gatekeeper of H_2O_2, specifically in the G41S variant, in which rotation of the Arg38 side chain creates a channel, stabilised by $2H_2O$ molecules (Rajagopal et al., 2013, Liptak et al., 2011). Further support for this comes from the crystal structure of the K72A variant of *Saccharomyces cerevisiae* C*c* that displayed a penta-coordinate haem, in which the Met80 ligand was dissociated and the Arg38 sidechain position was in the "out" position, as in the G41S variant of hC*c* (McClelland et al., 2014). As a consequence of the Met80 dissociation, there is forked

hydrogen bond network of H_2O molecules that connect from the Met80 side of the haem to the bulk solvent (McClelland et al., 2014). This Arg38 repositioning results in an altered haem propionate environment, particularly HP-7, and it has been suggested that these changes link the dynamics between the 40-57 and 71-85 Ω-loops, which result in the dissociation of the Met80 ligand (Karsisiotis et al., 2016, Rajagopal et al., 2013). Perhaps surprisingly, the Arg38 sidechain orientation in the Y48H variant is orientated as in the WT protein, as illustrated in the Y48H X-ray crystal structure (Figure 4.5). The introduction of the 41S and 48H mutations in the G41S and Y48H variants respectively, creates the opportunity for both side chains to form hydrogen bonds with the side chain of Asn52, which can then interact with the Met80 ligand though further H-bonding as illustrated in Figure 4.5B. As a result of this dynamic and structural information, there are ultimately two available conformational routes in which dynamic changes at the base of the haem can impact on the Met80 ligand. There is extensive documentation in the literature that the 40-57 Ω-loop and haem crevice have a significant conformational linkage. However, this was not always appreciated, as in the case of Robinson *et al*., who showed through an incomplete NMR dataset, that under native conditions the residues within the 40-57 Ω-loop undergo rapid interconversion between local conformational states (Robinson et al., 1983). In contrast, the suggested role of Asn52, as presented in this Chapter, is indeed consistent with the work of Schejter *et al.* (Schejter et al., 1994). An NMR structure obtained of a triple variant of *S. cerevisiae* C*c*, designed to stabilise the alkaline conformation (the His/Lys hexa-coordinate haem form) supports the link that the alkaline isomerisation of ferric C*c* also plays a role in the linkage with the Met80 dynamics, as in addition to the 71-85 Ω-loop (housing the displaced Met80 ligand), the 40-57 Ω-loop was the most

perturbed feature compared with the native structure (Maity et al., 2006, Assfalg et al., 2003).

The latest studies have shown that C*c* function can be controlled through phosphorylation, in which phosphorylation inhibits the ETC flux thus preventing hyperpolarization of the IMM, a known trigger of ROS and apoptosis (Huttemann et al., 2012, Huttemann et al., 2008). There have been three phosphorylation sites identified on a variety of tissue isolates of bovine C*c*, Thr 28, Tyr48 and Tyr97 (Lee et al., 2006, Yu et al., 2008, Mahapatra et al., 2017). Tyr48 is of particular interest, as when considering the pro-apoptotic behaviour of the Y48H variant, and indeed the disease phenotype in which it confers, as Tyr48 when phosphorylated abolishes apoptotic activity at the apoptosome level (De Rocco et al., 2014, Pecina et al., 2010, Moreno-Beltran et al., 2017). A current study has characterised a Tyr48 phosphomimetic, termed Tyr48p using a non-native amino acid in order to assess the effect of phosphorylation at this position on the hC*c* structure (Moreno-Beltran et al., 2017). It is important to note that the structural studies were conducted with the ferrous form of C*c*, the hexa-coordinate form responsible for the donation of a single electron to C*c*O (Ferguson-Miller and Babcock, 1996). The ferrous form is not the state which gives rise to the penta-coordinate, peroxidase active form fundamental to the work reported in this Thesis. The ferrous form of hC*c* under native physiological conditions has both a more ridged structure than its ferric counterpart, but also an equilibrium constant between the Met80-on and Met-80 off species has not been detected under non-apoptotic physiological conditions (Moore and Pettigrew, 1990). Despite these functional and molecular differences between the ferric and ferrous forms of C*c*, the dynamics reported on the μs-ms timescale for the Tyr48p variant of C*c* showed increased dynamics to that of the WT protein, particularly within the 40-57 Ω-loop,

however, this increase is still significantly lower than that reported for the ferric forms of the Y48H and G41S variants of hC*c*. Additionally, increased dynamics were also reported in the 71-85 Ω-loop, specifically pertaining to residues 75-78 for the ferrous Tyr48p C*c*, thus providing further support that the 40-57 Ω-loop and Met80 ligand are dynamically linked. A possible explanation for the decreased dynamics observed in the ferrous form of C*c* stems from the fact that the thioether sulphur of the Met80 residue has a far greater affinity for ferrous Fe(II) to that of Fe(III) (Moore and Pettigrew, 1991). Despite this, when in the ferric state the Tyr48p displays a 3-fold boost in peroxidase activity in relation to that of the WT protein (Moreno-Beltran et al., 2017). The Y48H variant on the other hand, displays a 7-fold increase in peroxidase activity as seen in Figure 4.11B. However, the Tyr48p peroxidase activity is boosted when complexed with CL, where there is a 7-fold increase in relation to that of the WT protein. These data therefore suggest that the equilibrium constant between the hexa- and penta-coordinate species lies in favour of the hexa-coordinate form in the Tyr48p relative to that of the Y48H variant, thus enabling CL to further boost the peroxidase activity of the phosphorylated protein. There may therefore be consequences in regard to both the pro- and anti-apoptotic behaviour as the data outlined in this Chapter has shown that the penta-coordinate haem species is critical in this respect.

Due to the thousands of biochemical reactions which occur within a cell, and the relatively few genes present in a genome, it was discovered that many proteins have more than one biological function (Henderson and Martin, 2014, Jeffery, 2014). Jeffrey coined the term “moonlighting” and listed several mechanisms by which a protein could switch between different biological roles (Jeffery, 1999). Such mechanisms include differential localisation within the cell, intracellular/extracellular localisation, oligomerization, variable ligand/substrate concentrations, chemical

regulation or activity, different binding sites for a variety of partner molecules and a component of multi-protein complexes (Jeffery, 1999). The notion that different protein structures would be involved with different biological roles was not considered, however, advances in this field have led to a rebranding of the term "moonlighting" to "Extreme Multifunctional Proteins" (EMF), in order to create focus on the functional attributes of the phenomena rather than the mechanistic routes (Chapple et al., 2015, Chapple and Brun, 2015). However, from a biochemical perspective, it is essential to understand how moonlighting/EMF proteins function. Energy landscape theory (Bryngelson et al., 1995) provides an explanation as to how proteins can moonlight, in which the ground-state structure (the prevalent form under physiological conditions) is in equilibrium with a small fraction of higher-energy form(s) that are structurally distinct. Protein folding, ligand binding and enzyme catalysis studies have identified such excited states in numerous systems (Henzler-Wildman and Kern, 2007, Baldwin and Kay, 2009) and therefore it is reasonable to conclude that this theory offers a route enabling proteins to moonlight. Interestingly, in the context of hC*c*'s roles as a histone chaperone inhibitor (González-Arzola et al., 2015) and as a component of the apoptosome (Yu et al., 2001), hC*c* binds to the relevant partner proteins at sites overlapping hC*c*'s binding sites to the cytochrome bc_1 and C*c*O aa_3 complexes (Speck et al., 1979, Rieder and Bosshard, 1980). Thus, in these moonlighting roles hC*c* is indeed consistent with the possible mechanisms given by Jeffery (Jeffery, 1999). From the work presented in this Chapter, the mechanism by which hC*c* carries out one of its moonlighting functions, its peroxidase activity, occurs through the population of an excited state structure lying energetically close to that of the ground state structure, and is not previously suggested or described in the literature on moonlighting or EMF proteins. Despite this, the mechanism is likely to be employed by other proteins,

particularly metalloproteins, as the energetic differences between different metal ion coordination schemes, such as loss of a coordinating ligand or changes in the second coordination sphere, which can be particularly subtle, can have considerable chemical consequences in regard to the reactivity of the metal ion. Currently, there are very few metalloproteins which are described as moonlighting or EMF proteins, for example there are only two iron dependent proteins and one zinc dependent protein listed in the moonlighting protein database, yet a bioinformatics study has suggested that 10 % of human proteins contain zinc (Andreini et al., 2006). As a result of this, it is likely that the number of discovered moonlighting metalloproteins shall increase in the future.

In conclusion, the data reported in this Chapter has demonstrated that the disease variants G41S and Y48H, when in the ferric haem state, are more peroxidatic than the ferric WT protein of the order WT < G41S < Y48H. In the case of the Y48H variant, the dynamic fluctuations in the 40-57 Ω-loop resulting in cross-talk with the 71-85 Ω-loop housing the Met80 ligand are further enhanced than in the G41S variant. Consequently, the Y48H variant has intrinsic peroxidase activity that is no longer enhanced in the presence of CL, due to an increased population of an excited penta-coordinate haem state structure with an energy that is close to that of the ground state Met80 coordinated structure. This finding is fundamental in the proposal that hC*c*'s EMF switch in function from electron transfer protein, to peroxidase is, at least partly, a result of the preexisting conformational equilibrium involving an excited penta-coordinate state. The third naturally occurring variant of hC*c*, A51V, also implicated in Thrombocytopenia 4, has not yet been characterised. However, due to its location within the 40-57 Ω-loop, one may predict that the A51V variant has similar traits to that of the G41S and Y48H variants. It would therefore be interesting to ascertain

where the A51V variant is located within the dynamic window (WT < G41S < Y48H) that has emerged from studies thus far.

Chapter 5

The contribution of Ω-loops in triggering the alkaline transition of cytochrome *c*

Results from this Chapter have been submitted as:

Deacon, O.M., Svistunenko, D.A., Moore, G.R., Wilson M.T., Worrall, J.A.R. (2018) "Naturally occurring disease-related mutations in the 40-57 Ω-loop of human cytochrome *c* control triggering of the alkaline isomerisation". *Biochemistry*.

5.1 Introduction

5.1.1 The alkaline transition

Theorell and Åkesson investigated the effects of pH on ferric and ferrous C*c*, and showed that over the pH range 0-14 there are five pH dependent optical spectral states (Theorell and Åkesson, 1941). These five states are linked by protonation events that correspond to four distinct p*K* values. In contrast to the ferric protein, the reduced protein has access to only three states which are linked by two de-protonation events. These findings are summarised below:

Ferricytochrome *c*:	I > II > III > IV > V	State
	0.4 2.5 9.35 12.5	p*K*
Ferrocytochrome *c*:	I > II > III	State
	< 4 >12	p*K*

In addition to increasing pH, it is also possible to induce these molecular reorganisations with high temperature and via the use of protein denaturants and other chaotrophic agents (Schejter and George, 1964, Greenwood and Wilson, 1971). The work reported in this Chapter will focus on transition III > IV, known as the "alkaline transition" and is associated with a bleaching of the 695 nm absorption band.

The first structure of eC*c* confirmed that it is Met80 which is the hexa-coordinate haem iron ligand (Dickerson et al., 1971), first postulated by (Aviram and Schejter, 1969, Schechter and Saludjian, 1967). Following from this structural work, spectroscopic investigations confirmed the accepted notion that it is the sulphur atom on the Met80 sidechain which bonds with the central haem iron atom giving rise to the 695 nm absorbance band, which at high pH is lost during the state III > IV transition

(Stellwagen and Cass, 1974). Further work revealed that all cytochromes possessing the 695 nm absorbance band possess a Methionine residue as the hexa-coordinate axial haem ligand (Moore and Pettigrew, 1990).

There are many possibilities for the origin of the 695 nm band in C*c*, however, the most widely accepted view is that the band represents the porphyrin > Fe(III) transition (Smith and Williams, 1970, Makinen, 1983). The band is z-polarised with a transition from a porphyrin π > Fe d_{xz} and d_{yz} orbitals, the energy of which is governed by the interaction between the haem and Met80 ligand (Scott and Mauk, 1996).

The 695 nm band in C*c* display a well resolved CD spectrum which is abolished at high pH (Greenwood and Wilson, 1971). It is known that both the magnitude and sign of this CD differs between C*c* of different species, which has been correlated through ^{1}H NMR spectroscopy to reveal that the orientation by which the Methionine axial ligand interacts with the haem iron varies. Specifically that a lone pair orbital on the Methionine sulphur atom are directed to different pyrrole rings (Senn and Wuthrich, 1985, Senn, 1985).

Despite the alkaline transition appearing simple at face value and occurring in a relatively small protein whose structure is well resolved, the precise mechanism remains obscure. As a result, it is the nature of the alkaline transition, i.e. displacement of the intrinsic methionine axial ligand and subsequent molecular rearrangement which has been the subject of considerable interest over the years since it was first discovered by (Theorell and Åkesson, 1941). The alkaline transition can be described as a "triggered", limited, conformational change that is coupled to a large redox potential, and therefore is likely to play a critical role in the ETC and energy transduction (Scott and Mauk, 1996).

5.1.2 Spectroscopic characteristics of the alkaline transition

Ferric C*c* possesses a low-spin hexa-coordinated haem at both neutral and alkaline pH. The forms of the protein under these conditions have been studied by spectroscopic techniques which have elucidated the local environment surrounding the iron, and the transition which connects the two species. Lambeth and co-workers demonstrated the pH dependence of the EPR spectrum of ferric C*c* and revealed that despite the low-spin haem signal remaining at high pH, the signal is distinctly different (Lambeth et al., 1973). At neutral pH the EPR signal of g = 3.07, whereas at high pH this signal is replaced by a signal at g = 3.42. The loss of the signal at g = 3.07 coincides with the bleaching of the 695 nm band under identical conditions. Gadsby and co-workers used magnetic-CD (MCD) to illustrate pH dependence, in which a band observed in the near infrared spectral region at 1725 nm at pH 7 is replaced by a band at 1465 nm at pH 11 (Gadsby et al., 1987). Interestingly, the p*K* of this transition is identical to that observed by either EPR or UV-visible spectroscopy and therefore provide consistent data that the Fe-S bond is broken at high pH. Conclusive evidence that the Met80 ligand dissociation occurs at high pH came from two magnetic spectroscopic studies, Wooten and colleagues used C*c* enriched with CD_3 or $^{13}CH_3$ to illustrate that the methionine ligand was dissociated from the paramagnetic iron with a pK_a of ~ 9 (Wooten et al., 1981). MCD has also proved to be a very powerful technique in determining haem ligands, it was Thomson and colleagues who established the spectroscopic signatures of a number of haem axial ligands, which in turn were correlated with their respective EPR signals. The major species at neutral pH displaying a band at 1725 nm, was conclusively assigned to His-Met ligation, in agreement with the X-ray crystal structure and the loss of the band at 1725 nm at high pH, providing irrefutable evidence of the dissociation of Met80 (Gadsby et al., 1987).

As mentioned earlier, ferric C*c* possesses a low-spin haem at high pH values, therefore, the Met80 dissociation must be followed by the ligation of another strong distal field ligand. Spectroscopic studies revealed that this second distal ligand is that of a Lysine NH_3^+ group, as a result of the MCD band present at 1425 nm and high pH being consistent with the wavelength range for His-NH_3^+ ligation. An example from the work of Gadsby and co-workers is the *n*-butylamine complex of leg haemoglobin, which displays a band at 1550 nm with consistent EPR data (Gadsby et al., 1987). Further support for this high pH hexa-coordinate ligation came from a 2D NMR spectroscopic study by Hoang and Dixon where chemical shift data was in agreement with His-NH_3^+ ligation (Hong, 1989).

The alkaline transition, in which there is a switch from Met80 to Lys ligation is more complex than one would imagine, as both EPR and NMR have confirmed that the alkaline from of the protein is not a single species. EPR spectra display g values of a minor species at 3.17, 3.6 and the major species at 3.42 confirm the mixed nature of the alkaline form (Gadsby et al., 1987). 2D NMR support came from the work of Hong and Dixon, who revealed the presence of at least two coexistent basic forms above pH 9.5 (Hong, 1989). Additional support came from the earlier broad titration conducted by Wooten and colleagues, who suggested the complex pH-dependent behaviour observed by NMR spectroscopy does not follow the simple $n = 1$ protonation-deprotonation transition that is observed through the optical, magneto-optical and EPR spectroscopies (Wooten et al., 1981).

5.1.3 What is the replacement axial ligand?

By examining the 3D tertiary structure of tuna ferric C*c* several possible alkaline distal ligands were identified, particularly as it was known that no gross structural reorganisation occurred during the alkaline transition and therefore a restricted number of options are available (Greenwood and Wilson, 1971). The options included a number of Lys residues (72, 73, 79, 86, 87 and 88) and Arg91 (Greenwood and Wilson, 1971).

Despite extensive work from a number of laboratories over the years, conclusive evidence as to the identity of the alkaline ligand(s) remains somewhat obscure, for example Bosshard and co-workers argued that none of the possible Lys residues could be the replacement ligand due to their acetylation rates (Bosshard, 1981). Further support for this notion came from the work of Wallace and Corthésy (1987) who used alkylamine derivatives of C*c* (Wallace and Corthesy, 1987). However, following the work of Wallace (1984) and future studies, this notion has been successfully countered through the use of MCD and NMR data, which has strongly suggested that it is in fact Lys73 and/or Lys79 that are the replacement ligands (Wallace, 1984, Rosell et al., 1998).

Identifying the alkaline ligand is problematic as the alkaline form of C*c* does not comprise a single species, instead there are at least two species which exist (possibly with two different distal ligands) in a conformational equilibrium (Scott and Mauk, 1996). Unfortunately experiments that endeavour to determine whether a specific Lys is the correct ligand prove unsuccessful, giving negative results, as modification to the Lys in question will inevitably perturb the conformational equilibrium in favour of non-native conformations (Scott and Mauk, 1996).

5.1.4 The "trigger" hypothesis

Although it is widely regarded that the alkaline ligands of C*c* are Lys residues (Lys 73 and 79), it is not the case that deprotonation of a Lys residue is the driving force resulting in dissociation of the intrinsic Met80 distal ligand (Scott and Mauk, 1996). The initial view was that a deprotonated ε amino group (NH_2) of a Lys residue will out compete the Met80 ligand due to its high affinity for ferric iron (Scott and Mauk, 1996). However, this is not the case as experiments which have rendered the entire compliment of Lys residues within C*c* modified by either trifluroacetylation, or guanidination, resulting in the protein being high-spin at high pH, unlike the native protein (Stellwagen et al., 1975). As the pK_a values of the modified and native proteins are so close at 9.9 and 8.8 respectively, it is clear that the trigger remains intact, as in the case of the modified protein the incoming Lys residue no longer acts as a strong field ligand (Scott and Mauk, 1996).

There are multiple candidates proposed as the trigger group ranging from a tyrosine, arginine, the proximal field ligand His18, HP-6, or a buried water molecule (Scott and Mauk, 1996). Luntz and colleagues dismissed the possibility that Tyr67 is the ionisable group that regulates the alkaline transition, as they showed that the Y67F mutation does not abolish the transition despite an increase in the p*K* of 1.1 pH units (Luntz et al., 1989). Furthermore, Schejter and co-workers demonstrated that a double C*c* variant of Y67F/P30A results in the p*K* of the alkaline transition reverting to pH 9.5, very close to that of the WT protein (Schejter et al., 1992). Pro30 interacts with the proximal haem ligand His18 via a H-bond between the backbone carbonyl of Pro30 and the imino nitrogen of His18, therefore the two substitutions are distant and located on opposite sides to the haem (Scott and Mauk, 1996). Schejter and colleagues state that the exact mechanism by which the above mutations confer their effect is open to

discussion, however, they suggest that Tyr67 is not the trigger, but instead it is the other components of the alkaline transition which are modified (Schejter et al., 1992). Frauenhoff and Scott (1992) suggest that Tyr67 forms a H-bond to the alkaline hexa-coordinate Lys ligand and in turn this interaction stabilises the alkaline conformation, thereby raising the p*K* (Frauenhoff and Scott, 1992). However, in order for this argument to hold water, the assumption that the Tyr67-Met80 bond does not stabilise the native haem pocket structure must be made (Scott and Mauk, 1996). This is difficult to believe as Tyr67 is a highly conserved residue and likely plays a role in limiting the access of a second water molecule into the haem crevice, thus maintaining C*c*'s high redox potential (Scott and Mauk, 1996). Frauenhoff and Scott (1992) demonstrated that the Y67F substitution lowers C*c*'s redox potential by 50 mV, and NMR experiments by Hong and Dixon (1989) have eliminated Tyr67 as the ionising group (Hong and Dixon, 1989).

Arg91 has been discounted both on terms of its very high p*K* and that substitution of Arg91 leaves the pK_{695} unchanged.

Gadsby and colleagues made an interesting suggestion as to the identity of the trigger, from a result of combined MCD and EPR experiments in 1987 (Gadsby et al., 1987). They determined the pH dependence of the 1-methylimidazole complex of eC*c* and found that the p*K* of the transition of the proximal His18 to Histidinate was 11.6, close to the value of the kinetically determined trigger. Figure 5.1 illustrates this hypothesis in conjunction with the spectral features of the alkaline species and the single de-protonation event leading to the alkaline transition.

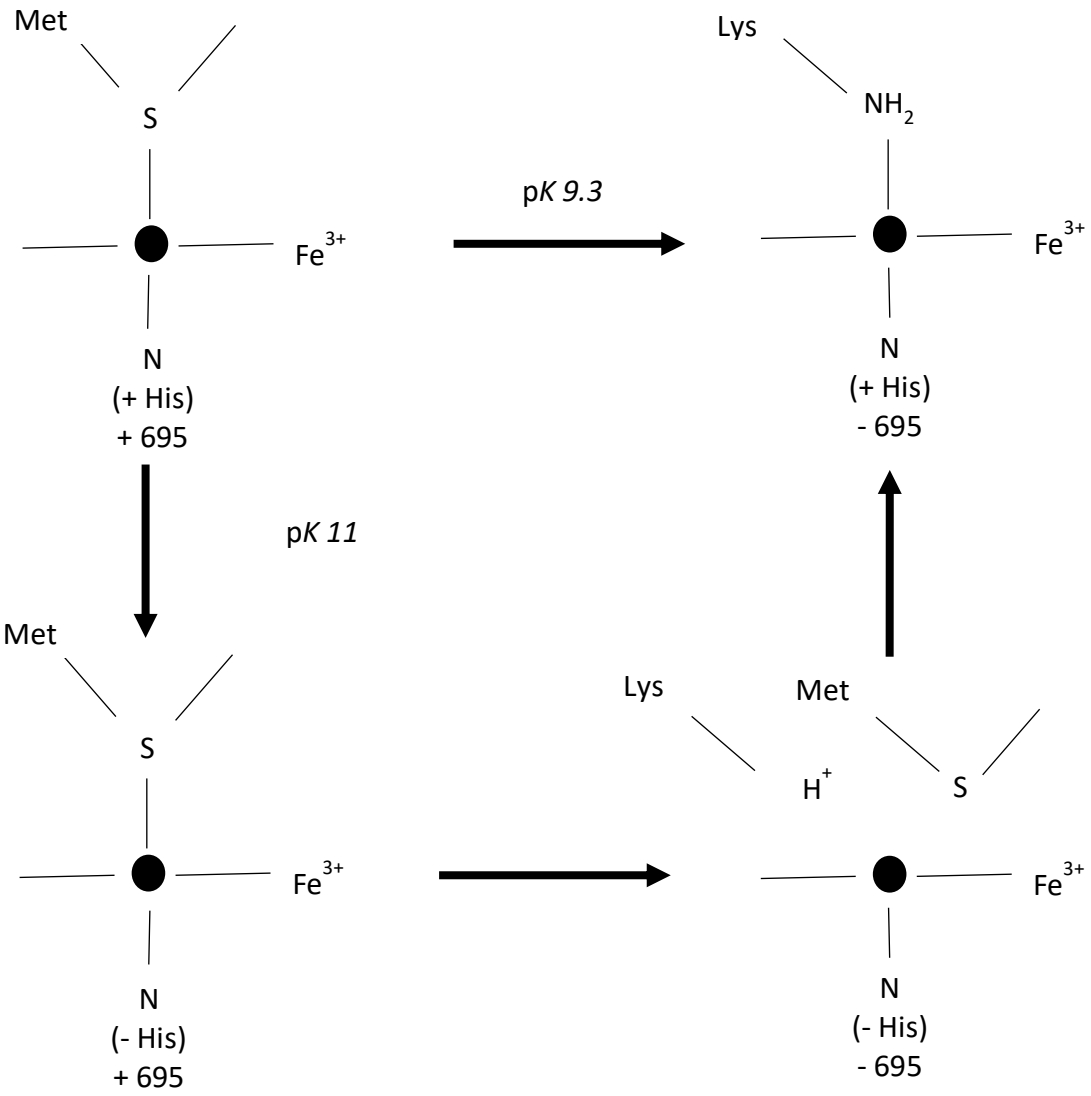

Figure 5.1 Schematic depiction of the low-spin intermediate (histidinate) first identified by (Kihara et al., 1976), adapted from (Gadsby et al., 1987) and (Scott and Mauk, 1996).

Figure 5.1 demonstrates that de-protonation of the proximal His18 yielding a Histidinate results in the dissociation of the *trans* Met80, thus exposing the ferric iron to an incoming Lys residue whose p*K* is lowered upon binding the iron. Finally, the dissociated proton from the newly coordinated Lys restored the proximal Histidinate

to Histidine. The result of this series of events is the substitution of the Met80-S to a Lys amino group and the bleaching of the 695 nm band with an observed p*K* of 9.3.

Moore and colleagues have proposed that Haem Propionate-6 (HP-6) is the likely trigger of the alkaline isomerisation, based on denaturation-induced proton uptake studies using ^{1}H NMR spectroscopy and Trp59 fluorescence (Hartshorn and Moore, 1989, Tonge et al., 1989). The assumption of this work is that the surface groups are not perturbed by denaturation and subsequently analysis of their data has shown that one of the haem propionic acid substituents of ferric C*c* has a p*K* of < 4.5, in contrast to the other which has a p*K* of > 9. Fourier-Transform Infrared (FT-IR) spectroscopy was used by Tonge and colleagues to identify an asymmetric carbonyl stretch at 1571 cm^{-1} characteristic of carboxylate anion formation at alkaline pH (Tonge et al., 1989). This spectral feature titrated with a p*K* of 6.14 in Cc_{551} which is in close agreement to the value reported by Leitch et al (1984) for Haem Propionate-7 (HP-7) (Leitch et al., 1984). In tuna C*c*, a comparable spectral feature is observed at 1565 cm^{-1} which titrates with a p*K* of 9.35, a value close to that of the alkaline transition (Scott and Mauk, 1996). In trifluroacetylated tuna ferric C*c*, where all Lys amino groups are modified, the transition from low-spin to high-spin haem upon increasing pH occurred with a p*K* of 10.2, whereas the carboxylate formation, as determined by FT-IR, occurred with a similar p*K* of 10.36. Due to these similarities, Tonge et al (1989) suggested that it is in fact the de-protonation of a haem propionate that triggers the alkaline transition (Tonge et al., 1989). In native WT ferric C*c*, the de-protonation of a haem propionate should occur with a p*K* of ~11 and therefore it is HP-6 which has been tentatively assigned as the trigger group (Scott and Mauk, 1996). In C*c* HP-6 is buried in a hydrophobic environment, likely accounting for the abnormal p*K* value (Scott and Mauk, 1996). Unfortunately, there is no conclusive experimental evidence

to account for the abnormally high p*K* values determined for HP-6, examination of the local environment of HP-6 and -7 also provides little insight as to their significantly differing p*K*'s (Scott and Mauk, 1996). Cutler and colleagues made substantial changes to the environment of HP-7 via a R38A mutation, however, this resulted in only a minimal change to the observed p*K* (Cutler et al., 1989). The change in p*K* is therefore likely to be attributed by a break in the peptide bond either before or after Arg38, this would considerably alter the local environment of the propionate and confer a drastically different p*K* of the alkaline transition (Wallace, 1987). It is still unknown whether this is a result of a change in the p*K* of a propionate as a result of increased solvent exposure, or a general change in protein tertiary structure (Scott and Mauk, 1996).

Analysis of the X-ray crystal structure of C*c* has revealed the presence of a buried water molecule near to the iron sulphur bond with Met80. This region confers the possibility of H-bonding and structural changes following de-protonation of the water molecule (Scott and Mauk, 1996). It has been suggested that the breaking of the H-bond to Thr78 is what triggers the alkaline transition (Takano and Dickerson, 1981), a view supported by Luntz and colleagues who have demonstrated that the buried water molecule is stabilised by H-bonds to Tyr67, Thr78 and Asn52 due to the p*K* of a Y67F variant being raised to 11 (Luntz et al., 1989). Additional support for the buried water molecule theory comes from *Pseudomonas* Cc_{551}, a C*c* which does not possess the buried water molecule and also display a p*K* of 11 (Scott and Mauk, 1996).

In ferrous C*c*, the buried water molecule moves ~ 0.5 Å away from the Fe-S bond and therefore confers a lesser destabilising effect raising the p*K* (Mathews, 1985). Schejter and Plotkin (1988) however, give a more plausible reason for the greater stability at alkaline pH, that is due to the Met80 sulphur atom being a strong field ligand

of ferrous iron due to the π-acid nature of Met80 and subsequent orbital overlaps (Schejter and Plotkin, 1988).

The identity of the trigger group remains a mystery, however, it is clear from available experiential data that neither Tyr67 or a lysine amino are candidates, Arg91 is also unlikely due to its high p*K* value (Scott and Mauk, 1996). Evidence for HP-6 relies on the abnormally high p*K* value of a carbonyl group within ferric C*c*. De-protonation of a buried water molecule and the proximal His18 are plausible due to their proximity to the Fe-S bond, however, it is possibly more likely to involve a mechanism involving the histidine-histidinate transition, as this is *trans* to the Fe-S bond and it is known that *trans* effects such as binding of NO weakens the *trans* ferrous-histidine bond (Traylor and Sharma, 1992). It is challenging to explain how His^- weakened the *trans* Fe(III)-S bond, in fact, it is likely to impart more ferrous character and therefore bind the Met80 ligand more tightly, as suggested by (Schejter and Plotkin, 1988). An additional complication is that this raises the question: if there is a *trans* effect why does it not occur in the same pH range in C*c* and Cc_{551} of *P. aeruginosa*, where the p*K* of the alkaline transition is ~ 11 (Scott and Mauk, 1996)? Pearce and colleagues have argued against the proximal His18 hypothesis, as their experimental data from Phe82 variants has shown a decrease in the p*K* of 2 pH units, contradicting what would be expected if His18 is the trigger, in which there should be an increase in the p*K* (Pearce et al., 1989). The buried water molecule is the more likely trigger candidate; however, the precise identity of the trigger is yet to be elucidated. Further support for the buried water molecule comes from Aviram and Schejter (1972) who demonstrated that when the buried water molecule is removed, by lyophilising, the 695 nm band is abolished, suggesting a loss of Met80 coordination,

however, when re-hydrating the protein the 695 nm band is restored and therefore Met80 coordination.

5.1.5 Kinetics of the alkaline transition

The variety of spectroscopic evidence available has revealed that the alkaline transition involves a ligand replacement from a sulphur to a nitrogen and may therefore be represented by a two-state transition coupled to a de-protonation event (Scheme 5.1).

$$\begin{array}{ccc} & H^+ & \\ & \updownarrow & \\ H^+(S-Fe^{III}-N) & \leftrightarrow & S-Fe^{III}-N \underset{k_b}{\overset{k_f}{\rightleftharpoons}} N-Fe^{III}-N \end{array}$$

[Scheme 5.1]

$$K_c = \frac{k_f}{k_b}$$ [Equation 5.1]

$$k_{obs} = k_b + k_f \frac{K_H}{K_H + [H^+]}$$ [Equation 5.2]

In equations 5.1 and 5.2, K_H and K_C denote the respective equilibrium constants for the deprotonation and conformational change respectively, whilst k_f and k_b are the rate constants for the conformational transition, as described in Scheme 5.1 (Scott and Mauk, 1996). As it is de-protonation which is linked to ligand exchange, the pH jump methodology provides powerful insights into the kinetics of the transition. Davis and colleagues (1974) conducted the initial work into kinetics of the alkaline transition by following the absorbance changes at 695 nm whilst rapidly changing the pH of the solution (Davis et al., 1974). They were able to show that it is unambiguously a de-protonation event which precedes the spectral changes, as the experimentally observed

rates showed strong pH dependency, with rates increasing significantly at pH's above the p*K* of the protein. This conclusion is entirely consistent with the view that it is de-protonation of a trigger group which precedes Met80 dissociation and ligand exchange. At 25 °C pK_H and *K*c were determined to be 11 ± 0.1 and 125 ± 36 respectively and therefore, the overall p*K* is close to that of the p*K* of the alkaline transition, determined by taking the log of the reciprocal of the products K_H and K_C (Scott and Mauk, 1996). Davies et al (1974) determined the thermodynamic parameters of the conformational change, which are in close agreement with values determined by other methods (where the values of k_b and k_f were reported as 0.049 and 6.1 ± 1.8 s^{-1} respectively), such as pH jump experiments by (Kihara et al., 1976), redox experiments by (Wilson and Greenwood, 1971), ^{1}H NMR experiments by (Hong and Dixon, 1989) and ligand-replacement techniques by (Alayash, 1979). For the forward and back reactions, the associated activation energies were reported to be E_{af} = 28 kcal mol^{-1} and E_{ab} = 16 kcal mol^{-1} by (Davis et al., 1974). Pearce and colleagues have furthered our insights into the mechanism and kinetics of the alkaline transition using pH jump experiments with variants of yeast iso-1-C*c*, in which mutations were created at Phe82 (Pearce et al., 1989). They found reductions in the overall p*K* by substituting Phe82, with the pK_H lowered by 1.5 pH units, which considering the pK_H is the p*K* of the trigger group, allowed them to conclude that the proximal His18 favoured by (Gadsby et al., 1987) is not the likely trigger group, as mutation at Phe82 would not further lower the abnormally high p*K* of this group. Rosell and colleagues determined the pK_a of the conformational equilibrium between states III and IV of WT iso-1 C*c* protein (8.7) to be intermediate to that of Lys73 (8.44) and Lys79 bound (8.82) alkaline conformers, respectively (Rosell et al., 1998).

As it is now known that there are at least two alkaline conformers, with two different lysine's coordinated, the model produced from the data obtained by Davis et al (1974) and Pearce et al (1989) must be taken further, however, this added complexity is not amenable to analytical solution. Computational simulations for the multiple alkaline ligands by Wilson and Hogg ((Wilson) unpublished result) support the conclusions of Davis et al (1974), in which the overall p*K* of the transition consists of the p*K* of a triggering group that is coupled to a conformation change. It is also likely that modelling the alkaline transition must account for the transient intermediate identified by (Kihara et al., 1976). This intermediate is supported by (Uno et al., 1984), who used stopped-flow resonance Raman spectroscopy to identify the presence of both high- and low-spin intermediates in pH jump experiments.

5.1.6 Carboxymethyl cytochrome c

(Schejter and George, 1965) demonstrated that carboxymethylation of Met80 renders the ligand unable to bind to the haem iron and therefore abolishes the 695 nm band in the ferric protein. This modification can serve as an effective model of the alkaline form, as at high pH values both carboxymethyl C*c* (CM-C*c*) and the native protein display similar affinities for extrinsic haem ligands, such as cyanide, with K_{ass} values of 1.8×10^4 M^{-1} and 5.5×10^4 M^{-1} respectively (Saleem and Wilson, 1988). Interestingly, at neutral and near neutral pH values, the native protein displays a lower affinity for extrinsic ligands, as a result of competition with the Met80 distal ligand (Scott and Mauk, 1996).

5.1.7 The alkaline transition, Ω-loops and cytochrome c biological function

As mentioned previously, the identity of the trigger group(s) has not been satisfactorily deduced and therefore intense debate exists in the C*c* literature. As described above, extensive spectroscopic studies have formulated several possible groups that could serve as the trigger (Greenwood and Wilson, 1971, Bosshard, 1981, Wallace and Corthesy, 1987, Wallace, 1984, Rosell et al., 1998). Most recently, studies have favoured the notion that deprotonation of the incoming hexa-coordinate Lys residue (Lys73/79) is itself the trigger. Alternatively, other groups have been suggested, namely Tyr67, an internal H_2O (wat166 in yeast) and HP-7. The latter three groups are significant, as interestingly they interact through an extensive H-bond network that also includes Asn52 and Thr78, culminating in the OH group of Tyr67 H-bonding to the Sγ atom of Met80. This extensive H-bond network confers communication between the 40-57 and 71-85 Ω-loops. These structural units are the first to unfold on the C*c* unfolding pathway and interestingly, the unfolding rate of the 71-85 Ω-loop matches the rate of the slow conformational change that is associated with Lys coordination as the distal ligand following Met80 dissociation (Hoang et al., 2003, Maity et al., 2006). The 40-57 Ω-loop unfolding rate is equal to that of an internal deprotonation rate at pH values greater than 10.5, an ionisation process not attributed to the trigger group (Hoang et al., 2003, Maity et al., 2006). The suggestion is that the trigger mechanism and the formation of the alkaline conformer appear to be governed by the interplay between the two Ω-loops.

Under neutral conditions, it is state III of ferric C*c* which can access a non-native conformer that is peroxidase active. The peroxidase activity arises through a dynamic equilibrium between the hexa- and penta-coordinate species. Despite the population of the penta-coordinate species being exceptionally low, it is nevertheless

responsible for the intrinsic peroxidase activity present in C*c* when in the presence of H_2O_2. The penta-coordinate species helps regulate the concentration of ROS, however, as has been discussed in previous Chapters, during the initial stages of apoptosis it is responsible for the peroxidation of CL. As shown in Chapter 4, the NMR studies reported provide firm evidence that the increased population of a penta-coordinate form in the G41S and Y48H variants arises through extensive dynamic fluctuations in the 40-57 Ω-loop and to a lesser extent in the 71-85 Ω-loop (Deacon et al., 2017, Karsisiotis et al., 2016). These works support the notion that a dynamic coupling between these two structural units play a key role in accessing the peroxidatic conformer of hC*c*, as is also the case for the formation of the alkaline conformer.

hC*c* peroxidase activity is required under normal physiological conditions, despite this, Bowler and colleagues have proposed the hypothesis that the 71-85 Ω-loop of hC*c* has evolved (based on sequence variation at the 81 and 83 positions) to supress the intrinsic peroxidase activity in comparison to that of lower eukaryotes, such as yeast C*c* (McClelland et al., 2014). An Ala and Gly are found at the 81 and 83 positions respectively, in yeast iso-1 C*c*, in contrast to the more sterically restrictive Ile and Val in hC*c*. The X-ray crystal structure of the K72A variant of yeast iso-1 C*c* revealed a protein conformer in which the hexa-coordinate Met80 ligand is replaced by a H_2O molecule (McClelland et al., 2014). The result in this altered hexa-coordinate ligation was significant movement of Ala81 and Gly83 resulting in an open haem crevice conformation (McClelland et al., 2014). The ~ 30-fold increase in peroxidase activity present in yeast iso-1 C*c* compared with WT hC*c*, has been attributed, based on the aforementioned structural observations, to altered residue volume at the 81 and 83 positions (McClelland et al., 2014). Bowler and colleagues argue that steric hindrance at these positions minimises access to the C*c* conformers that give rise to the

peroxidase activity (McClelland et al., 2014). Further support for this hypothesis comes from studies with the A81H variant of yeast iso-1 C*c*, which demonstrated that increased steric size at the residue 81 position inhibits Met80 dissociation (Bandi and Bowler, 2015).

The work presented in this Chapter has investigated the effect of steric control in the 71-85 Ω-loop, at positions 81 and 83 in hC*c*, both in terms of peroxidase activity and ligand binding kinetics. Furthermore, the conformational transition that leads to the ligand switch in the alkaline conformer has been probed for both the G41S and Y48H variants in the 40-57 Ω-loop and the residue 81 and 83 variants in the 71-85 Ω-loop. The data presented in this Chapter furthers our understanding of the roles played by titratable groups and the overall dynamics associated with this conformational change for these respective Ω-loop variants. Specifically, the findings reveal that the conformational transitions in the 71-85 Ω-loop, which give rise to both the alkaline and peroxidase active conformers, are controlled by the dynamics of the 40-57 Ω-loop, which also appears to regulate the pK_a values of two ionisable groups that are involved in Met80 dissociation. The results are discussed in terms of a mechanistic model, which although likely simplified, brings the various conformational and protonation/de-protonation events into a consistent picture, thus providing a platform from which future experimental approaches may be designed.

5.2 Materials and Methods

5.2.1 Site-directed mutagenesis

The 71-85 Ω-loop variants of hC*c* (I81A, V83G and I81A/V83G) were produced using the Quickchange mutagenesis protocol (Stratagene). The following forward and reverse mutagenic primers were used: I81A-F 5'-

GGAACAAAAATGGCCTTTGTCGGCATTAAG-3', I81A-R 5'-CTTAATGCCGACAAAGGCCATTTTTGTTCC-3', V83G-F 5'-GGAACAAAAATGATCTTTGGCGGCATTAAGAAG-3', V83G-R 5'-CTTCTTAATGCCGCCAAAGATCATTTTTGTTCC-3', I81A/V83G-F 5'-GGAACAAAAATGGCCTTTGGCGGCATTAAGAAG-3', I81A/V83G-R 5'-CTTCTTAATGCCGCCAAAGGCCATTTTTGTTCC-3'. A PCR reaction mixture consisting of primers (75 ng/µl), WT template (15 ng/µl), 10 mM dNTPs (Fermentas), Pfu Turbo polymerase (Stratagene), 10 x Pfu Buffer (Agilent) and deionised H_2O to yield a final volume of 50 µl was used. This reaction mixture was subjected to the following PCR protocol; 95 °C – 3 min, (95 °C – 1 min, 60 °C – 1 min, 53 °C – 1 min, 72 °C – 6 min, 72 °C – 10 min) x 18 cycles, 72 °C – 10 min. PCR products were digested with DpnI (Fermentas) and transformed into DH5α *Escherichia coli* cells. Isolated clones were DNA sequenced to corroborate the presence of the expected nucleotide change(s).

5.2.2 Protein over-expression and purification

The over-expression and purification protocols for the hC*c* variants I81A, V83G and I81A/V83G were identical to that of the WT protein and Y48H variant as described in Chapter 2.1.

Equine heart carboxymethyl C*c* was prepared from an adapted method (Silkstone et al., 2005) previously described (Schejter and George, 1965) and the concentration determined using the ε at 414 nm of 219 x 10^3 M^{-1} Cm^{-1} for the ferrous CO complex (Brunori et al., 1972).

5.2.3 Stopped-flow kinetics – pH jump experiments

All kinetic experiments were conducted with an Applied Photophysics (Leatherhead UK) SX20 stopped-flow spectrophotometer equipped with both photomultiplier and photodiode array detection systems, thermostatted at 25 °C. Various high pH buffers consisting of 50 mM KCl, 50 mM boric acid (pH 7 - 9) or 50 mM CAPS (pH 9 - 13) were produced. Protein stocks were oxidised and equilibrated (as described in Chapter 2) in H_2O and diluted to experimental concentrations in 50 mM KCl, to maintain ionic strength during mixing in the spectrophotometer, to ~ pH 7. The protein solutions were mixed with equal volume high pH buffer in the stopped-flow spectrophotometer. First order rate constants (k_{obs}) were obtained by fitting reaction time-courses to either a single, or at pH values above 10.5 a double exponential function. All kinetic analysis was conducted using the ProKineticist software (Applied Photophysics).

5.2.4 Stopped-flow Kinetics – N_3^- binding

Experiential protocols for eC*c* and the 71-85 Ω-loop variants were identical to those reported in Chapter 4.2.5.

5.2.5 Electron Paramagnetic Resonance spectroscopy

All EPR samples were frozen in Fluorochem SQ EPR tubes (Derbyshire, UK). Tube sizes with an outer diameter of 4.05 ± 0.07 mm and an inner diameter of 3.12 ± 0.04 mm (mean ± range) were used in order to minimise the effect on quantitative results. Random error in the EPR signal intensities was low (1-3 %). Two sample freezing methods were used for the low temperature EPR measurements, a slow freeze and Rapid Freeze Quench (RFQ) approach. For slow frozen samples, 250 μl of protein

was dispensed into the bottom of an EPR tube and placed into methanol stored in dry ice. Once frozen, the tube was transferred to liquid nitrogen and stored until measurement. The RFQ approach consisted of the combined use of an Update Instrument (Madison, WI) mixing machine and a home-built apparatus for freezing the ejected mixtures onto the surface of a rapidly rotating aluminium disk at liquid nitrogen temperature. The RFQ methodology has been described previously (Thompson et al., 2010). All EPR spectra were measured at 10 K on a Bruker EMX EPR spectrometer (X-band) with a high-quality spherical Bruker resonator (SP 9703) and an Oxford Instruments liquid helium system.

In order to estimate the concentrations of the high- and low-spin ferric haem forms in the Y48H variant EPR spectra at pH 11, a calibration experiment was conducted with equine heart Cm-C*c* in a range of buffers (pH 4.5 – 8.5) yielding samples with varying concentration of the high- and low-spin ferric haem species.

5.2.6 Peroxidase assays

For full experimental details, see Chapter 4.2.6.

5.2.7 Circular Dichroism spectroscopy

For full experimental details, see Chapter 4.2.7.

5.2.8 Static pKa titrations

For full experimental details, see Chapter 4.2.8.

5.3 Results

5.3.1 Global stability of the 81 and 83 variants in the 71-85 Ω-loop: UV-visible and far-UV CD spectroscopy

The optical absorbance of WT hC*c* and the 71-85 Ω-loop variants in both the ferric and ferrous forms are shown in Figure 5.2. As was the case with the disease variants G41S and Y48H, both their respective ferric and ferrous spectra are indistinguishable from that

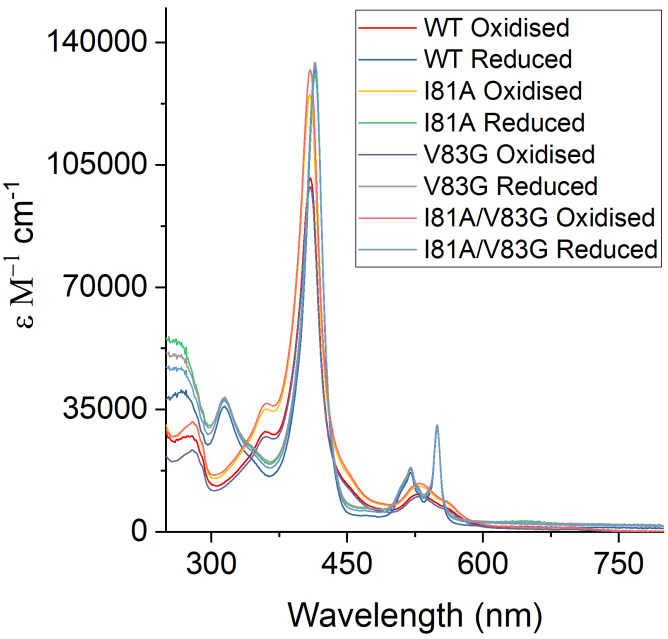

Figure 5.2 UV visible spectra of WT hC*c* and the 71-85 Ω-loop variants I81A, V83G and the double mutant (I81A/V83G) in both the ferric and ferrous forms at pH 6.5 (20 mM sodium phosphate, pH 6.5), room temperature.

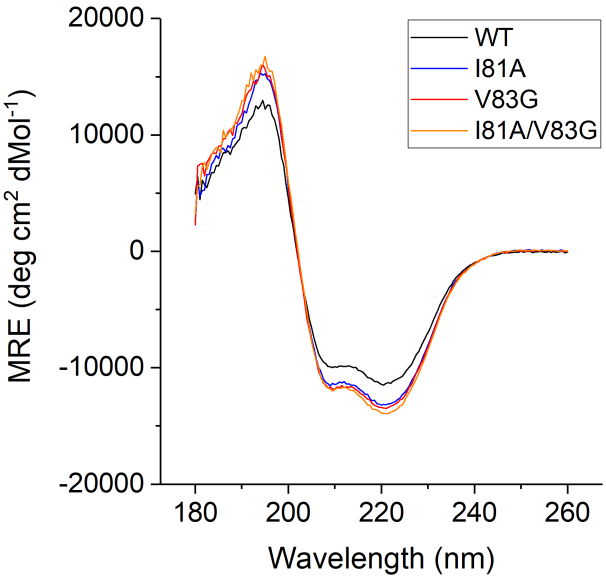

Figure 5.3 Far-UV CD spectra of ferric WT hCyt *c* and the steric mutants I81A, V83G and the double mutant I81A/V83G at pH 7.0, 15 °C.

of the WT protein. The far-UV CD spectra of the 71-85 Ω-loop variants display two negative minima at 208 nm and 222 nm, thereby indicating significant α-helical content and that the proteins are fully folded in solution, as in the case of the WT protein (Figure 5.3). Similarly, as was the case with the disease variants, the 71-85 Ω-loop variants appear to display somewhat greater α-helicity than the WT protein, though this result is open to criticism, as given the lower absorbance at 195 nm, this suggests a concentration discrepancy.

Table 5.1 Global stability and the kinetics of N_3^- binding to WT hC*c* and eC*c*, in addition to the series of hC*c* variants studied in this Thesis.

	WT hC*c*	**WT eC*c***	**G41S**	**Y48H**	**I81A**	**V83G**	**I81A/V83G**
pK_{695}	9.3 ± 0.2	9.2	8.5 ± 0.2	8.4 ± 0.1	9.4	10.1 ± 0.1	9.7 ± 0.1
ΔG_{unf}	9.7 ± 0.1	---	6.75 ± 0.1	5.51 ± 0.15	9.75 ± 0.19	9.95 ± 0.058	9.2 ± 0.12
m	3.8 ± 0.1	---	3.05 ± 0.05	2.65 ± 0.05	3.8 ± 0.033	3.85 ± 0.033	3.65 ± 0.033
C_m	2.53 ± 0.025	---	2.25 ± 0.05	1.93 ± 0.025	2.6 ± 0.017	2.63 ± 0.017	2.55 ± 0.017
K_{app}	0.31 ± 0.03	---	0.11 ± 0.01	0.07 ± 0.01	0.24 ± 0.02	0.3 ± 0.03	0.1 ± 0.01
$k_{1\ [Az]}$	5.77 ± 1.5	---	45 ± 18	125	14.91 ± 6.4	4.46 ± 0.5	73.95 ± 84
$k_{-2\ [Az]}$	3.5 ± 0.44	---	8.9 ± 0.3	12.1 ± 1.1	5.94 ± 0.49	1.73 ± 0.17	3.06 ± 0.1

An Ala and Gly residue occupy positions 81 and 83 respectively, in yeast iso-1 C*c*. In order to assess whether the increased residue volume, conferred by an Ile and Val respectively, at positions 81 and 83 in hC*c*, helps prevent Met80 lability and subsequent access to the peroxidatic conformer, both single variants (I81A, V83G) and

a double variant (I91A/V83G) were constructed. The double variant essentially mimics the 71-85 Ω-loop of yeast iso-1 C*c*. The effect on the global stability of hC*c* upon introduction of these residue variants in the 71-85 Ω-loop was determined by chemical denaturation studies using GuHCl as the denaturant and far UV-CD spectroscopy, as reported in Chapter 4 for the disease variants G41S and Y48H. Values for ΔG_{unf}, C_m and *m* have been determined from fits to the data plotted in Figure 5.4 and values reported in Table 5.1, together with values previously reported for the WT human protein under identical conditions (Karsisiotis et al., 2016, Deacon et al., 2017). Subtle differences are noted, the most prominent of which is the 0.7 kcal/mol decrease in ΔG_{unf} for the double variant I81A/V83G. Overall however, decreasing the residue volume at positions 81 and 83 in the 71-85 Ω-loop has minimal effect on the global stability relative to WT hC*c*. This contrasts with the disease variants G41S and Y48H in the 40-57 Ω-loop, in which the ΔG_{unf}, C_m and *m* values (Table 5.1) all decrease with respect to the WT protein of order Y48H < G41S < WT, suggesting a significant destabilisation of the folded state in these naturally occurring variants.

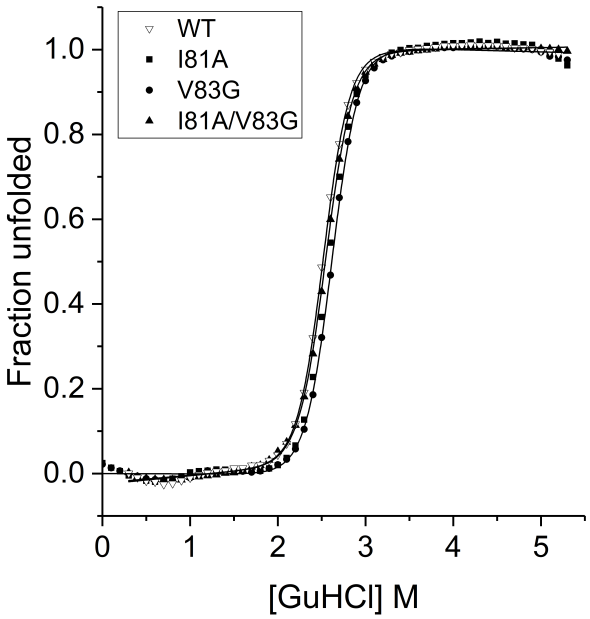

Figure 5.4 Equilibrium unfolding by GuHCl of the steric mutants of hCyt *c* I81A, V83G and the double mutants I81A/V83G, in addition to the WT protein at pH 7, 20 °C. Figure taken from Deacon *et al*., 2017 (unpublished).

5.3.2 N_3^- binding to the 81 and 83 variants in the 71-85 Ω-loop

N_3^- binding kinetics were used to determine the effect of the 81 and 83 mutations on the local stability of the 71-85 Ω-loop. In order for N_3^- to bind to the haem of hC*c*, there must first be dissociation of the hexa-coordinate haem ligand (Met80). Following Met80 dissociation, N_3^- binds through an SN_1 mechanism as the protein exists in dynamic equilibrium between the hexa- and penta-coordinate forms. This reaction is widely regarded to report on the Met80-Fe(III) bond lability. Upon mixing N_3^- with ferric hC*c*, an optical transition occurs as a result of the dissociation of the Met80 ligand from the ferric haem iron and the subsequent binding of N_3^- in its place (Karsisiotis et al., 2016). As was the case with the disease variants (G41S and Y48H) and the WT protein under identical experimental condition, the reaction time-course of this optical transition for the 81 and 83 variants conformed to a simple

exponential (Karsisiotis et al., 2016, Deacon et al., 2017). The amplitudes of such reaction time-courses follow a simple hyperbolic binding isotherm (Figure 5.5), determined over a broad range of [N_3^-], in which an apparent equilibrium constant (K_{app}) for N_3^- binding may be determined using equation 4.4 and respective K_{app} values reported for the 81 and 83 variants in Table 5.1. One can determine from equation 4.4 that when K is < 1, as is the case here due to the concentration of the penta-coordinate species being low, then K_{app} is ~ K_D/K. Assuming that the polypeptide mutations do not directly affect N_3^- binding to the penta-coordinate species, then K_D will be similar for both the WT protein and variants of hC*c*, in which the ratio of K_{app} values ($^{WT}K_{app}/^{variant}K_{app}$) reflects the ratio of K values ($^{variant}K/^{WT}K$). As $^{I81A/V83G}K > {}^{I81A}K > {}^{V83G}K = {}^{WT}K$ it is apparent that the penta-coordinate form of the I81A/V83G variant is populated to a greater concentration than in either of the two single variants (I81A, V83G) or the WT protein. The relationship between k_{obs} and [N_3^-] for the 71-85 Ω-loop variants, appears almost linear under the conditions employed, as was the previously reported case for the disease variants (G41S and Y48H) and the WT protein in Chapter 4

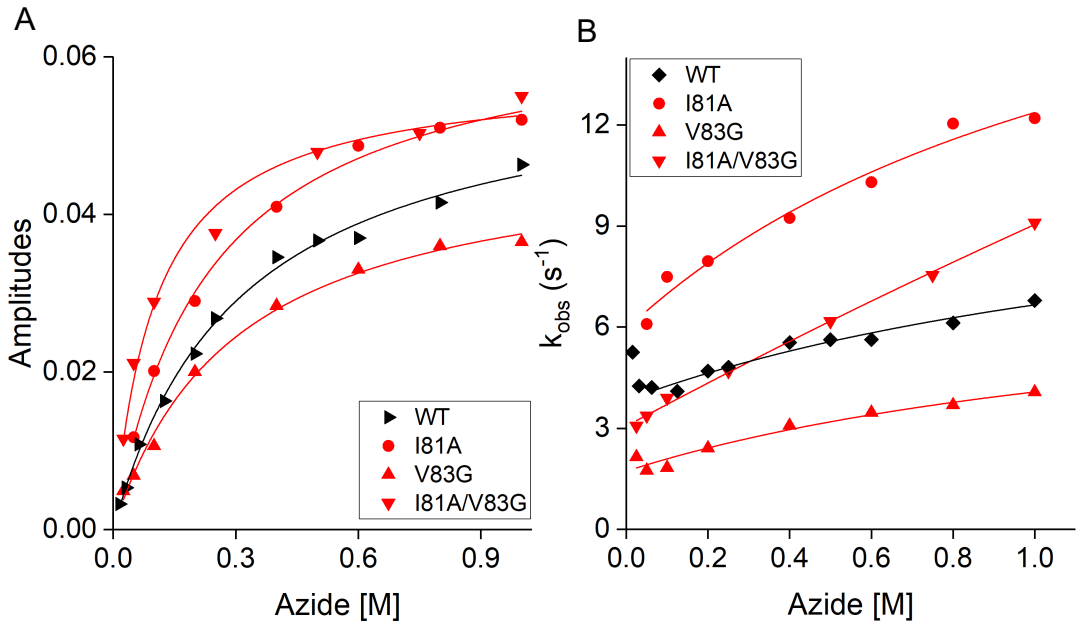

Figure 5.5 Stopped-flow kinetics of N_3^- binding to ferric hCyt *c*, in addition to the 81 and 83 variants at 25 °C, pH 7. **A** Amplitudes of the time courses recorded at 420 nm plotted as a function of N_3^- concentration. The subsequent binding curves are fitted to equation 4.4 yielding the K_{app} values reported in Table 4.1. **B** The rate constant (k_{obs}) determined for N_3^- binding fitted to equation 4.5 yielding k_1 and k_2 values reported in Table 4.1, where k_1 and k_2 values refer to the Met80 and N_3^- dissociation rate constants respectively. Adapted from Deacon *et al*, 2017 (submitted).

(Karsisiotis et al., 2016, Deacon et al., 2017). Using Equation 4.5 a prediction can be made that the relationship between k_{obs} *vs* $[N_3^-]$ follows a hyperbola, in which the curve is expected to reach a plateau (*i.e.* k_1, the Met80-off rate). As was the case with the disease variants G41S and Y48H, reported in Chapter 4 (Karsisiotis et al., 2016, Deacon et al., 2017), it was not possible to explore a sufficiently high $[N_3^-]$ so a plateau region could not be reached. In light of this, the k_1 errors are large, whereas the k_{-2} (the k_{obs} intercept and N_3^- dissociation constant) values are more reliable. Despite this, the k_1 values determined in this way follow the same pattern as observed for *K* with

$^{I81A/V83G}k_1 > {}^{I81A}k_1 > {}^{V83G}k_1 = {}^{WT}k_1$ (Table 5.1) consistent with the interpretation from N_3^- kinetics of a more labile Met80 ligand.

5.3.3 Peroxidase activity

C*c* can function as a peroxidase, either in isolation, or in complex with CL during the onset of apoptosis (Kagan et al., 2005). The peroxidase activity of the 81 and 83 variants was determined through ABTS peroxidase activity assays, both in the absence and presence of CL liposomes (Figure 5.6A). A lag phase in the peroxidase kinetics of C*c* has been extensively reported (Karsisiotis et al., 2016, Rajagopal et al., 2013), though recently attributed to the oxidative activation of a pre-catalytic form leading to the formation of oxidised proteoforms with high peroxidase activity (Yin et al., 2017). These oxidised proteoforms possess a penta-coordinate haem, in which the intrinsic Met80 ligand is dissociated and subsequently oxidised, in addition to an oxidised Tyr67 and carbonylated Lys72/73 (Yin et al., 2017). Interestingly, the 81 and 83 variants in the absence of CL liposomes do not display the distinct lag phase after the addition of H_2O_2 (Figure 5.6A inset) associated with the WT hC*c*, a characteristic previously observed in the disease variants G41S and Y48H (see Chapter 4) (Rajagopal et al., 2013, Deacon et al., 2017). The 81 and 83 variants all display increased peroxidase activity in the absence of CL liposomes relative to the WT protein, of order I81A > V83G > I81A/V83G = WT (Figure 5.6A). In the presence of CL liposomes, the peroxidase activity is further enhanced, consistent with expectation, to the greatest extent for the I81A variant with an order of activity I81A > I81A/V83G > V83G = WT (Figure 5.6A). It is important to note, that whilst the effect of decreasing residue volume at residues 81 and 83 does indeed yield a peroxidase rate increase, the enhancement is of a significantly lesser extent than that of the disease variants G41S

and Y48H, in which a 3- and 7-fold increase is observed respectively, relative to the WT protein (see Chapter 4) (Karsisiotis et al., 2016, Deacon et al., 2017). This suggests that the disease variants G41S and Y48H populate a higher concentration of the oxidised proteoforms, that give rise to the peroxidase active C*c* state.

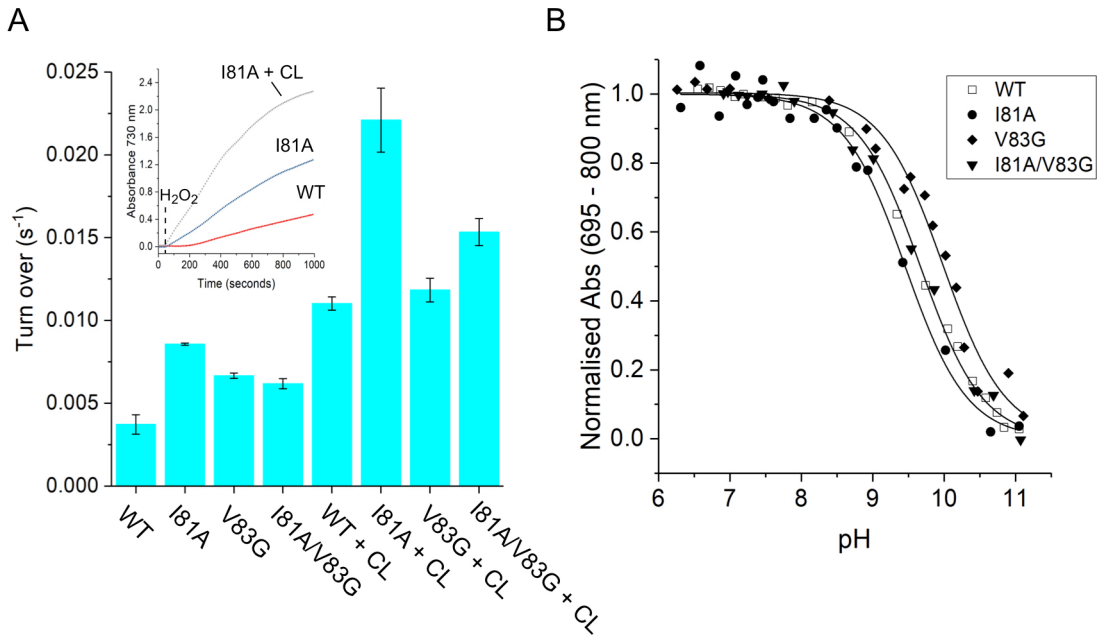

Figure 5.6 Peroxidase activity and the pH dependence of the 695 nm band. **A**) Illustrative reaction time courses (inset) for the oxidation of ABTS by ferric hC*c* upon addition of H_2O_2 (dashed line) with (+ CL) and without CL-containing liposomes. The average maximum rates of ABTS peroxidation obtained from such reaction time courses for the WT protein and various 71-85 Ω-loop variants plotted with (+ CL) and without CL-containing liposomes. The error bars are obtained from the standard error on triplicate measurements. **B**) Decrease of the 695 nm absorbance band plotted as a function of pH for the WT protein and 71-85 Ω-loop variants. Solid lines are representative fits to the data using a one-proton ionisation equilibrium equation with the apparent pK_a values reported in Table 5.1. Taken from (Deacon et al., 2017).

5.3.4 Equilibrium alkaline isomerisation of the 81 and 83 variants in the 71-85 Ω-loop

The 695-nm band in the absorption spectrum of C*c* is assigned to the LMCT properties of the Met80(Sγ)-Fe(III) haem bond (Stellwagen and Cass, 1974, Moore and Pettigrew, 1990, Theorell and Åkesson, 1941). Alkaline pH titration of this band conforms to a simple transition in which a single proton is dissociated upon increasing pH resulting in Met80 dissociation and subsequent replacement by a Lys residue within the 71-85 Ω-loop (state III to IV transition) (Stellwagen and Cass, 1974, Moore and Pettigrew, 1990, Theorell and Åkesson, 1941, Smith and Williams, 1970, Makinen, 1983, Scott and Mauk, 1996), as previously described. As explained previously, the apparent pK_a of the alkaline transition is generally interpreted as a reflection of the flexibility/stability of the 71-85 Ω-loop. Interestingly, the I81A variant does not alter the apparent pK_a relative to the WT protein (Figure 5.6B, Table 5.1), however, an increase of 0.8 pH units is observed for the V83G variant (Figure 5.6B, Table 5.1), whilst the double variant I81A/V83G possesses a pK_a of only 0.4 pH units higher than WT hC*c* (Figure 5.6B, Table 5.1). This pattern of the apparent pK_a V83G > I81A/V83G > I81A = WT provides a clear example of biochemical epistasis, in which the V83G variant clearly has a different effect in combination with the I81A variant than in isolation. Shifts to higher pK_a values for the V83G and I81A/V83G variants is consistent with a destabilisation of the alkaline state, relative to the WT protein. This finding is contradictory to the interpretation of enhanced Met80 ligand lability, based on the N_3^- binding kinetics, thus suggesting other underlying processes are involved. This contradiction between pH titration and N_3^- binding kinetics will be considered further below. In contrast, the disease variants G41S and Y48H, in the 40-57 Ω-loop, have an apparent pK_a ~ 1 pH unit lower than that of the WT protein, thus providing

experimental support for a stabilisation of the alkaline form relative to the WT protein (Table 5.1).

5.3.5 Kinetics of the alkaline transition below pH 10 for the 40-57 and 71-85 Ω-loop variants

The mechanistic features of the alkaline transition and the impact of mutation within the 40-57 and 71-85 Ω-loop variants on this were investigated using stopped-flow pH jump experiments. The kinetics of the alkaline transition in C*c* are generally described in terms of a simple model (Scheme 5.2), in which deprotonation of a group

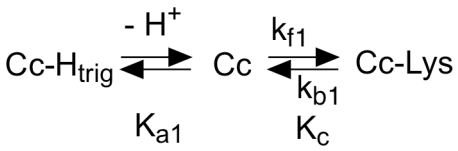

Scheme 5.2

that is not yet definitely identified, termed the trigger, initiates a conformational change which subsequently leads to the substitution of the Met80 ligand by a Lys residue from the 71-85 Ω-loop. In Scheme 5.2, C*c*-H_{trig} depicts the protein with the trigger protonated, C*c* the protein with the trigger deprotonated and C*c*-Lys the protein having undergone a conformational change from the acid (Met80 bound) to alkaline (Lys bound) form. K_{a1} and K_c are the deprotonation and conformational equilibria associated with the two steps and k_{f1} and k_{b1} are the forward and backward rate constants associated with the second step. A series of stopped-flow pH jump experiments were conducted with WT hC*c* and the respective variants in the 40-57 and 71-85 Ω-loops. Upon mixing WT hC*c* at pH 7 with buffer solutions of higher pH value, optical transitions were observed consistent with those reported previously for eC*c* and hC*c* (Karsisiotis et al., 2016). In the pH range 7-10, the WT variant proteins displayed

a single spectral transition, in which the Soret band is blue-shifted (Figure 5.7A) and the 695 nm band bleached. This transition comprises a single exponential phase (inset to Figure 5.7A), the rate constant of which (k_{obs1}) increases with increasing pH (Figure 5.7B). This behaviour is shown in Figure 5.7B, in which, for clarity, log k_{obs1} is plotted as a function of pH. Assuming that the de/protonation of the trigger group is rapid, then the model in Scheme 5.2 yields equation 5.2 thus relating k_{obs1} to K_{a1}, k_{f1} and k_{b1}.

$$k_{obs1} = k_{b1} + k_{f1}\left(\frac{K_{a1}}{K_{a1}+H^{+}}\right) \qquad (5.2)$$

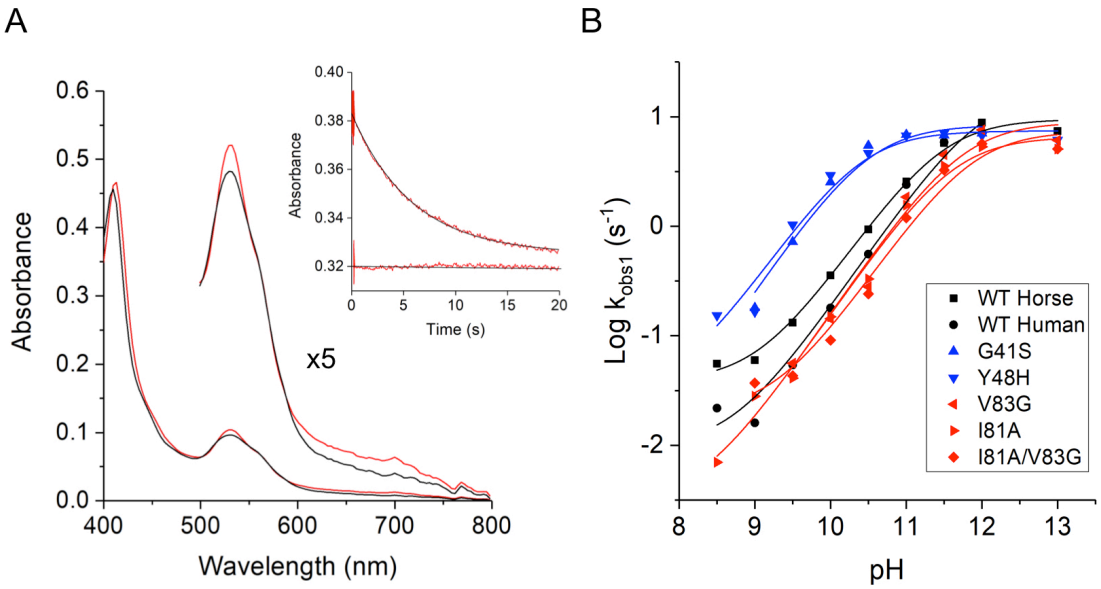

Figure 5.7 pH jump kinetics of the slow phase of ferric mammalian C*c* and variants. **A**) Optical spectral transitions observed using stopped-flow spectroscopy upon mixing oxidising WT hC*c* (pH 7) with an equal volume of pH 10 buffer. The ferric hexa-coordinate form (state III) at t = 2.5 ms is represented by the black line, whereas the hexa-coordinate alkaline form (state IV) at t = 20 s is represented by the red line. The spectral region between 500 – 800 nm has been magnified five-times. Inset) A typical reaction time-course stopped-flow trace at 420 nm (red) together with the corresponding fit to a single exponential function (black line) with residuals of the fit shown. **B**) The pH dependence of k_{obs1} for the slow phase of the alkaline transition. The lines are fits to the logarithmic transformation of equation 5.2 to yield the pK_{a1} of the trigger group. Taken from (Deacon et al., 2017).

This equation dictates that k_{obs1} follows a simple titration curve, in which k_{obs1} takes the value k_{b1} at low pH and $k_{b1} + k_{f1}$ at high pH values. k_{obs1} therefore increases with pH. The data plotted in Figure 5.7B has been fitted to equation 5.2, yielding the pK_{a1} value of the trigger (Table 5.2). In the case of the 71-85 Ω-loop variants, the pK_{a1} values are comparable to WT hC*c* and eC*c* (Table 5.2). eC*c* was used as a control, due to the extensive pH jump kinetic literature with this protein.

Table 5.2 Kinetic parameters determined by stopped-flow pH jump experiments

	WT hC*c*	**WT eC*c***	**G41S**	**Y48H**	**I81A**	**V83G**	**I81A/V83G**
pK_{a1} (Trigger)	11.97 ± 0.41	11.46 ± 0.08	10.51 ± 0.11	10.39 ± 0.17	11.62 ± 0.14	11.74 ± 0.24	11.85 ± 0.20
k_{fl}	17.01 ± 13	9.46 ± 1.19	8.37 ± 1.32	7.4 ± 1.33	6.53 ± 1.6	8.91 ± 3.36	7.34 ± 2.46
k_b	0.0096 ± 0.0059	0.038 ± 0.0068	0 ± 0	0.029 ± 0.053	0.003 ± 0.0025	0.0012 ± 0.028	0.02 ± 0.01

The disease variants G41S and Y48H are however, distinctly different, with pK_{a1} values lower by > 1 pH unit (Table 5.2). Therefore, one may conclude that the mutations in the 40-57 Ω-loop strongly influence the de/protonation behaviour of the trigger, whereas the mutations in the 71-85 Ω-loop do not. Furthermore, as the lowered pK_{a1} values of the disease variants are reflected in the in the pK_a of the alkaline transition (Table 5.1), one may conclude that in all variants the value of K_c is essentially unchanged. k_{fl} values may be determined to a reasonable degree of accuracy (Table 5.2) from the data in Figure 5.7B. The k_{fl} value determined for eC*c*, under the experiential conditions employed, correlate well with values previously reported. The k_{fl} values of the WT hC*c* and variant proteins are all of the same order of magnitude to that of the eC*c* (Table 5.2). Values of k_{b1} are not reported, as these are small and in the case of the WT protein and 71-85 Ω-loop variants measured from small amplitude changes at the end of the titration, and in the case of the disease variants G41S and Y48H, derived from extrapolation of the data to pH values far lower than explored in the experimental data set.

5.3.6 Kinetics of the alkaline transition above pH 10 for the 40-57 and 71-85 Ω-loop variants

At pH values > 10, a second rapid phase was observed for the WT protein and all variants, consistent with previous reports for both eC*c* and hC*c* (inset to Figure 5.8). The rate constant k_{obs2} is associated with the formation of a transient spectrum characteristic typical of a high-spin ferric haem species, with both a prominent band at 600 nm and possessing long wavelength features that obscure the bleaching of the 695 nm band at certain pH values (Figure 5.8). Thereafter, the spectrum decays to the final low-spin spectrum characteristic of C*c* in the alkaline conformation, in which Met80 is replaced by a Lys as the hexa-coordinate ligand (Figure 5.8). Significantly, the high-spin intermediate is populated to a greater extent in the disease variants G41S and Y48H than in the WT protein. Furthermore, for all proteins studied, the rate constant k_{obs2} was also found to be pH dependent (Figure 5.9A and B). In the case of WT hC*c*, k_{obs2} decreases with increasing pH in the range 10 to 11.5, taking values close to those of eC*c* (Figure 5.9A). Scheme 5.3 represents this behaviour and has been attributed to arise from a coupling between a conformational change that exposes a group that then undergoes deprotonation leading to the stabilisation, or facilitation, of the high-spin haem species.

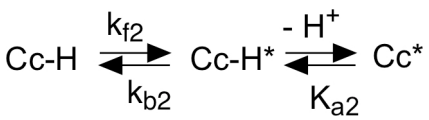

Scheme 5.3

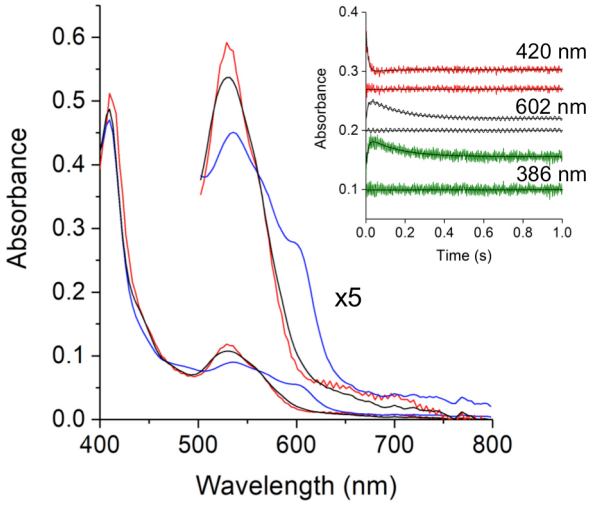

Figure 5.8 pH jump kinetics of the fast phase of the Y48H variant of hC*c* at pH > 10.5. Optical spectral transitions observed using stopped-flow absorption spectroscopy upon mixing ferric Y48H hC*c* (pH 7) with an equal volume of pH 11 buffer. The red line represents the ferric hexa-coordinate protein (state III) at t = 3.5 ms, the blue line represents the high-spin penta-coordinate form at t = 36 ms and the red line represents the final hexa-coordinate alkaline form (state IV) at t = 1 s. The spectral region between 500 – 800 nm has been magnified five-times. Inset) reaction time-courses of stopped-flow traces at three wavelengths with the residuals of the corresponding fit to a double exponential function shown. Taken from (Deacon et al., 2017).

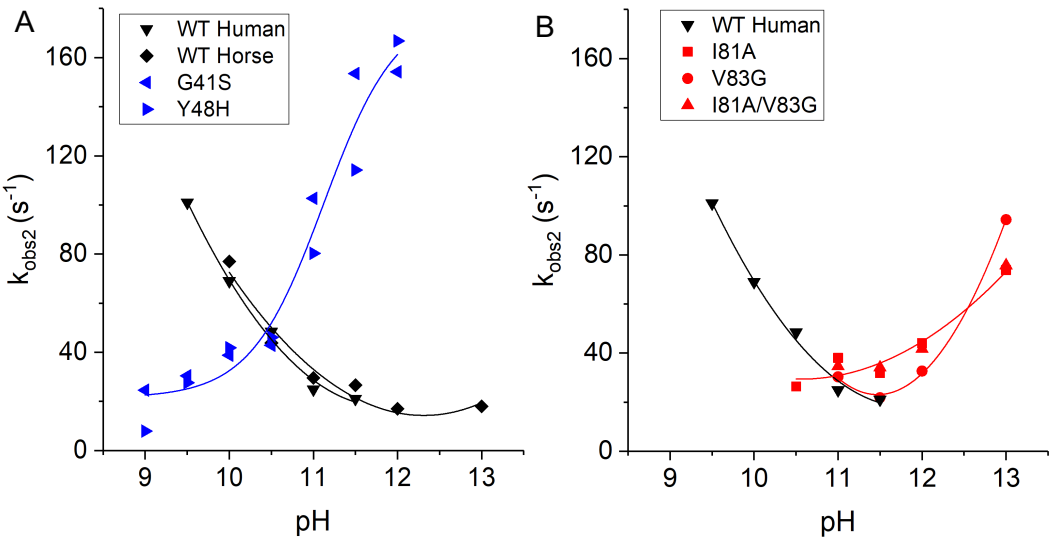

Figure 5.9 The pH dependence of k_{obs2}. **A)** The k_{obs2} values for WT hC*c*, WT eC*c*, the G41S and Y48H variants **B)** and the 71-85 Ω-loop variants, plotted as a function of pH. The lines through the data points for hC*c*, eC*c* and the 71-85 Ω-loop variants is to indicate the trends in the data. The blue line in **A)** is a fit to a one-proton ionisation equilibrium equation to yield an apparent pK_a. Taken from (Deacon et al., 2017).

In Scheme 5.3 C*c*-H and C*c*-H* represent the buried and exposed group of C*c* and C*c** the deprotonated high-spin haem species. The conformational transition in which the group in C*c*-H* is exposed, is proposed in the discussion to be the conformational change from hexa- to penta-coordinate haem. Equation 5.3 may be derived from Scheme 5.3 enabling the relation of k_{obs2} with k_{f2}, k_{b2} and K_{a2} for the formation of the high-spin haem species.

$$k_{obs2} = k_{f2} + k_{b2}\left(\frac{H^+}{(K_{a2}+H^+)}\right) \qquad (5.3)$$

Consistent with observations from WT hC*c* and eC*c* in Figure 5.9A, equation 5.3 predicts that k_{obs2} is inversely related to pH. Although the experiential data are inadequate to provide a clear pK_{a2}, estimates of ≤ 10 may be confidently surmised. In contrast, the disease variants G41S and Y48H behave differently, in that k_{obs2} for the production of the high-spin haem species increases with pH and is readily observed at pH values > 10 (Figure 5.9A). These data, when fitted to equation 5.3, yield a pK_{a2} of 11.1 ± 0.2 for the exposed group (C*c*-H* in Scheme 5.3). When interpreted together, these data imply that it is deprotonation before the conformational change that leads to dissociation of the Met80 ligand from the haem iron, hence the mechanism, at least in terms of intermediates on the pathway (or their order), is different to that of the WT protein.

In contrast, the 71-85 Ω-loop variants show different behaviour in k_{obs2} compared to either the WT protein, or the disease variants G41S and Y48H. Firstly, from pH values 7 to 10 there is no observable high-spin haem species, likely attributable to a low population and hence a low signal amplitude. Secondly, at pH values > 10.5, the high-spin haem species for the 71-85 Ω-loop variants is detected with values of k_{obs2} increasing with pH, up to pH 13 (Figure 5.9B). This pattern is also observed for WT hC*c* and it is suggested in Figure 5.9A, that this might also be the case for eC*c* at pH values > 13. Considering the high pH at which the increase in k_{obs2} is observed, it is likely that the process though which a high-spin haem species is generated is related to a more general denaturation of the protein and will therefore not be discussed further.

5.3.7 EPR spectroscopy to quantify the population of high-spin species

In order to verify that the intermediate observed through pH jump experiments was indeed a high-spin species, EPR experiments were conducted. Y48H was used for the EPR experiments, as based on the optical spectroscopy, the 40-57 Ω-loop variants populate a greater fraction of high-spin species. At pH 7, slow freezing the Y48H variant produces a high-spin haem species (g_1 = 6.03, g_2 = 5.67), that is not present when preparing the sample through a RFQ approach (Figure 5.10A and B). Additionally, there are intensity differences in the low-spin ferric haem signals (g_1 = 3.05, g_2 = 2.23) in the slow frozen and RFQ samples. These results demonstrate the effect different freezing regimes, either slow or fast, have on the quantities of quenched species in the frozen samples, that when in the liquid phase exist in dynamic equilibrium prior to freezing. The RFQ of the Y48H variant at 50 ms after the pH 7 – 11 jump results in an EPR spectrum with notable intensity of the high-spin ferric haem signal (g_1 = 3.10, g_2 = 5.76) and a significantly decreased low-spin ferric haem signal, as can be seen from its g_1 = 3.10 component (Figure 5.10B and C). In order to determine the absolute concentration of the high-spin species formed in the RFQ pH 11 sample (84 μM, Figure 5.10C), estimates were made using the Cm-C*c* calibration experiment. This concentration, 84 μM, constitutes ~ 42 % of the total haem concentration in the Y48H variant and therefore in general agreement with estimates made from the optical experiments.

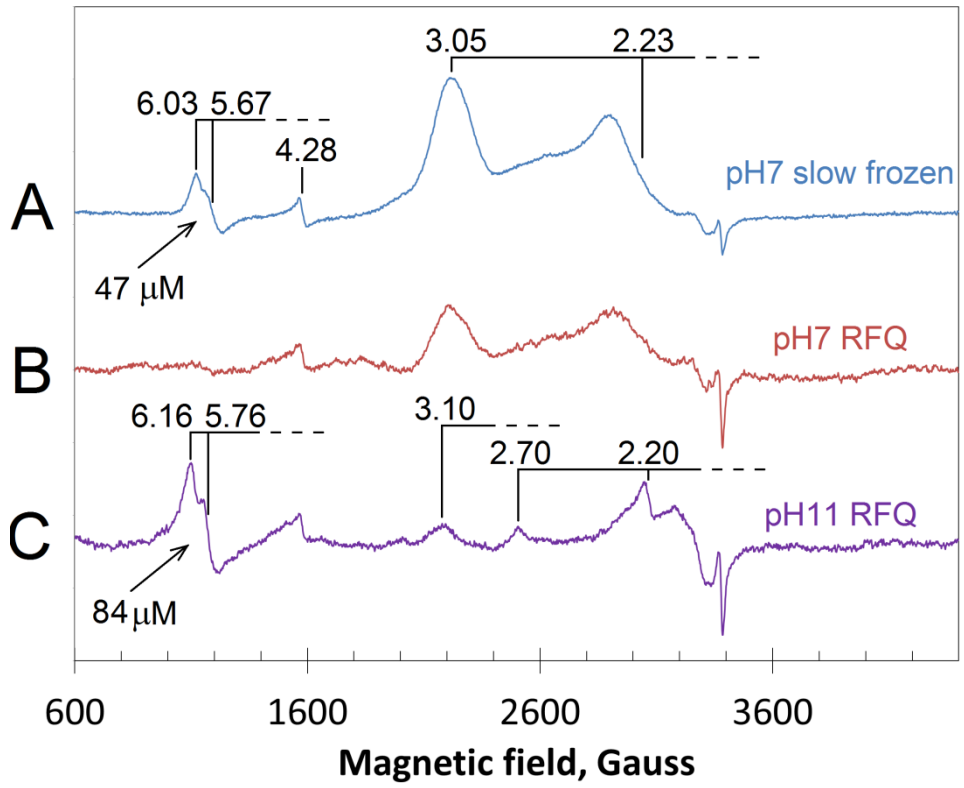

Figure 5.10 The effect of pH jumping from pH 7 to pH 11 on the low-spin and high-spin ferric haem states in the Y48H variant of hC*c* as determined by EPR spectroscopy. The final concentration of protein after mixing was 200 µM. **A**) EPR spectrum generated when protein (pH 7) is mixed with an equal volume of pH 7 buffer, followed by slow freezing. **B**) EPR spectrum generated when protein (pH 7) is mixed with an equal volume of pH 7 buffer, followed by RFQ at 50 ms. **C**) EPR spectrum generated when protein (pH 7) is mixed with an equal volume of pH 11 buffer, followed by RFQ at 50 ms. The concentration of the high-spin ferric haem form (indicated in the figure) was estimated from comparison with the acid-alkaline transition of the high-spin and low-spin forms in CM-C*c*. EPR spectra were measured at 10 K. To make all three spectra directly comparable, spectrum A was multiplied by a factor of 0.45 to account for imperfect packing of the freeze-quenched icicles in the EPR tubes.

5.4 Discussion

The production of the 81 and 83 variants of hC*c* result in a homologous 71-85 Ω-loop to that of yeast iso-1 C*c* and the hypothesis was that the steric factors within this loop which act to suppress peroxidase activity in WT hC*c* would diminish, thus enhancing peroxidase activity comparably to that of yeast iso-1 C*c*. On the contrary, the data presented in this Chapter demonstrate a minimal increase in peroxidase activity for both the single and double 71-85 Ω-loop variants (Figure 5.6A). Significantly and rather surprisingly, the double variant I81A/V83G is less peroxidase active than the single I81A variant, suggesting that replacing Val83 with the smaller side chain volume of a Gly residue compromises the peroxidatic conformer in the absence of Ile81. The picture is somewhat different in the presence of CL, as the compromising role of Gly83 is somewhat relieved in the double variant (Figure 5.6A), suggesting that there are differences in the peroxidatic conformer formed in the absence and presence of CL. Nevertheless, it is clear from the results obtained with the 71-85 Ω-loop variants that the enhancement in peroxidase activity, in relation to WT hC*c*, is minimal compared with the disease variants in the 40-57 Ω-loop. The disease variants G41S and Y48H, must therefore have higher concentrations of the oxidised proteoforms that give rise to peroxidase activity in C*c*. In contrast to the conclusion of Bowler and colleagues, the suggestion from the data presented in this Chapter is that in the case of hC*c*, it is not the side chain bulk at residues 81 and 83 in the 71-85 Ω-loop that is responsible for regulating the peroxidase active conformers, but instead the 40-57 Ω-loop which acts to regulate H_2O_2 access to the haem.

As mentioned in Chapter 4 and the above introduction to Chapter 5, determining the pK_{695} value and the use of kinetic experiments to monitor the binding of exogenous ligands, such as N_3^- to ferric C*c* are generally considered to provide

information on the stability/lability of the Fe(III)-S(Met80) bond. Furthermore, interpretation of peroxidase activity in absence of CL may also inform on these phenomena. To that end, the trend in pK_{695} values (V83G > I81A/V83G > I81A = WT) is consistent with the observed peroxidase activity, in which the local stability of the Met80 ligand correlates with the I81A variant being the most peroxidase active form of the 71-85 Ω-loop variants. Alternatively, it is also possible to say that based on the higher pK_{695} values, that there is a greater stabilisation of state III relative to state IV of the aforementioned variant order. The N_3^- binding stopped-flow kinetic studies have yielded both affinities for N_3^- binding and Met80-off rates (k_1), both of which follow the same trend (I81A/V83G > I81A > V83G = WT). This suggests that the double variant has greater Met80 lability and possibly, more readily able for N_3^- to bind ferric haem, whereas the V83G variant is identical to the WT protein. These stopped-flow N_3^- binding results are clearly contradictory to the trend observed in both the peroxidase activity assays and the pK_{695} values, instead adhering to the hypothesis that removing steric bulk at the 81 and 83 positions facilitates ligand binding due to conformational space for the Met80 ligand to move out of the way. The contradiction between the N_3^- binding kinetics and the peroxidase activity/pK_{695} experiments suggests that whilst they are probing stability/lability of the Met80 ligand, there must inherently be other underlying processes at play, which deepening on the type of experiments employed can affect the experimental result.

In order to provide a complete mechanistic description of both the pH dependencies of the equilibrium and kinetic parameters governing the transitions in hC*c* and the variants reported in this Thesis, a model that incorporates a sufficient number of steps is required. In this case, there must be a minimum of two "fast" de-protonation steps, one for the "trigger" group and one for the transition yielding the

high-spin species, additionally a conformational equilibrium between the hexa- (Met80-on) and penta-coordinate (Met80-off) forms. A further complication, is that additional Lys ligation must be considered, in order to yield the final alkaline form(s) (state IV). The simplest model that satisfies these requirements, yet consistent with Schemes 5.2 and 5.3 is shown in Figure 5.11. In this model, the various forms of hC*c* are located at the corners of a cube, the edges of the back and front faces of the cube reflect the protonation/de-protonation equilibria. The horizontal and vertical edges refer to the "trigger" and the second group responsible for the appearance of the high-spin form respectively (Figure 5.11).

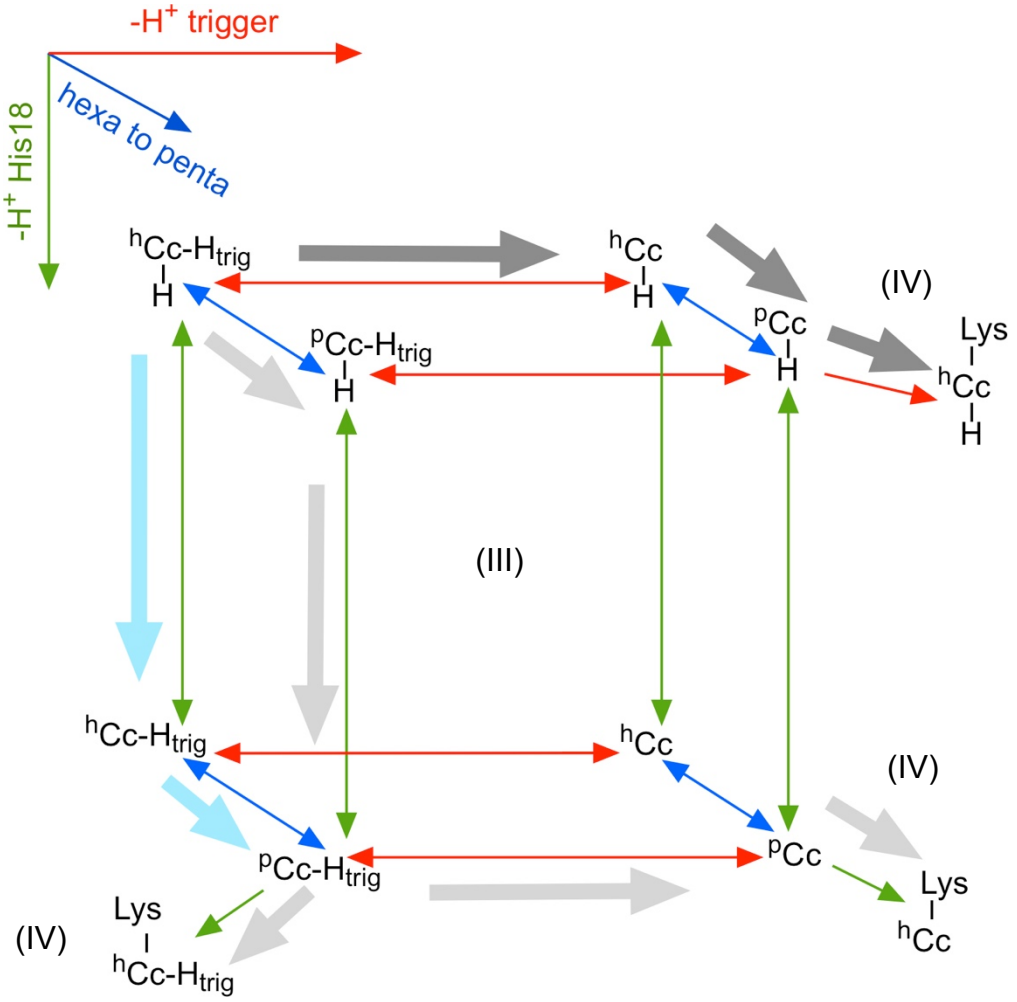

Figure 5.11 The mechanistic pathways linking de-protonation and conformational changes in hC*c*. Two de-protonation events are represented by the three dimensions of the cube, relating to the "trigger" and another group, possibly His18, respectively and a conformational change leading to Met80 dissociation. The penta-coordinate forms (^{p}C*c*) are shown on the front face of the cube and can in principle bind an amino group donated by a Lys. Likely routes through the framework are indicated by the larger grey and silver arrows for the WT protein and the 71-85 Ω-loop variants, whereas the pale blue arrows depict the route for the 40-57 Ω-loop variants to populate the ^{p}C*c*-H$_{trig}$ species, which proceeds to follow the silver arrows. Optical states III and IV represented by (III) and (IV) respectively.

The conformational equilibria are represented by the edges linking the back to the front face of the cube, possibilities for Lys binding to the penta-coordinate face are also indicated (Figure 5.11). In the case of WT hC*c*, starting in state III (back left-hand corner of the cube) where both ionisable groups are protonated and the protein hexa-coordinate, Scheme 5.2 is represented by the grey arrows in which deprotonation of the trigger precedes conformational change to a penta-coordinate form (H-^{p}C*c*), subsequently binding Lys. All variants studied follow this pathway, the pK_{trig} however, is variant dependent, which in the case of the disease variants G41S and Y48H is lower (Table 5.2). The experimentally observed high-spin haem species results from a conformational change preceding deprotonation (Scheme 5.3). Within the cube, this scheme is depicted by the silver arrows, where the suggestion from N_3^- binding experiments (Karsisiotis et al., 2016) is that a minor population of the penta-coordinate form at pH 7 (H-^{p}C*c*-H_{trig}) is stabilised by deprotonation of the second group. Therefore, the observed high-spin from is either, or both, ^{p}C*c*-H_{trig} or ^{p}C*c*, both of which decay through lysine ligation (Figure 5.11). In the case of the 71-85 Ω-loop variants there is no deviation from this mechanism and therefore, the residue volume at the 81 and 83 positions does not alter this ionisation process and furthermore, the route through the cube which can lead to the high-spin species. In the case of the disease variants G41S and Y48H, a contrasting picture emerges, in which the pH dependence of k_{obs2} reflects a mechanism in which deprotonation precedes conformational change (Figure 5.9A). In order to explain this behaviour consistently with the model shown in Figure 5.11, one would presume that the same "trigger" group is involved, however, as the value of pK_{a2} is 11.1 and therefore rather higher than the pK_{trig} determined for the G41S and Y48H variants (Table 5.2), this seems rather unlikely. Furthermore, it is particularly complicated to produce a model in which a single "trigger" group can be

simultaneously responsible for two apparently quite different transitions, namely the slow (alkaline transition) and fast (formation of high-spin species) processes.

Following from this view, one is forced to conclude, if matters are not further complicated than already defined in the model shown in Figure 5.11, that in the case of the disease variants G41S and Y48H, it is the enhanced dynamics that make the second group available for deprotonation. In this situation, the series of events follows that the initial step takes H-^{h}C*c*-H_{trig} to ^{h}C*c*-H_{trig} (pale blue arrows in Figure 5.11), the subsequent conformational change then leads to the generation of the penta-coordinate high-spin haem species that is experimentally observed (Figure 5.11).

As the cube has been devised to depict the kinetics of the alkaline transition and how the respective populations of the various states may occur as a result of deprotonation events and conformational changes, the question arises, what are the titratable groups responsible for the alkaline transition and transition to the high-spin haem state? Considering firstly the alkaline transition, characterised by the substitution of Met80 by a Lys residue with an apparent pK of ~ 9. As previously explained, there is titration of a group which leads to a conformational change and the subsequent dissociation of Met80. Furthermore, from consideration of the disease variants G41S and Y48H, it becomes apparent that mutation in the 40-57 Ω-loop increases the dynamics not only locally within the loop, but also confers greater dynamics within the 71-85 Ω-loop, which significantly leads to a reduction in the pK_a of the trigger. Several possibilities regarding the nature of the trigger have been extensively discussed in the literature and whilst the work reported in this Chapter does not definitely answer the question, the results are illuminating as to the properties of the trigger and perhaps more significantly, how these properties relate to the mechanism of the alkaline transition, as depicted in Figure 5.11. Solomon and colleagues (Kroll et al., 2014, Mara et al.,

2017) have suggested that the strength of the Met80-Fe(III) bond is enhanced through an entatic contribution of the polypeptide, that is derived from a H-bonding network that includes the hexa-coordinate Met80, Tyr67/wat166, Asn52, Thr78 and, as proposed by the work in this Chapter, HP-7. An appealing concept therefore, is to suggest that a single deprotonation event from within the linked H-bond network has a disrupting influence, in which the Fe(III)-S(Met80) bond is weakened. It follows that due to the H-bond nature, the pK_a of this deprotonation event is high and in the context of the disease variants G41S and Y48H, substitution in the 40-57 Ω-loop alters the H-bond network to HP-7 and Asn52, in which the pK_a of the stabilising unit is lowered and hence the measured pK_a of the trigger and the pK_a of the alkaline transition.

Interestingly, evidence has been presented which suggests that the alkaline coordinating Lys79 is in fact itself the trigger group. Lys79 differs from Lys73 (the other alkaline hexa-coordinate ligand) as a H-bond exists between itself, the backbone carbonyl of Ser47 and its side chain Nε amine. The result of this H-bonding is not only a stabilising influence, but also a link is formed between the 40-57 and 71-85 Ω-loops. Furthermore, the pK_a of the Lys79 amine could be raised to ~ 12 and therefore in agreement with the experimentally determined pK_a of the trigger (Table 5.2). Deprotonation of the H-bonded amine group may influence the dynamics of the Ω-loops, in which the propensity to dissociate the Met80 ligand is enhanced. The deprotonated Lys79 can now act as a coordinating ligand to ferric haem. In this framework mutations in the 40-57 Ω-loop, i.e. the disease variants G41S and Y48H, that alter the H-bond pattern and themselves enhance the dynamics of the Ω-loops result in the disruption of the H-bond between Lys79 and the carbonyl of Ser47. This in turn leads to the drop in the pK_a of the Lys, which is reflected in the lower trigger pK_a of the G41S and Y48H variants (Table 5.2). Deprotonation of the proximal His18

has also been suggested to be the trigger group (Gadsby et al., 1987), however, whereas this theory cannot be discounted, a more plausible explanation consistent with the data reported in this Chapter arises by retaining this group for consideration as the titratable group reasonable for the second deprotonation step which leads to the formation of the high-spin species (*vide infra*).

Both the optical and EPR spectroscopy experiments demonstrate that at pH values > 10 a high-spin haem species is indeed present. The kinetic data presented in Figure 5.9B and Scheme 5.3 fully supports the conclusions of Englander and colleagues, who suggested that transition to the high-spin species proceeds via the exposure of a hidden group through a conformational change. Upon deprotonation of this hidden group, a high-spin haem species is formed that subsequently decays by Lys coordination. The conformational change which exposes the hidden group is unknown. However, for simplicity and because one desires to stabilise a high-spin form, it is suggested that the conformational transition seen in the WT protein leads to the dissociation of the Met80 ligand (Figure 5.11). It is this conformational change in which a penta-coordinate high-spin species is formed in the WT protein and is the basis of interpretation for ligand binding, e.g. N_3^- and perhaps H_2O_2 binding to ferric C*c*. Following from this proposoal, dissociation of the Met80 ligand exposes a group which, once deprotonated, stabilises the high-spin species as depicted by the silver arrows in Figure 5.11.

Gadsby and colleagues have proposed through the use of EPR and MCD experiments that the proximal haem ligand His18 has a pK_a of 11 when the ferric protein-haem ligation is hexa-coordinate (His18/Met80) (Gadsby et al., 1987). It is noted that deprotonation of this group has a powerful *trans* effect on the Fe(III)-S(Met80) bond leading to Met80 dissociation and the subsequent formation of the

penta-coordinate form. The work reported in this Thesis proposes a reciprocal argument, namely, that the Met80 association/dissociation equilibrium in the native state leads to the population of a penta-coordinate form, in which the pK_a of His18 is lower. Thus, the mechanism depicted in Scheme 5.3 and Figure 5.11 proceeds via dissociation of Met80 and the stabilisation of the resulting high-spin species through deprotonation of the proximally coordinated His18, with a pK_a now lowered to ~ 9 for the WT protein and the 71-85 Ω-loop variants (Figure 5.9). In the disease variants G41S and Y48H the mechanism is changed, in which direct deprotonation of the proximally coordinated His18 precedes Met80 dissociation (Figure 5.9A). Following from the work presented in this Chapter it is proposed that mutations in the 40-57 Ω-loop which introduce hydrophilic/protonatable groups facilitate water access to the proximal His18. Furthermore, Bowler and colleagues have illustrated structurally that a non-native state of C*c* can generate a water channel involving the 40-57 Ω-loop and confer access to the proximal His18 (McClelland et al., 2014). This view of dynamic access to the proximal His18 is supported by the NMR work presented in Chapter 4 (Karsisiotis et al., 2016, Deacon et al., 2017). Such direct deprotonation of the His18 in the hexa-coordinate His/Met state would yield a pK_a of 11 (Gadsby et al., 1987), in keeping with the observed pK_{a2} for the G41S and Y48H variants.

Chapter 6

Conclusions and future work

6.1 Conclusions

6.1.1 Backbone resonance assignments of WT and Y48H hCc

The backbone NH resonance assignments of WT hC*c* were determined under aqueous and DMSO conditions, in addition, the backbone NH resonance assignments were determined for the Y48H variant under aqueous conditions. The assignments determined under aqueous conditions allowed the cH/D exchange and ^{1}H-^{15}N relaxation experiments to be interpreted in a sequence specific context, providing insight into both the global and local dynamics of both proteins (Karsisiotis et al., 2016, Deacon et al., 2017). Whereas the assignments determined for the WT protein under acid denatured DMSO conditions enabled the sequence specific interpretation of the iH/D exchange experiments.

6.1.2 Interrupted Hydrogen/Deuterium exchange methodology

Despite numerous attempts and optimisation experiments, the goal of developing a solution-based NMR technique capable of providing salient structural information on soluble protein/phospholipid interactions was ultimately unsuccessful. An inability to preserve the exchange state throughout the protein was a persistent issue, in which it was only for the very slow exchanging residues, in DMSO, for which exchange data could be followed. Furthermore, fundamental issues were encountered working with the hC*c*/CL complex, as it is essential that the intact complex transition from a protonated environment, to a deuterium rich environment without any disruption to the complex so as to not generate a "masking" free protein exchange profile. As a result of the issues encountered, it was not possible to determine quantitative, or qualitative binding site information on the WT hC*c*/CL interaction. If this method is to be explored further, it would be beneficial to utilise re-protonation

protocols, for the greater control conferred over the exchange conditions and the lower material costs. Furthermore, it would be beneficial to re-assign the WT DMSO HSQC spectra under less acidic conditions, so as to facilitate assignment mapping to the iH/D exchange samples.

6.1.3 Dynamics of the disease variants G41S and Y48H

The cH/D exchange, ^{15}N T_1, T_2 and [^1H]-^{15}N NOE relaxation experiments, CD, UV-visible, stopped-flow and EPR spectroscopies, in addition to the ABTS peroxidase activity assays all provide a consistent and coherent picture of the dynamic and functional differences between the WT protein and disease variants of hC*c*. This work has demonstrated how simple substitution mutations in hC*c* result in reduced global stability and a lower pK_{695}. The reduced stability and increased Met80 lability is reflected strongly in the NMR cH/D exchange and relaxation experiments, which demonstrate both enhanced global dynamics, but also the local dynamics in the 40-57 (site of mutations) and 71-85 (site of Met80 haem ligand) Ω-loops.

The stopped-flow spectroscopy presented in this Thesis has demonstrated how the disease-causing substitutions (G41S and Y48H) result in an increased Met80 off-rate, which, when correlated with the lowered pK_{695} values, confers an increased N_3^- binding affinity and binding rate due to an increased fraction of penta-coordinate haem under physiological conditions (Karsisiotis et al., 2016, Deacon et al., 2017).

Despite the comparable initial clinical characteristics reported (De Rocco et al., 2014) between G41S and Y48H hC*c*, the biochemical and biophysical properties of the Y48H variant are more extreme than that of the G41S variant (Deacon et al., 2017). In the context of the direct peroxidase activity measurements, it is clear that interaction

with CL is no longer a rate-limiting factor for the Y48H variant, a unique feature of all proteins reported in this Thesis.

6.1.4 The role of Ω-loops in the alkaline transition

The CD, UV-visible and stopped-flow spectroscopy experiments have demonstrated that mutation around the haem crevice of hC*c* does not perturb the global stability of the protein. Instead, the stopped-flow spectroscopy experiments suggest that there are local increases in dynamics within the haem crevice, in which the hexa-coordinate haem ligation is influenced. The increased haem crevice dynamics are proposed to result in both the greater N_3^- binding rate and binding affinity observed in the 71-85 Ω-loop variants than that of the WT protein. However, it is clear that as the global stability of the protein is not significantly reduced, as evident with the disease variants G41S and Y48H, that the haem crevice mutations influence haem dynamics and peroxidase activity to a far milder extent than that of the disease variants. Furthermore, pH jump experiments with both the 40-57 and 71-85 Ω-loop variants have provided further insights into the mechanism behind C*c* peroxidase activity, in which the disease variants G41S and Y48H have been shown to alter the p*K* of the trigger group, whereas the steric variants do not. The body of work reported has highlighted how the hexa-coordinate Met80 ligation is more strongly influenced through the dynamics of the 40-57 Ω-loop, than the local dynamics in the 71-85 Ω-loop.

6.1.5 Conclusions

Ultimately, the work reported in this Thesis has demonstrated how the 40-57 and 71-85 Ω-loops are dynamically linked. It is clear that gross tertiary structural

changes are not present in the disease variants of hC*c*, with structures virtually identical to that of the WT protein. Instead, this work proposes that heightened dynamics in the 40-57 Ω-loop confer heightened dynamics in the 71-85 Ω-loop, which in turn confer greater Met80-Fe(III) bond lability. Met80 is the critical hexa-coordinate haem ligand, which when dissociated, unlocks the haems peroxidase potential. Therefore, it is not structural changes that are responsible for hC*c* related disease, but instead, heightened dynamics in the cooperatively likened Ω-loops which dynamically alter the haems hexa-coordinate ligation.

6.2 Future work

With the recent discovery of the A51V variant of hC*c*, the next logical step in the C*c*/CL research would be to biochemically and biophysically characterise this variant, as has been conducted with the G41S and Y48H variants reported in this Thesis. The discovery of A51V in itself further supports the argument presented in this Thesis that there is cooperativity between the 40-57 and 71-85 Ω-loops, however, it is important to determine the effects of this mutation on hC*c*, which would perhaps lead to increased precision regarding which part of the 40-57 Ω-loop is most responsible.

As the Y48H variant peroxidase activity appears to not be rate-limited by CL, creating double variants (G41S/Y48H, G41S/A51V, Y48H/A51V) and a triple variant of G41S/Y48H/A51V would be interesting to determine whether the effects on global stability are additive.

^{15}N T_1, T_2 and [^{1}H]-^{15}N NOE relaxation experiments should be conducted on the 71-85 Ω-loop variants of hC*c* (I81A, V83G and the double variant I81A/V83G), as this would provide insight into the, currently speculative, local haem crevice dynamic increases that are proposed in Chapter 5. Furthermore, the high-spin intermediate

partially characterised in Chapter 5 could be probed further with the use of stopped-flow FT-IR spectroscopy. The aim of the FT-IR experiment would be to determine whether the high-spin intermediate observed through high pH jump stopped-flow kinetic experiments is associated with the Histidine to Histidinate transition. Preliminary FT-IR experiments through collaboration with Dr Joseph Wright (University of East Anglia) and Professor Mike Wilson (University of Essex) has provided a proof of concept. It is essential that deuterated solutions be used in order to observe the 1500 - 1550 wave number region where the high-spin intermediate is detected.

Due to the limited clinical and respiratory information available on the disease variants, electron transfer experiments by stopped-flow spectroscopy between C*c* and C*c*O would provide information on the respiratory impact of the aforementioned mutations. This information would not only provide insights into the primary biological impact of mutation (*i.e.* electron transfer), but also provide further information linking structure, dynamics and function. Preliminary work has been conducted by Mr Richard White (former Worrall group MSc Student) and Professor Mike Wilson, who have demonstrated that although electron transfer rates are largely unchanged, the access to non-native conformations influence the steady-state turnover of the C*c*/C*c*O complex.

Appendix A

Backbone NH and side chain C_α, C_β, CO and Hε resonance assignments of WT hC*c* under native state aqueous solution conditions and acid denatured in DMSO. Additionally, the Y48H variant under native state aqueous solution conditions.

Both sets of WT hC*c* resonance assignments have been deposited in the Biological Magnetic Resonance Databank under the accession numbers 25418 and 26973 for the aqueous and DMSO solution conditions respectively.

Table A.1 ^{1}H, ^{15}N, $^{13}C\alpha$ and $^{13}C\beta$ resonance assignments of WT hC*c* in native state aqueous solution conditions

	WT - Aqueous			
Assignment	**^{1}H (ppm)**	**^{15}N (ppm)**	**$^{13}C_{\alpha}$ (ppm)**	**$^{13}C_{\beta}$ (ppm)**
1Gly	---	---	40.34	---
2Asp	9.33	124.58	50.16	39.77
3Val	8.44	123.69	63.41	29.37
4Glu	7.97	120.43	56.50	25.91
5Lys	7.95	121.08	56.88	29.82
6Gly	8.53	107.06	43.87	---
7Lys	7.89	124.11	56.58	29.56
8Lys	6.81	117.07	56.91	29.12
9Ile	7.44	119.05	62.10	34.62
10Phe	8.33	120.50	59.72	36.76
11Ile	8.89	121.78	63.10	35.19
12Met	7.91	117.31	55.78	30.83
13Lys	8.46	112.48	54.00	31.54
14Cys	7.81	114.41	51.79	34.75
15Ser	7.99	116.41	59.70	60.85
	9.96		56.54	25.84
	Hε21 7.47	122.75		
16Gln	Hε22 6.74	Nε2 111.30		
17Cys	9.44	113.52	55.35	33.06
18His	10.81	118.41	74.20	24.25
19Thr	10.53	113.73	58.19	70.02
20Val	8.86	111.92	59.46	31.85
21Glu	---	---	54.43	27.64
22Lys	8.95	126.93	55.64	28.64
23Gly	9.32	117.91	42.67	---
24Gly	8.19	107.91	42.09	---
25Lys	8.71	118.95	53.58	30.74
26His	8.75	122.15	53.67	28.08
27Lys	8.04	126.12	52.53	29.40

28Thr	---	---	63.45	66.06
29Gly	7.09	103.40	34.50	---
30Pro	---	---	57.62	26.86
31Asn	11.60	127.49	53.50	38.45
32Leu	9.49	122.12	51.68	41.68
33His	8.01	120.30	58.04	25.99
34Gly	8.87	115.23	43.18	---
35Leu	6.99	117.13	55.36	41.58
36Phe	8.58	112.52	57.55	34.23
37Gly	8.81	111.04	42.22	---
38Arg	8.00	123.65	52.35	30.64
39Lys	8.01	122.35	53.06	30.92
40Thr	7.45	109.73	58.69	66.01
41Gly	8.97	109.34	43.07	---
	7.63		51.72	27.26
	Hε21 7.32	113.00		
42Gln	Hε22 6.81	Nε2 113.85		
43Ala	8.05	125.77	49.04	15.68
44Pro	---	---	---	---
45Gly	8.87	115.01	43.08	---
46Tyr	6.70	119.37	54.27	36.04
47Ser	6.50	122.63	53.08	58.53
48Tyr	7.50	124.58	55.38	38.78
49Thr	9.54	112.89	59.57	68.63
50Ala	8.70	124.93	52.44	14.42
51Ala	7.87	117.65	52.49	16.20
52Asn	8.46	117.27	52.44	37.39
53Lys	8.48	121.26	56.71	29.60
54Asn	8.12	112.79	50.38	36.10
55Lys	6.89	121.50	55.63	27.54
56Gly	7.71	103.22	44.24	---
57Ile	6.39	110.47	54.77	38.23
58Ile	8.10	119.19	55.99	35.44

	8.56	130.60	54.35	27.23
59Trp	Hε1 9.40	Nε1 125.31		
60Gly	7.59	111.23	41.63	---
61Glu	9.45	120.50	59.15	26.69
62Asp	8.23	115.32	54.47	36.90
63Thr	8.17	113.14	61.00	66.27
64Leu	8.42	120.47	55.47	39.34
65Met	7.61	118.97	55.33	28.16
66Glu	6.71	117.76	55.68	27.14
67Tyr	8.03	121.27	57.91	37.76
68Leu	7.94	110.86	52.78	38.37
69Glu	6.66	118.81	56.01	27.26
70Asn	6.57	105.19	49.61	34.85
71Pro	---	---	65.06	31.09
72Lys	9.35	11.71	56.61	30.02
73Lys	7.72	119.49	55.44	30.96
74Tyr	8.02	120.41	59.03	37.93
75Ile	9.35	114.82	56.89	35.52
76Pro	---	---	61.90	28.81
77Gly	9.29	111.74	42.08	---
78Thr	8.98	115.38	59.14	68.00
79Lys	8.18	122.99	52.59	29.05
80Met	9.18	123.25	62.19	4.09
81Ile	8.44	135.66	58.20	33.01
82Phe	9.04	126.34	56.42	38.73
83Val	8.06	126.87	62.43	29.18
84Gly	---	---	40.48	---
85Ile	7.80	120.25	56.67	36.53
86Lys	8.28	127.47	55.97	29.92
87Lys	8.16	120.26	54.22	29.95
88Lys	8.99	129.60	57.72	29.42
89Glu	9.20	118.00	57.12	26.15
90Glu	6.03	116.23	55.49	27.24

91Arg	7.03	116.92	58.29	28.57
92Ala	8.29	119.88	52.59	15.02
93Asp	7.90	121.98	55.41	36.79
94Leu	7.67	120.74	55.27	38.06
95Ile	8.37	119.57	63.55	34.84
96Ala	7.62	122.47	52.29	14.46
97Tyr	7.78	117.92	58.90	34.40
98Leu	8.61	118.77	54.96	38.76
99Lys	8.71	123.82	56.55	29.28
100Lys	6.60	116.85	55.32	30.61
101Ala	8.52	119.56	52.17	16.14
102Thr	7.78	102.04	59.54	67.05
103Asn	6.99	118.27	49.95	38.88
104Glu	7.32	125.06	55.38	28.49

Table A.2 ^{1}H, ^{15}N, $^{13}C\alpha$, $^{13}C\beta$ and ^{13}CO resonance assignments of WT hC*c* in acid-denatured dimethylsulfoxide solution conditions

WT - DMSO

Assignment	**^{1}H (ppm)**	**^{15}N (ppm)**	**$^{13}C_{\alpha}$ (ppm)**	**$^{13}C_{\beta}$ (ppm)**	**^{13}CO (ppm)**
1Gly	---	---	40.56	---	166.27
2Asp	8.67	118.71	50.05	36.87	170.75
3Val	7.94	114.99	58.42	30.70	171.29
4Glu	7.98	119.75	52.57	27.75	171.49
5Lys	7.86	117.21	52.36	31.44	176.10
6Gly	8.69	108.77	42.15	---	168.64
7Lys	---	---	52.80	32.22	172.02
8Lys	8.12	119.02	52.87	31.58	171.73
9Ile	7.73	116.18	57.18	37.46	171.41
10Phe	8.19	120.32	54.21	38.04	171.53
11Ile	8.19	117.61	57.76	37.23	172.03
12Met	8.76	121.35	53.84	34.19	173.16
13Lys	9.49	119.47	53.86	31.55	176.48

14Cys	8.04	117.69	53.06	27.46	172.25
15Ser	8.01	117.74	54.65	61.03	172.20
16Gln	8.62	120.72	53.10	29.56	171.21
17Cys	---	---	57.74	37.28	171.83
18His	8.50	121.25	53.01	33.14	172.19
19Thr	---	---	56.96	65.82	168.89
20Val	6.71	115.24	57.10	29.99	170.63
21Glu	7.34	119.32	51.98	27.08	171.03
22Lys	7.54	118.35	52.55	31.78	172.15
23Gly	8.14	106.00	41.34	---	---
24Gly	7.93	105.26	42.48	---	171.23
25Lys	8.16	117.70	52.97	31.61	172.06
26His	8.28	116.10	51.95	27.50	170.21
27Lys	8.08	118.80	53.20	31.67	172.32
28Thr	7.98	111.80	58.45	67.13	170.47
29Gly	7.88	105.92	41.99	---	169.60
30Pro	---	---	59.83	29.69	172.02
31Asn	8.22	116.51	50.15	37.24	171.64
32Leu	7.90	119.22	51.86	40.50	172.77
33His	8.17	114.85	52.59	27.10	170.67
34Gly	8.07	105.80	42.60	---	169.11
35Leu	7.91	118.50	52.63	41.27	172.22
36Phe	7.98	116.70	54.33	37.89	171.77
37Gly	8.14	105.81	42.50	---	169.07
38Arg	7.97	117.34	52.67	29.97	171.70
39Lys	8.16	119.16	52.95	31.41	172.19
40Thr	7.74	111.10	58.87	67.06	170.85
41Gly	8.04	107.05	42.63	---	169.10
42Gln	7.91	116.83	52.53	28.64	171.14
43Ala	8.15	122.22	46.84	17.26	173.10
44Pro	---	---	60.15	29.55	172.38
45Gly	7.98	104.21	42.46	---	168.96
46Tyr	7.80	115.95	54.48	37.35	171.81

47Ser	8.08	113.46	55.58	62.21	170.38
48Tyr	7.89	118.17	54.85	36.84	171.58
49Thr	7.87	111.05	58.53	67.11	170.11
50Ala	7.95	122.24	48.84	18.24	172.66
51Ala	7.98	119.30	48.88	18.19	172.73
52Asn	8.01	115.51	50.21	37.26	171.53
53Lys	7.89	117.39	53.00	31.31	171.91
54Asn	8.07	116.78	50.59	37.24	171.43
55Lys	7.86	117.35	53.07	31.37	172.19
56Gly	8.11	105.25	42.71	---	168.91
57Ile	7.64	115.50	57.24	37.19	171.30
58Ile	7.81	119.55	57.60	36.89	171.32
	7.91	121.53	53.97	28.22	172.06
	Hε1 10.74	Nε1			
59Trp		131.02			
60Gly	8.06	106.40	42.63	---	169.26
61Glu	7.98	116.46	52.55	27.96	171.74
62Asp	8.31	118.08	50.10	36.08	171.19
63Thr	7.63	111.05	58.89	66.83	170.33
64Leu	7.79	119.69	51.98	40.83	172.74
65Met	7.96	117.36	---	31.89	172.12
66Glu	---	---	---	---	---
67Tyr	---	---	51.75	40.49	---
68Leu	8.19	114.92	50.27	40.50	171.46
69Glu	8.05	119.47	59.14	32.28	171.56
70Asn	8.46	118.02	50.12	37.35	176.12
71Pro	---	---	60.32	29.63	172.07
72Lys	7.91	116.11	52.96	30.87	171.98
73Lys	7.65	116.45	50.14	31.66	171.39
74Tyr	---	---	---	---	---
75Ile	---	---	---	---	---
76Pro	---	---	59.93	29.80	172.60
77Gly	8.21	105.07	42.81	---	169.70

78Thr	7.63	110.46	58.90	67.08	170.45
79Lys	8.00	119.28	55.20	36.68	172.25
80Met	---	---	52.78	31.76	171.52
81Ile	7.70	116.34	57.78	37.21	---
82Phe	8.07	120.18	54.46	37.51	---
83Val	7.87	116.10	59.23	30.63	171.98
84Gly	8.05	108.23	42.92	---	169.75
85Ile	7.85	116.60	58.26	36.86	---
86Lys	8.12	121.39	53.94	31.10	---
87Lys	---	---	---	---	---
88Lys	---	---	---	---	---
89Glu	---	---	---	---	---
90Glu	---	---	53.09	27.58	---
91Arg	8.04	118.54	53.52	28.96	172.11
92Ala	8.05	120.82	49.55	18.14	173.38
93Asp	8.21	116.43	50.47	36.05	171.53
94Leu	7.82	118.52	52.63	40.87	173.09
95Ile	7.83	116.43	58.44	36.34	171.75
96Ala	7.89	122.36	49.79	17.99	173.05
97Tyr	7.76	115.26	55.49	36.79	171.79
98Leu	7.87	118.10	52.53	40.75	---
99Lys	---	---	---	---	---
100Lys	7.82	117.34	53.04	31.59	171.89
101Ala	8.01	120.86	48.88	18.10	172.79
102Thr	7.62	108.93	58.33	67.02	176.08
103Asn	8.00	118.04	49.99	37.37	171.39
104Glu	7.88	115.58	51.92	26.81	173.34

Table A.3 ^{1}H, ^{15}N, $^{13}C\alpha$ and $^{13}C\beta$ resonance assignments of the Y48H variant of hC*c* in native state aqueous solution conditions

	Y48H			
Assignment	**^{1}H (ppm)**	**^{15}N (ppm)**	**$^{13}C_{\alpha}$ (ppm)**	**$^{13}C_{\beta}$ (ppm)**
1Gly	---	---	38.23	---
2Asp	9.27	124.45	49.97	40.08
3Val	8.42	123.49	63.60	29.18
4Glu	7.91	120.32	56.58	25.73
5Lys	7.90	120.92	56.85	29.77
6Gly	8.44	106.99	43.76	---
7Lys	7.79	124.00	56.66	29.35
8Lys	6.71	116.83	56.86	29.00
9Ile	7.33	119.00	62.28	34.47
10Phe	8.20	120.44	59.65	36.49
11Ile	8.72	121.59	63.37	35.19
12Met	7.80	117.20	55.73	30.75
13Lys	8.41	112.36	54.10	31.40
14Cys	7.69	114.13	51.40	34.17
15Ser	8.00	115.80	59.28	61.26
16Gln	9.95	122.69	56.87	25.78
17Cys	9.61	113.63	55.69	34.41
18His	10.97	118.47	55.65	---
19Thr	---	---	58.11	70.13
20Val	8.76	112.17	59.65	31.59
21Glu	---	---	54.37	27.40
22Lys	8.92	126.60	55.52	28.43
23Gly	9.28	117.69	42.73	---
24Gly	8.13	107.72	41.97	---
25Lys	8.75	118.83	53.91	30.58
26His	8.81	122.44	56.13	29.30
27Lys	7.75	119.96	55.56	30.57
28Thr	---	---	69.88	73.65
29Gly	8.05	109.30	41.43	---

30Pro	---	---	---	---
31Asn	---	---	53.60	38.28
32Leu	9.42	122.16	51.35	41.19
33His	7.98	120.42	55.13	27.46
34Gly	8.83	114.94	43.00	---
35Leu	6.85	117.24	55.33	41.19
36Phe	8.52	113.22	57.44	33.80
37Gly	---	---	42.08	---
38Arg	7.94	123.53	52.73	30.04
39Lys	8.00	122.81	59.64	30.04
40Thr	---	---	59.24	67.21
41Gly	8.34	111.13	42.68	---
42Gln	---	---	59.28	35.57
43Ala	8.13	126.37	49.90	16.06
44Pro	---	---	---	---
45Gly	8.39	109.91	42.48	---
46Tyr	---	---	---	---
47Ser	8.14	119.37	59.33	67.12
48His	---	---	---	---
49Thr	---	---	---	---
50Ala	---	---	---	---
51Ala	8.00	119.45	55.41	16.26
52Asn	---	---	---	---
53Lys	---	---	---	---
54Asn	---	---	---	---
55Lys	---	---	---	---
56Gly	---	---	---	---
57Ile	---	---	---	---
58Ile	8.09	119.42	56.93	38.10
59Trp	8.68	130.08	54.51	27.01
60Gly	7.61	111.86	41.41	---
61Glu	9.38	120.56	59.52	26.37
62Asp	8.14	114.76	54.65	36.89

63Thr	8.12	112.73	61.05	66.45
64Leu	8.45	121.25	55.41	39.28
65Met	7.68	118.06	55.50	28.58
66Glu	6.63	116.62	55.61	30.65
67Tyr	8.04	120.55	57.80	38.03
68Leu	7.95	108.82	57.35	---
69Glu	---	---	---	---
70Asn	6.68	106.39	55.14	35.03
71Pro	---	---	---	---
72Lys	---	---	---	---
73Lys	---	---	---	---
74Tyr	---	---	58.67	37.37
75Ile	9.33	114.40	56.90	36.19
76Pro	---	---	---	---
77Gly	9.15	111.64	42.23	---
78Thr	8.86	116.21	57.20	70.47
79Lys	---	---	---	---
80Met	---	---	---	---
81Ile	---	---	---	---
82Phe	---	---	---	---
83Val	---	---	---	---
84Gly	---	---	---	---
85Ile	---	---	56.65	36.33
86Lys	8.32	127.63	55.96	29.76
87Lys	8.14	120.23	54.19	29.97
88Lys	8.96	129.64	57.92	29.56
89Glu	9.19	117.84	57.14	25.96
90Glu	6.01	116.19	55.51	27.00
91Arg	7.02	116.92	58.28	28.31
92Ala	8.29	119.85	52.64	14.77
93Asp	7.82	121.96	55.47	36.71
94Leu	7.59	120.56	55.36	37.95
95Ile	8.28	119.60	63.50	34.45

96Ala	7.53	122.69	52.37	14.19
97Tyr	7.67	117.96	58.72	34.14
98Leu	8.41	118.51	54.73	39.38
99Lys	8.56	123.72	56.69	28.98
100Lys	6.48	116.59	55.40	30.52
101Ala	8.39	119.38	52.09	15.89
102Thr	7.66	101.87	59.65	66.97
103Asn	6.92	118.34	49.81	38.82
104Glu	7.20	124.68	55.39	28.36

Appendix B

cH/D exchange rates (k_{ex}), calculated protection factors (LogPF), free energies of exchange (ΔG_{ex}) and proton occupancies (Occ.) of the ferric Y48H variant of hC*c* (pH 6.5 and 288 K)

Y48H

Residue	k_{ex} (h^{-1})	logPF	ΔG_{ex} (kcal/mol)	^{1}H Occ.
1Gly	---	---	---	---
2Asp	---	---	---	---
3Val	---	---	---	---
4Glu	---	---	---	---
5Lys	---	---	---	---
6Gly	---	---	---	---
7Lys	1.37E-01	1.74	2.29	0.27
8Lys	6.23E-01	1.05	1.39	0.18
9Ile	1.62E-02	2.22	2.93	0.18
10Phe	-1.21E-04	---	---	0.93
11Ile	4.90E-03	2.71	3.57	0.48
12Met	4.14E-01	1.04	1.37	0.15
13Lys	6.61E-03	3.02	3.98	0.43
14Cys	1.82E-02	2.98	3.93	0.59
15Ser	1.35E+00	1.22	1.61	0.69
16Gln	---	---	---	---
17Cys	---	---	---	---
18His	4.73E-01	1.94	2.55	0.12
19Thr	---	---	---	---
20Val	---	---	---	---
21Glu	---	---	---	---
22Lys	---	---	---	---
23Gly	---	---	---	---
24Gly	---	---	---	---
25Lys	---	---	---	---
26His	---	---	---	---
27Lys	---	---	---	---
28Thr	---	---	---	---
29Gly	---	---	---	---
30Pro	---	---	---	---
31Asn	---	---	---	---

32Leu	---	---	---	---
33His	4.68E-02	1.94	2.6	0.1
34Gly	---	---	---	---
35Leu	8.60E-02	1.94	2.92	---
36Phe	1.91E+00	1.94	1.55	0.58
37Gly	5.74E-01	1.94	1.05	0.15
38Arg	1.04E-01	1.94	1.99	0.34
39Lys	---	---	---	---
40Thr	---	---	---	---
41Gly	---	---	---	---
42Gln	---	---	---	---
43Ala	---	---	---	---
44Pro	---	---	---	---
45Gly	---	---	---	---
46Tyr	---	---	---	---
47Ser	---	---	---	---
48His	---	---	---	---
49Thr	---	---	---	---
50Ala	---	---	---	---
51Ala	---	---	---	---
52Asn	---	---	---	---
53Lys	---	---	---	---
54Asn	---	---	---	---
55Lys	---	---	---	---
56Gly	---	---	---	---
57Ile	---	---	---	---
58Ile	---	---	---	---
59Trp	---	---	---	---
60Gly	---	---	---	---
61Glu	---	---	---	---
62Asp	1.47E-01	1.73	2.28	0.15
63Thr	---	---	---	---
64Leu	---	---	---	---

65Met	---	---	---	---
66Glu	---	---	---	---
67Tyr	4.15E-02	1.95	2.57	0.26
68Leu	---	---	---	---
69Glu	---	---	---	---
70Asn	2.24E-01	1.66	2.19	---
71Pro	1.60E-02	2.67	3.51	0.16
72Lys	---	---	---	---
73Lys	---	---	---	---
74Tyr	---	---	---	---
75Ile	---	---	---	---
76Pro	---	---	---	---
77Gly	---	---	---	---
78Thr	---	---	---	---
79Lys	---	---	---	---
80Met	5.10E-01	0.68	0.9	0.12
81Ile	---	---	---	---
82Phe	---	---	---	---
83Val	---	---	---	---
84Gly	---	---	---	---
85Ile	---	---	---	---
86Lys	---	---	---	---
87Lys	---	---	---	---
88Lys	---	---	---	---
89Glu	---	---	---	---
90Glu	---	---	---	---
91Arg	---	---	---	---
92Ala	---	---	---	---
93Asp	---	---	---	---
94Leu	---	---	---	---
95Ile	---	---	---	---
96Ala	---	---	---	---
97Tyr	3.66E-02	2.52	3.32	0.14

98Leu	---	---	---	---
99Lys	2.13E-03	3.6	4.75	---
100Lys	8.26E-02	2.3	3.03	0.13
101Ala	2.37E-04	4.44	5.85	0.9
102Thr	2.00E-03	2.93	3.86	0.79
103Asn	4.41E-04	4.02	5.29	0.87
104Glu	2.29E-03	3.28	4.32	0.8

Appendix C

Summary of the iH/D exchange methodology development and the dilution/concentration, PD10 and reverse deuteration approaches

---

Table C1. Summary of iH/D exchange methodology development

Section	Content	Exp. observations
3.3.1	Solving solubility issues with increased quench TFA concentration	• Excellent solubility but no iH/D exchange observed. • Significant and non-uniform shifts with respect to triple resonance spectra. • Possibly due to lower pH and increased salt content.
3.3.2	**Observing iH/D exchange in H_2O**: Determine feasibility of quenching iH/D exchange in H_2O	• Ideal quench TFA concentration 0.05 %. • Further refinement possible.
		• Narrowed down ideal quench TFA concentration to 0.065 %
3.3.3	**Observing iH/D exchange in DMSO:** Identify best resuspension solution to observe iH/D exchange in DMSO.	• 0.25 % has the best exchange profile. • Extremes (0.15 % and 0.4 %) are worst.
3.3.4	Using FAST-HSQC to determine time zero	Exchange profile differences only observed for very slow exchanging residues.
3.3.5	Incorporating CL liposomes into iH/D exchange methodology	• 1:5 ratio of protein/liposome confers greatest peroxidase activity and complex stability. • Gentle, but thorough, mixing after addition of DEE yields lipid emulsion between organic and aqueous phases.
3.3.6	First iH/D exchange experiment with protein/liposome separated samples	• Significant difference between L2N and L4X, • Not clear for C1N and C3X, likely 0.085% (for the quench) and DEE results in not appropriate quench conditions
3.3.7	Attempts at observing iH/D exchange with protein/liposome	• No sign of complex formation (no line broadening observed)

	complexes in aqueous conditions.	• Some sample reduction • Evident lipid layer upon extraction
3.3.8	**Re-protonation** Determining optimal quench pH for the protein/lipid complex (re-protonation)	• Minimal solution volumes • Effective exchange through dilution in H_2O • Reduced D_2O requirement Comparable exchange rates to H/D exchange Sample 4 (0.1 % v/v TFA) demonstrated best preserved exchange.
3.3.9	"Dry" DMSO	Lower H_2O content in $_{d6}$-DMSO from sealed ampules

Table C2 Summary of exchange protocols used for protein/lipid complex samples

Step	PD10	Dilution/ Concentration	Reverse D/H Exchange
1	Liposome preparation in H_2O	Liposome preparation in H_2O	Full deuteration of hC*c* for at least 1 week at room temperature.
2	Complex formation at 1:5 ratio hC*c*/CL	Complex formation at 1:5 ration hC*c*/CL	Liposome preparation in D_2O
3	Deuteration through D_2O pre-equilibrated PD10 columns followed by elution with high salt buffer (20 mM NaPi, 1 M NaCl, pH 6.5)	Deuteration through 10-fold dilution	Complex
4	Concentration and dilution repeated as necessary to buffer	H/D exchange interval in D_2O	Reverse D/H exchange interval in H_2O through 10-fold dilution

	exchange into a lower ionic strength buffer (essential). Resulting volumes generally high.		
5	H/D exchange interval in D_2O	Concentration usually required as volumes typically high in order to minimise residual H_2O content.	Concentration not necessary as resulting volumes generally kept low. Ideal for both perseveration of the hC*c*/CL complex and minimising the population of unbound hCyt *c* minimal.
6	Quench with TFA	Quench with TFA	Quench with TFA
7	Diethyl Ether separation	Diethyl Ether separation	Diethyl Ether separation
8	Flash freezing in liquid N_2	Flash freezing in liquid N_2	Flash freezing in liquid N_2
9	Lyophilise	Lyophilise	Lyophilise
10	NMR detection in H_2O using a series of sequential FAST-HSQC experiments to determine H/D exchange time dependency.	NMR detection in H_2O using a series of sequential FAST-HSQC experiments to determine H/D exchange time dependency.	NMR detection in H_2O using a series of sequential FAST-HSQC experiments to determine H/D exchange time dependency.

References

ABE, M., NIIBAYASHI, R., KOUBORI, S., MORIYAMA, I. & MIYOSHI, H. 2011. Molecular mechanisms for the induction of peroxidase activity of the cytochrome c-cardiolipin complex. *Biochemistry,* 50**,** 8383-91.

ABRIATA, L. A., CASSINA, A., TORTORA, V., MARIN, M., SOUZA, J. M., CASTRO, L., VILA, A. J. & RADI, R. 2009. Nitration of solvent-exposed tyrosine 74 on cytochrome c triggers heme iron-methionine 80 bond disruption. Nuclear magnetic resonance and optical spectroscopy studies. *J Biol Chem,* 284**,** 17-26.

ADAMS, J. M. & CORY, S. 2001. Life-or-death decisions by the Bcl-2 protein family. *Trends Biochem Sci,* 26**,** 61-6.

AHMED, A. J., SMITH, H. T., SMITH, M. B. & MILLETT, F. S. 1978. Effect of specific lysine modification on the reduction of cytochrome c by succinate-cytochrome c reductase. *Biochemistry,* 17**,** 2479-83.

ALAYASH, A. I., WILSON, M. T. 1979. *Biochem. J.,* 177**,** 641-648.

ALEXANDRESCU, A. T. 2013. Amide Proton Solvent Protection in Amylin Fibrils Probed by Quenched Hydrogen Exchange NMR. *PLoS ONE,* 8**,** e56467.

ALVAREZ-PAGGI, D., HANNIBAL, L., CASTRO, M. A., OVIEDO-ROUCO, S., DEMICHELI, V., TÓRTORA, V., TOMASINA, F., RADI, R. & MURGIDA, D. H. 2017. Multifunctional Cytochrome c: Learning New Tricks from an Old Dog. *Chemical Reviews,* 117**,** 13382-13460.

AMACHER, J. F., ZHONG, F., LISI, G. P., ZHU, M. Q., ALDEN, S. L., HOKE, K. R., MADDEN, D. R. & PLETNEVA, E. V. 2015. A Compact Structure of

Cytochrome c Trapped in a Lysine-Ligated State: Loop Refolding and Functional Implications of a Conformational Switch. *Journal of the American Chemical Society,* 137**,** 8435-8449.

AMBLER, R. P. 1991. Sequence variability in bacterial cytochromes c. *Biochim Biophys Acta,* 1058**,** 42-7.

ANDREINI, C., BANCI, L., BERTINI, I. & ROSATO, A. 2006. Counting the zinc-proteins encoded in the human genome. *J Proteome Res,* 5**,** 196-201.

ÅNGSTRÖM, J., MOORE, G. R. & WILLIAMS, R. J. P. 1982. The magnetic susceptibility of ferricytochrome c. *Biochimica et Biophysica Acta (BBA) - Protein Structure and Molecular Enzymology,* 703**,** 87-94.

ASSFALG, M., BERTINI, I., DOLFI, A., TURANO, P., MAUK, A. G., ROSELL, F. I. & GRAY, H. B. 2003. *J. Am. Chem. Soc.,* 125**,** 2913.

AVIRAM, I. & SCHEJTER, A. 1969. Physicochemical Properties of Bakers' Yeast Iso-1-cytochrome c. *Journal of Biological Chemistry,* 244**,** 3773-3778.

BABU, C. R., FLYNN, P. F. & WAND, A. J. 2001. Validation of protein structure from preparations of encapsulated proteins dissolved in low viscosity fluids. *J Am Chem Soc,* 123**,** 2691-2.

BAI, Y., ENGLANDER, J. J., MAYNE, L., MILNE, J. S. & ENGLANDER, S. W. 1995a. Thermodynamic parameters from hydrogen exchange measurements. *Methods Enzymol,* 259**,** 344-56.

BAI, Y. & ENGLANDER, S. W. 1994. Hydrogen bond strength and beta-sheet propensities: the role of a side chain blocking effect. *Proteins,* 18**,** 262-6.

BAI, Y. & ENGLANDER, S. W. 1996. Future directions in folding: the multi-state nature of protein structure. *Proteins,* 24**,** 145-51.

BAI, Y., MILNE, J. S., MAYNE, L. & ENGLANDER, S. W. 1993. Primary structure effects on peptide group hydrogen exchange. *Proteins,* 17**,** 75-86.

BAI, Y., MILNE, J. S., MAYNE, L. & ENGLANDER, S. W. 1994. Protein stability parameters measured by hydrogen exchange. *Proteins,* 20**,** 4-14.

BAI, Y., SOSNICK, T. R., MAYNE, L. & ENGLANDER, S. W. 1995b. Protein folding intermediates: native-state hydrogen exchange. *Science,* 269**,** 192-7.

BALAKRISHNAN, G., HU, Y., OYERINDE, O. F., SU, J., GROVES, J. T. & SPIRO, T. G. 2007. A conformational switch to beta-sheet structure in cytochrome c leads to heme exposure. Implications for cardiolipin peroxidation and apoptosis. *J Am Chem Soc,* 129**,** 504-5.

BALDWIN, A. J. & KAY, L. E. 2009. NMR spectroscopy brings invisible protein states into focus. *Nat Chem Biol,* 5**,** 808-14.

BANCI, L., BERTINI, I., ROSATO, A. & VARANI, G. 1999. Mitochondrial cytochromes c: a comparative analysis. *J Biol Inorg Chem,* 4**,** 824-37.

BANDI, S. & BOWLER, B. E. 2015. Effect of an Ala81His mutation on the Met80 loop dynamics of iso-1-cytochrome c. *Biochemistry,* 54**,** 1729-42.

BARRY, M., HEIBEIN, J. A., PINKOSKI, M. J., LEE, S. F., MOYER, R. W., GREEN, D. R. & BLEACKLEY, R. C. 2000. Granzyme B short-circuits the need for caspase 8 activity during granule-mediated cytotoxic T-lymphocyte killing by directly cleaving Bid. *Mol Cell Biol,* 20**,** 3781-94.

BASANEZ, G., SHARPE, J. C., GALANIS, J., BRANDT, T. B., HARDWICK, J. M. & ZIMMERBERG, J. 2002. Bax-type apoptotic proteins porate pure lipid bilayers through a mechanism sensitive to intrinsic monolayer curvature. *J Biol Chem,* 277**,** 49360-5.

BASOVA, L. V., KURNIKOV, I. V., WANG, L., RITOV, V. B., BELIKOVA, N. A., VLASOVA, II, PACHECO, A. A., WINNICA, D. E., PETERSON, J., BAYIR, H., WALDECK, D. H. & KAGAN, V. E. 2007. Cardiolipin switch in mitochondria: shutting off the reduction of cytochrome c and turning on the peroxidase activity. *Biochemistry,* 46**,** 3423-34.

BATTISTUZZI, G., BORSARI, M. & SOLA, M. 2001. Redox properties of cytochrome c. *Antioxid Redox Signal,* 3**,** 279-91.

BAXTER, S. M. & FETROW, J. S. 1999. Hydrogen exchange behavior of [U-15N]-labeled oxidized and reduced iso-1-cytochrome c. *Biochemistry,* 38**,** 4493-503.

BAYIR, H., FADEEL, B., PALLADINO, M. J., WITASP, E., KURNIKOV, I. V., TYURINA, Y. Y., TYURIN, V. A., AMOSCATO, A. A., JIANG, J., KOCHANEK, P. M., DEKOSKY, S. T., GREENBERGER, J. S., SHVEDOVA, A. A. & KAGAN, V. E. 2006. Apoptotic interactions of cytochrome c: redox flirting with anionic phospholipids within and outside of mitochondria. *Biochim Biophys Acta,* 1757**,** 648-59.

BAZAN, S., MILEYKOVSKAYA, E., MALLAMPALLI, V. K., HEACOCK, P., SPARAGNA, G. C. & DOWHAN, W. 2013. Cardiolipin-dependent reconstitution of respiratory supercomplexes from purified Saccharomyces cerevisiae complexes III and IV. *J Biol Chem,* 288**,** 401-11.

BEDARD, S., MAYNE, L. C., PETERSON, R. W., WAND, A. J. & ENGLANDER, S. W. 2008. The foldon substructure of staphylococcal nuclease. *J Mol Biol,* 376**,** 1142-54.

BEITLICH, T., KUHNEL, K., SCHULZE-BRIESE, C., SHOEMAN, R. L. & SCHLICHTING, I. 2007. Cryoradiolytic reduction of crystalline heme

proteins: analysis by UV-Vis spectroscopy and X-ray crystallography. *J Synchrotron Radiat,* 14**,** 11-23.

BELIKOVA, N. A., JIANG, J., TYURINA, Y. Y., ZHAO, Q., EPPERLY, M. W., GREENBERGER, J. & KAGAN, V. E. 2007. Cardiolipin-specific peroxidase reactions of cytochrome C in mitochondria during irradiation-induced apoptosis. *Int J Radiat Oncol Biol Phys,* 69**,** 176-86.

BELIKOVA, N. A., VLADIMIROV, Y. A., OSIPOV, A. N., KAPRALOV, A. A., TYURIN, V. A., POTAPOVICH, M. V., BASOVA, L. V., PETERSON, J., KURNIKOV, I. V. & KAGAN, V. E. 2006. Peroxidase Activity and Structural Transitions of Cytochrome c Bound to Cardiolipin-Containing Membranes. *Biochemistry,* 45**,** 4998-5009.

BERGSTROM, C. L., BEALES, P. A., LV, Y., VANDERLICK, T. K. & GROVES, J. T. 2013. Cytochrome c causes pore formation in cardiolipin-containing membranes. *Proceedings of the National Academy of Sciences*.

BERTINI, I., CAVALLARO, G. & ROSATO, A. 2005. A structural model for the adduct between cytochrome c and cytochrome c oxidase. *J Biol Inorg Chem,* 10**,** 613-24.

BLANCHARD, H., KODANDAPANI, L., MITTL, P. R., MARCO, S. D., KREBS, J. F., WU, J. C., TOMASELLI, K. J. & GRUTTER, M. G. 1999. The three-dimensional structure of caspase-8: an initiator enzyme in apoptosis. *Structure,* 7**,** 1125-33.

BODENHAUSEN, G. & RUBEN, D. J. 1980. Natural abundance nitrogen-15 NMR by enhanced heteronuclear spectroscopy. *Chemical Physics Letters,* 69**,** 185-189.

BOEHNING, D., PATTERSON, R. L., SEDAGHAT, L., GLEBOVA, N. O., KUROSAKI, T. & SNYDER, S. H. 2003. Cytochrome c binds to inositol (1,4,5) trisphosphate receptors, amplifying calcium-dependent apoptosis. *Nat Cell Biol,* 5**,** 1051-61.

BOGAN, A. A. & THORN, K. S. 1998. Anatomy of hot spots in protein interfaces. *J Mol Biol,* 280**,** 1-9.

BOSSHARD, H. R. 1981. Alkaline isomerization of ferricytochrome c: lysine is not replacing methionine at the sixth co-ordination site of the haem iron. *J Mol Biol,* 153**,** 1125-49.

BOUILLET, P., METCALF, D., HUANG, D. C., TARLINTON, D. M., KAY, T. W., KONTGEN, F., ADAMS, J. M. & STRASSER, A. 1999. Proapoptotic Bcl-2 relative Bim required for certain apoptotic responses, leukocyte homeostasis, and to preclude autoimmunity. *Science,* 286**,** 1735-8.

BRADLEY, J. M., SILKSTONE, G., WILSON, M. T., CHEESMAN, M. R. & BUTT, J. N. 2011. *J. Am. Chem. Soc.,* 133**,** 19676.

BRAYER, G. D. & MURPHY, M. E. P. 1996. *in Cytochrome c: a multidisciplinary approach*.

BREN, K. L. & RAVEN, E. L. 2017. Locked and loaded for apoptosis. *Science,* 356**,** 1236.

BRUEY, J. M., DUCASSE, C., BONNIAUD, P., RAVAGNAN, L., SUSIN, S. A., DIAZ-LATOUD, C., GURBUXANI, S., ARRIGO, A. P., KROEMER, G., SOLARY, E. & GARRIDO, C. 2000. Hsp27 negatively regulates cell death by interacting with cytochrome c. *Nat Cell Biol,* 2**,** 645-52.

BRUNORI, M., WILSON, M. T. & ANTONINI, E. 1972. Properties of modified cytochromes. I. Equilibrium and kinetics of the pH-dependent transition in carboxymethylated horse heart cytochrome c. *J Biol Chem,* 247**,** 6076-81.

BRYNGELSON, J. D., ONUCHIC, J. N., SOCCI, N. D. & WOLYNES, P. G. 1995. Funnels, pathways, and the energy landscape of protein folding: a synthesis. *Proteins,* 21**,** 167-95.

BUDIHARDJO, I., OLIVER, H., LUTTER, M., LUO, X. & WANG, X. 1999. Biochemical pathways of caspase activation during apoptosis. *Annu Rev Cell Dev Biol,* 15**,** 269-90.

BURNS, P. D. & LA MAR, G. N. 1979. Detection of localized conformational flexibility in horse heart cytochrome c by proton nuclear magnetic resonance. *Journal of the American Chemical Society,* 101**,** 5844-5846.

BURNS, P. D. & LA MAR, G. N. 1981. Characterization of conformational heterogeneity in the heme pocket of ferricytochrome c using high field proton nuclear magnetic resonance spectroscopy. *J Biol Chem,* 256**,** 4934-9.

BUSHNELL, G. W., LOUIE, G. V. & BRAYER, G. D. 1990. *J. Mol. Biol.,* 214**,** 585.

CAI, M., HUANG, Y., SAKAGUCHI, K., CLORE, G. M., GRONENBORN, A. M. & CRAIGIE, R. 1998. An efficient and cost-effective isotope labeling protocol for proteins expressed in Escherichia coli. *J Biomol NMR,* 11**,** 97-102.

CALHOUN, D. B. & ENGLANDER, S. W. 1985. Internal protein motions, concentrated glycerol, and hydrogen exchange studied in myoglobin. *Biochemistry,* 24**,** 2095-100.

CAMPBELL, I. D. A. D., R. A. 1984. *Biological Spectroscopy*, The Benjamin/Cummings Publishing Company, Inc. .

CAPDEVILA, D. A., OVIEDO ROUCO, S., TOMASINA, F., TORTORA, V., DEMICHELI, V., RADI, R. & MURGIDA, D. H. 2015. Active Site Structure and Peroxidase Activity of Oxidatively Modified Cytochrome c Species in Complexes with Cardiolipin. *Biochemistry,* 54**,** 7491-504.

CAVANAGH, J., SKELTON, N. J., FAIRBROTHER, W. J., RANCE, M., PALMER III, A. G. 2006. *Protein NMR Spectroscopy: Principles and Practice* Academic Press

CECCONI, F., ALVAREZ-BOLADO, G., MEYER, B. I., ROTH, K. A. & GRUSS, P. 1998. Apaf1 (CED-4 homolog) regulates programmed cell death in mammalian development. *Cell,* 94**,** 727-37.

CHANDAK, M. S., NAKAMURA, T., MAKABE, K., TAKENAKA, T., MUKAIYAMA, A., CHAUDHURI, T. K., KATO, K. & KUWAJIMA, K. 2013. The H/D-exchange kinetics of the Escherichia coli co-chaperonin GroES studied by 2D NMR and DMSO-quenched exchange methods. *J Mol Biol,* 425**,** 2541-60.

CHAPPLE, C. E. & BRUN, C. 2015. Redefining protein moonlighting. *Oncotarget,* 6**,** 16812-16813.

CHAPPLE, C. E., ROBISSON, B., SPINELLI, L., GUIEN, C., BECKER, E. & BRUN, C. 2015. Extreme multifunctional proteins identified from a human protein interaction network. 6**,** 7412.

CHEN, Y.-R., DETERDING, L. J., STURGEON, B. E., TOMER, K. B. & MASON, R. P. 2002. Protein Oxidation of Cytochrome c by Reactive Halogen Species Enhances Its Peroxidase Activity. *Journal of Biological Chemistry,* 277**,** 29781-29791.

CLEARY, M. L., SMITH, S. D. & SKLAR, J. 1986. Cloning and structural analysis of cDNAs for bcl-2 and a hybrid bcl-2/immunoglobulin transcript resulting from the t(14;18) translocation. *Cell,* 47**,** 19-28.

CLUBB, R. T., THANABAL, V. & WAGNER, G. 1992. A constant-time three-dimensional triple-resonance pulse scheme to correlate intraresidue 1HN, 15N, and 13C′ chemical shifts in 15N□13C-labelled proteins. *Journal of Magnetic Resonance (1969),* 97**,** 213-217.

CONNELLY, G. P., BAI, Y., JENG, M. F. & ENGLANDER, S. W. 1993. Isotope effects in peptide group hydrogen exchange. *Proteins,* 17**,** 87-92.

COUTINHO, I. B. & XAVIER, A. V. 1994. Tetraheme cytochromes. *Methods Enzymol,* 243**,** 119-40.

CUMMINGS, C., WALDER, J., TREEFUL, A. & JEMMERSON, R. 2006. Serum leucine-rich alpha-2-glycoprotein-1 binds cytochrome c and inhibits antibody detection of this apoptotic marker in enzyme-linked immunosorbent assay. *Apoptosis,* 11**,** 1121-9.

CUTLER, R. L., DAVIES, A. M., CREIGHTON, S., WARSHEL, A., MOORE, G. R., SMITH, M. & MAUK, A. G. 1989. Role of arginine-38 in regulation of the cytochrome c oxidation-reduction equilibrium. *Biochemistry,* 28**,** 3188-97.

CZJZEK, M., ARNOUX, P., HASER, R. & SHEPARD, W. 2001. Structure of cytochrome c7 from Desulfuromonas acetoxidans at 1.9 A resolution. *Acta Crystallogr D Biol Crystallogr,* 57**,** 670-8.

DAVIS, I. W., LEAVER-FAY, A., CHEN, V. B., BLOCK, J. N., KAPRAL, G. J., WANG, X., MURRAY, L. W., ARENDALL, W. B., 3RD, SNOEYINK, J., RICHARDSON, J. S. & RICHARDSON, D. C. 2007. MolProbity: all-atom

contacts and structure validation for proteins and nucleic acids. *Nucleic Acids Res,* 35**,** W375-83.

DAVIS, L. A., SCHEJTER, A. & HESS, G. P. 1974. *J. Biol. Chem.,* 249**,** 2632.

DE BOTTON, S., SABRI, S., DAUGAS, E., ZERMATI, Y., GUIDOTTI, J. E., HERMINE, O., KROEMER, G., VAINCHENKER, W. & DEBILI, N. 2002. Platelet formation is the consequence of caspase activation within megakaryocytes. *Blood,* 100**,** 1310-7.

DE ROCCO, D., CERQUA, C., GOFFRINI, P., RUSSO, G., PASTORE, A., MELONI, F., NICCHIA, E., MORAES, C. T., PECCI, A., SALVIATI, L. & SAVOIA, A. 2014. Mutations of cytochrome c identified in patients with thrombocytopenia THC4 affect both apoptosis and cellular bioenergetics. *Biochim Biophys Acta,* 1842**,** 269-74.

DEACON, O. M., KARSISIOTIS, A. I., MORENO CHICANO, T., HOUGH, M. A., MACDONALD, C. J., BLUMENSCHEIN, T., WILSON, M. T., MOORE, G. R. & WORRALL, J. A. R. 2017. Heightened dynamics of the oxidized Y48H variant of human cytochrome c increases its peroxidatic activity. *Biochemistry*.

DESAGHER, S., OSEN-SAND, A., NICHOLS, A., ESKES, R., MONTESSUIT, S., LAUPER, S., MAUNDRELL, K., ANTONSSON, B. & MARTINOU, J. C. 1999. Bid-induced conformational change of Bax is responsible for mitochondrial cytochrome c release during apoptosis. *J Cell Biol,* 144**,** 891-901.

DICKERSON, R. E., TAKANO, T., EISENBERG, D., KALLAI, O. B., SAMSON, L., COOPER, A. & MARGOLIASH, E. 1971. Ferricytochrome c. I. General features of the horse and bonito proteins at 2.8 A resolution. *J Biol Chem,* 246**,** 1511-35.

DIEDERIX, R. E. M., UBBINK, M. & CANTERS, G. W. 2002. Peroxidase Activity as a Tool for Studying the Folding of c-Type Cytochromes. *Biochemistry,* 41**,** 13067-13077.

DÖPNER, S., HILDEBRANDT, P., ROSELL, F. I. & MAUK, A. G. 1998. *J. Am. Chem. Soc.,* 120**,** 11255.

DYSON, H. J., KOSTIC, M., LIU, J. & MARTINEZ-YAMOUT, M. A. 2008. Hydrogen-Deuterium Exchange Strategy for Delineation of Contact Sites in Protein Complexes. *FEBS letters,* 582**,** 1495-1500.

EKERT, P. G. & VAUX, D. L. 2005. The mitochondrial death squad: hardened killers or innocent bystanders? *Curr Opin Cell Biol,* 17**,** 626-30.

EMSLEY, P. & COWTAN, K. 2004. Coot: model-building tools for molecular graphics. *Acta Crystallogr D Biol Crystallogr,* 60**,** 2126-32.

ENGLANDER, S. W. & KALLENBACH, N. R. 1983. Hydrogen exchange and structural dynamics of proteins and nucleic acids. *Q Rev Biophys,* 16**,** 521-655.

ENGUITA, F. J., POHL, E., TURNER, D. L., SANTOS, H. & CARRONDO, M. A. 2006. Structural evidence for a proton transfer pathway coupled with haem reduction of cytochrome c" from Methylophilus methylotrophus. *J Biol Inorg Chem,* 11**,** 189-96.

ESKES, R., DESAGHER, S., ANTONSSON, B. & MARTINOU, J.-C. 2000. Bid Induces the Oligomerization and Insertion of Bax into the Outer Mitochondrial Membrane. *Molecular and Cellular Biology,* 20**,** 929-935.

EVANS, P. 2006. Scaling and assessment of data quality. *Acta Crystallogr D Biol Crystallogr,* 62**,** 72-82.

EVANS, P. R. & MURSHUDOV, G. N. 2013. How good are my data and what is the resolution? *Acta Crystallographica Section D: Biological Crystallography,* 69**,** 1204-1214.

FAZELINIA, H., XU, M., CHENG, H. & RODER, H. 2013. Ultrafast Hydrogen Exchange Reveals Specific Structural Events during the Initial Stages of Folding of Cytochrome c. *Journal of the American Chemical Society,* 136**,** 733-740.

FENG, Y. Q., RODER, H. & ENGLANDER, S. W. 1990. Assignment of paramagnetically shifted resonances in the 1H NMR spectrum of horse ferricytochrome c. *Biophys J,* 57**,** 15-22.

FERGUSON-MILLER, S. & BABCOCK, G. T. 1996. Heme/Copper Terminal Oxidases. *Chemical Reviews,* 96**,** 2889-2908.

FERGUSON-MILLER, S., BRAUTIGAN, D. L. & MARGOLIASH, E. 1978. *J. Biol. Chem.,* 253**,** 159.

FRAUENHOFF, M. M. & SCOTT, R. A. 1992. The role of tyrosine 67 in the cytochrome c heme crevice structure studied by semisynthesis. *Proteins,* 14**,** 202-12.

GADSBY, P. M., PETERSON, J., FOOTE, N., GREENWOOD, C. & THOMSON, A. J. 1987. Identification of the ligand-exchange process in the alkaline transition of horse heart cytochrome c. *Biochem J,* 246**,** 43-54.

GARCIA-HEREDIA, J. M., DIAZ-MORENO, I., NIETO, P. M., ORZAEZ, M., KOCANIS, S., TEIXEIRA, M., PEREZ-PAYA, E., DIAZ-QUINTANA, A. & DE LA ROSA, M. A. 2010. Nitration of tyrosine 74 prevents human cytochrome c to play a key role in apoptosis signaling by blocking caspase-9 activation. *Biochim Biophys Acta,* 1797**,** 981-93.

GARCIA-HEREDIA, J. M., DIAZ-QUINTANA, A., SALZANO, M., ORZAEZ, M., PEREZ-PAYA, E., TEIXEIRA, M., DE LA ROSA, M. A. & DIAZ-MORENO, I. 2011. Tyrosine phosphorylation turns alkaline transition into a biologically relevant process and makes human cytochrome c behave as an anti-apoptotic switch. *J Biol Inorg Chem,* 16**,** 1155-68.

GIORDANO, A., CALVANI, M., PETILLO, O., GRIPPO, P., TUCCILLO, F., MELONE, M. A., BONELLI, P., CALARCO, A. & PELUSO, G. 2005. tBid induces alterations of mitochondrial fatty acid oxidation flux by malonyl-CoA-independent inhibition of carnitine palmitoyltransferase-1. *Cell Death Differ,* 12**,** 603-13.

GODBOLE, S., DONG, A., GARBIN, K. & BOWLER, B. E. 1997. *Biochemistry,* 36**,** 119.

GODDARD, T. D., KNELLER, D. G. 2008. SPARKY 3. University of California, San Fransisco

GODOY, L. C., MUÑOZ-PINEDO, C., CASTRO, L., CARDACI, S., SCHONHOFF, C. M., KING, M., TÓRTORA, V., MARÍN, M., MIAO, Q., JIANG, J. F., KAPRALOV, A., JEMMERSON, R., SILKSTONE, G. G., PATEL, J. N., EVANS, J. E., WILSON, M. T., GREEN, D. R., KAGAN, V. E., RADI, R. & MANNICK, J. B. 2009. Disruption of the M80-Fe ligation stimulates the translocation of cytochrome c to the cytoplasm and nucleus in nonapoptotic cells. *Proceedings of the National Academy of Sciences,* 106**,** 2653-2658.

GOLDSTEIN, J. C., WATERHOUSE, N. J., JUIN, P., EVAN, G. I. & GREEN, D. R. 2000. The coordinate release of cytochrome c during apoptosis is rapid, complete and kinetically invariant. *Nat Cell Biol,* 2**,** 156-62.

GONZÁLEZ-ARZOLA, K., DÍAZ-MORENO, I., CANO-GONZÁLEZ, A., DÍAZ-QUINTANA, A., VELÁZQUEZ-CAMPOY, A., MORENO-BELTRÁN, B., LÓPEZ-RIVAS, A. & DE LA ROSA, M. A. 2015. Structural basis for inhibition of the histone chaperone activity of SET/TAF-Iβ by cytochrome c. *Proceedings of the National Academy of Sciences of the United States of America,* 112**,** 9908-9913.

GONZALVEZ, F. & GOTTLIEB, E. 2007. Cardiolipin: setting the beat of apoptosis. *Apoptosis,* 12**,** 877-85.

GRANINGER, W. B., SETO, M., BOUTAIN, B., GOLDMAN, P. & KORSMEYER, S. J. 1987. Expression of Bcl-2 and Bcl-2-Ig fusion transcripts in normal and neoplastic cells. *J Clin Invest,* 80**,** 1512-5.

GRAY, W. R. 1967. Dansyl chloride procedure *In:* COLOWICK, S. P., KAPLAN, N. O. (ed.) *Methods in Enzymology* Orlando, Fla. : Academic Press

GREEN, D. R. 2006. At the gates of death. *Cancer Cell,* 9**,** 328-30.

GREENHALGH, D. G. 1998. The role of apoptosis in wound healing. *Int J Biochem Cell Biol,* 30**,** 1019-30.

GREENWOOD, C. & WILSON, M. T. 1971. Studies on ferricytochrome c. I. Effect of pH, ionic strength and protein denaturants on the spectra of ferricytochrome c. *Eur J Biochem,* 22**,** 5-10.

GRIMM, S. & BRDICZKA, D. 2007. The permeability transition pore in cell death. *Apoptosis,* 12**,** 841-55.

GROSS, A., MCDONNELL, J. M. & KORSMEYER, S. J. 1999. BCL-2 family members and the mitochondria in apoptosis. *Genes Dev,* 13**,** 1899-911.

GRZESIEK, S. & BAX, A. 1992a. Correlating backbone amide and side chain resonances in larger proteins by multiple relayed triple resonance NMR. *Journal of the American Chemical Society,* 114**,** 6291-6293.

GRZESIEK, S. & BAX, A. 1992b. An efficient experiment for sequential backbone assignment of medium-sized isotopically enriched proteins. *Journal of Magnetic Resonance (1969),* 99**,** 201-207.

GRZESIEK, S. & BAX, A. 1992c. Improved 3D triple-resonance NMR techniques applied to a 31 kDa protein. *Journal of Magnetic Resonance (1969),* 96**,** 432-440.

GU, J., SHIN, D.-W. & PLETNEVA, E. V. 2017. Remote Perturbations in Tertiary Contacts Trigger Lysine Ligation to the Heme Iron in Cytochrome c. *Biochemistry,* 56**,** 2950-2966.

GUPTE, S., WU, E. S., HOECHLI, L., HOECHLI, M., JACOBSON, K., SOWERS, A. E. & HACKENBROCK, C. R. 1984. Relationship between lateral diffusion, collision frequency, and electron transfer of mitochondrial inner membrane oxidation-reduction components. *Proc Natl Acad Sci U S A,* 81**,** 2606-10.

GUPTE, S. S. & HACKENBROCK, C. R. 1988. Multidimensional diffusion modes and collision frequencies of cytochrome c with its redox partners. *Journal of Biological Chemistry,* 263**,** 5241-5247.

HACKENBROCK, C. R., CHAZOTTE, B. & GUPTE, S. S. 1986. The random collision model and a critical assessment of diffusion and collision in mitochondrial electron transport. *J Bioenerg Biomembr,* 18**,** 331-68.

HAKEM, R., HAKEM, A., DUNCAN, G. S., HENDERSON, J. T., WOO, M., SOENGAS, M. S., ELIA, A., DE LA POMPA, J. L., KAGI, D., KHOO, W., POTTER, J., YOSHIDA, R., KAUFMAN, S. A., LOWE, S. W., PENNINGER,

J. M. & MAK, T. W. 1998. Differential requirement for caspase 9 in apoptotic pathways in vivo. *Cell,* 94**,** 339-52.

HAMMACK, B. N., SMITH, C. R. & BOWLER, B. E. 2001. *J. Mol. Biol.,* 311**,** 1091.

HANNIBAL, L., TOMASINA, F., CAPDEVILA, D. A., DEMICHELI, V., TÓRTORA, V., ALVAREZ-PAGGI, D., JEMMERSON, R., MURGIDA, D. H. & RADI, R. 2016. Alternative Conformations of Cytochrome c: Structure, Function, and Detection. *Biochemistry,* 55**,** 407-428.

HANSKE, J., TOFFEY, J. R., MORENZ, A. M., BONILLA, A. J., SCHIAVONI, K. H. & PLETNEVA, E. V. 2012. Conformational properties of cardiolipin-bound cytochrome c. *Proceedings of the National Academy of Sciences,* 109**,** 125-130.

HAO, Z., DUNCAN, G. S., CHANG, C. C., ELIA, A., FANG, M., WAKEHAM, A., OKADA, H., CALZASCIA, T., JANG, Y., YOU-TEN, A., YEH, W. C., OHASHI, P., WANG, X. & MAK, T. W. 2005. Specific ablation of the apoptotic functions of cytochrome C reveals a differential requirement for cytochrome C and Apaf-1 in apoptosis. *Cell,* 121**,** 579-91.

HARTSHORN, R. T. & MOORE, G. R. 1989. *Biochem. J.,* 258**,** 598.

HASAN, S. S., YAMASHITA, E., RYAN, C. M., WHITELEGGE, J. P. & CRAMER, W. A. 2011. Conservation of lipid functions in cytochrome bc complexes. *J Mol Biol,* 414**,** 145-62.

HAW, J. F., SONG, W., MARCUS, D. M. & NICHOLAS, J. B. 2003. The mechanism of methanol to hydrocarbon catalysis. *Acc Chem Res,* 36**,** 317-26.

HENDERSON, B. & MARTIN, A. C. 2014. Protein moonlighting: a new factor in biology and medicine. *Biochem Soc Trans,* 42**,** 1671-8.

HENGARTNER, M. O. 1999. Programmed cell death in the nematode C. elegans. *Recent Prog Horm Res,* 54**,** 213-22; discussion 222-4.

HENGARTNER, M. O., ELLIS, R. E. & HORVITZ, H. R. 1992. Caenorhabditis elegans gene ced-9 protects cells from programmed cell death. *Nature,* 356**,** 494-9.

HENGARTNER, M. O. & HORVITZ, H. R. 1994. C. elegans cell survival gene ced-9 encodes a functional homolog of the mammalian proto-oncogene bcl-2. *Cell,* 76**,** 665-76.

HENZLER-WILDMAN, K. & KERN, D. 2007. Dynamic personalities of proteins. *Nature,* 450**,** 964-972.

HERSLETH, H. P., RYDE, U., RYDBERG, P., GORBITZ, C. H. & ANDERSSON, K. K. 2006. Structures of the high-valent metal-ion haem-oxygen intermediates in peroxidases, oxygenases and catalases. *J Inorg Biochem,* 100**,** 460-76.

HIGMAN, V. 2012. *Protein NMR: A Practical Guide* [Online]. Available: http://www.protein-nmr.org.uk [Accessed].

HOANG, L., MAITY, H., KRISHNA, M. M., LIN, Y. & ENGLANDER, S. W. 2003. Folding units govern the cytochrome c alkaline transition. *J Mol Biol,* 331**,** 37-43.

HOCKENBERY, D., NUNEZ, G., MILLIMAN, C., SCHREIBER, R. D. & KORSMEYER, S. J. 1990. Bcl-2 is an inner mitochondrial membrane protein that blocks programmed cell death. *Nature,* 348**,** 334-6.

HONG, X., DIXON, D. 1989. *FEBS Lett,* 246**,** 105-108.

HONG, X. L. & DIXON, D. W. 1989. *FEBS Lett.,* 246**,** 108.

HORVITZ, H. R. 1999. Genetic control of programmed cell death in the nematode Caenorhabditis elegans. *Cancer Res,* 59**,** 1701s-1706s.

HORVITZ, H. R., SHAHAM, S. & HENGARTNER, M. O. 1994. The genetics of programmed cell death in the nematode Caenorhabditis elegans. *Cold Spring Harb Symp Quant Biol,* 59**,** 377-85.

HOSHINO, M., KATOU, H., YAMAGUCHI, K. & GOTO, Y. 2007. Dimethylsulfoxide-quenched hydrogen/deuterium exchange method to study amyloid fibril structure. *Biochim Biophys Acta,* 1768**,** 1886-99.

HOURY, W. A., SAUDER, J. M., RODER, H. & SCHERAGA, H. A. 1998. Definition of amide protection factors for early kinetic intermediates in protein folding. *Proc Natl Acad Sci U S A,* 95**,** 4299-302.

HU, W., KAN, Z. Y., MAYNE, L. & ENGLANDER, S. W. 2016. Cytochrome c folds through foldon-dependent native-like intermediates in an ordered pathway. *Proc Natl Acad Sci U S A,* 113**,** 3809-14.

HUNTE, C., KOEPKE, J., LANGE, C., ROSSMANITH, T. & MICHEL, H. 2000. Structure at 2.3 A resolution of the cytochrome bc(1) complex from the yeast Saccharomyces cerevisiae co-crystallized with an antibody Fv fragment. *Structure,* 8**,** 669-84.

HUNTE, C., SOLMAZ, S. & LANGE, C. 2002. Electron transfer between yeast cytochrome bc(1) complex and cytochrome c: a structural analysis. *Biochim Biophys Acta,* 1555**,** 21-8.

HUTTEMANN, M., LEE, I., GROSSMAN, L. I., DOAN, J. W. & SANDERSON, T. H. 2012. Phosphorylation of mammalian cytochrome c and cytochrome c oxidase in the regulation of cell destiny: respiration, apoptosis, and human disease. *Adv Exp Med Biol,* 748**,** 237-64.

HUTTEMANN, M., LEE, I., PECINOVA, A., PECINA, P., PRZYKLENK, K. & DOAN, J. W. 2008. Regulation of oxidative phosphorylation, the mitochondrial

membrane potential, and their role in human disease. *J Bioenerg Biomembr,* 40**,** 445-56.

HUTTEMANN, M., PECINA, P., RAINBOLT, M., SANDERSON, T. H., KAGAN, V. E., SAMAVATI, L., DOAN, J. W. & LEE, I. 2011. The multiple functions of cytochrome c and their regulation in life and death decisions of the mammalian cell: From respiration to apoptosis. *Mitochondrion,* 11**,** 369-81.

JEFFERY, C. J. 1999. Moonlighting proteins. *Trends Biochem Sci,* 24**,** 8-11.

JEFFERY, C. J. 2014. An introduction to protein moonlighting. *Biochem Soc Trans,* 42**,** 1679-83.

JIANG, J., KINI, V., BELIKOVA, N., SERINKAN, B. F., BORISENKO, G. G., TYURINA, Y. Y., TYURIN, V. A. & KAGAN, V. E. 2004. Cytochrome c release is required for phosphatidylserine peroxidation during Fas-triggered apoptosis in lung epithelial A549 cells. *Lipids,* 39**,** 1133-42.

JIANG, X. & WANG, X. 2004. Cytochrome C-mediated apoptosis. *Annu Rev Biochem,* 73**,** 87-106.

JOHNSON, B., LOWE, G. C., FUTTERER, J., LORDKIPANIDZE', M., MACDONALD, D., SIMPSON, M. A., SANCHEZ GUIU', I., DRAKE, S., BEM, D., LEO, V., FLETCHER, S. J., DAWOOD, B., RIVERA, J., ALLSUP, D., BISS, T., BOLTON-MAGGS, P. H. B., COLLINS, P., CURRY, N., GRIMLEY, C., JAMES, B., MAKRIS, M., MOTWANI, J., PAVORD, S., TALKS, K., THACHIL, J., WILDE, J., WILLIAMS, M., HARRISON, P., GISSEN, P., MUNDELL, S., MUMFORD, A., DALY, M. E., WATSON, S. P. & MORGAN, N. V. 2016. Whole exome sequencing identifies genetic variants in inherited thrombocytopenia with secondary qualitative function defects. *Haematologica*.

JOSEPHS, T. M., LIPTAK, M. D., HUGHES, G., LO, A., SMITH, R. M., WILBANKS, S. M., BREN, K. L. & LEDGERWOOD, E. C. 2013. Conformational change and human cytochrome c function: mutation of residue 41 modulates caspase activation and destabilizes Met-80 coordination. *J Biol Inorg Chem,* 18**,** 289-97.

JOSEPHS, T. M., MORISON, I. M., DAY, C. L., WILBANKS, S. M. & LEDGERWOOD, E. C. 2014. Enhancing the peroxidase activity of cytochrome c by mutation of residue 41: implications for the peroxidase mechanism and cytochrome c release. *Biochemical Journal,* 458**,** 259-265.

KABSCH, W. 2010. XDS. *Acta Crystallographica Section D: Biological Crystallography,* 66**,** 125-132.

KAGAN, V. E., BAYIR, A., BAYIR, H., STOYANOVSKY, D., BORISENKO, G. G., TYURINA, Y. Y., WIPF, P., ATKINSON, J., GREENBERGER, J. S., CHAPKIN, R. S. & BELIKOVA, N. A. 2009a. Mitochondria-targeted disruptors and inhibitors of cytochrome c/cardiolipin peroxidase complexes: a new strategy in anti-apoptotic drug discovery. *Mol Nutr Food Res,* 53**,** 104-14.

KAGAN, V. E., BAYIR, H. A., BELIKOVA, N. A., KAPRALOV, O., TYURINA, Y. Y., TYURIN, V. A., JIANG, J., STOYANOVSKY, D. A., WIPF, P., KOCHANEK, P. M., GREENBERGER, J. S., PITT, B., SHVEDOVA, A. A. & BORISENKO, G. 2009b. Cytochrome c/cardiolipin relations in mitochondria: a kiss of death. *Free Radic Biol Med,* 46**,** 1439-53.

KAGAN, V. E., FABISIAK, J. P., SHVEDOVA, A. A., TYURINA, Y. Y., TYURIN, V. A., SCHOR, N. F. & KAWAI, K. 2000. Oxidative signaling pathway for externalization of plasma membrane phosphatidylserine during apoptosis. *FEBS Lett,* 477**,** 1-7.

KAGAN, V. E., GLEISS, B., TYURINA, Y. Y., TYURIN, V. A., ELENSTROM-MAGNUSSON, C., LIU, S. X., SERINKAN, F. B., ARROYO, A., CHANDRA, J., ORRENIUS, S. & FADEEL, B. 2002. A role for oxidative stress in apoptosis: oxidation and externalization of phosphatidylserine is required for macrophage clearance of cells undergoing Fas-mediated apoptosis. *J Immunol,* 169**,** 487-99.

KAGAN, V. E., TYURIN, V. A., JIANG, J., TYURINA, Y. Y., RITOV, V. B., AMOSCATO, A. A., OSIPOV, A. N., BELIKOVA, N. A., KAPRALOV, A. A., KINI, V., VLASOVA, I. I., ZHAO, Q., ZOU, M., DI, P., SVISTUNENKO, D. A., KURNIKOV, I. V. & BORISENKO, G. G. 2005. Cytochrome c acts as a cardiolipin oxygenase required for release of proapoptotic factors. *Nat Chem Biol,* 1**,** 223-232.

KALANXHI, E. & WALLACE, C. J. 2007. Cytochrome c impaled: investigation of the extended lipid anchorage of a soluble protein to mitochondrial membrane models. *Biochem J,* 407**,** 179-87.

KAPETANAKI, S. M., SILKSTONE, G., HUSU, I., LIEBL, U., WILSON, M. T. & VOS, M. H. 2009. Interaction of carbon monoxide with the apoptosis-inducing cytochrome c-cardiolipin complex. *Biochemistry,* 48**,** 1613-9.

KAPRALOV, A. A., KURNIKOV, I. V., VLASOVA, II, BELIKOVA, N. A., TYURIN, V. A., BASOVA, L. V., ZHAO, Q., TYURINA, Y. Y., JIANG, J., BAYIR, H., VLADIMIROV, Y. A. & KAGAN, V. E. 2007. The hierarchy of structural transitions induced in cytochrome c by anionic phospholipids determines its peroxidase activation and selective peroxidation during apoptosis in cells. *Biochemistry,* 46**,** 14232-44.

KARSISIOTIS, A. I., DEACON, O. M., MACDONALD, C., BLUMENSCHEIN, T. M., MOORE, G. R. & WORRALL, J. A. 2017. Near-complete backbone resonance assignments of acid-denatured human cytochrome c in dimethylsulfoxide: a prelude to studying interactions with phospholipids. *Biomol NMR Assign*.

KARSISIOTIS, A. I., DEACON, O. M., RAJAGOPAL, B. S., MACDONALD, C., BLUMENSCHEIN, T. M., MOORE, G. R. & WORRALL, J. A. 2015. Backbone resonance assignments of ferric human cytochrome c and the pro-apoptotic G41S mutant in the ferric and ferrous states. *Biomol NMR Assign,* 9**,** 415-9.

KARSISIOTIS, A. I., DEACON, O. M., WILSON, M. T., MACDONALD, C., BLUMENSCHEIN, T. M. A., MOORE, G. R. & WORRALL, J. A. R. 2016. Increased dynamics in the 40–57 Ω-loop of the G41S variant of human cytochrome c promote its pro-apoptotic conformation. *Scientific Reports,* 6**,** 30447.

KASSNER, R. J. 1991. Ligand binding properties of cytochromes c'. *Biochim Biophys Acta,* 1058**,** 8-12.

KAWAI, C., PRADO, F. M., NUNES, G. L., DI MASCIO, P., CARMONA-RIBEIRO, A. M. & NANTES, I. L. 2005. pH-Dependent interaction of cytochrome c with mitochondrial mimetic membranes: the role of an array of positively charged amino acids. *J Biol Chem,* 280**,** 34709-17.

KAY, L. E., CLORE, G. M., BAX, A. & GRONENBORN, A. M. 1990a. Four-dimensional heteronuclear triple-resonance NMR spectroscopy of interleukin-1 beta in solution. *Science,* 249**,** 411-4.

KAY, L. E., IKURA, M., TSCHUDIN, R. & BAX, A. 1990b. Three-dimensional triple-resonance NMR spectroscopy of isotopically enriched proteins. *Journal of Magnetic Resonance (1969),* 89**,** 496-514.

KEELER, J. (ed.) 2010. *Understanding NMR Spectroscopy* John Wiley & Sons Ltd.

KEKILLI, D., MORENO-CHICANO, T., CHAPLIN, A. K., HORRELL, S., DWORKOWSKI, F. S. N., WORRALL, J. A. R., STRANGE, R. W. & HOUGH, M. A. 2017. Photoreduction and validation of haem-ligand intermediate states in protein crystals by in situ single-crystal spectroscopy and diffraction. *IUCrJ,* 4**,** 263-270.

KERR, J. F. 2002. History of the events leading to the formulation of the apoptosis concept. *Toxicology,* 181-182**,** 471-4.

KERR, J. F., WYLLIE, A. H. & CURRIE, A. R. 1972. Apoptosis: a basic biological phenomenon with wide-ranging implications in tissue kinetics. *Br J Cancer,* 26**,** 239-57.

KIHARA, H., SAIGO, S., NAKATANI, H., HIROMI, K., IKEDA-SAITO, M. & IIZUKA, T. 1976. *Biochim. Biophys. Acta,* 430**,** 243.

KIM, T. H., ZHAO, Y., DING, W. X., SHIN, J. N., HE, X., SEO, Y. W., CHEN, J., RABINOWICH, H., AMOSCATO, A. A. & YIN, X. M. 2004. Bid-cardiolipin interaction at mitochondrial contact site contributes to mitochondrial cristae reorganization and cytochrome C release. *Mol Biol Cell,* 15**,** 3061-72.

KINNUNEN, P. K. 1992. Fusion of lipid bilayers: a model involving mechanistic connection to HII phase forming lipids. *Chem Phys Lipids,* 63**,** 251-8.

KINNUNEN, P. K., KOIV, A., LEHTONEN, J. Y., RYTOMAA, M. & MUSTONEN, P. 1994. Lipid dynamics and peripheral interactions of proteins with membrane surfaces. *Chem Phys Lipids,* 73**,** 181-207.

KITT, J. P., BRYCE, D. A., MINTEER, S. D. & HARRIS, J. M. 2017. Raman Spectroscopy Reveals Selective Interactions of Cytochrome c with Cardiolipin That Correlate with Membrane Permeability. *J Am Chem Soc,* 139**,** 3851-3860.

KLUCK, R. M., ESPOSTI, M. D., PERKINS, G., RENKEN, C., KUWANA, T., BOSSY-WETZEL, E., GOLDBERG, M., ALLEN, T., BARBER, M. J., GREEN, D. R. & NEWMEYER, D. D. 1999. The Pro-Apoptotic Proteins, Bid and Bax, Cause a Limited Permeabilization of the Mitochondrial Outer Membrane That Is Enhanced by Cytosol. *The Journal of Cell Biology,* 147**,** 809-822.

KLUCK, R. M., MARTIN, S. J., HOFFMAN, B. M., ZHOU, J. S., GREEN, D. R. & NEWMEYER, D. D. 1997. Cytochrome c activation of CPP32-like proteolysis plays a critical role in a Xenopus cell-free apoptosis system. *The EMBO Journal,* 16**,** 4639-4649.

KOKHAN, O., WRAIGHT, C. A. & TAJKHORSHID, E. 2010. The Binding Interface of Cytochrome c and Cytochrome c(1) in the bc(1) Complex: Rationalizing the Role of Key Residues. *Biophysical Journal,* 99**,** 2647-2656.

KONIG, B. W., OSHEROFF, N., WILMS, J., MUIJSERS, A. O., DEKKER, H. L. & MARGOLIASH, E. 1980. Mapping of the interaction domain for purified cytochrome c1 on cytochrome c. *FEBS Lett,* 111**,** 395-8.

KOSTRZEWA, A., PALI, T., FRONCISZ, W. & MARSH, D. 2000. Membrane location of spin-labeled cytochrome c determined by paramagnetic relaxation agents. *Biochemistry,* 39**,** 6066-74.

KRISHNA, M. M., LIN, Y., MAYNE, L. & ENGLANDER, S. W. 2003a. Intimate view of a kinetic protein folding intermediate: residue-resolved structure,

interactions, stability, folding and unfolding rates, homogeneity. *J Mol Biol,* 334**,** 501-13.

KRISHNA, M. M., LIN, Y., RUMBLEY, J. N. & ENGLANDER, S. W. 2003b. Cooperative omega loops in cytochrome c: role in folding and function. *J Mol Biol,* 331**,** 29-36.

KRISHNA, M. M., MAITY, H., RUMBLEY, J. N., LIN, Y. & ENGLANDER, S. W. 2006. Order of steps in the cytochrome C folding pathway: evidence for a sequential stabilization mechanism. *J Mol Biol,* 359**,** 1410-9.

KROEMER, G., GALLUZZI, L. & BRENNER, C. 2007. Mitochondrial membrane permeabilization in cell death. *Physiol Rev,* 87**,** 99-163.

KROLL, T., HADT, R. G., WILSON, S. A., LUNDBERG, M., YAN, J. J., WENG, T. C., SOKARAS, D., ALONSO-MORI, R., CASA, D., UPTON, M. H., HEDMAN, B., HODGSON, K. O. & SOLOMON, E. I. 2014. Resonant inelastic X-ray scattering on ferrous and ferric bis-imidazole porphyrin and cytochrome c: nature and role of the axial methionine-Fe bond. *J Am Chem Soc,* 136**,** 18087-99.

KUIDA, K., HAYDAR, T. F., KUAN, C. Y., GU, Y., TAYA, C., KARASUYAMA, H., SU, M. S., RAKIC, P. & FLAVELL, R. A. 1998. Reduced apoptosis and cytochrome c-mediated caspase activation in mice lacking caspase 9. *Cell,* 94**,** 325-37.

KUWANA, T., MACKEY, M. R., PERKINS, G., ELLISMAN, M. H., LATTERICH, M., SCHNEITER, R., GREEN, D. R. & NEWMEYER, D. D. 2002. Bid, Bax, and lipids cooperate to form supramolecular openings in the outer mitochondrial membrane. *Cell,* 111**,** 331-42.

LAMBETH, D. O., CAMPBELL, K. L., ZAND, R. & PALMER, G. 1973. The appearance of transient species of cytochrome c upon rapid oxidation or reduction at alkaline pH. *J Biol Chem,* 248**,** 8130-6.

LANGE, C. & HUNTE, C. 2002. Crystal structure of the yeast cytochrome bc1 complex with its bound substrate cytochrome c. *Proc Natl Acad Sci U S A,* 99**,** 2800-5.

LANGE, C., NETT, J. H., TRUMPOWER, B. L. & HUNTE, C. 2001. Specific roles of protein-phospholipid interactions in the yeast cytochrome bc1 complex structure. *Embo j,* 20**,** 6591-600.

LAWRENCE, A., JONES, C. M., WARDMAN, P. & BURKITT, M. J. 2003. Evidence for the role of a peroxidase compound I-type intermediate in the oxidation of glutathione, NADH, ascorbate, and dichlorofluorescin by cytochrome c/H2O2. Implications for oxidative stress during apoptosis. *J Biol Chem,* 278**,** 29410-9.

LEE, I., SALOMON, A. R., YU, K., DOAN, J. W., GROSSMAN, L. I. & HUTTEMANN, M. 2006. New prospects for an old enzyme: mammalian cytochrome c is tyrosine-phosphorylated in vivo. *Biochemistry,* 45**,** 9121-8.

LEE, W., TONELLI, M., MARKLEY, J. L. 2015. NMRFAM-SPARKY: Enhanced software for biomolecular NMR spectroscopy *Bioinformatics,* 31**,** 1325-1327.

LEITCH, F. A., MOORE, G. R. & PETTIGREW, G. W. 1984. Structural basis for the variation of pH-dependent redox potentials of Pseudomonas cytochromes c-551. *Biochemistry,* 23**,** 1831-8.

LI, H., ZHU, H., XU, C. J. & YUAN, J. 1998. Cleavage of BID by caspase 8 mediates the mitochondrial damage in the Fas pathway of apoptosis. *Cell,* 94**,** 491-501.

LI, K., LI, Y., SHELTON, J. M., RICHARDSON, J. A., SPENCER, E., CHEN, Z. J., WANG, X. & WILLIAMS, R. S. 2000. Cytochrome c deficiency causes embryonic lethality and attenuates stress-induced apoptosis. *Cell,* 101**,** 389-99.

LI, P., NIJHAWAN, D., BUDIHARDJO, I., SRINIVASULA, S. M., AHMAD, M., ALNEMRI, E. S. & WANG, X. 1997. Cytochrome c and dATP-dependent formation of Apaf-1/caspase-9 complex initiates an apoptotic protease cascade. *Cell,* 91**,** 479-89.

LINDERSTRØM-LANG, K. 1955a. Deuterium exchange between beta-lactoglobulin and water. *Society of Biological Chemists***,** 191-194.

LINDERSTRØM-LANG, K. 1955b. Deuterium exchange between peptides and water. *The Chemical Society's Special Publication No 2*.

LINDERSTRØM-LANG, K. Deuterium exchange and protein strucutre. Symposium on protein structure 1958 London: Methuen. In: Neuberger A, ed.

LINDERSTRØM-LANG, K., SCHELLMAN, J. A. 1959. *Protein structure and enzyme activity,* New York: Academic Press.

LIPTAK, M. D., FAGERLUND, R. D., LEDGERWOOD, E. C., WILBANKS, S. M. & BREN, K. L. 2011. The Proapoptotic G41S Mutation to Human Cytochrome c Alters the Heme Electronic Structure and Increases the Electron Self-Exchange Rate. *Journal of the American Chemical Society,* 133**,** 1153-1155.

LIU, Q. A. & HENGARTNER, M. O. 1999. The molecular mechanism of programmed cell death in C. elegans. *Ann N Y Acad Sci,* 887**,** 92-104.

LIU, X., KIM, C. N., YANG, J., JEMMERSON, R. & WANG, X. 1996. Induction of apoptotic program in cell-free extracts: requirement for dATP and cytochrome c. *Cell,* 86**,** 147-57.

LO CONTE, L., CHOTHIA, C. & JANIN, J. 1999. The atomic structure of protein-protein recognition sites. *J Mol Biol,* 285**,** 2177-98.

LORD, S. J., RAJOTTE, R. V., KORBUTT, G. S. & BLEACKLEY, R. C. 2003. Granzyme B: a natural born killer. *Immunol Rev,* 193**,** 31-8.

LUND, L. R., ROMER, J., THOMASSET, N., SOLBERG, H., PYKE, C., BISSELL, M. J., DANO, K. & WERB, Z. 1996. Two distinct phases of apoptosis in mammary gland involution: proteinase-independent and -dependent pathways. *Development,* 122**,** 181-93.

LUNTZ, T. L., SCHEJTER, A., GARBER, E. A. & MARGOLIASH, E. 1989. Structural significance of an internal water molecule studied by site-directed mutagenesis of tyrosine-67 in rat cytochrome c. *Proc Natl Acad Sci U S A,* 86**,** 3524-8.

LUO, X., BUDIHARDJO, I., ZOU, H., SLAUGHTER, C. & WANG, X. 1998. Bid, a Bcl2 interacting protein, mediates cytochrome c release from mitochondria in response to activation of cell surface death receptors. *Cell,* 94**,** 481-90.

LUTTER, M., FANG, M., LUO, X., NISHIJIMA, M., XIE, X. & WANG, X. 2000. Cardiolipin provides specificity for targeting of tBid to mitochondria. *Nat Cell Biol,* 2**,** 754-61.

LYUBENOVA, S., SIDDIQUI, M. K., VRIES, M. J., LUDWIG, B. & PRISNER, T. F. 2007. Protein-protein interactions studied by EPR relaxation measurements: cytochrome c and cytochrome c oxidase. *J Phys Chem B,* 111**,** 3839-46.

MAHAPATRA, G., VARUGHESE, A., JI, Q., LEE, I., LIU, J., VAISHNAV, A., SINKLER, C., KAPRALOV, A. A., MORAES, C. T., SANDERSON, T. H., STEMMLER, T. L., GROSSMAN, L. I., KAGAN, V. E., BRUNZELLE, J. S., SALOMON, A. R., EDWARDS, B. F. & HUTTEMANN, M. 2017.

Phosphorylation of Cytochrome c Threonine 28 Regulates Electron Transport Chain Activity in Kidney: IMPLICATIONS FOR AMP KINASE. *J Biol Chem,* 292**,** 64-79.

MAITY, H., MAITY, M. & ENGLANDER, S. W. 2004. How cytochrome c folds, and why: submolecular foldon units and their stepwise sequential stabilization. *J Mol Biol,* 343**,** 223-33.

MAITY, H., MAITY, M., KRISHNA, M. M., MAYNE, L. & ENGLANDER, S. W. 2005. Protein folding: the stepwise assembly of foldon units. *Proc Natl Acad Sci U S A,* 102**,** 4741-6.

MAITY, H., RUMBLEY, J. N. & ENGLANDER, S. W. 2006. Functional role of a protein foldon--an Omega-loop foldon controls the alkaline transition in ferricytochrome c. *Proteins,* 63**,** 349-55.

MAKINEN, M. W., CHURG, A.K. 1983. Structural and analytical aspects of of the electronic spectra of the proteins *In:* LEVER, A. B. P., GRAY, H.B. (ed.) *Iron Porphyrin, Part 1*. London and Amsterdam Addison and Wesley

MANDAL, A., HOOP, CODY L., DELUCIA, M., KODALI, R., KAGAN, VALERIAN E., AHN, J. & VAN DER WEL, PATRICK C. 2015. Structural Changes and Proapoptotic Peroxidase Activity of Cardiolipin-Bound Mitochondrial Cytochrome c. *Biophysical Journal,* 109**,** 1873-1884.

MANEG, O., MALATESTA, F., LUDWIG, B. & DROSOU, V. 2004. Interaction of cytochrome c with cytochrome oxidase: two different docking scenarios. *Biochim Biophys Acta,* 1655**,** 274-81.

MARA, M. W., HADT, R. G., REINHARD, M. E., KROLL, T., LIM, H., HARTSOCK, R. W., ALONSO-MORI, R., CHOLLET, M., GLOWNIA, J. M., NELSON, S., SOKARAS, D., KUNNUS, K., HODGSON, K. O., HEDMAN,

B., BERGMANN, U., GAFFNEY, K. J. & SOLOMON, E. I. 2017. Metalloprotein entatic control of ligand-metal bonds quantified by ultrafast x-ray spectroscopy. *Science,* 356**,** 1276-1280.

MASON, K. D., CARPINELLI, M. R., FLETCHER, J. I., COLLINGE, J. E., HILTON, A. A., ELLIS, S., KELLY, P. N., EKERT, P. G., METCALF, D., ROBERTS, A. W., HUANG, D. C. & KILE, B. T. 2007. Programmed anuclear cell death delimits platelet life span. *Cell,* 128**,** 1173-86.

MATHEWS, F. S. 1985. The structure, function and evolution of cytochromes. *Prog Biophys Mol Biol,* 45**,** 1-56.

MCCLELLAND, L. J., MOU, T. C., JEAKINS-COOLEY, M. E., SPRANG, S. R. & BOWLER, B. E. 2014. Structure of a mitochondrial cytochrome c conformer competent for peroxidase activity. *Proc Natl Acad Sci U S A,* 111**,** 6648-53.

MILAZZO, L., TOGNACCINI, L., HOWES, B. D., SINIBALDI, F., PIRO, M. C., FITTIPALDI, M., BARATTO, M. C., POGNI, R., SANTUCCI, R. & SMULEVICH, G. 2017. Unravelling the Non-Native Low-Spin State of the Cytochrome c-Cardiolipin Complex: Evidence of the Formation of a His-Ligated Species Only. *Biochemistry,* 56**,** 1887-1898.

MILLETT, F., DARLEY-USMAR, V. & CAPALDI, R. A. 1982. Cytochrome c is cross-linked to subunit II of cytochrome c oxidase by a water-soluble carbodiimide. *Biochemistry,* 21**,** 3857-62.

MILLETT, F., DE JONG, C., PAULSON, L. & CAPALDI, R. A. 1983. Identification of specific carboxylate groups on cytochrome c oxidase that are involved in binding cytochrome c. *Biochemistry,* 22**,** 546-52.

MOORE, G. R. & PETTIGREW, G. 1991. *Cytochrome c: Evolutionary, Structural and Physicochemical Aspects*.

MOORE, G. R. & PETTIGREW, G. W. 1990. *Cytochromes c. Evolutionary, structural and physiochemical aspects*.

MOOTHA, V. K., WEI, M. C., BUTTLE, K. F., SCORRANO, L., PANOUTSAKOPOULOU, V., MANNELLA, C. A. & KORSMEYER, S. J. 2001. A reversible component of mitochondrial respiratory dysfunction in apoptosis can be rescued by exogenous cytochrome c. *The EMBO Journal,* 20**,** 661-671.

MORENO-BELTRAN, B., GUERRA-CASTELLANO, A., DIAZ-QUINTANA, A., DEL CONTE, R., GARCIA-MAURINO, S. M., DIAZ-MORENO, S., GONZALEZ-ARZOLA, K., SANTOS-OCANA, C., VELAZQUEZ-CAMPOY, A., DE LA ROSA, M. A., TURANO, P. & DIAZ-MORENO, I. 2017. Structural basis of mitochondrial dysfunction in response to cytochrome c phosphorylation at tyrosine 48. *Proc Natl Acad Sci U S A,* 114**,** E3041-e3050.

MORISON, I. M., CRAMER BORDE, E. M., CHEESMAN, E. J., CHEONG, P. L., HOLYOAKE, A. J., FICHELSON, S., WEEKS, R. J., LO, A., DAVIES, S. M., WILBANKS, S. M., FAGERLUND, R. D., LUDGATE, M. W., DA SILVA TATLEY, F. M., COKER, M. S., BOCKETT, N. A., HUGHES, G., PIPPIG, D. A., SMITH, M. P., CAPRON, C. & LEDGERWOOD, E. C. 2008. A mutation of human cytochrome c enhances the intrinsic apoptotic pathway but causes only thrombocytopenia. *Nat Genet,* 40**,** 387-9.

MOSER, C. C. & DUTTON, P. L. 1988. Cytochrome c and c2 binding dynamics and electron transfer with photosynthetic reaction center protein and other integral membrane redox proteins. *Biochemistry,* 27**,** 2450-2461.

MUENZNER, J., TOFFEY, J. R., HONG, Y. & PLETNEVA, E. V. 2013. Becoming a Peroxidase: Cardiolipin-Induced Unfolding of Cytochrome c. *The Journal of Physical Chemistry B,* 117**,** 12878-12886.

MUGA, A., MANTSCH, H. H. & SUREWICZ, W. K. 1991. Membrane binding induces destabilization of cytochrome c structure. *Biochemistry,* 30**,** 7219-7224.

MUHANDIRAM, D. R. & KAY, L. E. 1994. Gradient-Enhanced Triple-Resonance Three-Dimensional NMR Experiments with Improved Sensitivity. *Journal of Magnetic Resonance, Series B,* 103**,** 203-216.

MURSHUDOV, G. N., VAGIN, A. A. & DODSON, E. J. 1997. Refinement of Macromolecular Structures by the Maximum-Likelihood Method. *Acta Crystallographica Section D,* 53**,** 240-255.

NANTES, I. L., ZUCCHI, M. R., NASCIMENTO, O. R. & FALJONI-ALARIO, A. 2001. Effect of heme iron valence state on the conformation of cytochrome c and its association with membrane interfaces. A CD and EPR investigation. *J Biol Chem,* 276**,** 153-8.

NEWMEYER, D. D., FARSCHON, D. M. & REED, J. C. 1994. Cell-free apoptosis in Xenopus egg extracts: inhibition by Bcl-2 and requirement for an organelle fraction enriched in mitochondria. *Cell,* 79**,** 353-64.

NICHOLLS, P. 1974. Cytochrome c binding to enzymes and membranes. *Biochim Biophys Acta,* 346**,** 261-310.

NIJHAWAN, D., HONARPOUR, N. & WANG, X. 2000. Apoptosis in neural development and disease. *Annu Rev Neurosci,* 23**,** 73-87.

NISHIMURA, C., DYSON, H. J. & WRIGHT, P. E. 2005. Enhanced picture of protein-folding intermediates using organic solvents in H/D exchange and quench-flow experiments. *Proc Natl Acad Sci U S A,* 102**,** 4765-70.

NOLD, S. M., LEI, H., MOU, T. C. & BOWLER, B. E. 2017. Effect of a K72A Mutation on the Structure, Stability, Dynamics, and Peroxidase Activity of Human Cytochrome c. *Biochemistry,* 56**,** 3358-3368.

NUCCI, N. V., VALENTINE, K. G. & WAND, A. J. 2014. High-resolution NMR spectroscopy of encapsulated proteins dissolved in low-viscosity fluids. *J Magn Reson,* 241**,** 137-47.

NYOLA, A. & HUNTE, C. 2008. A structural analysis of the transient interaction between the cytochrome bc1 complex and its substrate cytochrome c. *Biochem Soc Trans,* 36**,** 981-5.

O'BRIEN, E. S., NUCCI, N. V., FUGLESTAD, B., TOMMOS, C. & WAND, A. J. 2015. Defining the apoptotic trigger: the interaction of cytochrome c and cardiolipin. *Journal of Biological Chemistry*.

OLTEANU, A., PATEL, C. N., DEDMON, M. M., KENNEDY, S., LINHOFF, M. W., MINDER, C. M., POTTS, P. R., DESHMUKH, M. & PIELAK, G. J. 2003. Stability and apoptotic activity of recombinant human cytochrome c. *Biochem Biophys Res Commun,* 312**,** 733-40.

OPFERMAN, J. T. & KORSMEYER, S. J. 2003. Apoptosis in the development and maintenance of the immune system. *Nat Immunol,* 4**,** 410-5.

OSBORNE, B. A. 1996. Apoptosis and the maintenance of homoeostasis in the immune system. *Curr Opin Immunol,* 8**,** 245-54.

OW, Y.-L. P., GREEN, D. R., HAO, Z. & MAK, T. W. 2008. Cytochrome c: functions beyond respiration. *Nat Rev Mol Cell Biol,* 9**,** 532-542.

PALMER, A. G., RANCE, M. & WRIGHT, P. E. 1991. Intramolecular motions of a zinc finger DNA-binding domain from Xfin characterized by proton-detected natural abundance carbon-13 heteronuclear NMR spectroscopy. *Journal of the American Chemical Society,* 113**,** 4371-4380.

PANCHAL, S. C., BHAVESH, N. S. & HOSUR, R. V. 2001. Improved 3D triple resonance experiments, HNN and HN(C)N, for HN and 15N sequential correlations in (13C, 15N) labeled proteins: application to unfolded proteins. *J Biomol NMR,* 20**,** 135-47.

PANGBORN, M. C. 1942. ISOLATION AND PURIFICATION OF A SEROLOGICALLY ACTIVE PHOSPHOLIPID FROM BEEF HEART. *Journal of Biological Chemistry,* 143**,** 247-256.

PAWELETZ, N. 2001. Walther Flemming: pioneer of mitosis research. *Nat Rev Mol Cell Biol,* 2**,** 72-5.

PEARCE, L. L., GÄRTNER, A. L., SMITH, M. & MAUK, A. G. 1989. *Biochemistry,* 28**,** 3156.

PECINA, P., BORISENKO, G. G., BELIKOVA, N. A., TYURINA, Y. Y., PECINOVA, A., LEE, I., SAMHAN-ARIAS, A. K., PRZYKLENK, K., KAGAN, V. E. & HUTTEMANN, M. 2010. Phosphomimetic substitution of cytochrome C tyrosine 48 decreases respiration and binding to cardiolipin and abolishes ability to trigger downstream caspase activation. *Biochemistry,* 49**,** 6705-14.

PELLEGRINI, L. & SCORRANO, L. 2007. A cut short to death: Parl and Opa1 in the regulation of mitochondrial morphology and apoptosis. *Cell Death Differ,* 14**,** 1275-1284.

PETTIGREW, G. W., MOORE, G. R. 1987. *Cytochrome c: Biological Aspects* Berlin, Springer-Verlag.

PFEIFFER, K., GOHIL, V., STUART, R. A., HUNTE, C., BRANDT, U., GREENBERG, M. L. & SCHAGGER, H. 2003. Cardiolipin stabilizes respiratory chain supercomplexes. *J Biol Chem,* 278**,** 52873-80.

PIERRON, D., OPAZO, J. C., HEISKE, M., PAPPER, Z., UDDIN, M., CHAND, G., WILDMAN, D. E., ROMERO, R., GOODMAN, M. & GROSSMAN, L. I. 2011. Silencing, positive selection and parallel evolution: busy history of primate cytochromes C. *PLoS One,* 6**,** e26269.

PIERRON, D., WILDMAN, D. E., HUTTEMANN, M., LETELLIER, T. & GROSSMAN, L. I. 2012. Evolution of the couple cytochrome c and cytochrome c oxidase in primates. *Adv Exp Med Biol,* 748**,** 185-213.

PINHEIRO, T. J., ELOVE, G. A., WATTS, A. & RODER, H. 1997. Structural and kinetic description of cytochrome c unfolding induced by the interaction with lipid vesicles. *Biochemistry,* 36**,** 13122-32.

PINHEIRO, T. J. & WATTS, A. 1994. Lipid specificity in the interaction of cytochrome c with anionic phospholipid bilayers revealed by solid-state 31P NMR. *Biochemistry,* 33**,** 2451-8.

POLLOCK, W. B., ROSELL, F. I., TWITCHETT, M. B., DUMONT, M. E. & MAUK, A. G. 1998. Bacterial expression of a mitochondrial cytochrome c. Trimethylation of lys72 in yeast iso-1-cytochrome c and the alkaline conformational transition. *Biochemistry,* 37**,** 6124-31.

RADI, R., BECKMAN, J. S., BUSH, K. M. & FREEMAN, B. A. 1991. Peroxynitrite-induced membrane lipid peroxidation: the cytotoxic potential of superoxide and nitric oxide. *Arch Biochem Biophys,* 288**,** 481-7.

RAFFELD, M., WRIGHT, J. J., LIPFORD, E., COSSMAN, J., LONGO, D. L., BAKHSHI, A. & KORSMEYER, S. J. 1987. Clonal evolution of t(14;18) follicular lymphomas demonstrated by immunoglobulin genes and the 18q21 major breakpoint region. *Cancer Res,* 47**,** 2537-42.

RAFFERTY, S. P., SRNITH, M. & MAUK, A. G. 1996. Azide binding and active site dynamics of position-82 variants of ferricytochrome c. *Inorganica Chimica Acta,* 242**,** 171-177.

RAJAGOPAL, B. S., EDZUMA, A. N., HOUGH, M. A., BLUNDELL, K. L., KAGAN, V. E., KAPRALOV, A. A., FRASER, L. A., BUTT, J. N., SILKSTONE, G. G., WILSON, M. T., SVISTUNENKO, D. A. & WORRALL, J. A. 2013. The hydrogen-peroxide-induced radical behaviour in human cytochrome c-phospholipid complexes: implications for the enhanced pro-apoptotic activity of the G41S mutant. *Biochem J,* 456**,** 441-52.

RAJAGOPAL, B. S., SILKSTONE, G. G., NICHOLLS, P., WILSON, M. T. & WORRALL, J. A. 2012. An investigation into a cardiolipin acyl chain insertion site in cytochrome c. *Biochim Biophys Acta,* 1817**,** 780-91.

RAMIREZ, B. E., MALMSTRÖM, B. G., WINKLER, J. R. & GRAY, H. B. 1995. *Proc. Natl. Acad. Sci. U.S.A.,* 92**,** 11951.

RENEHAN, A. G., BOOTH, C. & POTTEN, C. S. 2001. What is apoptosis, and why is it important? *Bmj,* 322**,** 1536-8.

RICHTER, O. M. & LUDWIG, B. 2003. Cytochrome c oxidase--structure, function, and physiology of a redox-driven molecular machine. *Rev Physiol Biochem Pharmacol,* 147**,** 47-74.

RIEDER, R. & BOSSHARD, H. R. 1980. Comparison of the binding sites on cytochrome c for cytochrome c oxidase, cytochrome bc1, and cytochrome c1.

Differential acetylation of lysyl residues in free and complexed cytochrome c. *J Biol Chem,* 255**,** 4732-9.

ROBINSON, M. N., BOSWELL, A. P., HUANG, Z. X., ELEY, C. G. & MOORE, G. R. 1983. The conformation of eukaryotic cytochrome c around residues 39, 57, 59 and 74. *Biochemical Journal,* 213**,** 687-700.

ROSELL, F. I., FERRER, J. C. & MAUK, A. G. 1998. Proton-Linked Protein Conformational Switching: Definition of the Alkaline Conformational Transition of Yeast Iso-1-ferricytochrome c. *Journal of the American Chemical Society,* 120**,** 11234-11245.

ROTONDA, J., NICHOLSON, D. W., FAZIL, K. M., GALLANT, M., GAREAU, Y., LABELLE, M., PETERSON, E. P., RASPER, D. M., RUEL, R., VAILLANCOURT, J. P., THORNBERRY, N. A. & BECKER, J. W. 1996. The three-dimensional structure of apopain/CPP32, a key mediator of apoptosis. *Nat Struct Biol,* 3**,** 619-25.

RYTOMAA, M. & KINNUNEN, P. K. 1994. Evidence for two distinct acidic phospholipid-binding sites in cytochrome c. *J Biol Chem,* 269**,** 1770-4.

RYTOMAA, M. & KINNUNEN, P. K. 1995. Reversibility of the binding of cytochrome c to liposomes. Implications for lipid-protein interactions. *J Biol Chem,* 270**,** 3197-202.

RYTOMAA, M., MUSTONEN, P. & KINNUNEN, P. K. 1992. Reversible, nonionic, and pH-dependent association of cytochrome c with cardiolipin-phosphatidylcholine liposomes. *J Biol Chem,* 267**,** 22243-8.

SAKAMOTO, K., KAMIYA, M., IMAI, M., SHINZAWA-ITOH, K., UCHIDA, T., KAWANO, K., YOSHIKAWA, S. & ISHIMORI, K. 2011. NMR basis for

interprotein electron transfer gating between cytochrome c and cytochrome c oxidase. *Proc Natl Acad Sci U S A,* 108**,** 12271-6.

SALEEM, M. M. M. & WILSON, M. T. 1988. *Inorg. Chim. Acta,* 153**,** 93.

SANTOS, H. & TURNER, D. L. 1987. Proton NMR studies of horse ferricytochrome c. Completion of the assignment of the well resolved hyperfine shifted resonances. *FEBS Lett,* 226**,** 179-85.

SAREWICZ, M., BOREK, A., DALDAL, F., FRONCISZ, W. & OSYCZKA, A. 2008. Demonstration of Short-lived Complexes of Cytochrome c with Cytochrome bc1 by EPR Spectroscopy: IMPLICATIONS FOR THE MECHANISM OF INTERPROTEIN ELECTRON TRANSFER. *Journal of Biological Chemistry,* 283**,** 24826-24836.

SATO, W., HITAOKA, S., INOUE, K., IMAI, M., SAIO, T., UCHIDA, T., SHINZAWA-ITOH, K., YOSHIKAWA, S., YOSHIZAWA, K. & ISHIMORI, K. 2016. Energetic Mechanism of Cytochrome c-Cytochrome c Oxidase Electron Transfer Complex Formation under Turnover Conditions Revealed by Mutational Effects and Docking Simulation. *Journal of Biological Chemistry,* 291**,** 15320-15331.

SCAFFIDI, C., FULDA, S., SRINIVASAN, A., FRIESEN, C., LI, F., TOMASELLI, K. J., DEBATIN, K. M., KRAMMER, P. H. & PETER, M. E. 1998. Two CD95 (APO-1/Fas) signaling pathways. *Embo j,* 17**,** 1675-87.

SCHECHTER, E. & SALUDJIAN, P. 1967. *Biopolymers,* 5**,** 790.

SCHEJTER, A. & GEORGE, P. 1964. THE 695-MMM. BAND OF FERRICYTOCHROME C AND ITS RELATIONSHIP TO PROTEIN CONFORMATION. *Biochemistry,* 3**,** 1045-9.

SCHEJTER, A. & GEORGE, P. 1965. Production of a "cytochrome c" with myoglobin-like properties by alkylating the cyanide complex with bromoacetate. *Nature,* 206**,** 1150-1.

SCHEJTER, A., KOSHY, T. I., LUNTZ, T. L., SANISHVILI, R., VIG, I. & MARGOLIASH, E. 1994. Effects of mutating Asn-52 to isoleucine on the haem-linked properties of cytochrome c. *Biochemical Journal,* 302**,** 95-101.

SCHEJTER, A., LUNTZ, T. L., KOSHY, T. I. & MARGOLIASH, E. 1992. Relationship between local and global stabilities of proteins: site-directed mutants and chemically-modified derivatives of cytochrome c. *Biochemistry,* 31**,** 8336-43.

SCHEJTER, A. & PLOTKIN, B. 1988. The binding characteristics of the cytochrome c iron. *Biochem J,* 255**,** 353-6.

SCHLAME, M., RUA, D. & GREENBERG, M. L. 2000. The biosynthesis and functional role of cardiolipin. *Prog Lipid Res,* 39**,** 257-88.

SCHMIDT, T. R., WILDMAN, D. E., UDDIN, M., OPAZO, J. C., GOODMAN, M. & GROSSMAN, L. I. 2005. Rapid electrostatic evolution at the binding site for cytochrome c on cytochrome c oxidase in anthropoid primates. *Proc Natl Acad Sci U S A,* 102**,** 6379-84.

SCOTT, R. A. & MAUK, A. G. 1996. *Cytochrome C : a multidisciplinary approach,* Sausalito, Calif., University Science Books.

SENN, H., KELLER, R.M., WÜTHRICH, K. 1985. *Biochem Biophys Res Commun,* 92**,** 1362-1369.

SENN, H. & WUTHRICH, K. 1985. Amino acid sequence, haem-iron co-ordination geometry and functional properties of mitochondrial and bacterial c-type cytochromes. *Q Rev Biophys,* 18**,** 111-34.

SERPAS, L., MILOREY, B., PANDISCIA, L. A., ADDISON, A. W. & SCHWEITZER-STENNER, R. 2016. Autoxidation of Reduced Horse Heart Cytochrome c Catalyzed by Cardiolipin-Containing Membranes. *The Journal of Physical Chemistry B,* 120**,** 12219-12231.

SHARONOV, G. V., FEOFANOV, A. V., BOCHAROVA, O. V., ASTAPOVA, M. V., DEDUKHOVA, V. I., CHERNYAK, B. V., DOLGIKH, D. A., ARSENIEV, A. S., SKULACHEV, V. P. & KIRPICHNIKOV, M. P. 2005. Comparative analysis of proapoptotic activity of cytochrome c mutants in living cells. *Apoptosis,* 10**,** 797-808.

SHIMADA, S., SHINZAWA-ITOH, K., BABA, J., AOE, S., SHIMADA, A., YAMASHITA, E., KANG, J., TATENO, M., YOSHIKAWA, S. & TSUKIHARA, T. 2017. Complex structure of cytochrome c-cytochrome c oxidase reveals a novel protein-protein interaction mode. *Embo j,* 36**,** 291-300.

SHINZAWA-ITOH, K., AOYAMA, H., MURAMOTO, K., TERADA, H., KURAUCHI, T., TADEHARA, Y., YAMASAKI, A., SUGIMURA, T., KURONO, S., TSUJIMOTO, K., MIZUSHIMA, T., YAMASHITA, E., TSUKIHARA, T. & YOSHIKAWA, S. 2007. Structures and physiological roles of 13 integral lipids of bovine heart cytochrome c oxidase. *Embo j,* 26**,** 1713-25.

SHORTLE, D. 1995. Staphylococcal nuclease: a showcase of m-value effects. *Adv Protein Chem,* 46**,** 217-47.

SILKSTONE, G., JASAITIS, A., VOS, M. H. & WILSON, M. T. 2005. Geminate carbon monoxide rebinding to a c-type haem. *Dalton Transactions***,** 3489-3494.

SINIBALDI, F., FIORUCCI, L., PATRIARCA, A., LAUCERI, R., FERRI, T., COLETTA, M. & SANTUCCI, R. 2008. Insights into cytochrome c-cardiolipin interaction. Role played by ionic strength. *Biochemistry,* 47**,** 6928-35.

SINIBALDI, F., HOWES, B. D., PIRO, M. C., POLTICELLI, F., BOMBELLI, C., FERRI, T., COLETTA, M., SMULEVICH, G. & SANTUCCI, R. 2010. Extended cardiolipin anchorage to cytochrome c: a model for protein-mitochondrial membrane binding. *J Biol Inorg Chem,* 15**,** 689-700.

SMITH, D. W. & WILLIAMS, R. J. P. 1970. *Struct. Bond.,* 7**,** 45.

SMITH, H. T., AHMED, A. J. & MILLETT, F. 1981. Electrostatic interaction of cytochrome c with cytochrome c1 and cytochrome oxidase. *J Biol Chem,* 256**,** 4984-90.

SMITH, H. T., STAUDENMAYER, N. & MILLETT, F. 1977. Use of specific lysine modifications to locate the reaction site of cytochrome c with cytochrome oxidase. *Biochemistry,* 16**,** 4971-4974.

SOENGAS, M. S., ALARCON, R. M., YOSHIDA, H., GIACCIA, A. J., HAKEM, R., MAK, T. W. & LOWE, S. W. 1999. Apaf-1 and caspase-9 in p53-dependent apoptosis and tumor inhibition. *Science,* 284**,** 156-9.

SOENGAS, M. S., CAPODIECI, P., POLSKY, D., MORA, J., ESTELLER, M., OPITZ-ARAYA, X., MCCOMBIE, R., HERMAN, J. G., GERALD, W. L., LAZEBNIK, Y. A., CORDON-CARDO, C. & LOWE, S. W. 2001. Inactivation of the apoptosis effector Apaf-1 in malignant melanoma. *Nature,* 409**,** 207-11.

SOLMAZ, S. R. & HUNTE, C. 2008. Structure of complex III with bound cytochrome c in reduced state and definition of a minimal core interface for electron transfer. *J Biol Chem,* 283**,** 17542-9.

SPAAR, A., FLOCK, D. & HELMS, V. 2009. Association of cytochrome c with membrane-bound cytochrome c oxidase proceeds parallel to the membrane rather than in bulk solution. *Biophys J,* 96**,** 1721-32.

SPECK, S. H., FERGUSON-MILLER, S., OSHEROFF, N. & MARGOLIASH, E. 1979. Definition of cytochrome c binding domains by chemical modification: kinetics of reaction with beef mitochondrial reductase and functional organization of the respiratory chain. *Proc Natl Acad Sci U S A,* 76**,** 155-9.

SPOONER, P. J. & WATTS, A. 1991. Reversible unfolding of cytochrome c upon interaction with cardiolipin bilayers. 2. Evidence from phosphorus-31 NMR measurements. *Biochemistry,* 30**,** 3880-5.

SPOONER, P. J. & WATTS, A. 1992. Cytochrome c interactions with cardiolipin in bilayers: a multinuclear magic-angle spinning NMR study. *Biochemistry,* 31**,** 10129-38.

SRINIVASULA, S. M., DATTA, P., FAN, X. J., FERNANDES-ALNEMRI, T., HUANG, Z. & ALNEMRI, E. S. 2000. Molecular determinants of the caspase-promoting activity of Smac/DIABLO and its role in the death receptor pathway. *J Biol Chem,* 275**,** 36152-7.

STELLWAGEN, E., BABUL, J. & WILGUS, H. 1975. The alkaline isomerization of lysine-modified ferricytochrome c. *Biochim Biophys Acta,* 405**,** 115-21.

STELLWAGEN, E. & CASS, R. 1974. Alkaline isomerization of ferricytochrome C from Euglena gracilis. *Biochem Biophys Res Commun,* 60**,** 371-5.

STEWART, J. M., BLAKELY, J. A. & JOHNSON, M. D. 2000. The interaction of ferrocytochrome c with long-chain fatty acids and their CoA and carnitine esters. *Biochem Cell Biol,* 78**,** 675-81.

SUN, X.-M., BRATTON, S. B., BUTTERWORTH, M., MACFARLANE, M. & COHEN, G. M. 2002. Bcl-2 and Bcl-xL Inhibit CD95-mediated Apoptosis by Preventing Mitochondrial Release of Smac/DIABLO and Subsequent Inactivation of X-linked Inhibitor-of-Apoptosis Protein. *Journal of Biological Chemistry,* 277**,** 11345-11351.

SUTIN, N. & YANDELL, J. K. 1972. Mechanisms of the Reactions of Cytochrome c : RATE AND EQUILIBRIUM CONSTANTS FOR LIGAND BINDING TO HORSE HEART FERRICYTOCHROME c. *Journal of Biological Chemistry,* 247**,** 6932-6936.

TAHA, T. S. M. & FERGUSON-MILLER, S. 1992. Interaction of cytochrome c with cytochrome c oxidase studied by monoclonal antibodies and a protein modifying reagent. *Biochemistry,* 31**,** 9090-9097.

TAKANO, T. & DICKERSON, R. E. 1981. *J. Mol. Biol.,* 153**,** 115.

THEORELL, H. & ÅKESSON, Å. 1941. Studies on Cytochrome c. I. Electrophoretic Purification of Cytochrome c and its Amino Acid Composition*. *Journal of the American Chemical Society,* 63**,** 1804-1811.

THOMPSON, M. K., FRANZEN, S., GHILADI, R. A., REEDER, B. J. & SVISTUNENKO, D. A. 2010. Compound ES of Dehaloperoxidase Decays via Two Alternative Pathways Depending on the Conformation of the Distal Histidine. *Journal of the American Chemical Society,* 132**,** 17501-17510.

THORNBERRY, N. A. & LAZEBNIK, Y. 1998. Caspases: enemies within. *Science,* 281**,** 1312-6.

TILLY, J. L., KOWALSKI, K. I., JOHNSON, A. L. & HSUEH, A. J. 1991. Involvement of apoptosis in ovarian follicular atresia and postovulatory regression. *Endocrinology,* 129**,** 2799-801.

TOGNACCINI, L., CIACCIO, C., D'ORIA, V., CERVELLI, M., HOWES, B. D., COLETTA, M., MARIOTTINI, P., SMULEVICH, G. & FIORUCCI, L. 2016. Structure-function relationships in human cytochrome c: The role of tyrosine 67. *J Inorg Biochem,* 155**,** 56-66.

TONGE, P., MOORE, G. R. & WHARTON, C. W. 1989. *Biochem. J.,* 258**,** 605.

TRAYLOR, T. G. & SHARMA, V. S. 1992. Why NO? *Biochemistry,* 31**,** 2847-9.

TRUMPOWER, B. L. 1990a. Cytochrome bc1 complexes of microorganisms. *Microbiol Rev,* 54**,** 101-29.

TRUMPOWER, B. L. 1990b. The protonmotive Q cycle. Energy transduction by coupling of proton translocation to electron transfer by the cytochrome bc1 complex. *Journal of Biological Chemistry,* 265**,** 11409-11412.

TRUMPOWER, B. L. & GENNIS, R. B. 1994. Energy transduction by cytochrome complexes in mitochondrial and bacterial respiration: the enzymology of coupling electron transfer reactions to transmembrane proton translocation. *Annu Rev Biochem,* 63**,** 675-716.

TSUJIMOTO, Y., GORHAM, J., COSSMAN, J., JAFFE, E. & CROCE, C. M. 1985a. The t(14;18) chromosome translocations involved in B-cell neoplasms result from mistakes in VDJ joining. *Science,* 229**,** 1390-3.

TSUJIMOTO, Y., JAFFE, E., COSSMAN, J., GORHAM, J., NOWELL, P. C. & CROCE, C. M. 1985b. Clustering of breakpoints on chromosome 11 in human B-cell neoplasms with the t(11;14) chromosome translocation. *Nature,* 315**,** 340-3.

TUOMINEN, E. K., WALLACE, C. J. & KINNUNEN, P. K. 2002. Phospholipid-cytochrome c interaction: evidence for the extended lipid anchorage. *J Biol Chem,* 277**,** 8822-6.

TYURIN, V. A., TYURINA, Y. Y., OSIPOV, A. N., BELIKOVA, N. A., BASOVA, L. V., KAPRALOV, A. A., BAYIR, H. & KAGAN, V. E. 2007. Interactions of cardiolipin and lyso-cardiolipins with cytochrome c and tBid: conflict or assistance in apoptosis. *Cell Death Differ,* 14**,** 872-5.

UBBINK, M., WORRALL, J. A., CANTERS, G. W., GROENEN, E. J. & HUBER, M. 2002. Paramagnetic resonance of biological metal centers. *Annu Rev Biophys Biomol Struct,* 31**,** 393-422.

UNO, T., NISHIMURA, Y. & TSUBOI, M. 1984. *Biochemistry,* 23**,** 6806.

VALENTINE, K. G., PETERSON, R., SAAD, J. S., SUMMERS, M. F., XU, X., AMES, J. B. & WAND, A. J. 2010. Reverse micelle encapsulation of membrane anchored proteins for solution NMR studies. *Structure (London, England : 1993),* 18**,** 9-16.

VALLEE, B. L. & WILLIAMS, R. J. 1968. Metalloenzymes: the entatic nature of their active sites. *Proceedings of the National Academy of Sciences of the United States of America,* 59**,** 498-505.

VAUX, D. L., CORY, S. & ADAMS, J. M. 1988. Bcl-2 gene promotes haemopoietic cell survival and cooperates with c-myc to immortalize pre-B cells. *Nature,* 335**,** 440-2.

VAUX, D. L., WEISSMAN, I. L. & KIM, S. K. 1992. Prevention of programmed cell death in Caenorhabditis elegans by human bcl-2. *Science,* 258**,** 1955.

VEITCH, N. C. 2004. Horseradish peroxidase: a modern view of a classic enzyme. *Phytochemistry,* 65**,** 249-59.

VIKULINA, A. S., ALEKSEEV, A. V., PROSKURNINA, E. V. & VLADIMIROV, Y. A. 2015. Cytochrome c–cardiolipin complex in a nonpolar environment. *Biochemistry (Moscow),* 80**,** 1298-1302.

VLADIMIROV, Y. A., PROSKURNINA, E. V. & ALEKSEEV, A. V. 2013. Molecular mechanisms of apoptosis. structure of cytochrome c-cardiolipin complex. *Biochemistry (Mosc),* 78**,** 1086-97.

VOLKOV, A. N., NICHOLLS, P. & WORRALL, J. A. R. 2011. The complex of cytochrome c and cytochrome c peroxidase: The end of the road? *Biochimica et Biophysica Acta (BBA) - Bioenergetics,* 1807**,** 1482-1503.

VOLKOV, A. N., VANWETSWINKEL, S., VAN DE WATER, K. & VAN NULAND, N. A. J. 2012. Redox-dependent conformational changes in eukaryotic cytochromes revealed by paramagnetic NMR spectroscopy. *Journal of biomolecular NMR,* 52**,** 245-256.

VON SONNTAG, C. & SCHUCHMANN, H.-P. 1991. The Elucidation of Peroxyl Radical Reactions in Aqueous Solution with the Help of Radiation-Chemical Methods. *Angewandte Chemie International Edition in English,* 30**,** 1229-1253.

VRANKEN, W. F., BOUCHER, W., STEVENS, T. J., FOGH, R. H., PAJON, A., LLINAS, M., ULRICH, E. L., MARKLEY, J. L., IONIDES, J. & LAUE, E. D. 2005. The CCPN data model for NMR spectroscopy: development of a software pipeline. *Proteins,* 59**,** 687-96.

WALKER, N. P., TALANIAN, R. V., BRADY, K. D., DANG, L. C., BUMP, N. J., FERENZ, C. R., FRANKLIN, S., GHAYUR, T., HACKETT, M. C., HAMMILL, L. D. & ET AL. 1994. Crystal structure of the cysteine protease interleukin-1 beta-converting enzyme: a (p20/p10)2 homodimer. *Cell,* 78**,** 343-52.

WALLACE, C. J. & CORTHESY, B. E. 1987. Alkylamine derivatives of cytochrome c. Comparison with other lysine-modified analogues illuminates structure/function relations in the protein. *Eur J Biochem,* 170**,** 293-8.

WALLACE, C. J., PROUDFOOT, A. E. I., 1987. *Biochemical Journal,* 245**,** 773-779.

WALLACE, C. J. A. 1984. *Biochem. J.,* 217**,** 604.

WAND, A. J., EHRHARDT, M. R. & FLYNN, P. F. 1998. High-resolution NMR of encapsulated proteins dissolved in low-viscosity fluids. *Proceedings of the National Academy of Sciences of the United States of America,* 95**,** 15299-15302.

WANG, X. 2001. The expanding role of mitochondria in apoptosis. *Genes Dev,* 15**,** 2922-33.

WANG, Z., ANDO, Y., NUGRAHENI, A. D., REN, C., NAGAO, S. & HIROTA, S. 2014. Self-oxidation of cytochrome c at methionine80 with molecular oxygen induced by cleavage of the Met-heme iron bond. *Mol Biosyst,* 10**,** 3130-7.

WANG, Z. H., LIN, Y. W., ROSELL, F. I., NI, F. Y., LU, H. J., YANG, P. Y., TAN, X. S., LI, X. Y., HUANG, Z. X. & MAUK, A. G. 2007. Converting cytochrome C into a peroxidase-like metalloenzyme by molecular design. *Chembiochem,* 8**,** 607-9.

WATT, W., KOEPLINGER, K. A., MILDNER, A. M., HEINRIKSON, R. L., TOMASSELLI, A. G. & WATENPAUGH, K. D. 1999. The atomic-resolution structure of human caspase-8, a key activator of apoptosis. *Structure,* 7**,** 1135-43.

WEI, M. C., ZONG, W. X., CHENG, E. H., LINDSTEN, T., PANOUTSAKOPOULOU, V., ROSS, A. J., ROTH, K. A., MACGREGOR, G. R., THOMPSON, C. B. & KORSMEYER, S. J. 2001. Proapoptotic BAX and BAK: a requisite gateway to mitochondrial dysfunction and death. *Science,* 292**,** 727-30.

WENZ, T., COVIAN, R., HELLWIG, P., MACMILLAN, F., MEUNIER, B., TRUMPOWER, B. L. & HUNTE, C. 2007. Mutational analysis of cytochrome b at the ubiquinol oxidation site of yeast complex III. *J Biol Chem,* 282**,** 3977-88.

WIDEGREN, J. A., BENNETT, M. A. & FINKE, R. G. 2003. Is it homogeneous or heterogeneous catalysis? Identification of bulk ruthenium metal as the true catalyst in benzene hydrogenations starting with the monometallic precursor, Ru(II)(eta 6-C6Me6)(OAc)2, plus kinetic characterization of the heterogeneous nucleation, then autocatalytic surface-growth mechanism of metal film formation. *J Am Chem Soc,* 125**,** 10301-10.

WILSON, K. P., BLACK, J. A., THOMSON, J. A., KIM, E. E., GRIFFITH, J. P., NAVIA, M. A., MURCKO, M. A., CHAMBERS, S. P., ALDAPE, R. A., RAYBUCK, S. A. & ET AL. 1994. Structure and mechanism of interleukin-1 beta converting enzyme. *Nature,* 370**,** 270-5.

WILSON, M. T. & GREENWOOD, C. 1971. Studies on ferricytochrome c. 2. A correlation between reducibility and the possession of the 695mm absorption band of ferricytochrome c. *Eur J Biochem,* 22**,** 11-8.

WILSON, M. T. & GREENWOOD, C. 1996. *Cytochrome c: A Multidisciplinary Approach*.

WILSON, M. T., HOGG

WITT, H., MALATESTA, F., NICOLETTI, F., BRUNORI, M. & LUDWIG, B. 1998a. Cytochrome-c-binding site on cytochrome oxidase in Paracoccus denitrificans. *Eur J Biochem,* 251**,** 367-73.

WITT, H., MALATESTA, F., NICOLETTI, F., BRUNORI, M. & LUDWIG, B. 1998b. Tryptophan 121 of subunit II is the electron entry site to cytochrome-c

oxidase in Paracoccus denitrificans. Involvement of a hydrophobic patch in the docking reaction. *J Biol Chem,* 273**,** 5132-6.

WOOTEN, J. B., COHEN, J. S., VIG, I. & SCHEJTER, A. 1981. pH-induced conformational transitions of ferricytochrome c: a carbon-13 and deuterium nuclear magnetic resonance study. *Biochemistry,* 20**,** 5394-402.

WUNDER, S., LU, Y., ALBRECHT, M. & BALLAUFF, M. 2011. Catalytic Activity of Faceted Gold Nanoparticles Studied by a Model Reaction: Evidence for Substrate-Induced Surface Restructuring. *ACS Catalysis,* 1**,** 908-916.

WÜTHRICH, K. 1969. HIGH-RESOLUTION PROTON NUCLEAR MAGNETIC RESONANCE SPECTROSCOPY OF CYTOCHROME c. *Proceedings of the National Academy of Sciences,* 63**,** 1071-1078.

XU, G. & CHANCE, M. R. 2007. Hydroxyl radical-mediated modification of proteins as probes for structural proteomics. *Chem Rev,* 107**,** 3514-43.

XU, Y., MAYNE, L. & ENGLANDER, S. W. 1998. Evidence for an unfolding and refolding pathway in cytochrome c. *Nat Struct Biol,* 5**,** 774-8.

YANAMALA, N., KAPRALOV, A. A., DJUKIC, M., PETERSON, J., MAO, G., KLEIN-SEETHARAMAN, J., STOYANOVSKY, D. A., STURSA, J., NEUZIL, J. & KAGAN, V. E. 2014. Structural Re-arrangement and Peroxidase Activation of Cytochrome c by Anionic Analogues of Vitamin E, Tocopherol Succinate and Tocopherol Phosphate. *Journal of Biological Chemistry,* 289**,** 32488-32498.

YANG, J., LIU, X., BHALLA, K., KIM, C. N., IBRADO, A. M., CAI, J., PENG, T. I., JONES, D. P. & WANG, X. 1997. Prevention of apoptosis by Bcl-2: release of cytochrome c from mitochondria blocked. *Science,* 275**,** 1129-32.

YIN, V., SHAW, G. S. & KONERMANN, L. 2017. Cytochrome c as a Peroxidase: Activation of the Precatalytic Native State by H2O2-Induced Covalent Modifications. *Journal of the American Chemical Society,* 139**,** 15701-15709.

YING, T., WANG, Z. H., LIN, Y. W., XIE, J., TAN, X. & HUANG, Z. X. 2009. *Chem. Commun.***,** 4512.

YOSHIDA, H., KONG, Y. Y., YOSHIDA, R., ELIA, A. J., HAKEM, A., HAKEM, R., PENNINGER, J. M. & MAK, T. W. 1998. Apaf1 is required for mitochondrial pathways of apoptosis and brain development. *Cell,* 94**,** 739-50.

YOSHIKAWA, S. & SHIMADA, A. 2015. Reaction mechanism of cytochrome c oxidase. *Chem Rev,* 115**,** 1936-89.

YOULE, R. J. & STRASSER, A. 2008. The BCL-2 protein family: opposing activities that mediate cell death. *Nat Rev Mol Cell Biol,* 9**,** 47-59.

YU, H., LEE, I., SALOMON, A. R., YU, K. & HUTTEMANN, M. 2008. Mammalian liver cytochrome c is tyrosine-48 phosphorylated in vivo, inhibiting mitochondrial respiration. *Biochim Biophys Acta,* 1777**,** 1066-71.

YU, T., WANG, X., PURRING-KOCH, C., WEI, Y. & MCLENDON, G. L. 2001. A mutational epitope for cytochrome C binding to the apoptosis protease activation factor-1. *J Biol Chem,* 276**,** 13034-8.

YUAN, J. & HORVITZ, H. R. 1992. The Caenorhabditis elegans cell death gene ced-4 encodes a novel protein and is expressed during the period of extensive programmed cell death. *Development,* 116**,** 309.

YUAN, J., SHAHAM, S., LEDOUX, S., ELLIS, H. M. & HORVITZ, H. R. 1993. The C. elegans cell death gene ced-3 encodes a protein similar to mammalian interleukin-1 beta-converting enzyme. *Cell,* 75**,** 641-52.

ZELDIN, O., GERSTEL, M. & GARMAN, E. 2013. *RADDOSE-3D: Time- and space-resolved modelling of dose in macromolecular crystallography*.

ZHANG, Y. Z., PATERSON, Y. & RODER, H. 1995. Rapid amide proton exchange rates in peptides and proteins measured by solvent quenching and two-dimensional NMR. *Protein Sci,* 4**,** 804-14.

ZHAO, Y., WANG, Z.-B. & XU, J.-X. 2003. Effect of Cytochrome c on the Generation and Elimination of O and H2O2 in Mitochondria. *Journal of Biological Chemistry,* 278**,** 2356-2360.

ZHONG, L., WEN, X., RABINOWITZ, T. M., RUSSELL, B. S., KARAN, E. F. & BREN, K. L. 2004. Heme axial methionine fluxionality in Hydrogenobacter thermophilus cytochrome c552. *Proc Natl Acad Sci U S A,* 101**,** 8637-42.

ZOU, H., HENZEL, W. J., LIU, X., LUTSCHG, A. & WANG, X. 1997. Apaf-1, a human protein homologous to C. elegans CED-4, participates in cytochrome c-dependent activation of caspase-3. *Cell,* 90**,** 405-13.

ZOU, H., LI, Y., LIU, X. & WANG, X. 1999. An APAF-1.cytochrome c multimeric complex is a functional apoptosome that activates procaspase-9. *J Biol Chem,* 274**,** 11549-56.

Publications

Biomol NMR Assign
DOI 10.1007/s12104-015-9621-3

ARTICLE

Backbone resonance assignments of ferric human cytochrome *c* and the pro-apoptotic G41S mutant in the ferric and ferrous states

Andreas Ioannis Karsisiotis[1] · Oliver M. Deacon[1] · Badri S. Rajagopal[1] · Colin Macdonald[2] · Tharin M. A. Blumenschein[2] · Geoffrey R. Moore[2] · Jonathan A. R. Worrall[1]

Received: 14 January 2015 / Accepted: 26 June 2015

Abstract Human cytochrome *c* is a multi-functional protein with key roles in both the mitochondrial electron transfer chain and in apoptosis. In the latter, a complex formed between the mitochondrial phospholipid cardiolipin and cytochrome *c* is crucial for instigating the release of pro-apoptotic factors, including cytochrome *c*, from the mitochondrion into the cytosol. The G41S mutant of human cytochrome *c* is the only known disease-related variant of cytochrome *c* and causes increased apoptotic activity in patients with autosomal dominant thrombocytopenia. NMR spectroscopy can be used to investigate the interaction of human cytochrome *c* with cardiolipin and the structural and dynamic factors, which may contribute to enhanced apoptotic activity for the G41S mutant. We present here essentially full backbone amide resonance assignments for ferric human cytochrome *c* (98 %) as well as assignments of both the ferric (92 %) and ferrous (95 %) forms of the G41S mutant. Backbone amide chemical shift differences between the wild type and G41S mutant in the ferric state reveals significant changes around the mutation site, with many other amides also affected. This suggests the possibility of increased dynamics and/or a change in the paramagnetic susceptibility tensor of the G41S mutant relative to the wild type protein.

Keywords Human cytochrome *c* · Mitochondria · Apoptosis · Paramagnetic NMR

✉ Jonathan A. R. Worrall
jworrall@essex.ac.uk

[1] School of Biological Sciences, University of Essex, Wivenhoe Park, Colchester CO4 3SQ, UK

[2] School of Chemistry, University of East Anglia, Norwich Research Park, Norwich NR4 7TJ, UK

Biological context

Mitochondrial cytochrome *c* (cyt *c*) participates in two important cellular processes in invertebrates (Huttemann et al. 2011). As a redox protein it shuttles electrons from complex III to complex IV in the mitochondrial respiratory chain leading to the production of ATP. In cells undergoing apoptosis it first functions as a peroxidase upon complex formation with cardiolipin (CL), prior to its release from the mitochondrion (Kagan et al. 2005), where it is then required along with dATP and Apoptotic peptidase activating factor 1 (Apaf-1) to form the cytosolic apoptosome assembly that initiates caspase activity and cell death (Liu et al. 1996; Wang 2001).

Cyt *c* is a small (~12.5 kDa) α-helical protein with a *c*-type haem covalently attached to the polypeptide chain via two thioether linkages arising from Cys residues present in a CXXXCH motif (Moore and Pettigrew 1990). The haem-iron is six-coordinate with the Nε2 atom of a His, part of the CXXXCH motif, acting as one axial ligand and the Sδ atom of a Met residue as the second. The haem-iron is redox active and when six-coordinate can access the ferric (Fe^{3+}) and ferrous (Fe^{2+}) oxidation states, with the ferric state paramagnetic (S = ½) and the ferrous state diamagnetic (S = 0). In the ferric form an equilibrium between a six- and five-coordinate haem exists, resulting from the dissociation/association of the axial Met ligand (Moore and Pettigrew 1990). At physiological pH this equilibrium lies firmly towards the six-coordinate species. Cyt *c* from horse heart and *Saccharomyces cerevisiae* have been the subject of extensive biophysical and biochemical studies over the years, including numerous NMR studies (Pielak et al. 1996). However, from a biophysical perspective human cyt *c* has been less well studied.

Published online: 30 June 2015

The discovery of the role in apoptotic cells of the cyt *c*/CL complex has stimulated numerous biophysical investigations of this complex (Bradley et al. 2011; Hanske et al. 2012; Hong et al. 2012; Rajagopal et al. 2012; Sinibaldi et al. 2008). The interaction is proposed to cause a 'loosening' of the cyt *c* structure leading to dissociation of the axial Met ligand enabling the reactive oxygen species, H_2O_2, to readily react with the five-coordinate haem, resulting in the peroxidation of the bound CL (Kagan et al. 2005). Further interest in the biophysical properties of human cyt *c* has stemmed from the discovery of the G41S mutation in a group of patients suffering from autosomal dominant thrombocytopenia; a condition consistent with enhanced apoptotic activity (Morison et al. 2008). In vitro the G41S mutant has an enhanced ability to activate caspases (Morison et al. 2008). Furthermore, in its native state and when complexed to CL the G41S mutant displays increased peroxidatic activity (Josephs et al. 2014; Rajagopal et al. 2013). In the native state this likely arises from a change in the 'on' rate of the axial Met equilibrium, which may stem from changes in the dynamic properties as a result of the mutation.

Currently, no atomic resolution information of the cyt *c*/CL complex is available, but the development of new methodologies that incorporate NMR spectroscopy to study protein:phospholipid complexes in solution have the potential to provide this information. Likewise, NMR is well suited to explore dynamics over multiple time-scales, and can therefore be suitably applied to investigate the dynamic properties of the G41S mutant. As a prelude to the aforementioned investigations, this assignment note reports the backbone resonance assignments of the ferric human cyt *c* and the ferric and ferrous forms of its G41S mutant and compares backbone amide (HN) chemical shift differences between the pair.

Methods and experiments

Protein expression and purification

Construction of the G41S mutant of human cyt *c* has been previously reported (Rajagopal et al. 2013). Overexpression of uniformly-labelled ^{13}C, ^{15}N wild type (WT) and G41S proteins was carried out in *Escherichia coli* using BL21(DE3) RIL cells (Invitrogen) by the co-expression of genes for the WT or G41S and yeast haem lyase in a $pUC19^{Amp}$ vector. Starting cultures, consisting of 3 ml of Terrific Broth (Melford Chemicals), were inoculated with overnight transformants and grown at 37 °C with shaking at 220 rpm for ~4 h. Autoclaved M9 minimal media salts were supplemented with 0.8 g/L $^{15}NH_4Cl$, 5 g/L $^{13}C_6$-glucose, 10 ml/L trace elements mix, 10 ml/L vitamin mix, 10 ml/L 1 M $MgCl_2$, and 6 ml/L thiamine as described in (Cai et al. 1998). In addition δ-aminolevulinic acid (Sigma) as the first committed precursor of haem biosynthesis was added to a final concentration of 0.1 mM. A 2 L flask containing ~360 ml of supplemented minimal media mix was inoculated with 2 ml of pre-culture and growth continued at 37 °C with shaking at 250 rpm until induction at an OD_{600} of 0.6–0.8 with IPTG (Melford) to a final concentration of 1 mM. Cells were harvested after 16 h by centrifugation and purification was carried out as previously described (Pollock et al. 1998; Rajagopal et al. 2013).

Sample preparation and NMR spectroscopy

Ferric cyt *c* was prepared by the addition of 1.5-fold excess of $K_3[Fe(CN)_6]$ (Sigma) followed by removal of the excess $K_3[Fe(CN)_6]$ and $K_4[Fe(CN)_6]$ and exchange into 20 mM sodium phosphate pH 6.8, 50 mM NaCl using a PD-10 column (GE-Healthcare). For reduced samples excess sodium ascorbate (Sigma) was added followed by removal and exchange into the same buffer as the ferric samples. All NMR samples contained 1 mM of the respective protein with 8–10 % D_2O (Sigma) for the lock. A set of 2D [^1H, ^{15}N]-HSQC and 3D HNCACB and CBCA(CO)NH spectra were recorded at 293 K for ferric WT human cyt *c* on a Bruker 800 MHz spectrometer equipped with a 5 mm HCN inverse triple resonance z-axis gradient probe. For the ferrous G41S, all spectra were acquired at 288 K on a Varian INOVA 900 MHz spectrometer equipped with a 5 mm HCN cryogenic probe, while for the G41S ferric protein all spectra were acquired at 288 K on a Bruker AVANCE III 900 MHz spectrometer equipped with a 5 mm TCI cryogenic probe. Both 900 MHz probes were equipped with z-axis pulse field gradients. The same set of spectra as for WT cyt *c* were acquired for the ferrous G41S protein. Non-uniform sampling (NUS) experiments of the 3D HNCACB, CBCA(CO)NH and HNCO spectra were collected for the ferric G41S protein, with NUS versions of C(CCO)NH and H(CCO)NH TOCSY spectra used to confirm assignments. Non-NUS spectra were processed using the NMRPipe/NMRDraw software package (Delaglio et al. 1995) or using Topspin (Bruker BioSpin). NUS spectra were processed with software qMDD (Orekhov and Jaravine 2011), in conjunction with NMRPipe. All assignments were obtained using the graphical NMR assignment program Sparky (Goddard and Kneller 2008) and/or the CCPN Analysis program (Vranken et al. 2005).

Resonance assignments

Figure 1 shows the [^1H, ^{15}N]-HSQC spectra with resonance assignments indicated for the WT and G41S mutant

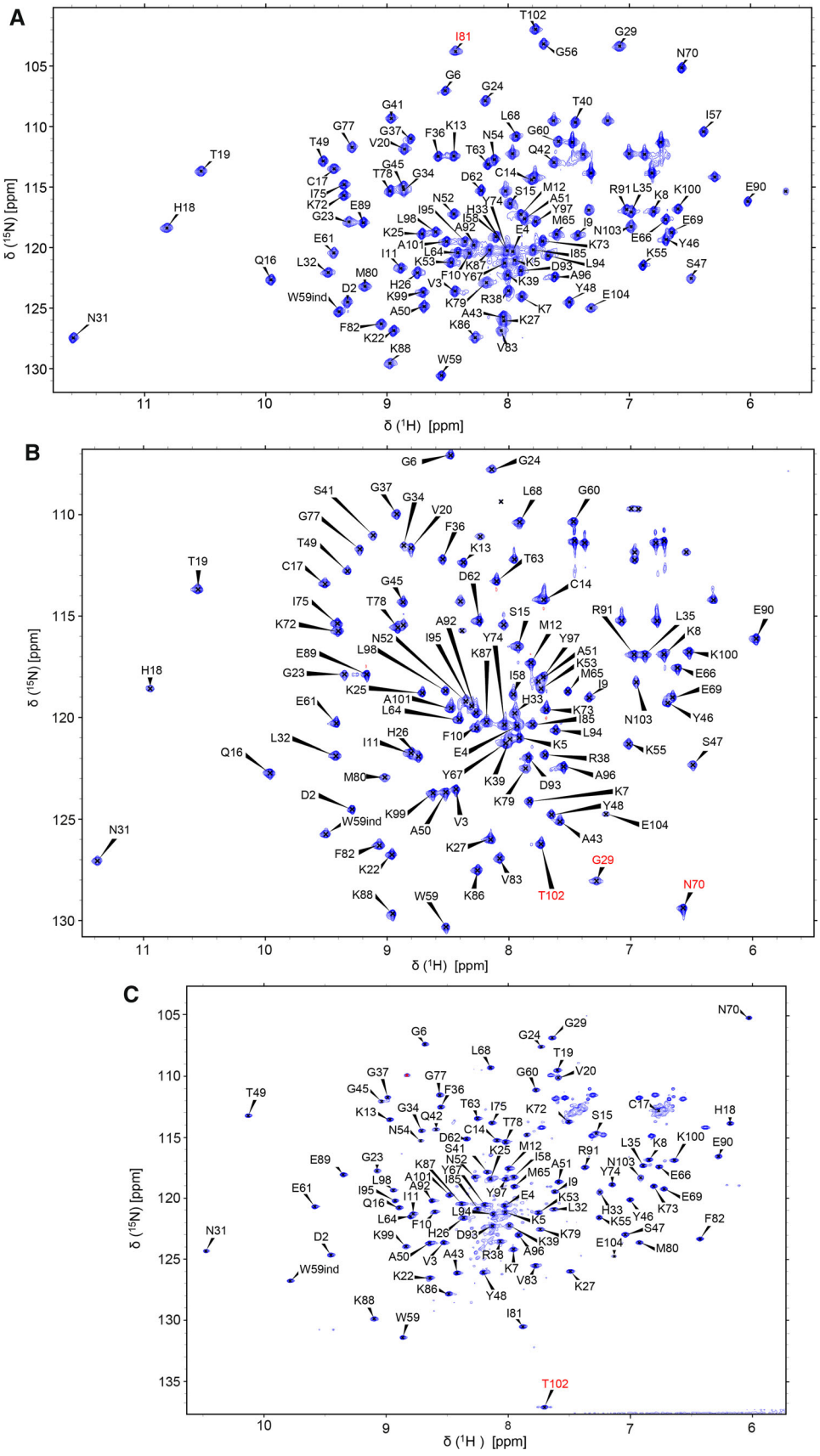

Fig. 1 [^{1}H, ^{15}N]-HSQC spectra of human cyt *c* **a** WT ferric (293 K), **b** G41S ferric (288 K) and **c** G41S ferrous (288 K). The resonance assignments of the backbone HN and tryptophan indole resonances are indicated. Aliased residues in the ^{15}N dimension are marked in *red*

of human cyt *c*. Out of the 99 non-proline residues all HN resonances were assigned for the WT ferric cyt *c*, with the exception of E21 and T28, which were not observed. These resonances were also not observed in the ferric or ferrous states of the G41S mutant. Resonances for these residues are also not assigned in equine cyt *c* (Volkov et al. 2012). A strongly shifted upfield H^N resonance (~4.45 and ~4.29 ppm for ferric and ferrous species, respectively, ~104.25 ppm in ^{15}N) is observed in all spectra regardless of mutation or haem oxidation state. Volkov et al. (2012) have assigned this resonance to G84 in horse heart cyt *c* based on the HN of G84 being located close to the centre of the F82 phenyl ring and therefore likely to experience a strong ring-current effect. Inspection of the human cyt *c* crystal structure (PDB entry 3ZCF) (Rajagopal et al. 2013), indicates a similar orientation and thus we assign our observed upfield shifted H^N resonance in human cyt *c* to G84.

For the ferric G41S protein the HN resonances of T40, Q42, N54, G56, I57 and I81 are not assigned, whilst for the ferrous protein the HN resonances of T40, G56 and I57 remain unassigned. The HN resonances for these residues are not observed in the [^1H, ^{15}N]-HSQC spectra and triple resonance peaks associated are either absent or of poor quality. This could be explained by mobility around the mutation site in regions 40–42 and 54–57 of the G41S mutant leading to broad resonances. Residue 81 in the ferric G41S protein is aliased in the ^{15}N dimension and not observed in the NUS triple resonance spectra.

Chemical shift differences

A set of 2D [^1H, ^{15}N]-HSQC spectra of ferric and ferrous WT human cyt *c* were recorded at 288 K so as to analyse chemical shift differences between the G41S mutant. The HN assignments for the WT ferric were transferred readily to the 288 K spectrum, whereas assignments for the WT ferrous spectrum were acquired from those previously deposited (BMRB accession number 5406) (Jeng et al. 2002). Representations of the combined backbone HN chemical shift differences between WT and the G41S mutant in the different haem oxidation states are shown in Fig. 2. The two pairs of HSQC spectra were referenced with respect to each other based on their corresponding ^1H and ^{15}N carrier frequencies where the ^1H carrier was placed on the water resonance. It is apparent that the G41S mutation introduces large chemical shift differences in both oxidation states for residues 41, 42 and 43 (mutation site) as well as 48 and 53 (HN groups in hydrogen bond distance of the S41 side-chain). However, the ferric state of the mutant reveals more extensive changes (residues 29–38, 49–52, 55–60 and 79–80) and the magnitude of perturbation is greater (Fig. 2a). The ferric state of mitochondrial

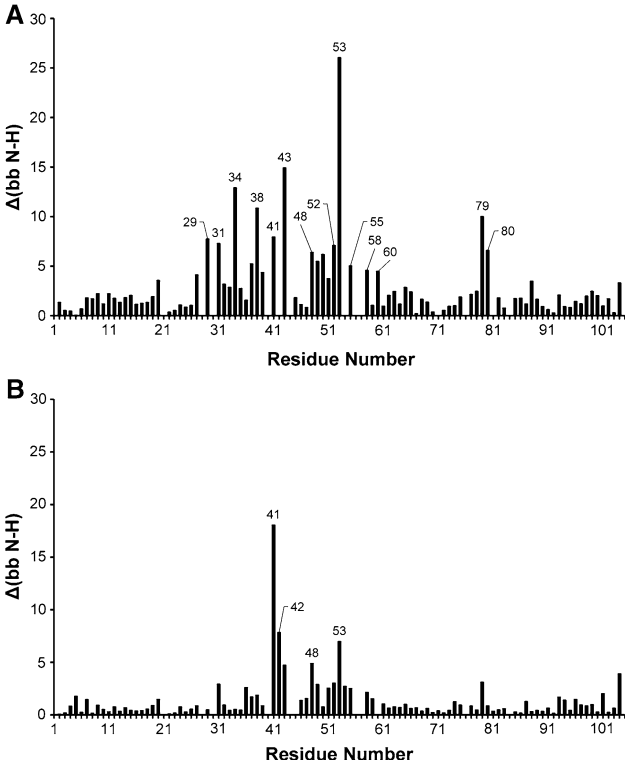

Fig. 2 Backbone HN chemical shift perturbations caused by the G41S mutation for the ferric (**a**) and ferrous (**b**) forms of human cyt *c*. Combined chemical shift differences at 288 K are presented as a function of the amino acid sequence and were calculated as $\sqrt{[(\Delta H^N/0.03)^2 + (\Delta N^H/0.3)^2]}$

cyt *c* is more dynamic than the ferrous state (Barker et al. 2001; Moore and Pettigrew 1990), which could account for some of the differences between the two oxidation states of the G41S mutant and may also imply that the G41S protein is more dynamic than the ferric WT. Another explanation could be that the haem paramagnetic susceptibility tensor is perturbed in the G41S mutant relative to the WT ferric. This would alter the contact shift contribution (e.g. M80 Fig. 2a) and the pseudocontact contribution to the chemical shift, with the latter experienced by many of the residues in the protein. Further investigations into this and the dynamics of the G41S mutant are underway.

Data bank deposition

Backbone (H^N, N, Cα, Cβ) resonance assignments for ferric WT and the ferric and ferrous G41S human cyt *c* have been deposited in the BioMagResBank database under the accession numbers 25,418, 25,422 and 25,420, respectively. For the ferric G41S protein backbone CO resonances have also been deposited.

Acknowledgments We acknowledge the open access use of the Wellcome Trust-funded (grants 083796/Z/07/Z and 099185/Z/12/Z)

900 MHz spectrometer at the HWB-NMR facility at the University of Birmingham and thank Dr Sara Whittaker for assistance with the acquisition of the triple resonance experiments at this facility. This work was supported by a Leverhulme Trust project grant (RPG-2013-164) to JARW and a Leverhulme Trust emeritus fellowship (EM-2014-088) to GRM.

References

Barker PD et al (2001) A further clue to understanding the mobility of mitochondrial yeast cytochrome c: a (15)N T1rho investigation of the oxidized and reduced species. Eur J Biochem 268: 4468–4476

Bradley JM, Silkstone G, Wilson MT, Cheesman MR, Butt JN (2011) Probing a complex of cytochrome C and cardiolipin by magnetic circular dichroism spectroscopy: implications for the initial events in apoptosis. J Am Chem Soc 133:19676–19679

Cai M, Huang Y, Sakaguchi K, Clore GM, Gronenborn AM, Craigie R (1998) An efficient and cost-effective isotope labeling protocol for proteins expressed in *Escherichia coli*. J Biomol NMR 11:97–102

Delaglio F, Grzesiek S, Vuister GW, Zhu G, Pfeifer J, Bax A (1995) NMRPipe: a multidimensional spectral processing system based on UNIX pipes. J Biomol NMR 6:277–293

Goddard TD, Kneller DG (2008) SPARKY 3 University of California, San Francisco

Hanske J, Toffey JR, Morenz AM, Bonilla AJ, Schiavoni KH, Pletneva EV (2012) Conformational properties of cardiolipin-bound cytochrome c. Proc Natl Acad Sci USA 109:125–130. doi:10.1073/pnas.1112312108

Hong Y, Muenzner J, Grimm SK, Pletneva EV (2012) Origin of the conformational heterogeneity of cardiolipin-bound cytochrome C. J Am Chem Soc 134:18713–18723. doi:10.1021/ja307426k

Huttemann M et al (2011) The multiple functions of cytochrome c and their regulation in life and death decisions of the mammalian cell: from respiration to apoptosis. Mitochondrion 11:369–381. doi:10.1016/j.mito.2011.01.010

Jeng WY, Chen CY, Chang HC, Chuang WJ (2002) Expression and characterization of recombinant human cytochrome c in *E. coli*. J Bioenerg Biomembr 34:423–431

Josephs TM, Morison IM, Day CL, Wilbanks SM, Ledgerwood EC (2014) Enhancing the peroxidase activity of cytochrome c by mutation of residue 41: implications for the peroxidase mechanism and cytochrome c release. Biochem J 458:259–265. doi:10.1042/bj20131386

Kagan VE et al (2005) Cytochrome c acts as a cardiolipin oxygenase required for release of proapoptotic factors. Nat Chem Biol 1:223–232

Liu X, Kim CN, Yang J, Jemmerson R, Wang X (1996) Induction of apoptotic program in cell-free extracts: requirement for dATP and cytochrome c. Cell 86:147–157

Moore GR, Pettigrew GW (1990) Cytochrome c: evolutionary, structural and physicochemical aspects. Springer, London

Morison IM et al (2008) A mutation of human cytochrome c enhances the intrinsic apoptotic pathway but causes only thrombocytopenia. Nat Genet 40:387–389

Orekhov VY, Jaravine VA (2011) Analysis of non-uniformly sampled spectra with multi-dimensional decomposition. Prog Nucl Magn Reson Spectrosc 59:271–292. doi:10.1016/j.pnmrs.2011.02.002

Pielak GJ, Auld DS, Betz SF, Hilgen-Willis SE, Garcia LL (1996) Cytochrome c: a multidisciplinary approach. University Science Books, Sausalito

Pollock WB, Rosell FI, Twitchett MB, Dumont ME, Mauk AG (1998) Bacterial expression of a mitochondrial cytochrome c. Trimethylation of lys72 in yeast iso-1-cytochrome c and the alkaline conformational transition. Biochemistry 37:6124–6131

Rajagopal BS, Silkstone GG, Nicholls P, Wilson MT, Worrall JA (2012) An investigation into a cardiolipin acyl chain insertion site in cytochrome c. Biochim Biophys Acta 1817:780–791. doi:10.1016/j.bbabio.2012.02.010

Rajagopal BS et al (2013) The hydrogen-peroxide-induced radical behaviour in human cytochrome c-phospholipid complexes: implications for the enhanced pro-apoptotic activity of the G41S mutant. Biochem J 456:441–452. doi:10.1042/bj20130758

Sinibaldi F, Fiorucci L, Patriarca A, Lauceri R, Ferri T, Coletta M, Santucci R (2008) Insights into cytochrome c-cardiolipin interaction. Role played by ionic strength. Biochemistry 47:6928–6935

Volkov AN, Vanwetswinkel S, Van de Water K, van Nuland NA (2012) Redox-dependent conformational changes in eukaryotic cytochromes revealed by paramagnetic NMR spectroscopy. J Biomol NMR 52:245–256. doi:10.1007/s10858-012-9607-8

Vranken WF et al (2005) The CCPN data model for NMR spectroscopy: development of a software pipeline. Proteins 59:687–696. doi:10.1002/prot.20449

Wang X (2001) The expanding role of mitochondria in apoptosis Genes and development 15:2922–2933

Biomol NMR Assign
DOI 10.1007/s12104-017-9740-0

ARTICLE

Near-complete backbone resonance assignments of acid-denatured human cytochrome *c* in dimethylsulfoxide: a prelude to studying interactions with phospholipids

Andreas Ioannis Karsisiotis[1] · Oliver M. Deacon[1] · Colin Macdonald[2] · Tharin M. A. Blumenschein[2] · Geoffrey R. Moore[2] · Jonathan A. R. Worrall[1]

Received: 18 December 2016 / Accepted: 24 February 2017

Abstract Human cytochrome *c* plays a central role in the mitochondrial electron transfer chain and in the intrinsic apoptosis pathway. Through the interaction with the phospholipid cardiolipin, cytochrome *c* triggers release of pro-apoptotic factors, including itself, from the mitochondrion into the cytosol of cells undergoing apoptosis. The cytochrome *c*/cardiolipin complex has been extensively studied through various spectroscopies, most recently with high-field solution and solid-state NMR spectroscopies, but there is no agreement between the various studies on key structural features of cytochrome *c* in its complex with cardiolipin. In the present study, we report backbone ^{1}H, ^{13}C, ^{15}N resonance assignments of acid-denatured human cytochrome *c* in the aprotic solvent dimethylsulfoxide. These have led to the assignment of a reference 2D ^{1}H-^{15}N HSQC spectrum in which out of the 99 non-proline residues 87% of the backbone amides are assigned. These assignments are being used in an interrupted H/D exchange strategy to map the binding site of cardiolipin on human cytochrome *c*.

Keywords Human cytochrome *c* · Apoptosis · Cardiolipin · Acid-denatured · DMSO

✉ Jonathan A. R. Worrall
jworrall@essex.ac.uk

[1] School of Biological Sciences, University of Essex, Wivenhoe Park, Colchester CO4 3SQ, UK

[2] School of Chemistry, University of East Anglia, Norwich Research Park, Norwich NR4 7TJ, UK

Biological context

Mitochondrial cytochrome *c* (cyt *c*) is a small (~12.5 kDa) soluble heme containing protein that plays a key role in life and death decisions of the cell (Huttemann et al. 2011). For life-sustaining energy production, cyt *c* acts as an electron carrier (redox protein) in the mitochondrial electron transfer chain (ETC) leading to the production of adenosine triphosphate (ATP). When problems caused by stress outweigh the benefits of sustaining viability of a cell, various signals can initiate the programmed cell death process through intrinsic (mitochondrial) type II apoptosis. In cells undergoing type II apoptosis, the phospholipid 1,3-bis(sn-3′-phosphatidyl)-sn-glycerol, commonly referred to as cardiolipin (CL) hijacks the ETC function of cyt *c* to create a protein-phospholipid complex in which cyt *c* is converted to a peroxidase enzyme through the dissociation of the axial Met80 heme ligand (Kagan et al. 2005). This new function of cyt *c* when bound to CL leads to the peroxidation of CL upon reaction of H_2O_2 with the cyt *c* heme, resulting in the dissociation of the complex. The modified CL then serves as a signal for downstream events that culminate in the permeabilisation of the outer mitochondrial membrane and subsequent release of pro-apoptotic factors, including cyt *c*, into the cytoplasm (Ow et al. 2008).

NMR spectroscopy is an amenable technique to study protein complexes, with complex interfaces being readily mapped through simple chemical shift perturbation experiments (Rajagopal et al. 1997). In recent times advances in site-specific isotope labelling methods and the development of paramagnetic probes have pushed the boundaries of conventional liquid-state NMR to encompass the study of large and dynamic complexes (Clore et al. 2007). The characterisation of phospholipid-bound soluble proteins is a challenge by liquid-state NMR. One approach that we

Published online: 04 March 2017

are adapting to address this problem is to employ an interrupted H/D exchange method. This relies on the dissociation of the protein-phospholipid complex under the conditions that preserve the backbone amide protection patterns established in the complex by measuring the sample in an aprotic solvent, such as dimethysulfoxide (DMSO), preventing further H/D exchange. In this way information relating to the phospholipid binding site will be preserved and this can be extracted by comparing backbone amide protection factors in the absence of the phospholipid, creating an initial snapshot of the phospholipid binding site. A similar approach to determine the structure of amyloid fibrils (Hoshino et al. 2002), in protein-folding studies (Nishimura et al. 2005) and to delineate contact sites in a protein–protein complex (Dyson et al. 2008) have been reported.

Two recent NMR studies investigating the interaction of horse heart cyt *c* and CL have been reported. The first reports on a multidimensional magic angle spinning (MAS) solid-sate NMR investigation with CL containing lipid-bilayers (Mandal et al. 2015) and the second is a liquid-state study with cyt *c* encapsulated in a CL-containing micelle (O'Brien et al. 2015). Surprisingly, both studies reveal only minimal chemical shift changes upon interaction with CL, implying no gross structural changes. This is opposed to FRET and other spectroscopic studies whereby large structural changes are inferred to occur on binding CL that drive the creation of the peroxidase form (Hanske et al. 2012; Hong et al. 2012; Muenzner et al. 2013). We aim to investigate the complex of human cyt *c* (hcyt *c*) and CL using a tailored interrupted H/D-exchange approach as outlined above. As a prelude to this we report here the near complete ^{1}H, ^{15}N, ^{13}C sequential assignments of acid-denatured hcyt *c* in DMSO.

Materials and experiments

Sample preparation and NMR spectroscopy

Over-expression and purification of uniformly-labelled ^{13}C, ^{15}N wild-type hcyt *c* was carried out as previously described (Karsisiotis et al. 2015). Ferric hcyt c was prepared by the addition of 1.5-fold excess of $K_3[Fe(CN)_6]$ (Sigma) followed by removal of the excess $K_3[Fe(CN)_6]$ and $K_4[Fe(CN)_6]$ and desalted into 20 mM sodium phosphate pH 7 using a PD-10 column (GE-Healthcare). Samples were then concentrated using 5 kDa cut-off concentrators, acid-quenched with 0.3% v/v trifluoracetic acid (TFA) (Acros Chemicals), flash frozen, freeze-dried overnight and stored at −20 °C. Lyophilised samples were dissolved in 100% DMSO (Sigma) with the addition of a small amount of D_2O for the lock, supplemented with 0.2% v/v TFA to aid solubility during resuspension, to give a final volume of 500 µl and a concentration of ~1 mM. All NMR experiments were performed at 308 K and acquired on a Bruker 800 MHz spectrometer equipped with a 5 mm HCN inverse triple resonance z-axis gradient probe. Data were processed with either Topspin (Bruker Biospin) or the NMRPipe and NMRDraw package (Delaglio et al. 1995) or a combination of both programs. Data analysis was performed with the graphical NMR assignment program Sparky (Goddard and Kneller 2008) and the CCPNmr Analysis program (Vranken et al. 2005).

Assignments strategy

The NMR method we have been developing to investigate the interaction of hcyt *c* with CL is based around an interrupted H/D-exchange approach. To arrest H/D exchange the pH of the sample is acidified through the addition of TFA, which also acts as a counter-ion in enabling the freeze-quenched sample at a set-exchange time point, to be more easily dissolved in the aprotic solvent DMSO. As expected therefore, the amide proton chemical shift dispersion of acid-denatured hcyt *c* in DMSO falls into a very narrow spectral width (Fig. 1). This caused severe overlap in traditional sequence specific assignment experiment pairs, such as the 3D HNCACB/CBCA(CO)NH spectra. Therefore, experiments relying on carbonyl (i) and ($i-1$) connectivities, were additionally acquired, such as the HNCO/HN(CA)CO pair. However, these experiments are also susceptible to the narrow amide proton spectral width and were thus only used to corroborate existing assignment steps. An essential component of the assignment strategy to tackle resonance overlap in an unfolded protein was the use of the HNN experiment (Panchal et al. 2001). This provides ($i-1$), (i) and ($i+1$) connectivities and exploits the ^{15}N chemical shift dispersions which are less affected in unfolded proteins, compared to folded proteins. Specifically, for any ^{1}H–^{15}N plane intra-residual (i), sequential ($i-1$) and ($i+1$) ^{15}N peaks are provided, thus connecting any amide with the amide nitrogen chemical shift of the preceding and the following residue. In addition, a very important secondary source of information is that, in these peak triplets, the sign of the diagonal (i) and sequential ($i-1$) and ($i+1$) peaks is dependent on the nature of adjacent residues (glycines and prolines particularly) (Panchal et al. 2001). This feature provided additional sequence specific assignment checkpoints or starting points to use in conjunction with the traditional triple resonance experiment pairs. While the HNN experiment was particularly useful in the identification or verification of possible assignments, it was also susceptible to resonance overlap and poor spectral quality for some residues.

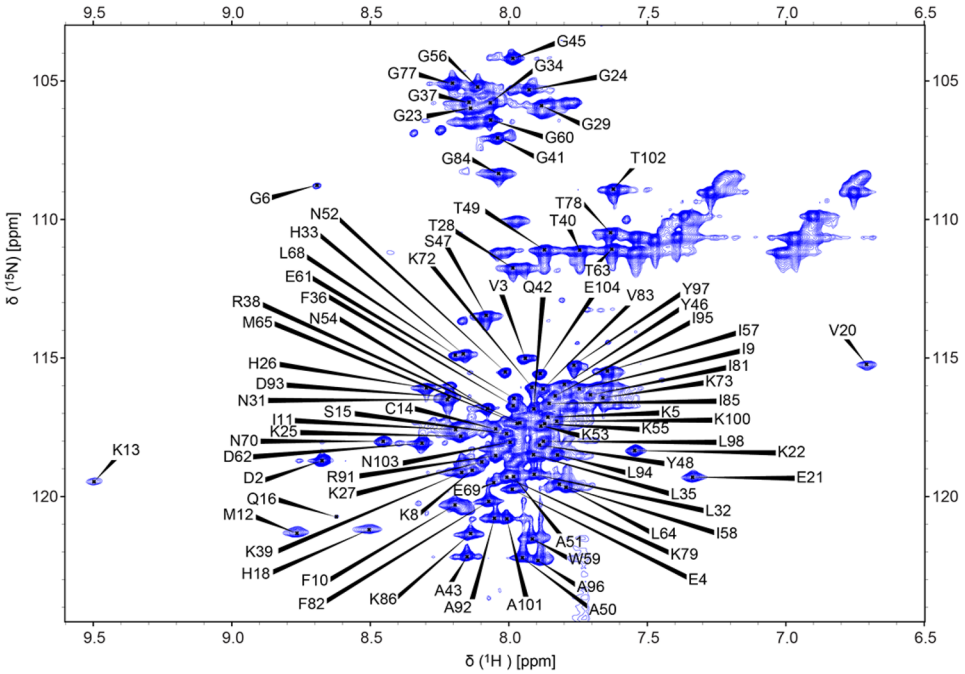

Fig. 1 [^{1}H, ^{15}N]-HSQC spectrum (308 K) of acid-denatured hcyt *c* in the aprotic solvent DMSO. The resonance assignments of the backbone HN resonances are indicated

Extent of resonance assignments

Backbone amide proton and nitrogen resonance assignments were obtained for 87% of the 99 non-proline residues in hcyt *c* (Fig. 1). This compares to the 98% of backbone amide resonances assigned in hcyt *c* under native conditions (Karsisiotis et al. 2015). Resonances which were not assigned in the present work are: K7, C17, T19, E66, Y67, Y74, I75, M80, K87, K88, E89, E90 and K100. These reflect either resonances not observed or severe overlap that cannot be resolved. The assignments for K8, H18, L68 and E69 have more ambiguity but they were included in the current dataset. This set of assignments are being used in conjunction with the development of an interrupted H/D exchange strategy to obtain both dynamic and structural information regarding the cardiolipin binding site on hcyt *c*. Encouragingly a good number of 2D ^{1}H–^{15}N HSQC assignments, between 40 and 50, are transferable between data sets, subject to small chemical shift perturbations when the acid-quench and DMSO conditions vary. However, in the highly-overlapped region of the spectrum (^{15}N: 115–121 and ^{1}H: 7.6–8.3 ppm), assignment transfer becomes difficult or impossible. Therefore, upon finalising exchange method conditions, a new set of triple resonance experiments is required, but the current assignments greatly speed up assignments of the new dataset. Alternatively, assignments can be transferred through a ^{1}H–^{15}N HSQC titration between the initial and final conditions. Finally, a factor that greatly enhances the usability of the current assignment set is that the proposed site(s) of CL interaction does not encompass the residues for which assignments are missing (O'Brien et al. 2015).

Data bank deposition

Backbone (H^{N}, N, CA, CB CO) resonance assignments have been deposited in the BioMagResBank database under the accession number 26973.

Acknowledgements This work was supported by a Leverhulme Trust project grant (RPG-2013-164) to JARW and a Leverhulme Trust emeritus fellowship (EM-2014-088) to GRM.

References

Clore GM, Tang C, Iwahara J (2007) Elucidating transient macromolecular interactions using paramagnetic relaxation enhancement. Curr Opin Struct Biol 17:603–616. doi:10.1016/j.sbi.2007.08.013

Delaglio F, Grzesiek S, Vuister GW, Zhu G, Pfeifer J, Bax A (1995) NMRPipe: a multidimensional spectral processing system based on UNIX pipes. J Biomol NMR 6:277–293

Dyson HJ, Kostic M, Liu J, Martinez-Yamout MA (2008) Hydrogen-deuterium exchange strategy for delineation of contact sites in protein complexes. FEBS Lett 582:1495–1500

Goddard TD, Kneller DG (2008) SPARKY 3. University of California, San Francisco

Hanske J, Toffey JR, Morenz AM, Bonilla AJ, Schiavoni KH, Pletneva EV (2012) Conformational properties of cardiolipin-bound cytochrome *c*. Proc Natl Acad Sci U S A 109:125–130. doi:10.1073/pnas.1112312108

Hong Y, Muenzner J, Grimm SK, Pletneva EV (2012) Origin of the conformational heterogeneity of cardiolipin-bound cytochrome *c*. J Am Chem Soc 134:18713–18723. doi:10.1021/ja307426k

Hoshino M, Katou H, Hagihara Y, Hasegawa K, Naiki H, Goto Y (2002) Mapping the core of the beta(2)-microglobulin amyloid fibril by H/D exchange. Nat Struct Biol 9:332–336

Huttemann M et al (2011) The multiple functions of cytochrome *c* and their regulation in life and death decisions of the mammalian cell: From respiration to apoptosis. Mitochondrion 11:369–381. doi:10.1016/j.mito.2011.01.010

Kagan VE et al (2005) Cytochrome *c* acts as a cardiolipin oxygenase required for release of proapoptotic factors. Nat Chem Biol 1:223–232

Karsisiotis AI, Deacon OM, Rajagopal BS, Macdonald C, Blumenschein TM, Moore GR, Worrall JA (2015) Backbone resonance assignments of ferric human cytochrome *c* and the pro-apoptotic G41S mutant in the ferric and ferrous states. Biomol NMR Assign 9:415–419 doi:10.1007/s12104-015-9621-3

Mandal A, Hoop CL, DeLucia M, Kodali R, Kagan VE, Ahn J, van der Wel PC (2015) Structural changes and proapoptotic peroxidase activity of cardiolipin-bound mitochondrial cytochrome *c*. Biophys J 109:1873–1884. doi:10.1016/j.bpj.2015.09.016

Muenzner J, Toffey JR, Hong Y, Pletneva EV (2013) Becoming a peroxidase: cardiolipin-induced unfolding of cytochrome *c*. J Phys Chem B 117:12878–12886 doi:10.1021/jp402104r

Nishimura C, Dyson HJ, Wright PE (2005) Enhanced picture of protein-folding intermediates using organic solvents in H/D exchange and quench-flow experiments. Proc Natl Acad Sci U S A 102:4765–4770

O'Brien ES, Nucci NV, Fuglestad B, Tommos C, Wand AJ (2015) Defining the apoptotic trigger: The interaction of cytochrome *c* and cardiolipin. J Biol Chem 290:30879–30887. doi:10.1074/jbc.M115.689406

Ow YP, Green DR, Hao Z, Mak TW (2008) Cytochrome *c*: functions beyond respiration. Nat Rev Mol Cell Biol 9:532–542

Panchal SC, Bhavesh NS, Hosur RV (2001) Improved 3D triple resonance experiments, HNN and HN(C)N, for HN and ^{15}N sequential correlations in (13 C, 15 N) labeled proteins: application to unfolded proteins. J Biomol NMR 20:135–147

Rajagopal P, Waygood EB, Reizer J, Saier MH Jr, Klevit RE (1997) Demonstration of protein-protein interaction specificity by NMR chemical shift mapping. Protein Sci 6:2624–2627. doi:10.1002/pro.5560061214

Vranken WF et al (2005) The CCPN data model for NMR spectroscopy: development of a software pipeline. Proteins 59:687–696. doi:10.1002/prot.20449

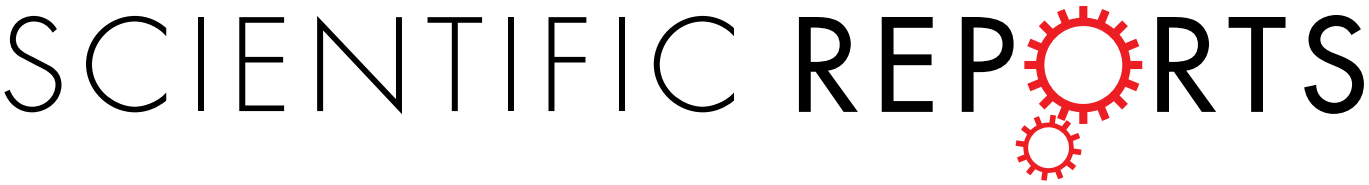

OPEN

Increased dynamics in the 40–57 Ω-loop of the G41S variant of human cytochrome *c* promote its pro-apoptotic conformation

Received: 28 April 2016
Accepted: 05 July 2016
Published: 27 July 2016

Andreas Ioannis Karsisiotis[1], Oliver M. Deacon[1], Michael T. Wilson[1], Colin Macdonald[2], Tharin M. A. Blumenschein[2], Geoffrey R. Moore[2] & Jonathan A. R. Worrall[1]

Thrombocytopenia 4 is an inherited autosomal dominant thrombocytopenia, which occurs due to mutations in the human gene for cytochrome *c* that results in enhanced mitochondrial apoptotic activity. The Gly41Ser mutation was the first to be reported. Here we report stopped-flow kinetic studies of azide binding to human ferricytochrome *c* and its Gly41Ser variant, together with backbone amide H/D exchange and ^{15}N-relaxation dynamics using NMR spectroscopy, to show that alternative conformations are kinetically and thermodynamically more readily accessible for the Gly41Ser variant than for the wild-type protein. Our work reveals a direct conformational link between the 40–57 Ω-loop in which residue 41 resides and the dynamical properties of the axial ligand to the heme iron, Met80, such that the replacement of glycine by serine promotes the dissociation of the Met80 ligand, thereby increasing the population of a peroxidase active state, which is a key non-native conformational state in apoptosis.

Mitochondrial cytochrome *c* (cyt) is a multifunctional protein that can act as an electron carrier in oxidative phosphorylation as a peroxidase in the early stages of the intrinsic apoptosis pathway, as a component of the apoptosome, a key complex in the apoptotic pathway and as a signalling molecule affecting the activity of the nuclear oncoprotein SET/template-activating factor-Iβ (SET/TAF-Iβ) complex[1–4]. Cyt possesses a hexacoordinate heme iron, where His18 and Met80 serve as the axial heme iron ligands, with the heme encapsulated in a hydrophobic environment created by a polypeptide fold of five α-helices and 3 Ω-loops (Fig. 1A). Under native conditions ferricyt possesses a low level of peroxidase activity[5] due to the existence of an equilibrium between the dominant hexacoordinate native form, and a minor populated pentacoordinate form in which Met80 is not coordinated to the heme iron[6]. Preceding its release from the mitochondrion at the onset of apoptosis, cyt forms a complex with the phospholipid cardiolipin (CL), which drives the formation of the pentacoordinate form and greatly boosts peroxidase activity[2,7]. Further to this, at alkaline pH, ferricyt can access a conformational state whereby a Lys residue (73 or 79) within the 71–85 Ω-loop replaces the native Met80 ligand[8]. This alkaline isomerisation occurs with an apparent pK of ~8–9, depending on solution conditions and temperature[9]. Thus ferricyt has several energetically accessible conformational states with very different properties from the native state.

Thrombocytopenia 4 (THC4; OMIM 612004) is an inherited autosomal disease, which occurs due to mutations in the human cytochrome *c* gene (*CYCS*) resulting in enhanced mitochondrial apoptotic activity[10]. Two mutations in the *CYCS* gene have been identified that produce the G41S and Y48H variants of human cytochrome *c* (H-cyt)[10,11]. The G41S and Y48H substitutions are located in the 40–57 Ω-loop[12–15], which has the lowest free energy of the five cooperative folding/unfolding units (foldons) assigned in cyt[16,17] (Fig. 1A). In the absence of CL the G41S variant has been shown to have increased peroxidase activity relative to the wild-type (WT) protein[18,19]. High-resolution X-ray structures for the WT and G41S variant of H-cyt have been determined[20,21] with no gross structural differences between them detected. However, subtle differences in a hydrogen-bond network in the vicinity of the heme propionate-7 substituent were observed[21] (Fig. 1B) and these may be significant as the electronic properties of the heme propionates are known to affect heme reactivity[22]. The increase in polarity

[1]School of Biological Sciences, University of Essex, Wivenhoe Park, Colchester, CO4 3SQ, UK. [2]School of Chemistry, University of East Anglia, Norwich Research Park, NR4 7TJ, UK. Correspondence and requests for materials should be addressed to G.R.M. (email: g.moore@uea.ac.uk) or J.A.R.W. (email: jworrall@essex.ac.uk)

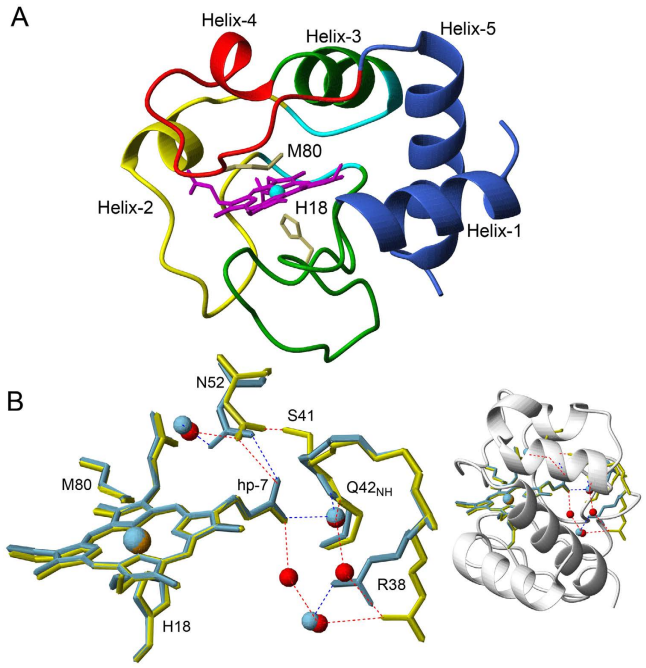

Figure 1. Structure of human cytochrome *c*. (**A**) Cartoon representation of H-cyt with the five foldons identified in horse cyt indicated and coloured as follows: the blue unit (N and C-terminal helices, residues 1–13, 86–104), the green unit (residues 14–36 Ω-loop, 62–70), the cyan neck unit (residues 37–39 and 58–61), the red unit (residues 71–85 Ω-loop) and the yellow unit (residues 40–57 Ω-loop). The His18 and Met80 ligands are labelled (PDB code: 3ZCF)[21]. (**B**) Positional movement of the Arg38 and Asn52 side chains identified in the G41S variant (yellow, PDB code: 3NWV)[20] compared to the WT protein (light blue, PDB code: 3ZCF)[21]. H-bond networks are illustrated as blue (WT) and red broken lines (G41S), with H_2O molecules shown as light blue (WT) and red (G41S) spheres. Note that in the G41S structure two additional H_2O molecules neighbour Arg38.

of the heme environment of the G41S protein resulting from the movement of Arg38 and the incorporation of additional water molecules (Fig. 1B) may also contribute to an ease of access of H_2O_2 to the heme of the G41S variant leading directly to its enhanced peroxidase activity[19,23]. In addition to the small conformational difference between WT and the G41S variant there is a substantial difference in global stability with the free energy of denaturation of WT H-ferricyt at 10.5 kcal mol^{-1} being 2.6 kcal mol^{-1} greater than that of the G41S variant[21].

Based on the inherent ability of ferricyt to access non-native conformations, it is a possibility that the G41S variant perturbs the dynamics of the H-ferricyt energy landscape, thereby changing the relative populations and kinetics of conversion between the native state and a non-native conformer. Solution state NMR spectroscopy is well suited to provide insight at atomic resolution on the dynamics and conformational changes that serve to regulate function in biomolecules[24,25]. Past NMR investigations have probed the backbone dynamics of cyt with the rationale of assessing whether differences in dynamics exist between the heme redox states[26–28]. In addition to NMR the dynamics of cyt are open to investigation by a variety of heme-centred approaches, particularly with ligand binding studies[6,29]. From such studies, combined with NMR data, a consensus exists that the energy landscapes of mitochondrial cyt differ considerably between redox states with the ferric form being more flexible[22,27] and having a lower stability than the ferrous form[22,30]. This may have functional implications for cyt function in apoptosis, as it is the ferric oxidation state that has been demonstrated to be necessary for interaction with key components of the apoptotic pathway such as the Apoptotic protease activating factor 1 (Apaf-1)[31] and also to facilitate peroxidase activity[32].

In the present study we have used azide (N_3^-) binding to the heme iron of H-ferricyt, backbone amide proton H/D exchange and ^{15}N relaxation dynamics of the oxidised protein to assess whether the G41S variant has altered dynamics compared to WT H-ferricyt. We find that the population of the pentacoordinate form is significantly greater for the G41S variant than the WT protein, and that the G41S variant has distinctly enhanced dynamics, particularly in the 40–57 Ω-loop foldon, which give rise to the increased lability of the Met80 ligand. These findings offer a direct structural insight into how main chain dynamics relate to key structural properties of the heme iron of H-ferricyt and importantly how the G41S variant is proapoptotic[10,19,21,23] in the context of thrombocytopenia 4.

Results and Discussion

The pentacoordinate heme form is more populated in the G41S variant. Exogenous ligand binding to ferricyt can be used as a diagnostic probe to assess the lability of the Met80 ligand. On mixing N_3^- with WT or G41S H-ferricyt an optical transition was observed (Fig. 2A) with differing time courses for the two proteins,

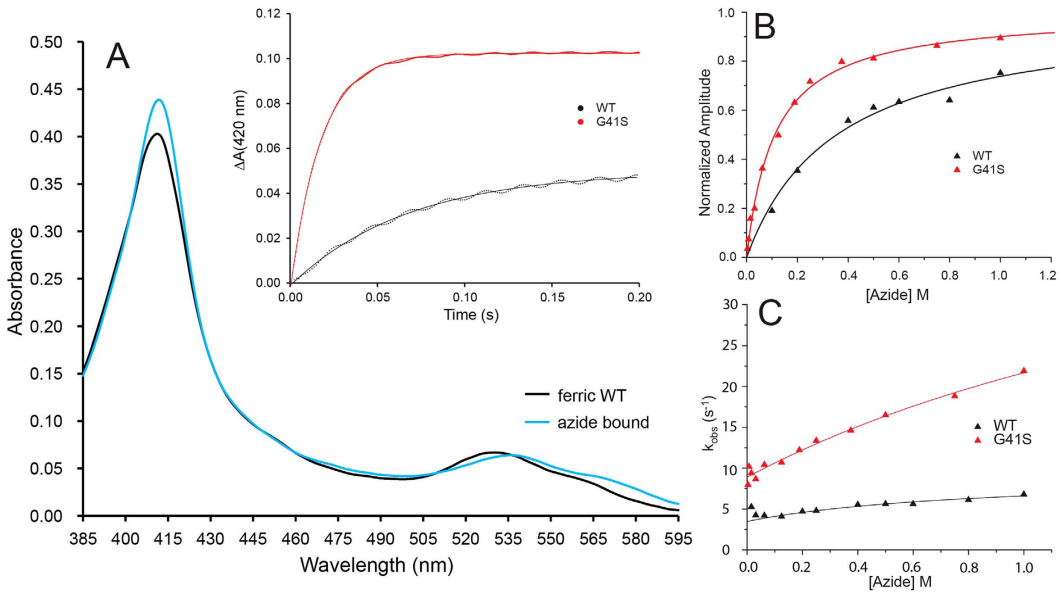

Figure 2. Stopped-flow kinetics of N_3^- binding to H-ferricyt at pH 7 and 25 °C. (**A**) Spectra generated on mixing H-ferricyt with N_3^-. Global analysis indicated a single transition with the initial spectrum (black) and the N_3^- bound spectrum (light blue). Inset: time courses for N_3^-binding to WT (black) and G41S (red) (5 μM after mixing) are shown together with exponential fits. (**B**) The normalised amplitudes of the time courses recorded at 420 nm plotted against $[N_3^-]$. Binding curves are fitted to a hyperbolic equation to yield the K_{app} values reported in the main text. (**C**) The rate constant (k_{obs}) determined for N_3^- binding with solid lines representative of fits to Eq. 2, to give the k_1 and k_{-2} values reported in the main text.

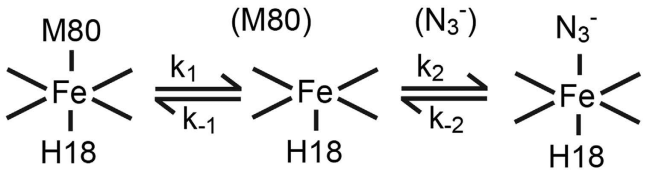

Figure 3. SN1 mechanism of N_3^- binding to H-ferricyt. The dissociation and re-association of the Met80 ligand to the Fe(III) occur with rates of k_1 and k_{-1}, respectively, prior to N_3^- association.

as shown in the inset to Fig. 2A. Such an optical transition reflects the dissociation of the Met80 ligand from the heme and the binding of N_3^- in its place. Confirmation of this assignment was obtained in separate experiments at higher [H-ferricyt] (Fig. S1) that revealed the addition of N_3^- to WT and G41S led to the bleaching of the 695 nm band, which is diagnostic for the loss of the Met80 ligand. The optical transition consisted of a single exponential at every wavelength with no intermediates detected (inset Fig. 2A). The normalised amplitudes of such time courses, taken over a range of $[N_3^-]$ conform to a simple hyperbolic binding isotherm (Fig. 2B) to yield apparent equilibrium dissociation constants (K_{app}) of 0.31 ± 0.03 and 0.11 ± 0.01 M for WT and G41S H-ferricyt, respectively. The dependence of the observed rate constant (k_{obs}) for N_3^- binding obtained from plots such as those in the inset to Fig. 2A is under the $[N_3^-]$ measureable, almost linear (*vide infra*) for both WT and G41S (Fig. 2C). Since the apparent p*K* values for the alkaline transitions of WT and G41S H-ferricyt are different, at 9.3 and 8.2, respectively, N_3^- binding experiments at higher pH values (see Figs S2 and S3) were conducted and revealed that the alkaline transition is not significant for the binding of N_3^- to H-ferricyt at pH 7. It is therefore concluded that N_3^- binding to the G41S variant occurs faster and with a higher binding affinity than it does to WT H-ferricyt.

Ligand binding to the heme iron of ferricyt is generally discussed in terms of an SN1 mechanism as depicted in Fig. 3, where the hexacoordinate ferricyt is in equilibrium with a pentacoordinate form in which the Met80 is dissociated from the heme. This equilibrium lies strongly in favour of the hexacoordinate form, with N_3^- binding to the pentacoordinate form yielding the low-spin hexacoordinate N_3^- adduct (Fig. 3). The mechanism given is amenable to full analysis but this leads to unwieldy equations to describe the kinetic behaviour of the system. However, a simplifying assumption can be made in that the concentration of the pentacoordinate species, that is at all times small, is in a steady-state throughout the reaction[29]. Furthermore, as the $[N_3^-]$ is high relative to the [H-ferricyt] the binding kinetics may be considered to be pseudo-first order. These simplifications allow for equations 1 and 2 to be derived that describe the K_{app} (Eq. 1) and the dependence of k_{obs} for N_3^-binding as a function of $[N_3^-]$ (Eq. 2).

$$K_{app} = K_D(K + 1/K) \quad (1)$$

$$k_{obs} = \frac{(k_1 - k_{-2})[N_3^-]}{(k_1 + k_{-1}/k') + [N_3^-]} + k_{-2} \quad (2)$$

where $K = k_1/k_{-1}$ and $K_D = k_{-2}/k_2$, with k_2 the pseudo-first order rate constant for N_3^- binding *i.e.* $k_2 = k'[N_3^-]$, k' the second order rate constant and k_{obs} is ~k_1 at high $[N_3^-]$. Equation 1 shows that if $K < 1$ (as here where the pentacoordinate concentration is very low) then K_{app} is ~K_D/K. Assuming that N_3^- binding to the pentacoordinate species is not directly affected by a distant mutation in the protein, then K_D will be the same for both proteins and the ratio of K_{app} values ($^{WT}K_{app}/^{G41S}K_{app}$) reflect the ratio of K values ($^{G41S}K/^{WT}K$). On this basis $^{G41S}K > {}^{WT}K$ and thus the pentacoordinate form is more populated in the G41S variant than in the WT protein.

Equation 2 predicts that plots of k_{obs} versus $[N_3^-]$ follow hyperbolae that intercept the k_{obs} axis at the value of k_{-2}, the N_3^- dissociation rate constant, and plateau at k_1, the Met80 dissociation rate constant. Fitting the data in Fig. 2C to Eq. 2 gives k_{-2} values of 3.5 ± 0.4 and $8.9 \pm 0.3\,s^{-1}$ for WT and G41S, respectively. Over the $[N_3^-]$ range that was accessible experimentally the hyperbolic curvature was not discerned and thus reliable values of the Met80 dissociation constants (k_1) cannot be provided. However, it is possible to estimate minimum values for k_1 of 5.77 ± 1.5 and $45 \pm 18\,s^{-1}$, for WT and G41S, respectively, consistent both with Eq. 2 and the data (Fig. 2C). The k_1 for H-ferricyt may be compared to the value of $11–16\,s^{-1}$ for horse ferricyt obtained by non-linear fitting procedures of the data reported by Sutin and Yandell using N_3^- as the competing ligand[6]. The differences between horse and H-ferricyt is possibly associated with the sequence difference at position 83 in the 71–85 Ω-loop that may effect the dynamics of the Met80 ligand as proposed by Bowler and co-workers[33]. Thus the considerably larger estimates for the rate of Met80 dissociation for the G41S variant is again consistent with the pentacoordinate form being more populated in the G41S variant than in the WT protein, pointing towards a more flexible and labile heme crevice.

The lowest free energy cyt foldon has increased H/D-exchange in the G41S variant. Monitoring H/D exchange for backbone amide protons with NMR spectroscopy is a tool that provides per residue resolution of structural features and thermodynamic stability of a protein, with exchange rates influenced mainly by hydrogen bonding, particularly in secondary structure, and solvent accessibility[34]. A convenient form of expressing variation in H/D exchange behaviour is to compare the amide protection actors (PF), defined as the ratio between the observed experimental and intrinsic exchange rates (k_{ex}/k_{in}), where the intrinsic exchange rates are the rates of exchange for the given amino acid sequence, pH and temperature determined using unstructured peptides[35]. Table S1 reports the exchange rates, calculated PFs, free energies of exchange (ΔG_{ex}) and proton occupancy values for each residue. For both WT and G41S H-ferricyt, 32 and 46 amides, respectively, are fully exchanged within the first 10 min. Figure 4A shows the sequence dependence of the PFs for the 63 remaining residues of WT for which H/D exchange rates could be calculated and Fig. 4B, the comparable figure for the 44 residues for which H/D exchange data could be determined for the G41S variant. The H/D exchange profile of WT can be broadly divided into six continuous regions of increased protection, residues 6–15, 32–45, 51–54, 64–70, 73–75 and 90–103 (Fig. 4A). With the exception of segment 32–45, the protected regions correlate well with the presence of α-helical secondary structure (Fig. 5A). This profile is largely retained for the G41S variant, however the helix 2 region (residues 51–54) and residues between 27–43 are notable exceptions (Fig. 4B). As is clear from Fig. 5B, many of the residues in the G41S variant having reduced protection to H/D exchange are close to the heme on the Met80 side of the heme. This is consistent with the results of the N_3^- binding experiments, which shows that there is a greater amount of the pentacoordinate form for the G41S variant.

The H/D exchange data for H-ferricyt is comparable to that reported for yeast and horse ferricyt[36,37]. Protons showing the slowest exchange are mostly confined to the N- and C-terminal foldon[37,38]. In general, H/D exchange for amides that are in H-bonds in the ground-state structure of a protein can occur via global unfolding of the protein, through local unfolding, or by a combination of the two. An indicator that global unfolding is the key event is shown by a correspondence between the $\Delta G_{stability}$, as determined from denaturant-induced equilibrium unfolding, and ΔG_{ex} for the amide H/D exchange process. When $\Delta G_{stability} > \Delta G_{ex}$ local unfolding promotes the H/D exchange. This is the case in horse ferricyt where most of the amides involved in H-bonds in the ground-state structure have $\Delta G_{stability} > \Delta G_{ex}$ and thus local unfolding is important for this protein[36]. This is also the case here for WT H-ferricyt as $\Delta G_{stability}$ measured under the same conditions as the H/D exchange (Table S2) is significantly greater than the ΔG_{ex} values given in Table S1. Maity *et al.*[39] describe H/D exchange in horse cyt in terms of five foldon units that fold with different folding free energies in a stepwise sequential manner. The foldon with the greatest stability corresponds to the C-terminal and N-terminal α-helices, whilst the two foldons with the lowest stability are the 71–85 and 40–57 Ω-loops both involving residues packed around the heme (Fig. 1A)[16,39]. Our H/D exchange data for H-ferricyt are broadly in agreement with their foldon model (Figs 4 and 5).

While WT and G41S H-ferricyt share a broadly similar H/D exchange profile, differences are apparent (Fig. 4C). The decreased level of protection in the G41S variant maps onto the three lowest stability foldons (Fig. 1A)[39] and are assigned to residues 34–43 (the neck), 51–54 (40–57 Ω-loop), 59 and 60 (the neck), 73–75, 79 and 80 (71–85 Ω-loop) (Fig. 5C), which predominately encompass the heme propionate-7 region of the protein, whose conformation is altered in the G41S variant (Fig. 1B)[21]. The most affected residues of G41S in terms of increased susceptibility to H/D exchange are Arg38 and Trp59 (the neck), Ile75 (71–85 Ω-loop) and their near neighbours, but Lys27 and Gly34 (14–36 Ω-loop), Ser41, Asp51, Asn52, Lys53 (40–57 Ω-loop), and Lys79 and Met80 (71–85 Ω-loop) also stand out with a significantly diminished H/D exchange protection compared to the corresponding residues of WT (Fig. 4C). Residues Asn52 and Trp59 are conserved in 99% of the mitochondrial

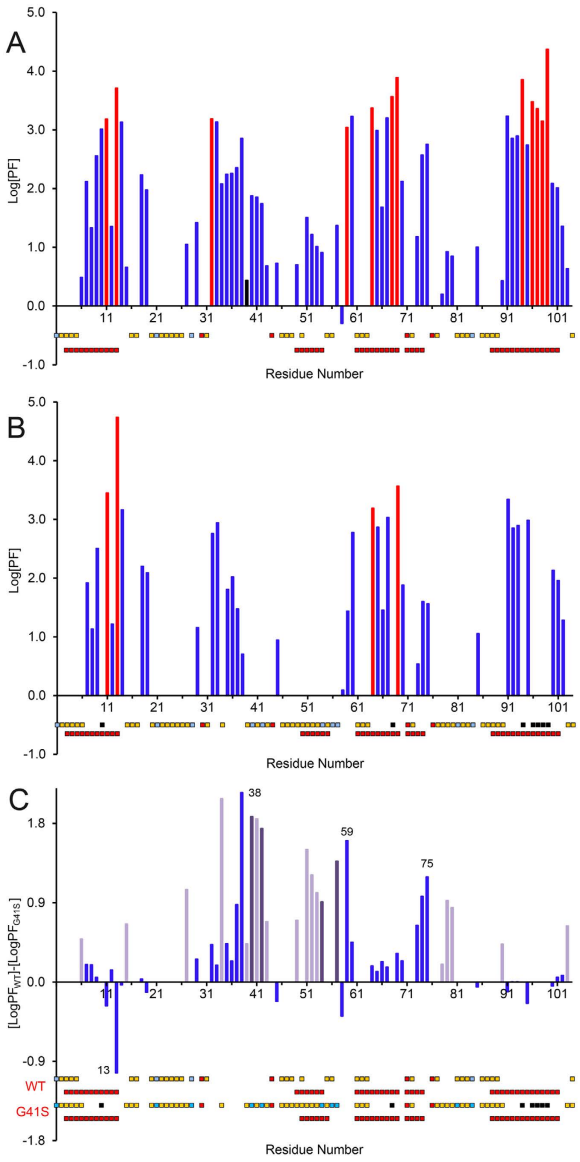

Figure 4. Backbone amide proton H/D exchange analysis of H-ferricyt and its G41S variant. PFs for WT (**A**) and the G41S variant (**B**) plotted against the residue number. For WT, 12 residues underwent fast-exchange (logPF ≤ 1), 16 medium (1 < logPF ≤ 2), 23 slow (2 < logPF) and 12 extremely slow-exchange (residual proton occupancy >80% after ~68 h, corresponding to exchange rates < 0.003 h^{-1}, shown in red). For G41S, 4 residue underwent fast-exchange, 14 medium, 15 slow and 4 extremely slow-exchange (residual proton occupancy >80%, after ~72 h, corresponding to exchange rates < 0.003 h^{-1}, shown in red). Secondary structure (α-helix) is indicated by the bottom red squares, while red squares above represent Pro residues. Unassigned and very fast-exchanging residues are indicated in light blue and yellow squares, respectively. Residues for which PFs could not be calculated due to the slowness of the exchange in the G41S variant are indicated with black squares (7 residues). (**C**) PF difference plot of [logP_{WT}]-[logP_{G41S}] shown in blue. Residues that are fully exchanged in G41S have the PFs observed for WT displayed (light purple). Residues that are unassigned only for the G41S variant have the PFs observed for WT displayed (dark purple).

cyt sequences and the H-bonds between their side chains and propionate-7 are expected to be conserved in 90% of the same sequences[38]. However, there are more potential H-bonding groups within H-bonding distance of the heme propionates than can be simultaneously accommodated in H-bonds[22]. The apparent differences in H-bond networks in different structures suggests that some of the weaker H-bonds are continually being broken and remade, a view that ties in with the demonstration from H/D exchange that 40–57 Ω-loop has considerable dynamics[16,17]. The rapid H/D exchange for the amide resonances of residues Thr40, Gln42, Gly54, Gly56 and Ile57 in the G41S variant is further evidence that this region of the variant has increased dynamics since most of these residues have significant H/D exchange protection in the WT protein.

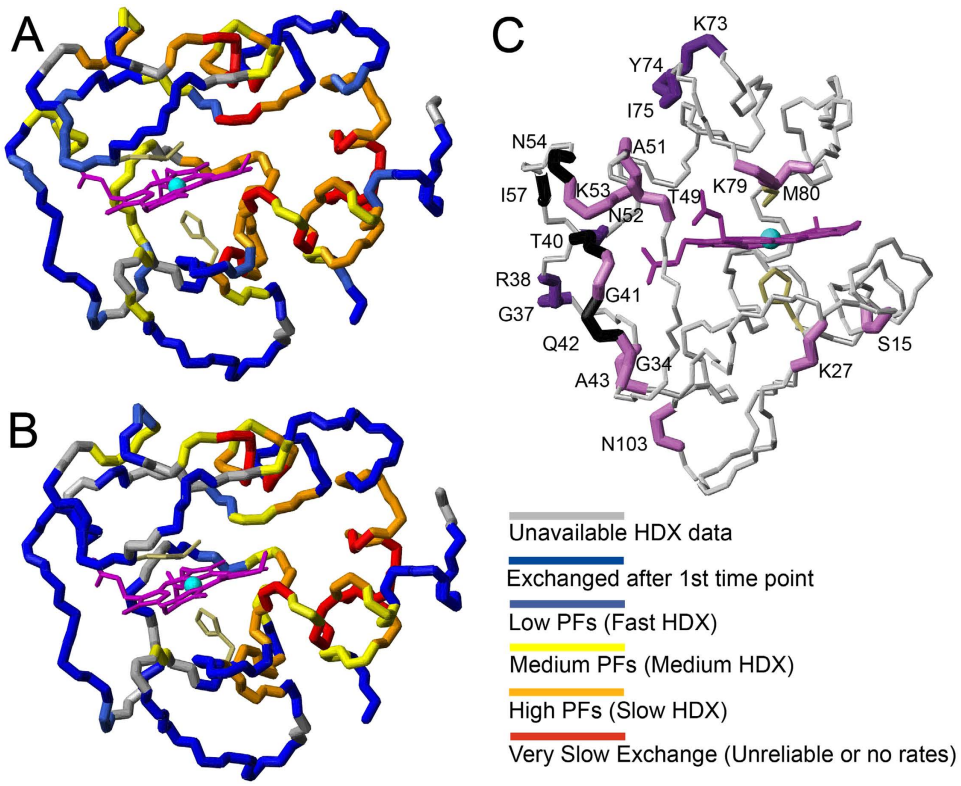

Figure 5. PF mapping for H-ferricyt. PFs are colour coded as indicated on (**A**) the WT and (**B**) the G41S X-ray structures[20,21]. The WT cartoon representation in Fig. 1A can be used to aid orientation. (**C**) H/D exchange difference profile mapped onto the X-ray structure of the G41S variant. Residues highlighted in violet have PF > 0.5 in WT but are fully exchanged in G41S, residues highlighted in dark violet have [$\Delta(LogPF_{WT}$-$LogPF_{G41S}) > 0.5$] and residues highlighted in black have PF > 0.5 in WT but are unassigned for G41S.

The G41S variant has enhanced conformational exchange in all three Ω-loops. Backbone amide groups of ^{15}N-labelled proteins have been extensively used to identify regions of proteins that undergo a range of dynamics on both a ps-ns and μs-ms timescale[24]. Out of the 96 assigned backbone resonances for the WT protein, full relaxation data were obtained for 93 residues (Fig. S4). The average relaxation rates (R_1 ($1/T_1$) and R_2 ($1/T_2$)), for the WT protein were $R_1 = 0.99 \pm 0.01\,s^{-1}$ and $R_2 = 14.23 \pm 0.22\,s^{-1}$ with an average NOE = 0.84 ± 0.01. Full relaxation data were obtained for all 92 assigned backbone resonances of the G41S variant (Fig. S4). The average values obtained were: $R_1 = 1.07 \pm 0.03\,s^{-1}$, $R_2 = 14.48 \pm 0.38\,s^{-1}$ and NOE = 0.84 ± 0.01. Heteronuclear {^{1}H}-^{15}N NOE values are indicators of motions in the ps timescale with values close to 1 suggesting rigidity and lower values indicating increased local flexibility. Both WT and the G41S variant are rigid in this respect with only the C-terminal residue E104 having a NOE value below 0.65 (Fig. 6A,B). The R_1 rates are sensitive to motion on the ns to ps timescales, and are relatively constant throughout both the WT and G41S sequence. However, a handful of R_2 rates for the WT are significantly increased above the average, notably those for residues Val20, Gly23, Gly56 and Asn103, probably reflecting contributions to relaxation from slower conformational exchange contributions, as observed with other proteins (Fig. S4). Significantly more residues for the G41S variant have R_2 rates deviating from the average (Fig. S4). Plots of R_2/R_1 ratios, which are a useful indicator for identifying residues experiencing chemical exchange, show that the G41S variant has significantly more residues displaying slower conformational exchange behaviour than the WT protein (Fig. 6A,C). In particular, residues in the 19–35 Ω-loop (Val20, Gly23, His33, Gly34), the neck unit (Gly37, Arg38, Lys39 and Ile58), the 40–57 Ω-loop (Ser41, Ser47, Ala51, Asn52, Lys53, Lys55), the 71–85 Ω-loop (Gly77) and A101 and N103 at the end of the C-terminal α-helix.

Further analysis of the relaxation data was performed with the Model-free formalism[40] (see SI and Table S3), which provides three main dynamic parameters: a) the generalized order parameter, S^2, b) the effective correlation time, τ_e and c) the chemical exchange contribution rate, R_{ex}. The average S^2 values, which specify the degree of spatial restriction of the N-H bond, for WT and the G41S variant are comparable at 0.924 ± 0.046 and 0.934 ± 0.050, respectively (Fig. 7). This is consistent with both proteins being relatively rigid, presumably due to the α-helical secondary structure and the compact core held together by hydrophobic interactions associated with the heme. For WT H-ferricyt, large R_{ex} terms (between 12 and 16 s^{-1}) were observed for Val20 and Gly23 (average of $14.52 \pm 1.01\,s^{-1}$) and smaller R_{ex} terms ($<5\,s^{-1}$) for residues Ile9, His18, Gly24, Lys25, Lys39, Gly41, Gly45, Ile57, Trp59, Gly60, Ile95, Tyr97 and Ala101 (average of $1.56 \pm 0.76\,s^{-1}$) (Fig. 7A). For the G41S variant, large R_{ex} terms (between 8 and 16 s^{-1}) were observed for Val20, Gly23, His33, Ser41, Lys53, Lys55, Ile58 and Gly77 (average of $13.40 \pm 3.97\,s^{-1}$) and smaller R_{ex} terms ($<5\,s^{-1}$) for His18, His26, Gly37, Lys39, Gly45 and Thr49 (average of $2.58 \pm 1.29\,s^{-1}$) (Fig. 7B). Overall, 13 residues have R_{ex} terms of small magnitude and 2 residues large

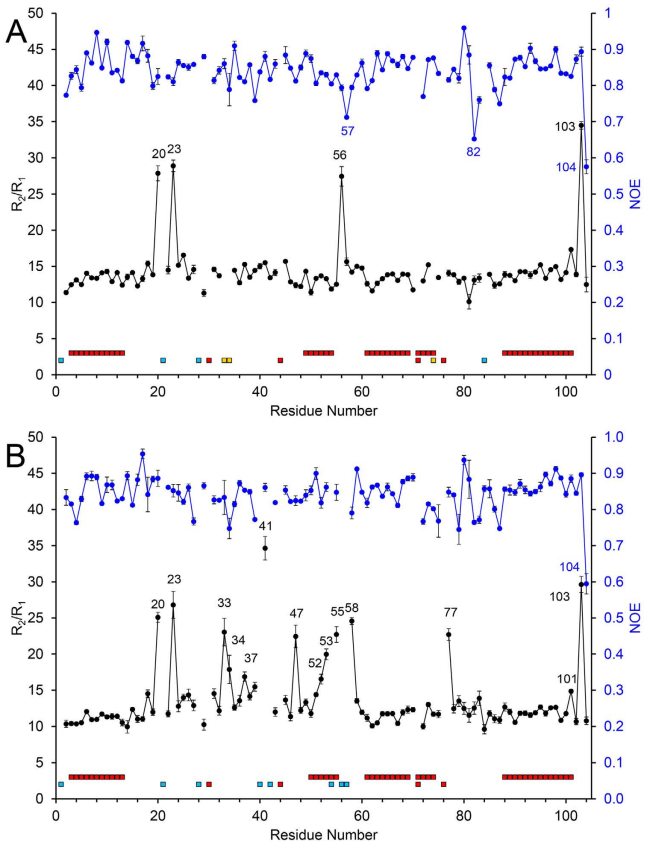

Figure 6. ^{15}N Relaxation parameters for H-ferricyt. R_2/R_1 (in black) and {^{1}H}-^{15}N NOE (in blue) for WT (**A**) and G41S (**B**). α-helices are indicated by the top red squares while below Pro residues and unassigned residues are indicated with red and light blue squares, respectively. Residues excluded from the analysis due to peak overlap or weak intensity are indicated with yellow squares.

magnitude for WT, while for the G41S variant 6 residues have R_{ex} terms of small magnitude and 8 residues large magnitude, thus indicating enhanced conformational exchange on the ms to μs timescale in the G41S variant. The less informative number of residues with a correlation time (τ_e) indicating internal motion was 23 and 20 for the WT and G41S variant, respectively (Fig. S5), with many of these assigned to model 5, which reflects both fast and slow motions (Table S3) and is difficult to accurately characterise with relaxation data. The significant finding is the number of residues exhibiting relatively large R_{ex} terms.

The distribution of residues requiring an R_{ex} term to describe their relaxation data for both WT (15 residues) and G41S (14 residues) H-ferricyt have been mapped onto the respective structures in Fig. 8. A striking overall resemblance to the H/D exchange difference map shown in Fig. 5C is observed. Furthermore it highlights that under native conditions the regions experiencing conformational exchange for both the WT and G41S proteins are essentially identical, with the switching of a glycine to a serine at position 41 enhancing the dynamics in 3 out of the 5 H-ferricyt foldons, and in particular the lowest energy foldon (40–57 Ω-loop). Thus the G41S variant nicely illustrates a previous prediction that foldon substructure may determine additional properties[16], such as apoptotic activity.

Conformational dynamics in the 40–57 Ω-loop modulate the pentacoordinate form and apoptotic interactions. The NMR data and N_3^- binding kinetics strongly support a linkage in the dynamics of the region surrounding heme propionate-7, *i.e.* the 40–57 Ω-loop and lability of the Met80 heme ligand. A recent X-ray structure of the K72A variant of yeast cyt provides further compelling evidence of a direct conformational link between Met80 and the heme propionate-7 region by being a conformer in which the Met80 ligand is dissociated from the heme and the Arg38 side chain has moved in a similar manner to that observed in the G41S structure (Fig. 1B)[20,33]. These structural changes coincide with the creation of a H_2O channel leading from the vacant Met80 position to beyond heme propionate-7 and ending at the Arg38 side chain, resembling more the conformation of the G41S H-ferricyt than the WT protein in this region. This channel, with Arg38 proposed to act as a seal, has been suggested to enable facile entry of H_2O_2 into the heme environment and/or provide a H^+ exit route[33]. β-sheet formation in the 40s region of the 40–57 Ω-loop has been reported for yeast ferricyt at low pH as a result of breaking a H-bond between His26-Pro44. This was suggested to trigger rearrangement in the Met80 loop since β-sheet formation was accompanied by dissociation of Met80 from the heme iron[41,42]. This event also causes disruption of the H-bonding network associated with heme propionate-7 resulting in a change of the heme position relative to the polypeptide and increased mobility for aromatic residues such as Trp59[41,42]. A further

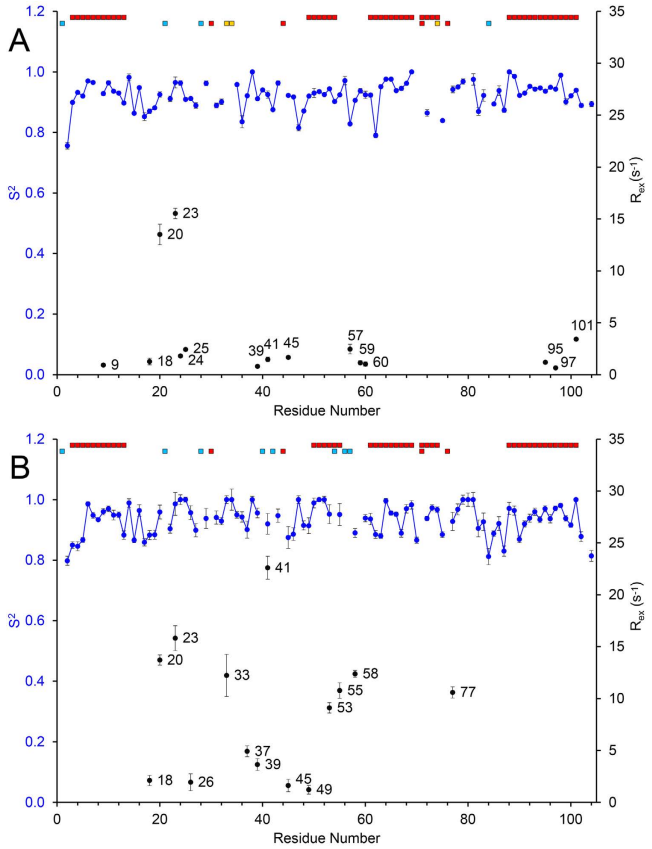

Figure 7. Model-free parameters for H-ferricyt. S^2 order parameters (in blue) and R_{ex} contributions (in black) for WT (**A**) and G41S (**B**). α-helices are indicated by the top red squares while below Pro residues and unassigned residues are indicated with red and light blue squares, respectively. Residues excluded from the analysis due to peak overlap or weak intensity are indicated with yellow squares.

recent crystal structure of the T78C/K79G yeast cyt variant reveals a non-native form whereby Lys73 replaces the Met80 ligand and a conserved stretch of the Met80 loop (^{76}PGTK^{79}) refolds into a β-hairpin structure, with Gly77 being a critical element of this hairpin and central to the flexibility of this peptide fragment[43]. Furthermore, a positional change in helix-2 (residues 51–54) occurs to accommodate the refolded Met80 loop which has the effect of increasing the volume of the heme pocket and causing peroxidase activity to increase in this T78C/K79G variant[43]. Facets of these structural changes in this non-native conformer are therefore comparable with the regions displaying increased dynamics in the G41S variant. This suggests that, in solution, alternative conformations are kinetically and thermodynamically accessible in the G41S variant, whereby the heightened dynamics in 40–57 Ω-loop foldon is coupled to an increased population of a peroxidase pentacoodinate state, resulting in the elevated peroxidase activity akin to the WT protein when bound to CL[18,19]. In addition to the X-ray structures of the variants mentioned above, an important finding from H/D exchange studies is that the dynamics of the 40–57 Ω-loop controls the rate of the alkaline isomerisation of ferricyt, which leads to Met80 being replaced by a lysine as an axial ligand[44]. Though the alkaline isomerisation is not a factor in our N_3^- binding experiments, and thus not a factor in generation of the pentacoordinate, it is a further demonstration that the dynamics of the 40–57 Ω-loop and Met80 lability are linked and can govern function[16].

Finally, the 40–57 Ω-loop is the least conserved in cyt evolution. This has been highlighted recently through the discovery of a species-dependent interaction between cyt and Apaf-1 in cytosolic extracts, which is proposed to arise due to sequence variation between mitochondrial species in the 40–57 Ω-loop[45]. Further to this discovery, residues flanking Pro44 have for some time been associated with a conformational change in cells undergoing apoptosis[46] and recent modelling studies suggest H-cyt interacts with Apaf-1 through contact via the 40–57 Ω-loop[45,47]. Thus based on the present work we propose that the dynamics of 40–57 Ω-loop may be species-specific and tuned to regulate interaction with the cognate Apaf-1.

Experimental

NMR sample preparation. ^{15}N-labelled samples of WT H-ferricyt and the G41S variant ranging in concentration from 0.8 to 1 mM were used for all experiments and prepared as described previously[48].

NMR Spectroscopy. All NMR experiments were performed at 288 K (unless specified otherwise) and acquired on a Bruker 800 MHz spectrometer equipped with either a 5 mm HCN inverse triple resonance z-axis gradient probe or a 5 mm broad band inverse z-axis gradient probe, and a Bruker 500 MHz spectrometer

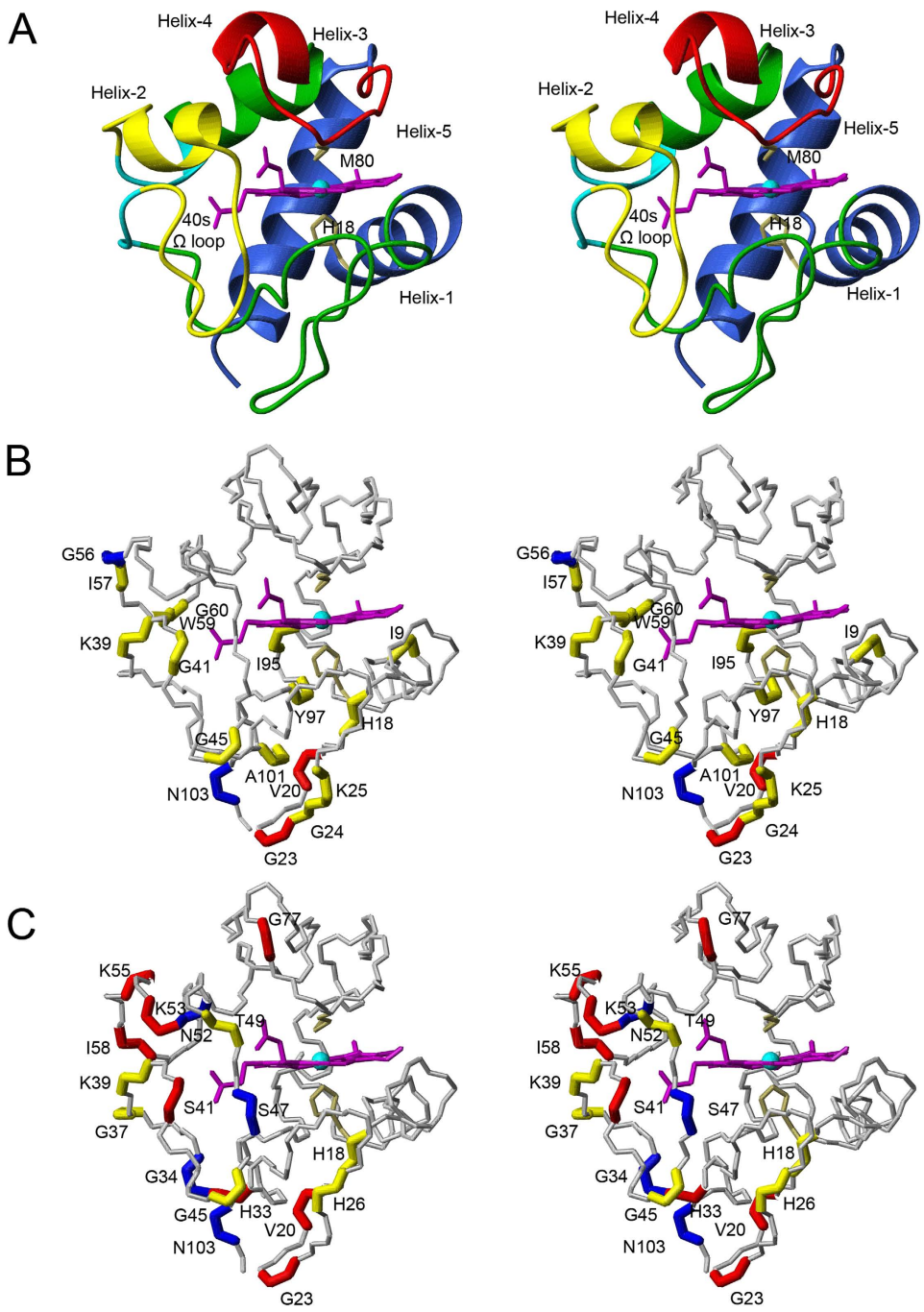

Figure 8. Dynamic profile mapping of H-ferricyt. Stereo pairs representation of (**A**) WT with the five foldon units coloured as described in the legend to Fig. 1A. NMR dynamics plotted on the X-ray structures of WT (**B**) and G41S (**C**). Residues highlighted in yellow and red have low ($<5\,s^{-1}$) and high ($>5\,s^{-1}$) R_{ex} terms, respectively, with those in blue having R_2/R_1 deviating from the average but without an associated R_{ex} term. In all depictions heme and axial ligands are shown in stick representation.

equipped with a 5 mm HCN inverse triple resonance z-axis gradient probe. Data were processed with either Topspin (Bruker Biospin) or the NMRPipe and NMRDraw package[49]. Data analysis was performed with the programs CCPNmr Analysis[50] and Sparky[51]. The amide chemical shifts used in this work for the WT and G41S variant have been previously determined (BMRB accession numbers 25418 and 25422, respectively)[48].

H/D exchange. Freeze-dried ^{15}N-labelled and desalted samples of both WT and G41S H-ferricyt at 1 mM concentration were re-dissolved in 20 mM sodium phosphate pH 6.5, 50 mM NaCl pre-made in 99.9% ^2H_2O (Sigma). All H/D exchange NMR data were acquired at 500 MHz as matrices of 1024 × 64 complex data points with 4 scans and spectral widths of 15 (^1H) and 42 (^{15}N) ppm (39.8 ppm for G41S) centred at 4.7 and 118.6 ppm,

respectively. The acquisition of consecutive ^{1}H-^{15}N-HSQC spectra started approximately 5 min after sample resuspension. Acquisition proceeded for WT with consecutive HSQC spectra of approximately 5 min acquisition time for a period of 68 h, totalling 792 experiments. The first 49 experiments (to ensure maximum coverage of the fast-exchanging residues) were followed by 74 experiments at 50 min intervals, totalling 123 experiments, which were used for the extrapolation of the H/D exchange rates. For the G41S variant, acquisition of ^{1}H-^{15}N-HSQC spectra of identical acquisition parameters was executed at specific timed intervals, *i.e.* 49 consecutive experiments followed by 79 experiments at 50 min intervals. CCPNmr Analysis was used to fit peak volumes as a function of time to a two-parameter single exponential decay function[50]. Rates of exchange were extracted from this fitting and were used for the calculation of PFs[35,52]. Intrinsic exchange rate constants required for the calculation of PFs were obtained as described previously[35]. ΔG_{ex} (Table S1) values were obtained from $\Delta G_{ex} = -RTln(PF)$ where R is the gas constant and T is the temperature in Kelvin[52].

^{15}N relaxation data. ^{15}N T_1, T_2, and {^{1}H}-^{15}N NOE data were collected at 800 MHz. Spectra were acquired as matrices of 1024 × 256 complex data points with 8 scans for T_1 and T_2 data and 64 scans for {^{1}H}-^{15}N NOE data. Spectral widths of 15 (^{1}H) and 39.3 (^{15}N) ppm centred at 4.7 and 118.6 ppm respectively, were used. T_1 experiments were acquired with relaxation delays of 10, 50, 80, 200, 500, 750, 2000 and 3500 ms with duplicates at 10, 200 and 500 ms. T_2 experiments were acquired with relaxation delays of 16.96, 33.92, 50.88, 67.84, 101.76, 135.68, 203.52 and 254.40 ms with duplicates at 16.96, 50.88 and 101.76 ms. Recycle delays for both experiments were 5 s. The repeated relaxation delays were used for the determination of peak height uncertainties[53]. Identical delays were used for both WT and G41S with the exception of the first T_1 delay for G41S, which was 20 ms due to pulse sequence limitations. Both T_1 and T_2 series of experiments were acquired with interleaved delay values to minimize sample heating. T_1 and T_2 data for G41S were acquired as a pseudo-3D experiment, and processed as individual 2D planes using NMRPipe[49]. T_1 and T_2 values were extracted through the fitting of peak heights as a function of the relaxation delay to a two-parameter single exponential decay function using the follow intensity changes function of CCPN Analysis. These were subsequently converted to R_1 and R_2 rate constants (R, where $R_1 = 1/T_1$ and $R_2 = 1/T_2$). The fit errors for T_1 and T_2 were also converted into R_1 and R_2 errors through the equality of the T_1/T_2 and R_2/R_1 errors. Heteronuclear {^{1}H}-^{15}N NOEs were measured with a proton saturation period of 5 s. Interleaved saturated and unsaturated experiments were acquired in triplicate in order to determine the experimental errors as the standard deviation of the average NOE value. NOE values were calculated as the ratio of the peak heights with and without proton saturation.

Model-free analysis. Model-free analysis was performed using the Model-free4 program[54] complemented with the FAST-Modelfree program[55] to facilitate and speed-up data analysis and interpretation. The first step consisted of the estimation of the rotational correlation time using the program r2r1_tm (http://www.palmer.hs.columbia.edu/) from the relaxation data. The program quadric_diffusion (http://www.palmer.hs.columbia.edu/) was used to calculate the rotational diffusion parameters from the output local correlation times. This program uses a 3D structure translationally centred on the centre of mass and rotated to the inertia tensor principal axes. These manipulations were achieved with the program pdbinertia (http://www.palmer.hs.columbia.edu/). Initial pdb manipulations preceding the use of pdbinertia were performed with molecular graphics program MOLMOL[56]. Quadric_diffusion also produces a pdb structure rotated to axially symmetric principal axes, subsequently used as an input for FAST-Model-free. The paramagnetic contribution from the low-spin (S = ½) heme to the nitrogen relaxation rates is considered negligible because of the low gyromagnetic ratio of the ^{15}N nucleus[57]. The Tjandra-Bax conditions[58] were applied in order to exclude residues with a large-amplitude fast internal motions and residues subject to conformational exchange from the rotational correlation time calculations. The former applies if the {^{1}H}-^{15}N NOE < 0.65 and the later applies if $[(T_{2,av} - T_{2,n})/T_{2,av} - (T_{1,av} - T_{1,n})/T_{2av}] > 1.5$ x standard deviation, where $T_{1,av}$ and $T_{2,av}$ the average values, and $T_{1,n}$ and $T_{2,n}$ are the relaxation times for each individual residue, n. These conditions identify the 'rigid' residues with relaxation parameter values corresponding to the global rotational dynamics.

The five models considered for the interpretation of dynamic parameters using the Model-free approach[40,59,60] were: model 1 (with only the generalized order parameter S^2), model 2 (S^2 and the correlation time for internal motion τ_e), model 3 (S^2 and the exchange contribution to the relaxation rate, R_{ex}, or model 1 with R_{ex}), model 4 (S^2, τ_e and R_{ex} or model 2 with R_{ex}) and finally the extended model 5 (with the generalized order parameter for faster and slower timescales, $S^2 = S^2_f S^2_s$ and τ_e) which accounts for a fast and a slow internal motion. The models with R_{ex} terms (3 and 4) reflect on conformational exchange processes on the ms to μs timescale. The models with effective correlation time reflect on internal motions on the ps to ns timescale. Model-free analysis was performed with ^{15}N gyromagnetic ratio of −2.71, N-H bond distance of 1.02 Å and ^{15}N chemical shift anisotropy of −160. FAST-Model-free calculations were performed with confidence limit for χ^2-testing of 0.95, confidence limit for F-testing of 0.80, 50 iterations, sum squared error cut-off of 200, 500–1000 Monte-Carlo simulations and optimization of the diffusion tensor.

Stopped-flow kinetics. Kinetic experiments were carried out using an Applied Photophysics (Leatherhead, UK) SX20 stopped-flow spectrophotometer equipped with both photomultiplier and diode array detection systems and thermostatted at 25 °C. Stocks of sodium azide 2 M were prepared in 50 mM sodium phosphate and 50 mM MES pH 7 and diluted to the desired N^{3-} concentration with the same buffer but containing 2 M NaCl to maintain the ionic strength. Time courses were taken at 420 nm with known [N^{3-}] (between 0.08–2 M before mixing) and 10 μM protein (before mixing) with the transient fitted to a single exponential function yielding both pseudo first-order rate constants and amplitudes. All errors reported are standard errors.

References

1. Li, P. *et al.* Cytochrome *c* and dATP-dependent formation of Apaf-1/caspase-9 complex initiates. *Cell* **91,** 479–489 (1997).
2. Kagan, V. E. *et al.* Cytochrome *c* acts as a cardiolipin oxygenase required for release of proapoptotic factors. *Nat Chem Biol* **1,** 223–232 (2005).
3. Huttemann, M. *et al.* The multiple functions of cytochrome *c* and their regulation in life and death decisions of the mammalian cell: From respiration to apoptosis. *Mitochondrion* **11,** 369–381, doi: 10.1016/j.mito.2011.01.010 (2011).
4. Gonzalez-Arzola, K. *et al.* Structural basis for inhibition of the histone chaperone activity of SET/TAF-Ibeta by cytochrome *c*. *Proc Natl Acad Sci USA* **112,** 9908–9913, doi: 10.1073/pnas.1508040112 (2015).
5. Diederix, R. E., Ubbink, M. & Canters, G. W. Peroxidase activity as a tool for studying the folding of *c*-type cytochromes. *Biochemistry* **41,** 13067–13077 (2002).
6. Sutin, N. & Yandell, J. K. Mechanisms of reactions of cytochrome *c* - Rate and equilibrium constants for ligand binding to horse heart ferricytochrome c. *J Biol Chem.* **247,** 6932–6936 (1972).
7. Vladimirov, Y. A., Proskurnina, E. V. & Alekseev, A. V. Molecular mechanisms of apoptosis. structure of cytochrome *c*-cardiolipin complex. *Biochemistry-Moscow* **78,** 1086–1097, doi: 10.1134/s0006297913100027 (2013).
8. Rosell, F. I., Ferrer, J. C. & Mauk, A. G. Proton-linked protein conformational switching: Definition of the alkaline conformational transition of yeast iso-1-ferricytochrome c. *J Am Chem Soc* **120,** 11234–11245, doi: 10.1021/ja971756+ (1998).
9. Wilson, M. T. *Cytochrome c: A multidisciplinary approach*. (University Science Books, 1996).
10. Morison, I. M. *et al.* A mutation of human cytochrome *c* enhances the intrinsic apoptotic pathway but causes only thrombocytopenia. *Nat Genet* **40,** 387–389 (2008).
11. De Rocco, D. *et al.* Mutations of cytochrome *c* identified in patients with thrombocytopenia THC4 affect both apoptosis and cellular bioenergetics. *Biochim Biophys Acta* **1842,** 269–274, doi: 10.1016/j.bbadis.2013.12.002 (2014).
12. Hunte, C., Koepke, J., Lange, C., Rossmanith, T. & Michel, H. Structure at 2.3 Å resolution of the cytochrome bc(1) complex from the yeast *Saccharomyces cerevisiae* co-crystallized with an antibody Fv fragment. *Structure* **8,** 669–684, doi: 10.1016/S0969-2126(00)00152-0 (2000).
13. Lange, C. & Hunte, C. Crystal structure of the yeast cytochrome bc(1) complex with its bound substrate cytochrome *c*. *Proc Natl Acad Sci USA* **99,** 2800–2805, doi: 10.1073/pnas.052704699 (2002).
14. Sakamoto, K. *et al.* NMR basis for interprotein electron transfer gating between cytochrome *c* and cytochrome *c* oxidase. *Proc Natl Acad Sci USA* **108,** 12271–12276, doi: 10.1073/pnas.1108320108 (2011).
15. Volkov, A. N., Nicholls, P. & Worrall, J. A. R. The complex of cytochrome *c* and cytochrome *c* peroxidase: The end of the road? *Biochim Biophys Acta* **1807,** 1482–1503, doi: 10.1016/j.bbabio.2011.07.010 (2011).
16. Krishna, M. M., Lin, Y., Rumbley, J. N. & Englander, S. W. Cooperative omega loops in cytochrome *c*: role in folding and function. *J Mol Biol* **331,** 29–36 (2003).
17. Krishna, M. M., Maity, H., Rumbley, J. N., Lin, Y. & Englander, S. W. Order of steps in the cytochrome *c* folding pathway: evidence for a sequential stabilization mechanism. *J Mol Biol* **359,** 1410–1419, doi: 10.1016/j.jmb.2006.04.035 (2006).
18. Rajagopal, B. S., Silkstone, G. G., Nicholls, P., Wilson, M. T. & Worrall, J. A. R. An investigation into a cardiolipin acyl chain insertion site in cytochrome *c*. *Biochim Biophys Acta* **1817,** 780–791, doi: 10.1016/j.bbabio.2012.02.010 (2012).
19. Josephs, T. M., Morison, I. M., Day, C. L., Wilbanks, S. M. & Ledgerwood, E. C. Enhancing the peroxidase activity of cytochrome *c* by mutation of residue 41: implications for the peroxidase mechanism and cytochrome *c* release. *Biochem J* **458,** 259–265, doi: 10.1042/bj20131386 (2014).
20. Liptak, M. D., Fagerlund, R. D., Ledgerwood, E. C., Wilbanks, S. M. & Bren, K. L. The proapoptotic G41S mutation to human cytochrome *c* alters the heme electronic structure and increases the electron self-exchange rate. *J Am Chem Soc* **133,** 1153–1155, doi: 10.1021/ja106328k (2011).
21. Rajagopal, B. S. *et al.* The hydrogen-peroxide-induced radical behaviour in human cytochrome *c*-phospholipid complexes: implications for the enhanced pro-apoptotic activity of the G41S mutant. *Biochem J* **456,** 441–452, doi: 10.1042/bj20130758 (2013).
22. Moore, G. R. & Pettigrew, G. W. Cytochrome *c*: Evolutionary,structural and physicochemical aspects. Springer-Verlag, London (1990).
23. Josephs, T. M. *et al.* Conformational change and human cytochrome *c* function: mutation of residue 41 modulates caspase activation and destabilizes Met-80 coordination. *J Biol Inorg Chem*, doi: 10.1007/s00775-012-0973-1 (2013).
24. Akke, M. NMR methods for characterizing microsecond to millisecond dynamics in recognition and catalysis. *Curr Opin Struct Biol* **12,** 642–647 (2002).
25. Henzler-Wildman, K. & Kern, D. Dynamic personalities of proteins. *Nature* **450,** 964–972 (2007).
26. Fetrow, J. S. & Baxter, S. M. Assignment of ^{15}N chemical shifts and ^{15}N relaxation measurements for oxidized and reduced iso-1-cytochrome *c*. *Biochemistry* **38,** 4480–4492 (1999).
27. Barker, P. D. *et al.* A further clue to understanding the mobility of mitochondrial yeast cytochrome *c*: a ^{15}N T1rho investigation of the oxidized and reduced species. *Eur J Biochem* **268,** 4468–4476 (2001).
28. Sakamoto, K., Kamiya, M., Uchida, T., Kawano, K. & Ishimori, K. Redox-controlled backbone dynamics of human cytochrome *c* revealed by ^{15}N NMR relaxation measurements. *Biochem Biophys Res Commun* **398,** 231–236, doi: 10.1016/j.bbrc.2010.06.065 (2010).
29. Rafferty, S. P., Smith, M. & Mauk, A. G. Azide binding and active site dynamics of position-82 variants of ferricytochrome *c*. *Inorg Chim Acta* **242,** 171–177, doi: 10.1016/0020-1693(95)04863-4 (1996).
30. Winkler, J. R. Cytochrome c folding dynamics. *Curr Opin Chem Biol* **8,** 169–174 (2004).
31. Borutaite, V. & Brown, G. C. Mitochondrial regulation of caspase activation by cytochrome oxidase and tetramethylphenylenediamine via cytosolic cytochrome *c* redox state. *J Biol Chem* **282,** 31124–31130 (2007).
32. Diederix, R. E., Ubbink, M. & Canters, G. W. The peroxidase activity of cytochrome c_{550} from Paracoccus versutus. *Eur J Biochem* **268,** 4207–4216 (2001).
33. McClelland, L. J., Mou, T. C., Jeakins-Cooley, M. E., Sprang, S. R. & Bowler, B. E. Structure of a mitochondrial cytochrome *c* conformer competent for peroxidase activity. *Proc Natl Acad Sci USA* **111,** 6648–6653, doi: 10.1073/pnas.1323828111 (2014).
34. Englander, S. W. & Kallenbach, N. R. Hydrogen-exchange and structural dynamics of proteins and nucleic-acids. *Q Rev Biophys* **16,** 521–655 (1983).
35. Bai, Y., Milne, J. S., Mayne, L. & Englander, S. W. Primary structure effects on peptide group hydrogen exchange. *Proteins* **17,** 75–86 (1993).
36. Milne, J. S., Mayne, L., Roder, H., Wand, A. J. & Englander, S. W. Determinants of protein hydrogen exchange studied in equine cytochrome *c*. *Protein Sci* **7,** 739–745 (1998).
37. Baxter, S. M. & Fetrow, J. S. Hydrogen exchange behavior of [U-^{15}N]-labeled oxidized and reduced iso-1-cytochrome *c*. *Biochemistry* **38,** 4493–4503 (1999).
38. Banci, L., Bertini, I., Rosato, A. & Varani, G. Mitochondrial cytochromes *c*: a comparative analysis. *J Biol Inorg Chem* **4,** 824–837 (1999).
39. Maity, H., Maity, M., Krishna, M. M., Mayne, L. & Englander, S. W. Protein folding: the stepwise assembly of foldon units. *Proc Natl Acad Sci USA* **102,** 4741–4746, doi: 10.1073/pnas.0501043102 (2005).
40. Lipari, G. & Szabo, A. Model-Free Approach to the interpretation of nuclear magnetic-resonance relaxation in macromolecules.1. Theory and range of validity. *J Am Chem Soc* **104,** 4546–4559, doi: 10.1021/ja00381a009 (1982).

41. Balakrishnan, G. *et al.* A conformational switch to beta-sheet structure in cytochrome *c* leads to heme exposure. Implications for cardiolipin peroxidation and apoptosis. *J Am Chem Soc* **129,** 504–505, doi: 10.1021/ja0678727 (2007).
42. Balakrishnan, G., Hu, Y. & Spiro, T. G. His26 protonation in cytochrome *c* triggers microsecond beta-sheet formation and heme exposure: implications for apoptosis. *J Am Chem Soc* **134,** 19061–19069, doi: 10.1021/ja307100a (2012).
43. Amacher, J. F. *et al.* A compact structure of cytochrome *c* trapped in a lysine-ligated state: Loop refolding and functional implications of a conformational switch. *J Am Chem Soc* **137,** 8435–8449, doi: 10.1021/jacs.5b01493 (2015).
44. Maity, H., Rumbley, J. N. & Englander, S. W. Functional role of a protein foldon–an Omega-loop foldon controls the alkaline transition in ferricytochrome *c*. *Proteins* **63,** 349–355, doi: 10.1002/prot.20757 (2006).
45. Josephs, T. M., Hibbs, M. E., Ong, L., Morison, I. M. & Ledgerwood, E. C. Interspecies variation in the functional consequences of mutation of cytochrome *c*. *PloS one* **10,** e0130292, doi: 10.1371/journal.pone.0130292 (2015).
46. Jemmerson, R. *et al.* A conformational change in cytochrome *c* of apoptotic and necrotic cells is detected by monoclonal antibody binding and mimicked by association of the native antigen with synthetic phospholipid vesicles. *Biochemistry* **38,** 3599–3609, doi: 10.1021/bi9809268 (1999).
47. Shalaeva, D. N., Dibrova, D. V., Galperin, M. Y. & Mulkidjanian, A. Y. Modeling of interaction between cytochrome *c* and the WD domains of Apaf-1: bifurcated salt bridges underlying apoptosome assembly. *Biol. Direct* **10,** 29, doi: 10.1186/s13062-015-0059-4 (2015).
48. Karsisiotis, A. I. *et al.* Backbone resonance assignments of ferric human cytochrome *c* and the pro-apoptotic G41S mutant in the ferric and ferrous states. *Biomol NMR Assign* **9,** 415–419, doi: 10.1007/s12104-015-9621-3 (2015).
49. Delaglio, F. *et al.* NMRPipe: a multidimensional spectral processing system based on UNIX pipes. *J Biomol NMR* **6,** 277–293 (1995).
50. Vranken, W. F. *et al.* The CCPN data model for NMR spectroscopy: development of a software pipeline. *Proteins* **59,** 687–696, doi: 10.1002/prot.20449 (2005).
51. Goddard, T. D. & Kneller, D. G. *SPARKY 3*. University of California, San Francisco (2008).
52. Hoshino, M., Katou, H., Yamaguchi, K.-I. & Goto, Y. Dimethylsulfoxide-quenched hydrogen/deuterium exchange method to study amyloid fibril structure. *Biochim Biophys Acta* **1768,** 1886–1899, doi: 10.1016/j.bbamem.2007.03.001 (2007).
53. Palmer, A. G., Rance, M. & Wright, P. E. Intramolecular motions of a Zinc finger DNA-binding domain from Xfin characterized by proton-detected natural abundance C-12 heteronuclear NMR-Spectroscopy. *J Am Chem Soc* **113,** 4371–4380, doi: 10.1021/ja00012a001 (1991).
54. Mandel, A. M., Akke, M. & Palmer, A. G., 3rd. Backbone dynamics of *Escherichia coli* ribonuclease HI: correlations with structure and function in an active enzyme. *J Mol Biol* **246,** 144–163 (1995).
55. Cole, R. & Loria, J. P. FAST-Modelfree: a program for rapid automated analysis of solution NMR spin-relaxation data. *J Biomol NMR* **26,** 203–213 (2003).
56. Koradi, R., Billeter, M. & Wuthrich, K. MOLMOL: A program for display and analysis of macromolecular structures. *J Mol Graph* **14,** 51-&, doi: 10.1016/0263-7855(96)00009-4 (1996).
57. Ubbink, M., Worrall, J. A. R., Canters, G. W., Groenen, E. J. & Huber, M. Paramagnetic resonance of biological metal centers. *Annu Rev Biophys Biomol Struct* **31,** 393–422 (2002).
58. Tjandra, N., Feller, S. E., Pastor, R. W. & Bax, A. Rotational diffusion anisotropy of human ubiquitin from ^{15}N NMR relaxation. *J Am Chem Soc* **117,** 12562–12566, doi: 10.1021/ja00155a020 (1995).
59. Lipari, G. & Szabo, A. Model-Free approach to the interpretation of nuclear magnetic-resonance relaxation in macromolecules.2. Analysis of experimental results. *J Am Chem Soc* **104,** 4559–4570, doi: 10.1021/ja00381a010 (1982).
60. Clore, G. M. *et al.* Deviations from the simple 2-parameter Model-Free approach to the interpretation of ^{15}N nuclear magnetic-relaxation of proteins. *J Am Chem Soc* **112,** 4989–4991, doi: 10.1021/ja00168a070 (1990).

Acknowledgements

This work was supported by a Leverhulme Trust project grant (RPG-2013-164) to JARW and a Leverhulme Trust emeritus fellowship (EM-2014-088) to GRM.

Author Contributions

A.I.K. and O.M.D. prepared all protein samples. A.I.K. recorded and analysed all NMR data. O.M.D. and M.T.W. carried out the stopped-flow kinetics and analysed the data. C.M. and T.M.A.B. assisted with NMR data collection. G.R.M. and J.A.R.W. designed and supervised the project and wrote the manuscript, with contributions from all authors.

Additional Information

Supplementary information accompanies this paper at http://www.nature.com/srep

Competing financial interests: The authors declare no competing financial interests.

How to cite this article: Karsisiotis, A. I. *et al.* Increased dynamics in the 40–57 Ω-loop of the G41S variant of human cytochrome *c* promote its pro-apoptotic conformation. *Sci. Rep.* **6**, 30447; doi: 10.1038/srep30447 (2016).

Biochemistry

Article

pubs.acs.org/biochemistry

Heightened Dynamics of the Oxidized Y48H Variant of Human Cytochrome *c* Increases Its Peroxidatic Activity

Oliver M. Deacon,[†] Andreas Ioannis Karsisiotis,[†] Tadeo Moreno-Chicano,[†] Michael A. Hough,[†] Colin Macdonald,[‡] Tharin M. A. Blumenschein,[‡] Michael T. Wilson,[†] Geoffrey R. Moore,*[,‡] and Jonathan A. R. Worrall*[,†]

[†]School of Biological Sciences, University of Essex, Wivenhoe Park, Colchester CO4 3SQ, U.K.

[‡]School of Chemistry, University of East Anglia, Norwich Research Park, Norwich NR4 7TJ, U.K.

Supporting Information

ABSTRACT: Proteins performing multiple biochemical functions are called "moonlighting proteins" or extreme multifunctional (EMF) proteins. Mitochondrial cytochrome *c* is an EMF protein that binds multiple partner proteins to act as a signaling molecule, transfers electrons in the respiratory chain, and acts as a peroxidase in apoptosis. Mutations in the cytochrome *c* gene lead to the disease thrombocytopenia, which is accompanied by enhanced apoptotic activity. The Y48H variant arises from one such mutation and is found in the 40−57 Ω-loop, the lowest-unfolding free energy substructure of the cytochrome *c* fold. A 1.36 Å resolution X-ray structure of the Y48H variant reveals minimal structural changes compared to the wild-type structure, with the axial Met80 ligand coordinated to the heme iron. Despite this, the intrinsic peroxidase activity is enhanced, implying that a pentacoordinate heme state is more prevalent in the Y48H variant, corroborated through determination of a Met80 "off rate" of >125 s^{-1} compared to a rate of ∼6 s^{-1} for the wild-type protein. Heteronuclear nuclear magnetic resonance measurements with the oxidized Y48H variant reveal heightened dynamics in the 40−57 Ω-loop and the Met80-containing 71−85 Ω-loop relative to the wild-type protein, illustrating communication between these substructures. Placed into context with the G41S cytochrome *c* variant, also implicated in thrombocytopenia, a dynamic picture associated with this disease relative to cytochrome *c* is emerging whereby increasing dynamics in substructures of the cytochrome *c* fold serve to facilitate an increased population of the peroxidatic pentacoordinate heme state in the following order: wild type < G41S < Y48H.

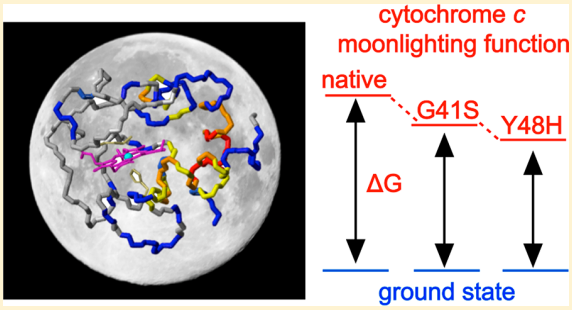

The discovery that many proteins have more than one biological function was an important advance in understanding how complex organisms can have relatively few genes to perform the many thousands of biochemical functions that occur within it.[3,4] Jeffery listed a variety of mechanisms by which the function of a protein can switch between its different activities and termed this ability "moonlighting".[6] In addition to genetic origins governing expression, these mechanisms included differential localization within the cell, intracellular versus extracellular location, oligomerization, variable ligand/substrate concentrations, chemical regulation of activity, different binding sites for different partner molecules, and being part of different multiprotein complexes.[6] Advances in the field have led to the recent suggestion that the phrase "extreme multifunctional (EMF) proteins" be employed instead of moonlighting proteins.[7] The rebranding is to create focus on the functional aspects of the phenomenon, rather than the mechanistic, noting that what makes moonlighting proteins worth studying is the fact that they perform diverse functions and so that is what their definition should emphasize.[8] However, from a chemical perspective, it is important to understand how moonlighting or EMF proteins operate. Energy landscape theory[9] suggests that one way a protein could moonlight is if the ground state structure, which is the prevalent form under physiological conditions, is in equilibrium with one or more higher-energy forms of different structure present in small amounts. Such excited states of proteins have been identified in numerous systems in recent years, particularly through studies of protein folding, but also in ligand binding and enzyme catalysis,[10,11] and thus, it is reasonable to think that this offers a route to enable proteins to moonlight.

Cytochrome *c* (Cc) is well-known for its role in mitochondrial electron transfer as an electron carrier between the cytochrome bc_1 and aa_3 complexes,[12] but it also plays two important roles in apoptosis.[13,14] One role is as a peroxidase to oxidize lipids as part of the process of creating a pore in the outer mitochondrial membrane,[15] and the second set of roles is as a component of various multiprotein complexes, including

Received: September 7, 2017
Revised: October 7, 2017
Published: October 30, 2017

DOI: 10.1021/acs.biochem.7b00890
Biochemistry XXXX, XXX, XXX−XXX

the cytoplasmic apoptosome multiprotein complex,[16] heat shock protein 27,[17] and inositol triphosphate receptors in the endoplasmic reticulum.[18] Cc also functions as an inhibitor of a histone chaperone activity in the nucleus following DNA damage by binding to a nucleosome assembly protein[19] and as an extracellular ligand to serum leucine-rich α-2-glycoprotein-1,[20] an interaction that helps lymphocytes to survive from the toxicity resulting from Cc being released from cells undergoing apoptosis. From the available structural information, it appears that Cc in its role as a histone chaperone inhibitor[19] and as a component of the apoptosome[21] binds to the relevant partner proteins at sites overlapping its binding sites for the cytochrome bc_1 and aa_3 complexes.[22,23] Thus, in these moonlighting roles, Cc appears to fit in well with the possible mechanisms described by Jeffery.[6] However, to turn Cc from an electron carrier into a peroxidase requires a major change in the way the heme group interacts with the polypeptide chain. The electron-transfer form of Cc, which we can call the ground state conformation, possesses a hexacoordinate heme iron with the side chains of His18 and Met80 acting as the axial heme iron ligands. To act as a peroxidase, Cc needs a pentacoordinate heme to allow the Fe(III) to react directly with H_2O_2, and it is this pentacoordinate state that we have suggested is the poorly populated excited state in equilibrium with the ground state[1]

Mutations in the human Cc (hCc) gene (*CYCS*) give rise to an inherited autosomal dominant disease, thrombocytopenia 4 (THC4; OMIM 612004), which is accompanied by enhanced mitochondrial apoptotic activity.[24] To date, three mutations have been identified in the *CYCS* gene that give rise to the G41S, Y48H, and A51V protein variants.[24−26] We, and others, have shown that the oxidized form of the hCc G41S variant has an intrinsic peroxidase activity greater than that of the wild-type (WT) protein.[27,28] Furthermore, using nuclear magnetic resonance (NMR) and azide binding kinetics, we have shown that an equilibrium exists between the hexacoordinate ground state and a pentacoordinate excited state, with more of the G41S variant in the excited state than for the WT protein.[1] Here we report on studies of the second pro-apoptotic variant of hCc, Y48H, and show for the ferric form even more of this variant is in the excited pentacoordinate state than the G41S variant, and that this population difference is correlated with their relative stabilities and peroxidase activities.

■ MATERIALS AND METHODS

Site-Directed Mutagenesis and Purification of the Y48H Human cyt *c* Variant. The Y48H variant of hCc was constructed using the QuikChange mutagenesis (Stratagene) protocol. The forward and reverse mutagenic primers were 5′-GCC CCT GGA TAC TCT CAT ACA GCC GCC AAT AAG AAC-3′ and 5′-GTT CTT ATT GGC GGC TGT ATG AGA GTA TCC AGG GGC-3′, respectively. A polymerase chain reaction (PCR) mix consisting of primers (75 ng/μL), the wild-type template (15 ng/μL), 10 mM dNTPs (Fermentas), PFU Turbo polymerase (Stratagene), 10 X Pfu Buffer (Agilent), and deionized water to give a final volume of 50 μL was prepared and subjected to the following PCR cycle; 95 °C for 3 min; 18 cycles of 95 °C for 1 min, 65 °C for 1 min, and 72 °C for 6 min; and 72 °C for 10 min. Overexpression of the Y48H variant together with the wild type and G41S variant in *Escherichia coli* was performed in BL21(DE3) RIL (Invitrogen) cells with isolation and purification performed as reported previously.[27]

Protein Preparation. Oxidized Cc proteins were prepared by the addition of excess $K_3[Fe(CN)_6]$, followed by removal of $K_3[Fe(CN)_6]$ and $K_4[Fe(CN)_6]$ and exchange into a desired buffer using a PD-10 column (GE Healthcare). The protein concentration was determined with a Cary 60 spectrophotometer (Agilent) and a molar extinction coefficient (ε) of 106 mM^{-1} cm^{-1} at 409 nm.

Chemical Denaturation and Alkaline pH Titrations. Far-ultraviolet (far-UV) circular dichroism (CD) spectra at 15 °C for oxidized Cc proteins (20 μM) in 10 mM potassium phosphate and 50 mM potassium fluoride (pH 6.5) were recorded in the wavelength range of 190−250 nm with an Applied Photophysics (Leatherhead, U.K.) Chirascan CD spectrophotometer. Oxidized Cc stabilities were determined by titrating a 6 M stock solution of guanidine hydrochloride (GuHCl) (Fluka) to a 20 μM protein sample and the changes in molar ellipticity at 222 nm (θ_{222}) monitored. All titrations were performed in triplicate. The fraction unfolded (F_u) at any given GuHCl concentration was determined,[29] and the free energy of unfolding (ΔG_{unf}) and dependence of ΔG_{unf} on denaturant concentration (m value) were calculated using an equation for a two-state unfolding process.[2] The pH dependence of the 695 nm band in the ultraviolet−visible (UV−vis) spectrum was monitored at room temperature by determining its absorbance at various pH values for a solution of 100 μM oxidized Cc in a quartz cuvette (Hellma) with a small aliquot of $K_3[Fe(CN)_6]$ present to maintain an oxidizing environment. The pH of the buffer [20 mM sodium phosphate (pH 6.0)] was adjusted with microliter aliquots of 1 M NaOH and measured after each addition using a semimicro glass pH electrode. pH titrations were repeated up to three times with different batches of proteins. Data were fitted to a one-proton ionization equilibrium equation to yield an apparent pK_a.

Preparation of Liposomes and Peroxidase Assays. The phospholipids 1,1′,2,2′-tetraoleoyl cardiolipin (TOCL) and 1,2-dioleoyl-*sn*-glycero-3-phosphocholine (DOPC) (Avanti Polar Lipids, Alabaster, AL) were mixed in a 1:1 ratio, vortexed with the appropriate amount of buffer [20 mM sodium phosphate (pH 6.5)], and sonicated for 5 min in a high-power sonicating water bath filled with ice-cold water to give the desired stock concentration as previously described.[27] Peroxidase assays of the ferriCc proteins were performed in the absence and presence of liposomes using H_2O_2 (Sigma) and 2,2-azinobis(3-ethylbenzthiazoline-6-sulfonic acid) (ABTS) (Sigma). The oxidation of ABTS was monitored at 730 nm on a Hewlett-Packard 8453 diode array spectrophotometer scanning between 190 and 1100 nm and thermostated at 20 °C. The reaction was initiated by the addition of 1 mM H_2O_2 (after 40 s) to a series of cuvettes containing 5 μM ferriCc and 200 μM ABTS with or without 25 μM TOCL/DOPC from a 2.5 mM stock. Using the wavelength pair of 475 and 730 nm, the slope of each trace (post-lag phase) was determined to obtain a rate in absorbance units per second. The rate of ferriCc turnover is reported in inverse seconds obtained by dividing absorbance units per second by the product of the concentration of oxidized ABTS (ε = 14 mM^{-1} cm^{-1}) and the total protein concentration of 5 μM. All assays were performed in triplicate with errors reported as the standard error.

Stopped-Flow Kinetics. An Applied Photophysics SX20 stopped-flow spectrophotometer thermostated at 25 °C and equipped with both photomultiplier and diode array detection systems was used to monitor the kinetics of binding of azide (N_3^-) to the oxidized Y48H hCc variant. A stock solution of 2 M sodium azide (Sigma) was prepared in 50 mM MES (pH 7.0) and diluted to the desired N_3^- concentration with the

DOI: 10.1021/acs.biochem.7b00890
Biochemistry XXXX, XXX, XXX−XXX

same buffer containing 2 M NaCl to maintain the ionic strength. Reaction time courses were taken at 420 nm with the N_3^- concentration varying between 0.08 and 2 M before mixing and 10 μM protein (before mixing). All transients were fitted to a single-exponential function yielding both pseudo-first-order rate constants and amplitudes.

Crystallization and X-ray Structure Determination. Crystals were grown using the sitting-drop vapor diffusion method at 18 °C. A 0.2 μL solution containing 56 mg/mL oxidized Y48H Cc variant in 20 mM sodium phosphate (pH 6.5) was mixed with an equal volume of a reservoir solution [33% PEG6000 and 100 mM Tris-HCl (pH 7.5)] using a Crystal Gryphon robot (Art Robbins Instruments). Crystals were transferred to a cryoprotectant solution containing the reservoir solution and 15% glycerol, before being flash-cooled by being plunged into liquid nitrogen. Crystallographic data were measured at the Swiss Light Source (SLS, Villigen, Switzerland) at beamline X10SA using a Pilatus 6M-F detector (Dectris) and an X-ray wavelength of 1.0 Å. Data were indexed using XDS[30] and scaled and merged using Aimless[31] in the CCP4 suite with the CCP4i2 interface. The structure was determined by molecular replacement in Phaser[32] using the WT hCc structure[27] [Protein Data Bank (PDB) entry 3zcf] as the search model. The structure was refined with Refmac5,[33] with model building between refinement cycles in Coot.[34] Riding hydrogen atoms were added when refinement of the protein atoms had converged. Structures were validated using the Molprobity server[35] and the JCSG Quality Control Server and tools within Coot.[34] Structural superpositions were performed using GESAMT in CCP4i2.[36] Coordinates and structure factors were deposited in the PDB as entry 5O10. A summary of data, refinement statistics, and quality indicators for the structure is given in Table 1.

NMR Spectroscopy. All NMR data were collected with a Bruker 500 MHz (H/D exchange) or 800 MHz [one-dimensional (1D), ^{15}N relaxation, and sequence specific assignments] spectrometer, both equipped with 5 mm HCN inverse triple-resonance z-axis gradient probes. Samples for 1D ^{1}H NMR spectroscopy were oxidized and buffer exchanged into 20 mM sodium phosphate (pH 6.5) and freeze-dried. Samples were redissolved in 500 μL of 99.9% D_2O (sigma) and allowed to deuterate at room temperature for ∼72 h. 4,4-Dimethyl-4-silapentane-1-sulfonic acid (DSS) (Sigma) (final concentration of 200 μM) and $K_3[Fe(CN)_6]$ (final concentration of 100 μM to maintain an oxidizing environment) were added to each sample, and 1D spectra were recorded at temperatures ranging from 288 to 313 K using presaturation to suppress the solvent signal with spectral widths of 20 and 80 ppm. Spectra were processed in Topsin (Bruker Biospin).

Singly (^{15}N) and doubly (^{13}C and ^{15}N) labeled samples of the Y48H hCc variant were prepared using procedures previously described.[37] NMR samples of the oxidized Y48H variant were prepared in 20 mM sodium phosphate (pH 6.5) and contained 1 mM protein with 10% D_2O (Sigma) for the lock. A set of two-dimensional (2D) ^{1}H−^{15}N HSQC and three-dimensional (3D) HNCACB and CBCA(CO)NH spectra were recorded at 288 K and processed in Topsin (Bruker Biospin). Sequence specific assignments were obtained using the CCPNmr Analysis[38] and Sparky[39] programs.

H/D exchange NMR data were acquired at 288 K. Freeze-dried samples of the oxidized Y48H variant (1 mM) were redissolved in 20 mM sodium phosphate (pH 6.5) and 50 mM NaCl premade in 99.9% D_2O (Sigma). Spectra were recorded as matrices of 1024 × 64 complex data points with four scans and spectral widths of 15 (^{1}H) and 42 (^{15}N) ppm centered at 4.7 and 118.6 ppm, respectively. The acquisition of consecutive ^{1}H−^{15}N HSQC spectra started ∼5 min after sample resuspension. Acquisition proceeded with consecutive HSQC spectra with an acquisition time of ∼5 min for a period of 134 h, totalling 191 experiments. The first 100 experiments were performed with a 10 s delay between each to ensure maximum coverage of the fast-exchanging residues, with the following 74 experiments at 45 min intervals, followed by 17 experiments at 4 h intervals. CCPNmr Analysis[38] was used to fit peak volumes as a function of time to a single-exponential decay function to yield decay rates from which protection factors (PFs) were calculated[40,41] (Table S1). The free energies of exchange (ΔG_{ex}) were calculated from the equation $\Delta G_{ex} = -RT \ln(PF)$, where R is the gas constant and T is the temperature in kelvin[41] (Table S1).

^{15}N T_1 and T_2 and [^{1}H]−^{15}N NOE data were collected at 288 K with spectra acquired as matrices of 1024 × 256 complex data points and eight scans for T_1 and T_2 data and 64 scans for [^{1}H]−^{15}N NOE data. Spectral widths of 15 (^{1}H) and 39.3 (^{15}N) ppm centered at 4.7 and 118.6 ppm, respectively, were used. T_1 experiments were performed with relaxation delays of 20, 50, 80, 200, 500, 750, 2000, and 3500 ms with duplicates at 20, 200, and 500 ms. T_2 experiments were performed with relaxation delays of 16.96, 33.92, 50.88, 67.84, 101.76, 135.68, 203.52, and 254.40 ms with duplicates at 16.96, 50.88, and 101.76 ms. Recycle delays for both experiments were 5 s. The repeated relaxation delays were used for the determination of peak height uncertainties.[42] The T_1 and T_2 series of experiments were performed as a pseudo-3D experiment and processed as individual 2D planes using NMRPipe.[43] Residues with peak overlap or weak intensity were excluded from the analysis. T_1 and T_2 values were extracted through the fitting of peak heights as a function of time to a single-exponential function in CCPNmr Analysis.[38] These were subsequently converted to R_1 and R_2 rate constants ($R_1 = 1/T_1$, and $R_2 = 1/T_2$). The fit errors for T_1 and T_2 were also converted into R_1

Table 1. Crystallographic Data Processing and Refinement Statistics for the Y48H hCc Variant[a]

space group	$P2_1$
unit cell dimensions	a = 56.9 Å, b = 36.5 Å, c = 60.7 Å, β = 116.7°
resolution (Å)	1.36
R_{merge}	0.072 (1.115)
no. of unique reflections	45812 (2124)
M_n (I/SD)	13.3 (1.4)
$CC_{1/2}$	0.998 (0.512)
completeness (%)	95.3 (90.2)
redundancy	6.2 (5.4)
R_{cryst}	0.144
R_{free}	0.175
root-mean-square deviation for bond lengths (Å)	0.015
root-mean-square deviation for bond angles (deg)	2.18
Ramachandran favored (%)	97.0
accumulated dose (MGy)	2.54
PDB entry	5O10

[a]Values in parentheses refer to the outermost resolution shell of 1.39−1.36 Å.

DOI: 10.1021/acs.biochem.7b00890
Biochemistry XXXX, XXX, XXX−XXX

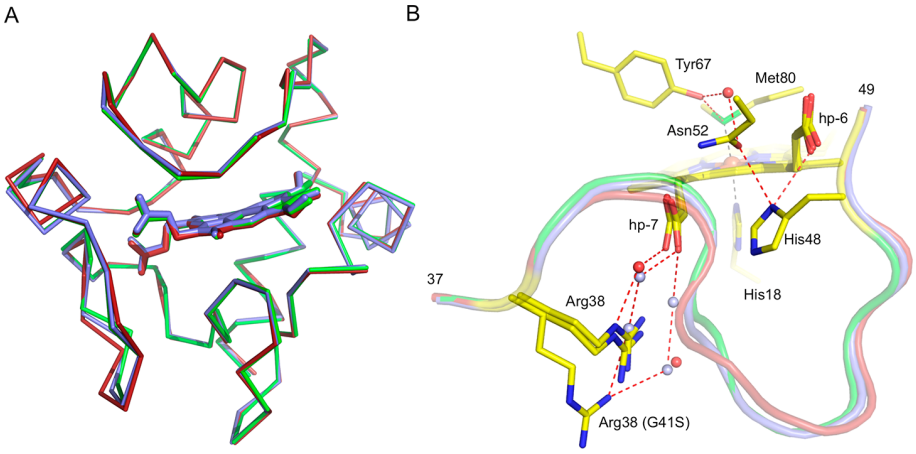

Figure 1. X-ray crystal structure of the Y48H variant of hCc. (A) Ribbon representations of a Cα superposition (molecule A) of the Y48H variant (green, PDB entry 5O10) with the G41S variant (red, PDB entry 3nwv) and WT protein (blue, PDB entry 3zcf). The heme groups are shown as sticks. (B) Cartoon and stick representation of the region between residues 37 and 49 of the WT protein (blue) and the Y48H (green) and G41S (red) variants. The coordinate bonds (black dashes) of the axial His18 and Met80 ligands to the heme iron in the Y48H variant are indicated, and H-bonding is represented as red dashes. The side chain positions of His48, Asn52, and Tyr67 in the Y48H variant are shown together with the side chain position of Arg38 in all three structures. Water molecules are shown as red spheres for the WT and Y48H structures and as gray spheres for the G41S variant.

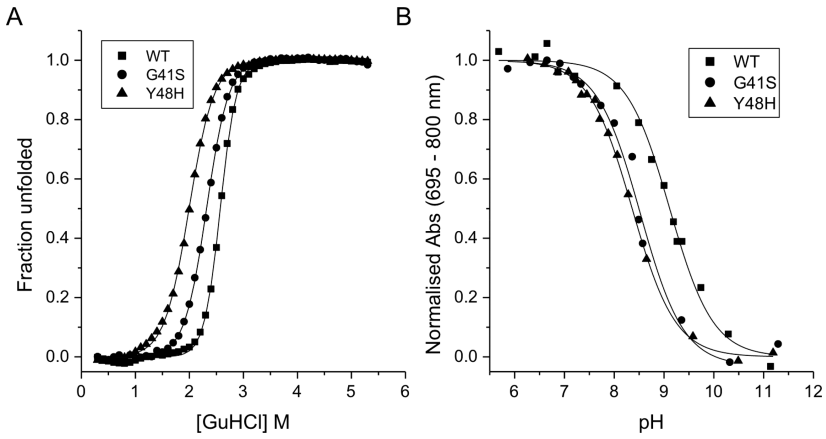

Figure 2. Global stability and pK_{695} measurement of the oxidized Y48H variant of hCc compared under identical experimental conditions with those of the WT protein and G41S variant. (A) Plots of fraction unfolded as a function of GuHCl at pH 6.5 and 15 °C. Solid lines are fits to the data using a two-state equilibrium unfolding equation,[2] with the determined ΔG_{unf} values reported in Table 2. (B) pH dependence of the 695 nm absorbance band. Solid lines are representative fits to the data using a one-proton equilibrium equation with pK_{695} values reported in Table 2.

and R_2 errors through the equality of the T_1/T_2 and R_2/R_1 errors, respectively. Heteronuclear $[^1H]-^{15}N$ NOEs were measured with a proton saturation period of 5 s. Interleaved saturated and unsaturated experiments were performed in triplicate to determine the experimental errors as the standard deviation of the average NOE value. NOE values were calculated as the ratio of peak heights with and without proton saturation.

RESULTS

X-ray Structure of the Pro-Apoptotic Y48H hCc Variant. The X-ray structure of the Y48H variant of hCc was determined to 1.36 Å resolution. A space group of $P2_1$ was determined with two hCc molecules found in the crystallographic asymmetric unit, contrasting with the reported X-ray structures of the WT protein[27] and G41S variant,[44] both of which had a P_1 space group and four hCc molecules in the asymmetric unit. The diffraction-weighted dose[45] incurred during collection of the high-resolution X-ray data set for the Y48H variant was 2.54 MGy, a dose greatly exceeding that required to fully reduce ferric heme proteins to the ferrous form (typically tens to hundreds of kilograys).[46,47] Hence, while the crystals were obtained from solutions of the ferric protein, in light of the extensive previous studies, measuring the doses typically required for ferric to ferrous heme protein reduction, we consider the structure to likely be predominantly that of the ferrous state. It is important to note that earlier X-ray studies of tuna Cc[48] and *Saccharomyces cerevisiae* iso-1 Cc[49] with X-ray doses much smaller than in the study presented here show that the conformation of the protein is largely independent of the heme oxidation state. Electron density in the heme region is consistent with a hexacoordinate species, with the Nε2 atom of His18 and the Sδ atom of Met80 coordinating the heme iron. The overall fold of each molecule in the asymmetric unit is identical to that of the WT protein and the G41S variant, with an overall root-mean-square deviation in Cα positions of 0.18 Å among the three X-ray structures (Figure 1A). It is noted that the Cα deviation between residues 37 and 61 increases to 0.27

DOI: 10.1021/acs.biochem.7b00890
Biochemistry XXXX, XXX, XXX−XXX

Table 2. Summary of Thermodynamic and Kinetic Parameters for the Y48H Human Ferricyt *c* Variant and Comparison with Those of the WT Protein and the G41S Variant

	GuHCl denaturation			azide binding			
protein	ΔG_{unf} (kcal mol^{-1})	m (kcal mol^{-1} M^{-1})	C_m (M)	pK_{695}	K_{app} (M)	k_1 (s^{-1})	k_{-2} (s^{-1})
Y48H	5.09 ± 0.16	2.57 ± 0.1	1.98 ± 0.05	8.4 ± 0.1	0.07 ± 0.01	125	12.1 ± 1.1
WT	10.65 ± 0.55	4.10 ± 0.25	2.60 ± 0.05	9.3 ± 0.2	0.31 ± 0.03[a]	5.77 ± 1.5[a]	3.5 ± 0.44[a]
G41S	6.75 ± 0.10	3.0 ± 0.1	2.25 ± 0.05	8.5 ± 0.2	0.11 ± 0.01[a]	45 ± 18[a]	8.9 ± 0.3[a]

[a]Data taken from ref 1.

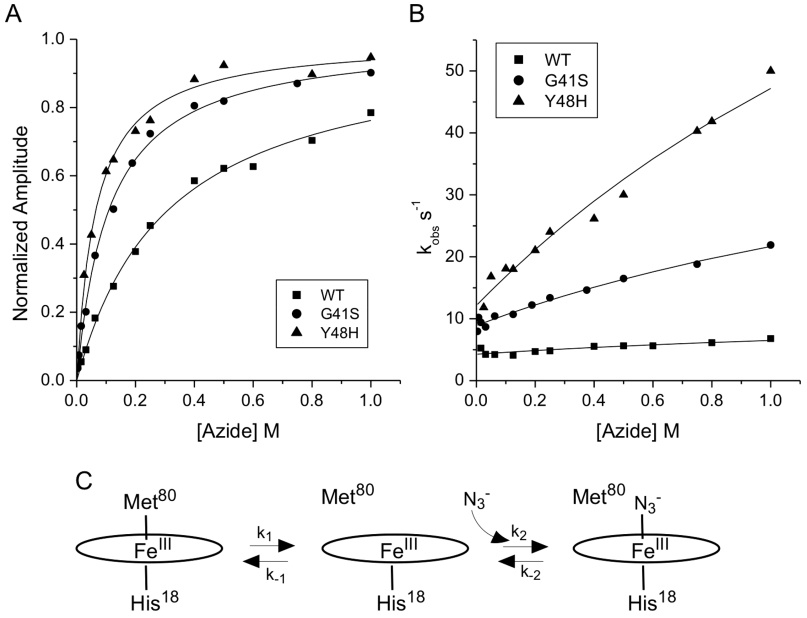

Figure 3. Binding of azide to the oxidized Y48H variant of the hCc variant compared with data for the WT protein and G41S variant[1] at pH 7.0 and 25 °C. (A) Normalized amplitudes from the reaction time courses obtained using stopped-flow absorption spectroscopy at 420 nm plotted vs azide concentration. Data are fitted to a hyperbolic equation to yield the K_{app} values listed in Table 2. (B) Rate constants (k_{obs}) determined for azide binding with solid lines representing the fits to eq 2, to give the k_1 and k_{-2} values listed in Table 2. (C) SN_1 mechanism of binding of azide to oxidized Cc.

Å. Replacing Tyr48 with a His residue alters a H-bonding arrangement involving the heme propionates. In the WT protein structure, the OH group of the Tyr48 side chain forms a H-bond (2.57 Å) to the O1A atom of heme propionate 7.[27] Such an interaction is lost in the Y48H variant, and the Nδ1 atom of the His48 side chain is favorably oriented to form a medium length polar interaction with the O2D atom of heme propionate 6 (3.19 Å) (Figure 1B). The number of H-bond interactions with the OD2 atom of heme propionate 6 therefore increases to two, with the second H-bond interaction involving the backbone amide of Thr49. A second medium length polar interaction between the Nδ1 atom of His48 and the OD1 atom of Asn52 (3.19 Å) is also noted, leading to His48 communicating with the Met80 ligand through a H-bond network that extends from Asn52, involving a H_2O molecule and Tyr67 (Figure 1B). Interestingly, the Arg38 side chain in the Y48H structure is positioned as in the WT structure, with its ε-amido group coupled to heme propionate 7 via a H_2O molecule (Figure 1B). In the G41S structure, the Arg38 side chain moves away from heme propionate 7, leading to the presence of two additional H_2O molecules (Figure 1B). These waters enable the ε-amido group of Arg38 to remain coupled to heme propionate 7 via a forked hydrogen bond network (Figure 1B).

The Y48H Variant Has a Global Stability That Is Lower Than That of the G41S Variant but a Similar Alkaline Isomerization p*K*. The Y48H variant of hCc displayed optical absorbance properties in the ferric and ferrous oxidation states and a far-UV CD spectrum identical to that of the WT protein. Far-UV CD spectroscopy is a convenient method for determining the global stabilization of a protein through chemical denaturation studies using GuHCl as illustrated in Figure 2A. It is apparent from Figure 2A that there is a progressive loss of cooperativity of unfolding (WT > G41S > Y48H), with the Y48H variant having the lowest global stability [ΔG_{unf} (Table 2)]. The m value (Table 2), which is a measure of the change in hydrophobic surface area that has become desolvated upon denaturation, decreases in the following order: WT > G41S > Y48H. This suggests that the variants have an increasingly more compact denatured state relative to the WT protein.[50] Interestingly, the K54H variant of *S. cerevisiae* iso-1 Cc stabilizes the denatured state through a His−heme loop leading to a decreased m value relative to that of the WT protein.[51] It may be that a similar effect occurs for the Y48H variant. Alternatively, the Y48H variant may simply be partially unfolded in buffer, which would also lower the m value,[52] with the NMR data (Figure 6A) providing some support for this interpretation (*vide infra*).

DOI: 10.1021/acs.biochem.7b00890
Biochemistry XXXX, XXX, XXX−XXX

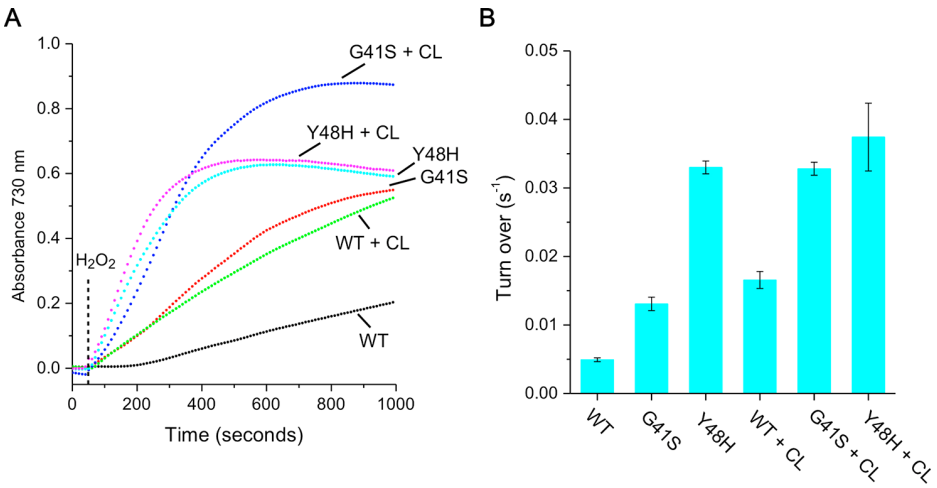

Figure 4. Peroxidase activity at pH 6.5. (A) Illustrative reaction time courses for the oxidation of ABTS in the presence of H_2O_2 with (+CL) or without CL-containing liposomes. The vertical dashed line indicates the time point in each assay at which H_2O_2 was added. (B) Maximum rates of peroxidation of ABTS with the various forms of ferriCc with (+CL) and without CL-containing liposomes. The error bars are the standard errors from triplicate measurements.

Figure 2B shows the variation in absorbance of the 695 nm band for the oxidized Y48H variant as a function of pH compared to data for WT and the G41S variant. Although the latter pK_{695} values for the WT and G41S variant have been previously reported,[27] they have been re-determined in this study so that a true comparison under identical conditions can be made (i.e., in the absence of NaCl that is known to affect the pK_{695} value[53]). The bleaching of the 695 nm band is a consequence of a deprotonation event in which the axial Met80 heme ligand becomes dissociated. The apparent pK_{695} value for the Y48H variant, which was obtained from these data, is nearly identical to that of the G41S variant but significantly lower than that of the WT protein (Table 2). Thus, whereas the global stability for the Y48H variant is clearly decreased, the Met80−Fe(III) bond lability as determined through pK_{695} values is indistinguishable from that of the G41S pro-apoptotic variant.

Exogenous Ligand Binding Reveals the Pentacoordinate Form of the Oxidized Y48H Variant Is More Populated Than for the G41S Variant or WT hCc. To probe further variances in Met80−Fe(III) bond lability, the kinetics of N_3^- binding was studied using stopped-flow spectrometry. When N_3^- is mixed with the oxidized Y48H hCc, an optical transition caused by the dissociation of Met80 from the heme iron and the binding of N_3^- in its place occurred. The reaction time course of this transition conformed to a simple exponential, as reported previously for the WT protein and the G41S variant under the same experimental conditions.[1] Over a broad range of N_3^- concentrations, the normalized amplitudes of such reaction time courses follow a simple hyperbolic binding isotherm (Figure 3A), enabling an apparent equilibrium constant (K_{app}) for N_3^- binding to be determined. From Table 2, it is apparent that the Y48H variant binds N_3^- with an affinity higher than that of either the G41S variant or the WT protein. As previously reported, the relationship between k_{obs} and N_3^- concentration under the conditions employed is almost linear,[1] which is also the case here for the Y48H variant (Figure 3B). Assuming binding of N_3^- to oxidized Cc is an SN_1 mechanism, in which the hexacoordinate heme form is in equilibrium with a pentacoordinate form, the latter being the form that binds N_3^- (Figure 3C), then, as outlined previously,[1] eqs 1 and 2 that describe the K_{app} and the dependence of k_{obs} for N_3^- binding as a function of N_3^- concentration may be derived.

$$K_{app} = K_D\left(\frac{K+1}{K}\right) \quad (1)$$

$$k_{obs} = \frac{(k_1 - k_{-2})[N_3^-]}{\frac{k_1 + k_{-1}}{k'} + [N_3^-]} + k_{-2} \quad (2)$$

where $K = k_1/k_{-1}$, with k_1 and k_{-1} being the rate constants for Met80 dissociation and association, respectively, and $K_D = k_{-2}/k_2$, with k_2 being the pseudo-first-order rate constant for N_3^- binding; i.e., $k_2 = k'[N_3^-]$, where k' is the second-order rate constant and $k_{obs} \sim k_1$ at high N_3^- concentrations. Equation 2 predicts that plots of k_{obs} versus N_3^- concentration (Figure 3B) follow hyperbolae that intercept the k_{obs} axis at the value of k_{-2} (N_3^- dissociation rate constant) and plateau at k_1, the Met80 ligand dissociation rate constant. Fits of the normalized amplitude data are satisfactory and yield the values of K_{app} listed in Table 2. Fitting the Y48H kinetic data to eq 2 presented a problem because it was not possible to explore a sufficiently high N_3^- concentration where the curve is expected to reach a plateau region, and thus, it was difficult to discriminate between linear and hyperbolic curves. Given this, we have estimated a minimum value of k_1 that provides a fit (Figure 3B), with a value (125 s^{-1}) quoted without error in Table 2, and a reliable k_{-2} value (Table 2). Nevertheless, from this estimation of k_1, it is apparent that the Y48H variant has a Met80 off rate significantly higher than those of the WT protein and the G41S variant. Furthermore, eq 1 shows that when $K <$ 1, as seen here because the concentration of the pentacoordinate species is low, then $K_{app} \sim K_D/K$. With the assumption that binding of N_3^- to the pentacoordinate species is not directly affected by a distant mutation in the protein, K_D will be similar for both the WT protein and the Y48H variant, so that the ratio of K_{app} values ($^{WT}K_{app}/^{Y48H}K_{app}$) reflects the ratio of K values ($^{Y48H}K/^{WT}K$). On this basis, $^{Y48H}K > {}^{G41S}K > {}^{WT}K$, and thus, the pentacoordinate form of the Y48H variant is more populated than in either the G41S variant or the WT protein.

The Population of the Peroxidase Active Pentacoordinate Form of the Y48H Variant Does Not Increase

DOI: 10.1021/acs.biochem.7b00890
Biochemistry XXXX, XXX, XXX−XXX

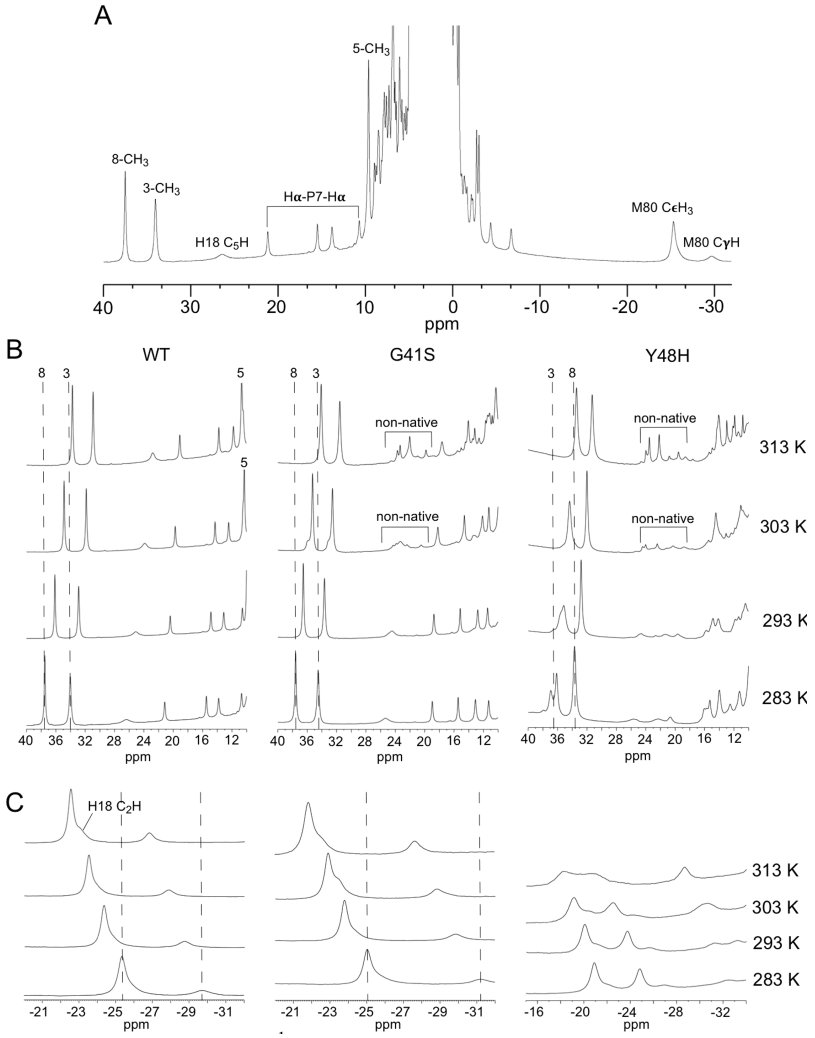

Figure 5. Paramagnetic ^{1}H NMR spectra in D_2O at pH 6.5 of oxidized hCc. (A) WT Cc spectrum with several well-resolved hyperfine-shifted resonances arising from heme substituents and protein labeled with their assignments. (B and C) Temperature dependence in the downfield and upfield regions of the spectra for the various hCc proteins. Changes in chemical shift with an increase in temperature for the 8- and 3-methyl heme substituents are indicated with dashed lines, along with those of Met80 CεH$_3$, Met80 CγH, and His18 C$_2$H.

When CL Binds. The peroxidase activity of the oxidized Y48H hCc variant was compared to that of the WT protein and the G41S variant under the same experimental conditions. From the reaction time courses given in Figure 4A, it is apparent that the WT protein displays a considerable lag phase (~160 s following addition of H_2O_2) in the absence of CL-containing liposomes. The lag phase is essentially absent for both the G41S and Y48H variants (Figure 4A). The peroxidase activity of the G41S variant is greater than that of the WT protein but less than that of the Y48H variant (Figure 4B). The progressive increase in peroxidase activity observed correlates with the increase in the level of less cooperative global unfolding (Figure 2A). In the presence of CL-containing liposomes, the lag phase is now absent for the WT protein (Figure 4A) with a significant boost in peroxidase activity evident (Figure 4B). No change in peroxidase activity is observed for the Y48H variant in the presence of CL-containing liposomes, in contrast to the case for the G41S variant, for which peroxidase activity is increased to a level similar to that of the Y48H variant (Figure 4B). The secondary increase would indicate that the binding of CL to this variant pushes the equilibrium between the hexa- and pentacoordinate heme forms farther toward the latter (Figure 3C), a finding that further confirms the interpretation from the N_3^- binding kinetics, that for the Y48H variant the pentacoordinate form of the oxidized protein is energetically more favored than it is for the G41S variant and the WT protein.

^{1}H NMR Spectroscopy Reveals an Increase in Heme Pocket Dynamics for the Y48H Variant. The ^{1}H NMR spectrum of oxidized Cc has many resonances that are shifted both downfield and upfield because their nuclei experience a hyperfine interaction from the unpaired electron on the low-spin heme iron.[54] These paramagnetic signals can inform the electronic structure of the heme and also provide insight into heme−ligand dynamics and non-native heme−ligand states.[55] The ^{1}H NMR spectrum of the oxidized WT hCc is shown in Figure 5A with some of the upfield- and downfield-shifted hyperfine resonances of known assignments labeled.[56,57] For the WT protein and G41S variant, the pattern of chemical shifts for the heme−methyl signals is 8 > 3 > 5 > 1 as expected.[58] With an increase in temperature (from 283 to 313 K), the hyperfine chemical shifts for the 8- and 3-methyl groups of the

DOI: 10.1021/acs.biochem.7b00890
Biochemistry XXXX, XXX, XXX−XXX

WT protein and G41S variant display a Curie-type temperature dependence (Figure 5B), whereas the 5-methyl group displays an anti-Curie dependence. A similar temperature dependence is observed for the upfield hyperfine-shifted resonances assigned to protons of the axial His18 and Met80 heme−iron ligands (Figure 5C). For the Y48H variant, the spectrum is notably different in the upfield or downfield regions (Figure 5B,C). At 283 K, there is a splitting of the hyperfine peak found at ∼36 ppm (Figure 5B). It is known that the 3-methyl group in certain Cc's, including horse heart Cc, displays excess line broadening compared with the other heme methyl peaks at room temperature and splits into two resonances at lower temperatures.[59,60] This view is consistent with exchange broadening due to rapid interconversion between heterogeneous protein environments around the 3-methyl group.[60] The splitting into two peaks at 283 K observed for the peak at ∼36 ppm in the Y48H variant is therefore consistent with it being assigned to the 3-methyl group (Figure 5B). Increasing the temperature causes the interconversion rate to increase, and the two components become dynamically averaged leading to a single broadened peak (Figure 5B). Burns and La Mar[60] showed at 298 K and pH 5.8 that the rate of the exchange process in oxidized horse heart Cc was $\sim 10^3\ s^{-1}$, and a similar rate for Y48H Cc at 283 K and pH 6.5 can be determined from the chemical shift difference between the heme methyl 3 resonances in the two environments (Figure 5B), a rate considerably faster than the rate (k_1) we determine for the Met80−Fe(III) bond dissociation (Table 2), showing that the unusual dynamic process affecting heme 3-methyl is not associated with the formation of the pentacoordinate state. Furthermore, the Y48H variant alters the pattern of heme methyl chemical shifts, which now becomes 3 > 8 > 5 > 1. Such an order of heme methyl shifts has not been previously observed in mitochondrially or bacterially oxidized Cc, where the order is either 8 > 3 > 5 > 1 or 5 > 1 > 8 > 3, noting that 8 is always >3 and 5 is always >1 in $S = {}^1/_2$ oxidized Cc.[61] These patterns are governed by the distribution of the unpaired electron, which reflects the orientation of heme axial ligands and is largely dependent on two conformers of the Met80 side chain related through inversion of the Met thioether sulfur.[58] In this context, we note that the upfield region of the spectrum where hyperfine signals for protons of the His18 and Met80 side chains are observed in the WT and G41S spectrum is distinctly different in the Y48H variant. Thus, although the conformation of the axial ligands is the same in the three X-ray structures, the orientation of at least Met80 for the Y48H variant in solution is different. Bren and co-workers[61] have demonstrated that fluxional solution behavior of the Met80 ligand is commonplace in Cc's. We suggest that the altered fluxional behavior causes a change in the magnetic susceptibility axes that perturbs the relative chemical shifts of the 3- and 8-methyl resonances.[61]

Finally, we note the presence of non-native hyperfine signals in the G41S and Y48H variants in the downfield region between 18 and 26 ppm at ≥303 K (Figure 5B). A similar set of non-native resonances has been observed for oxidized horse Cc at temperatures of >315 K,[62] along with the WT resonances, and assigned to the alkaline conformer with Lys and His coordination of the heme Fe(III). For the G41S and Y48H variants, we suggest that as the equilibrium between the hexa- and pentacoordinate heme form is pushed farther toward the latter species with an increase in temperature, these non-native species similarly arise from a fraction of the protein that populates the alkaline conformation. The fact that these resonances are not observed for the WT protein under similar conditions is a further indication that these pro-apoptotic variants have a more labile Met80−Fe(III) ligand. Note that the N_3^- binding study of the G41S variant[1] showed that under the conditions employed for these measurements the alkaline conformer was not significantly populated. With the higher protein concentrations and longer experimental times needed for the NMR experiments, it is clear that at elevated temperatures the alkaline conformer becomes populated.

The Y48H Variant Has Increased Main Chain Mobility Relative to That of the G41S Variant. To explore in more detail the dynamics of the oxidized Y48H variant, ^{15}N backbone amide H/D exchange and ^{15}N relaxation studies using NMR spectroscopy were performed. The $^1H-^{15}N$ HSQC spectrum of the Y48H variant is shown in Figure 6A overlaid with the

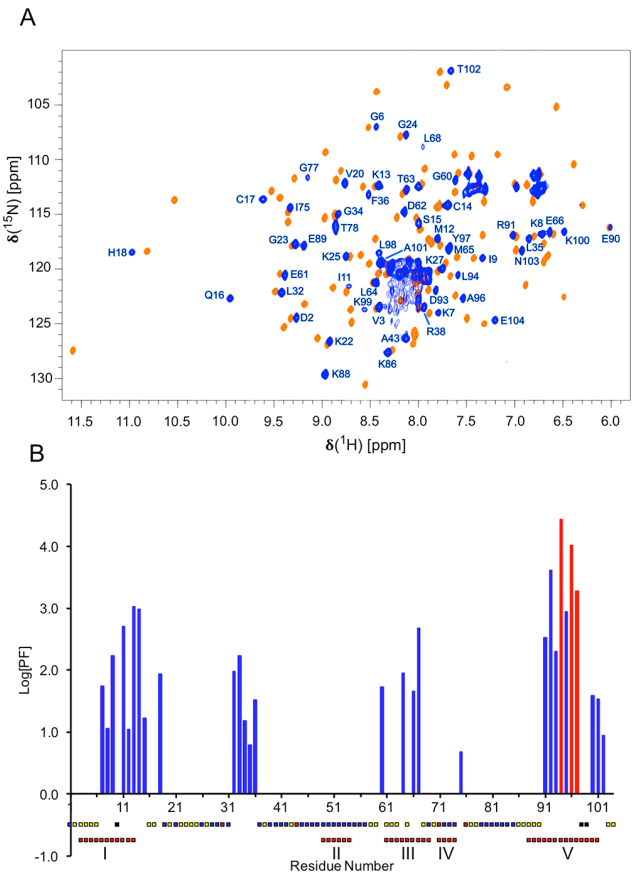

Figure 6. Backbone amide assignments and amide proton H/D exchange analysis of the oxidized Y48H hCc variant. (A) Overlay of the 800 MHz $^1H-^{15}N$ HSQC spectrum of the Y48H variant (blue) with the WT protein spectrum (orange) at 288 K. Assignments for most of the assigned backbone amide resonances in the Y48H spectrum are colored blue. (B) PFs for the Y48H variant plotted vs residue number. For the PFs that could be calculated, three residues underwent fast (log PF ≤ 1), 13 medium (1 < log PF ≤ 2), 10 slow (2 < log PF), and three extremely slow (residual proton occupancy of >80% after ∼134 h corresponding to exchange rates of <0.003 h^{-1}; colored red) exchange. Secondary structure (α-helix) is indicated by the bottom red squares with the α-helices numbered I−V, while red squares above represent Pro residues. Unassigned and fast-exchanging residues are shown as dark blue and yellow squares, respectively. Residues for which PFs could not be calculated because of the slowness of the exchange are shown as black squares (three residues).

DOI: 10.1021/acs.biochem.7b00890
Biochemistry XXXX, XXX, XXX−XXX

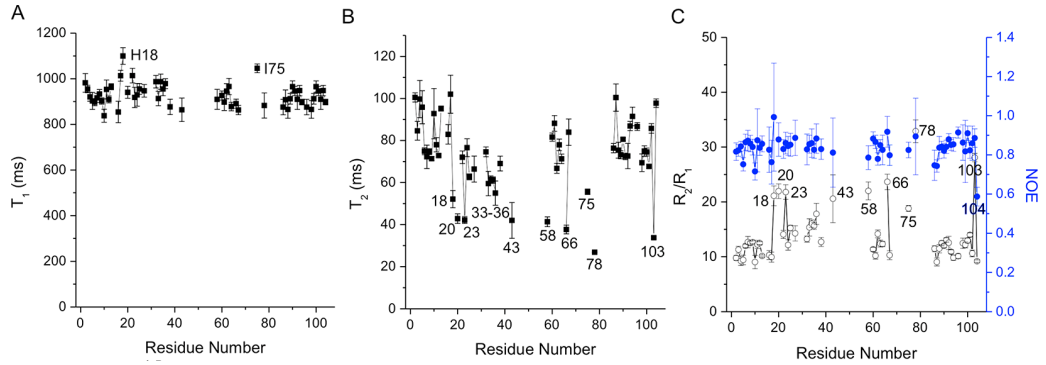

Figure 7. ^{15}N relaxation parameters for the oxidized Y48H hCc variant acquired at 800 MHz and 288 K. (A) T_1 and (B) T_2 times plotted vs residue number. (C) R_2/R_1 ratio (black empty circles) and [^{1}H]−^{15}N NOE (blue circles) plotted vs residue number.

WT protein spectrum under identical conditions.[1] Clear differences between the two spectra exist (Figure 6A). Most notable is the significant number of backbone amide resonances absent in the Y48H spectrum compared with the WT spectrum, with a total of 64 backbone amide resonances of a possible 99 non-proline residues being assigned (Table S1). The missing resonances are found predominately in the 40−57 Ω-loop encompassing helix II and the 71−85 Ω-loop. At a lower magnetic field strength (500 MHz), no new peaks in the Y48H ^{1}H−^{15}N HSQC spectrum arise, which coupled with the increased line widths of the backbone amide resonances at 800 MHz is indicative of the Y48H variant having conformational heterogeneity significantly greater than that of the WT protein.[1,37]

H/D exchange behavior of the oxidized Y48H hCc variant was monitored, and backbone amide PFs, defined as the ratio between the observed experimental and intrinsic exchange rates (k_{ex}/k_{in}), were determined[40] (Table S1). Exchange rates are influenced by H-bonding, particularly in secondary structure and solvent accessibility.[63] Of the 64 assigned backbone amides, 32 are fully exchanged within the first 10 min, leaving only 32 residues for which H/D exchange behavior could be analyzed. From these, PFs were calculated for 29 residues, with three residues having exchange that is too slow to calculate within the experimental time frame (Figure 6B). The rapid H/D exchange of many backbone amide resonances and the absence of resonances for 28 backbone amides can be seen from the sequence dependence of the PFs plotted in Figure 6B for the Y48H variant. Only interlocking helices I and V along with portions of helix III and the 32−36 turn maintain various levels of protection, with the remaining segments of the protein likely to be undergoing extensive dynamic fluctuations (Figure 6B).

^{15}N relaxation parameters, T_1, T_2, and NOE, were obtained for 55 residues, with plots of these parameters versus residue number shown in Figure 7 for the Y48H variant. The average relaxation rates were as follows: R_1 = 1.08 ± 0.03 s^{-1}, and R_2 = 14.99 ± 0.72 s^{-1}, with an average NOE of 0.84 ± 0.06. These values are similar to those of the WT protein (R_1 = 0.99, R_2 = 14.23, and NOE = 0.84) and the G41S variant (R_1 = 1.07, R_2 = 14.48, and NOE = 0.84).[1] The T_1 values, reporting on nanosecond to picosecond motions, are relatively constant, with the notable exceptions of His18 and Ile75 (Figure 7A). In contrast, the T_2 plot reveals a significant number of residues that deviate below the average (Figure 7B), probably reflecting contributions to relaxation from slower conformational exchange equilibria. A useful indicator to identify residues experiencing chemical exchange is a plot of the R_2/R_1 ratio (Figure 7C). Despite the smaller size of the relaxation data set for the Y48H variant (55 residues) compared to that of the G41S variant (92 residues),[1] a similar pattern of residues experiencing slow conformational exchange emerges (i.e., 14−36, 40−57, and 71−85 Ω-loops) and is also in keeping with the regions experiencing rapid H/D exchange (Figure 6B).

DISCUSSION

The past two decades of Cc research have placed this essential redox protein firmly into the category of a moonlighting or EMF protein.[64] For Cc to have a peroxidatic moonlighting function, access to an alternative structural state or conformer is required. Such a form could come about because Cc binding of CL results in a conformational change to create the peroxidatic state or because the ground state structure is in equilibrium with one or more minor higher-energy forms of different structure and CL binding displaces the equilibrium by binding preferentially to a higher-energy state. We have shown for the pro-apoptotic G41S variant of hCc enhanced conformational dynamics of the 40−57 Ω-loop exists and is directly linked to the dissociation of the Met80−Fe(III) ligand in the 71−85 Ω-loop. Cross-talk between Ω-loops results in an increased population of the peroxidatic pentacoordinate state,[1] which under healthy conditions aids in controlling levels of reactive oxygen species (ROS) but during the early phase of mitochondrial apoptosis results in Cc peroxidizing the membrane lipid CL. Furthermore, once released from the mitochondrion, Cc has also been implicated in the peroxidation of the plasma membrane lipid phosphatidylserine.[65] The second thrombocytopenia 4-associated mutation of hCc to be discovered was the Y48H variant,[25] which is also located within the 40−57 Ω-loop. In Cc evolution, this is the least conserved Ω-loop and has the lowest free energy of the five cooperative folding/unfolding units (foldons) assigned in Cc.[66,67] Perhaps not surprisingly, therefore, the Y48H variant displays enhanced mobility and dynamics. However, it is apparent that the dynamics, both local and global, are further enhanced in the Y48H variant compared to those in the G41S variant. Such behavior is revealed by the fact that ∼35% of backbone amide resonances for the Y48H variant remain unassigned because of their absence in the ^{1}H−^{15}N HSQC spectrum compared to 2 and 6% for the WT protein and G41S variant, respectively, under identical conditions. Except for Ala43, the whole of the 40−57 Ω-loop is unassigned, along with the latter half (residues 79−85) of the 71−85 Ω-loop, the second least stable foldon,[67] housing the Met80−Fe(III) ligand. These missing resonances in the Y48H variant are a likely consequence of a decreased T_2

DOI: 10.1021/acs.biochem.7b00890
Biochemistry XXXX, XXX, XXX−XXX

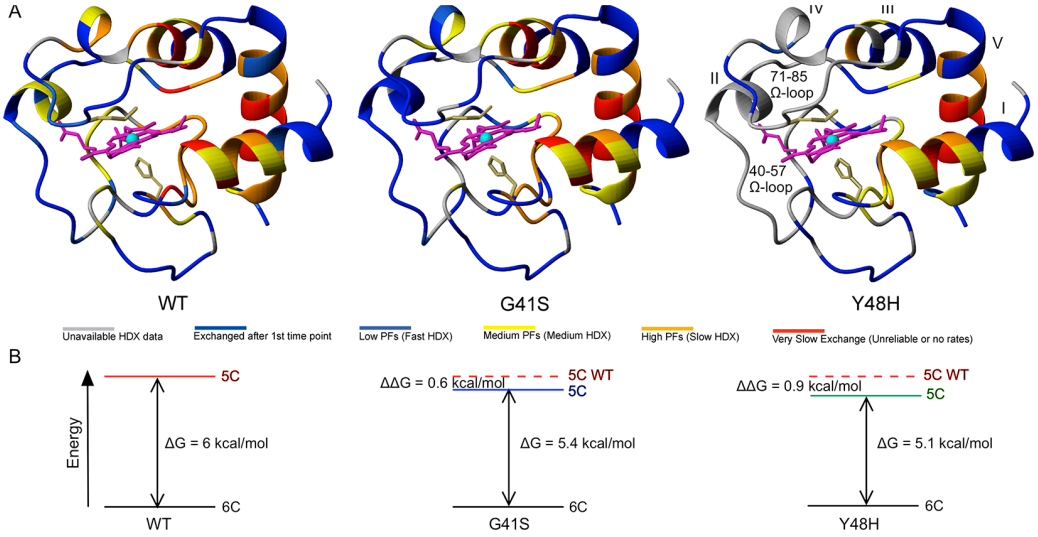

Figure 8. Dynamics in the hCc variants identified as causing thrombocytopenia 4. (A) PF mapping onto the respective X-ray structures of hCc, with PFs color-coded as indicated. The data for the ferric WT protein and ferric G41S variant were taken from ref 1, with the data for the Y48H variant taken from the LogP plot in Figure 6B. The heme and axial ligands are shown as sticks and helices labeled I−V. (B) Energy diagrams illustrating the calculated differences in the free energy change ($\Delta\Delta G$) between the pentacoordinate forms in the various species derived from the equation $\Delta G = -RT \ln({}^{WT}K_{app}/{}^{variant}K_{app})$ from N_3^- binding kinetics. The ΔG for the WT protein is based on data from ref 5.

resulting from exchange between different conformations. Although we cannot demonstrate unequivocally from direct NMR measurements, because of the missing resonances, that the Y48H variant has enhanced dynamics on the microsecond to millisecond time scale (i.e., compute R_{ex} terms), it is apparent for the resonances that allow an amide H/D exchange PF to be calculated (i.e., those from the N- and C-terminal helices, the end of the 14−36 Ω-loop, and some of helix 3) that these are generally smaller for the Y48H variant than for the other proteins.[1] Visualization of the spread in increasing dynamics can be appreciated from mapping amide H/D exchange data onto the respective Cc X-ray structures (Figure 8A). From this, it is apparent that helices I, III, and V for all proteins maintain similar H/D profiles, with the mutations clearly resulting in more rapid exchange and thus enhanced dynamics (WT < G41S < Y48H) in the 40−57 and 71−85 Ω-loops, as well as helix II (Figure 8A).

Englander and colleagues have elegantly determined how Cc folds through uncovering its foldon substructure.[66,67] Of the five foldons, the two with the lowest stability are the 40−57 and 71−85 Ω-loops.[5,68] The correlation between the conformational dynamics linking the G41S and Y48H mutations with the displacement of the Met80 ligand and the energetics of the foldon substructure is striking. Making the assumption that the pentacoordinate state of oxidized Cc is equivalent to the partially unfolded form, with the two lowest-energy foldons unfolded, places the pentacoordinate state 6 kcal/mol above the ground state structure, based on the analyses of Hu et al.[5] and assuming the energetics of horse Cc are the same as those of hCc. From $\Delta G = -RT \ln({}^{WT}K_{app}/{}^{Y48H}K_{app})$ (determined from the kinetics of N_3^- binding), the relative $\Delta\Delta G$ of the pentacoordinate state of the various Cc forms may be calculated as illustrated by the energy level diagrams in Figure 8B, because, as noted above, the ${}^{WT}K_{app}/{}^{Y48H}K_{app}$ ratio reflects the ratio of equilibrium constants for dissociation and reassociation of the Met80 ligand (${}^{Y48H}K/{}^{WT}K$), with the assumption that the free energy of the ground state is the same for both the variant and the WT protein. Thus, as illustrated in Figure 8B, the pentacoordinate form is 0.9 and 0.6 kcal/mol lower in energy for the Y48H and G41S variants, respectively, than for the WT protein. Each kilocalorie per mole change denotes an ∼5-fold change in the equilibrium constant governing the distribution between the hexa- and pentacoordinate forms. If the minor component in such an equilibrium, here the pentacoordinate form, plays a significant mechanistic role, then for a kilocalorie per mole change in stability the concentration of this minor component increases ∼5-fold. Our proposal that the G41S and Y48H variants cause small changes in the oxidized hCc energy landscape should be considered alongside the recent finding that the Fe(III)−S(Met) bond of Cc is weak and requires constraints imposed by the protein structure, such as extensive H-bonding of neighboring residues, to be maintained under physiological conditions.[69,70] Stabilization of a weak bond by a protein structure is an example of entasis, originally proposed to account for some of the apparently unusual properties of metalloproteins by suggesting that the metal center "constituted an energetically poised domain",[71] and Mara et al.[70] have determined that the protein entatic contribution to the Fe(III)−S(Met) bond is ∼4 kcal/mol. It is readily apparent therefore that small changes in the energy landscape can have mechanistic effects and contribute to this moonlighting function of Cc.

From the peroxidase assays, it is particularly noteworthy that the turnover of H_2O_2 by the Y48H variant is not boosted in the presence of CL liposomes, as is the case for the WT protein and the G41S variant (Figure 4B). An absence of a CL boosting effect for G41 variants has been reported by others[28] and thus contrasts with both our previous observations using an Amplex red assay[27] and in the study presented here using ABTS. Our findings that there is a boost in peroxidase activity for the G41S variant in the presence of CL liposomes are wholly consistent with our dynamic appraisal of these two variants. The Y48H variant is more dynamic than the G41S variant with the equilibrium between the hexa- and pentacoordinate species no longer being rate-limiting in this peroxidase assay for the Y48H

DOI: 10.1021/acs.biochem.7b00890
Biochemistry XXXX, XXX, XXX−XXX

variant as the concentration of the reactive pentacoordinate form is further increased (Figure 8B).

Access of small molecules such as H_2O_2 to the heme has been suggested to occur through a gating motion of Arg38 based on its side chain repositioning in the G41S variant creating a "channel" to enable H_2O molecules to access the heme.[27,44] A subsequent X-ray structure of the K72A variant of *S. cerevisiae* Cc revealed the Met80 ligand to be dissociated from the heme iron and the Arg38 side chain positioned in an "out" position as observed in the G41S structure.[72] A network of H-bonded H_2O molecules connects the Met80 side of the heme to the bulk solvent in the K72A structure.[72] Repositioning of Arg38 thus causes perturbations to the environment of the heme propionate substituent at position 7 and may be considered to influence the dynamics of the 40−57 Ω-loop, which is linked to the dissociation of the Met80 ligand.[1,27] However, we note that in the X-ray structure of the Y48H variant the Arg38 side chain is in the same position as in the WT protein (Figure 1B). Comparison of the G41S and Y48H X-ray structures reveals that the introduction of a Ser or His at positions 41 and 48, respectively, creates the opportunity for both side chains to form a H-bond to the side chain of Asn52 (Figure 1B). The latter communicates with the Met80 ligand through further H-bond interactions (Figure 1B). Thus, we propose that there are two possible conformational routes by which dynamical changes at the base of the heme could be communicated to the Met80 ligand. Indeed, the literature contains many reports showing that the 40−57 Ω-loop and heme crevice have an important conformational linkage, though this was not something always recognized at the time. For example, Robinson et al.,[73] on the basis of incomplete NMR data, showed that residues in the 40−57 Ω-loop rapidly interconverted between different local conformational states under native conditions. Our suggested role of Asn52 is consistent with observations of Schejter et al.,[74] who present data on binding of CN^- to a N52I variant of *S. cerevisiae* Cc, that are indicative of a reduced population of the pentacoordinate form. A linkage has also been discussed in connection with the alkaline isomerization of oxidized Cc[75] and is supported by the NMR structure of a triple variant of *S. cerevisiae* ferric Cc engineered to stabilize the alkaline conformer.[76] The triple variant structure showed that the 71−85 Ω-loop with the displaced Met80 ligand and the 40−57 Ω-loop were the most perturbed features compared with the WT structure.[76]

Recent studies have highlighted that Cc function can be governed by phosphorylation, where it regulates the electron-transport chain flux preventing hyperpolarization of the mitochondrial membrane potential, a known cause of ROS and trigger of apoptosis.[77,78] Three phosphorylation sites on isolates of bovine Cc have been identified from different tissues and include Thr28, Tyr48, and Tyr97.[79−81] Considering the reported pro-apoptotic behavior of the Y48H variant,[25] it is interesting to note that one of the phosphorylation sites is Tyr48, which when phosphorylated abolishes the capability to trigger apoptosis at the apoptosome level.[82−84] A recent study has characterized a Tyr48 phosphomimetic (designated Tyr48p) using a non-native amino acid to assess the effect of phosphorylation at this position on the hCc structure.[84] Structural studies were conducted with the ferrous form, which is the heme oxidation state that donates an electron to Cc oxidase,[12] and not the state that gives rise to the peroxidatic pentacoordinate form, central to our work. The WT reduced Cc is more rigid than its oxidized counterpart, and an equilibrium between the Met80-on and Met80-off forms has not been detected under non-apoptosis physiological conditions.[85] Despite this, the dynamics on the microsecond to millisecond time scale for the reduced Tyr48p Cc showed increased mobility compared to that of the WT protein, particularly in the 40−57 Ω-loop, but with an overall increase significantly smaller than those of the G41S and Y48H variants in their oxidized forms. Furthermore, an increase in mobility for the Tyr48p reduced Cc was also observed for residues 75−78 in the 71−85 Ω-loop, again highlighting the link between the 40−57 Ω-loop and the Met80 ligand. In the ferric state, Tyr48p exhibits a 3-fold increase in peroxidase activity relative to the WT protein,[84] in contrast to the Y48H variant, for which a 7-fold increase in activity is observed (Figure 4B). In the presence of CL liposomes, Tyr48p displays a 7-fold boost in peroxidase activity relative to that of the WT protein and thus on par with the Y48H variant in the absence or presence of CL (Figure 4B). Therefore, these data suggest that the equilibrium constant between the hexacoordinate and pentacoordinate heme forms (Figure 3C) favors the hexacoordinate form in Tyr48p relative to the Y48H variant, enabling CL to further regulate the activity of the phosphorylated protein, which may have consequences for pro- and anti-apoptotic behavior insofar as we have shown that the pentacoordinate heme form is critical for this.

In conclusion, we have shown that the naturally occurring Y48H variant of hCc in its oxidized heme state is more peroxidatic than either the WT protein or the G41S variant that is also implicated in thrombocytopenia. The dynamic fluctuations in the 40−57 Ω-loop resulting in cross-talk with the 71−85 Ω-loop containing the Met80 ligand are further amplified in the Y48H variant. Consequently, the Y48H protein has intrinsic peroxidase activity that is no longer enhanced in the presence of CL because of the increased population of an excited pentacoordinate heme state structure with an energy that is close to that of to the ground state Met80 coordinated structure. This finding underpins our proposal that the switch in function of the moonlighting Cc from electron transfer to peroxidase is, at least partly, a result of its preexisting conformational equilibrium involving an excited pentacoordinate state. A third naturally occurring variant, A51V, also implicated in thrombocytopenia has not yet been characterized. Because of the location of the variant on the 40−57 Ω-loop, one may predict that is has traits similar to those of the G41S and Y48H variants, and it will therefore be interesting to discover where this variant is located within the dynamic window (WT < G41S < Y48H) that has emerged from the studies so far.

■ ASSOCIATED CONTENT

Supporting Information

The Supporting Information is available free of charge on the ACS Publications website at DOI: 10.1021/acs.biochem.7b00890.

Chemical shift assignments and H/D exchange rates (k_{ex}), calculated protection factors (LogP), free energies of exchange (ΔG_{ex}), and proton occupancies (Occ) of oxidized Y48H hCc (pH 6.5 and 288 K) (Table S1) (PDF)

DOI: 10.1021/acs.biochem.7b00890
Biochemistry XXXX, XXX, XXX−XXX

AUTHOR INFORMATION

Corresponding Authors

*E-mail: g.moore@uea.ac.uk. Telephone: +44 1603 592003.
*E-mail: jworrall@essex.ac.uk. Telephone: +44 1206 872095.

ORCID

Jonathan A. R. Worrall: 0000-0002-1863-834X

Funding

Our work was supported by a Leverhulme Trust project grant (RPG-2013-164) to J.A.R.W. and a Leverhulme Trust emeritus fellowship (EM-2014-088) to G.R.M. Access to the Swiss Light Source was made possible by Long-Term award 20160704 to M.A.H.

Notes

The authors declare no competing financial interest.

REFERENCES

(1) Karsisiotis, A. I., Deacon, O. M., Wilson, M. T., Macdonald, C., Blumenschein, T. M., Moore, G. R., and Worrall, J. A. (2016) Increased dynamics in the 40−57 Ω-loop of the G41S variant of human cytochrome c promote its pro-apoptotic conformation. *Sci. Rep. 6*, 30447.

(2) Santoro, M. M., and Bolen, D. W. (1992) A test of the linear extrapolation of unfolding free energy changes over an extended denaturant concentration range. *Biochemistry 31*, 4901−4907.

(3) Henderson, B., and Martin, A. C. (2014) Protein moonlighting: a new factor in biology and medicine. *Biochem. Soc. Trans. 42*, 1671−1678.

(4) Jeffery, C. J. (2014) An introduction to protein moonlighting. *Biochem. Soc. Trans. 42*, 1679−1683.

(5) Hu, W., Kan, Z. Y., Mayne, L., and Englander, S. W. (2016) Cytochrome c folds through foldon-dependent native-like intermediates in an ordered pathway. *Proc. Natl. Acad. Sci. U. S. A. 113*, 3809−3814.

(6) Jeffery, C. J. (1999) Moonlighting proteins. *Trends Biochem. Sci. 24*, 8−11.

(7) Chapple, C. E., Robisson, B., Spinelli, L., Guien, C., Becker, E., and Brun, C. (2015) Extreme multifunctional proteins identified from a human protein interaction network. *Nat. Commun. 6*, 7412.

(8) Chapple, C. E., and Brun, C. (2015) Redefining protein moonlighting. *Oncotarget 6*, 16812−16813.

(9) Bryngelson, J. D., Onuchic, J. N., Socci, N. D., and Wolynes, P. G. (1995) Funnels, pathways, and the energy landscape of protein folding: a synthesis. *Proteins: Struct., Funct., Genet. 21*, 167−195.

(10) Henzler-Wildman, K., and Kern, D. (2007) Dynamic personalities of proteins. *Nature 450*, 964−972.

(11) Baldwin, A. J., and Kay, L. E. (2009) NMR spectroscopy brings invisible protein states into focus. *Nat. Chem. Biol. 5*, 808−814.

(12) Ferguson-Miller, S., and Babcock, G. T. (1996) Heme/Copper Terminal Oxidases. *Chem. Rev. 96*, 2889−2908.

(13) Ow, Y. P., Green, D. R., Hao, Z., and Mak, T. W. (2008) Cytochrome c: functions beyond respiration. *Nat. Rev. Mol. Cell Biol. 9*, 532−542.

(14) Huttemann, M., Pecina, P., Rainbolt, M., Sanderson, T. H., Kagan, V. E., Samavati, L., Doan, J. W., and Lee, I. (2011) The multiple functions of cytochrome c and their regulation in life and death decisions of the mammalian cell: From respiration to apoptosis. *Mitochondrion 11*, 369−381.

(15) Kagan, V. E., Tyurin, V. A., Jiang, J., Tyurina, Y. Y., Ritov, V. B., Amoscato, A. A., Osipov, A. N., Belikova, N. A., Kapralov, A. A., Kini, V., Vlasova, II, Zhao, Q., Zou, M., Di, P., Svistunenko, D. A., Kurnikov, I. V., and Borisenko, G. G. (2005) Cytochrome c acts as a cardiolipin oxygenase required for release of proapoptotic factors. *Nat. Chem. Biol. 1*, 223−232.

(16) Wang, X. (2001) The expanding role of mitochondria in apoptosis. *Genes Dev. 15*, 2922−2933.

(17) Bruey, J. M., Ducasse, C., Bonniaud, P., Ravagnan, L., Susin, S. A., Diaz-Latoud, C., Gurbuxani, S., Arrigo, A. P., Kroemer, G., Solary, E., and Garrido, C. (2000) Hsp27 negatively regulates cell death by interacting with cytochrome c. *Nat. Cell Biol. 2*, 645−652.

(18) Boehning, D., Patterson, R. L., Sedaghat, L., Glebova, N. O., Kurosaki, T., and Snyder, S. H. (2003) Cytochrome c binds to inositol (1,4,5) trisphosphate receptors, amplifying calcium-dependent apoptosis. *Nat. Cell Biol. 5*, 1051−1061.

(19) Gonzalez-Arzola, K., Diaz-Moreno, I., Cano-Gonzalez, A., Diaz-Quintana, A., Velazquez-Campoy, A., Moreno-Beltran, B., Lopez-Rivas, A., and De la Rosa, M. A. (2015) Structural basis for inhibition of the histone chaperone activity of SET/TAF-Ibeta by cytochrome c. *Proc. Natl. Acad. Sci. U. S. A. 112*, 9908−9913.

(20) Cummings, C., Walder, J., Treeful, A., and Jemmerson, R. (2006) Serum leucine-rich alpha-2-glycoprotein-1 binds cytochrome c and inhibits antibody detection of this apoptotic marker in enzyme-linked immunosorbent assay. *Apoptosis 11*, 1121−1129.

(21) Yu, T., Wang, X., Purring-Koch, C., Wei, Y., and McLendon, G. L. (2001) A mutational epitope for cytochrome C binding to the apoptosis protease activation factor-1. *J. Biol. Chem. 276*, 13034−13038.

(22) Speck, S. H., Ferguson-Miller, S., Osheroff, N., and Margoliash, E. (1979) Definition of cytochrome c binding domains by chemical modification: kinetics of reaction with beef mitochondrial reductase and functional organization of the respiratory chain. *Proc. Natl. Acad. Sci. U. S. A. 76*, 155−159.

(23) Rieder, R., and Bosshard, H. R. (1980) Comparison of the binding sites on cytochrome c for cytochrome c oxidase, cytochrome bc1, and cytochrome c1. Differential acetylation of lysyl residues in free and complexed cytochrome c. *J. Biol. Chem. 255*, 4732−4739.

(24) Morison, I. M., Cramer Borde, E. M., Cheesman, E. J., Cheong, P. L., Holyoake, A. J., Fichelson, S., Weeks, R. J., Lo, A., Davies, S. M., Wilbanks, S. M., Fagerlund, R. D., Ludgate, M. W., da Silva Tatley, F. M., Coker, M. S., Bockett, N. A., Hughes, G., Pippig, D. A., Smith, M. P., Capron, C., and Ledgerwood, E. C. (2008) A mutation of human cytochrome c enhances the intrinsic apoptotic pathway but causes only thrombocytopenia. *Nat. Genet. 40*, 387−389.

(25) De Rocco, D., Cerqua, C., Goffrini, P., Russo, G., Pastore, A., Meloni, F., Nicchia, E., Moraes, C. T., Pecci, A., Salviati, L., and Savoia, A. (2014) Mutations of cytochrome c identified in patients with thrombocytopenia THC4 affect both apoptosis and cellular bioenergetics. *Biochim. Biophys. Acta, Mol. Basis Dis. 1842*, 269−274.

(26) Johnson, B., Lowe, G. C., Futterer, J., Lordkipanidze, M., MacDonald, D., Simpson, M. A., Sanchez-Guiu, I., Drake, S., Bem, D., Leo, V., Fletcher, S. J., Dawood, B., Rivera, J., Allsup, D., Biss, T., Bolton-Maggs, P. H., Collins, P., Curry, N., Grimley, C., James, B., Makris, M., Motwani, J., Pavord, S., Talks, K., Thachil, J., Wilde, J., Williams, M., Harrison, P., Gissen, P., Mundell, S., Mumford, A., Daly, M. E., Watson, S. P., and Morgan, N. V. (2016) Whole exome sequencing identifies genetic variants in inherited thrombocytopenia with secondary qualitative function defects. *Haematologica 101*, 1170−1179.

(27) Rajagopal, B. S., Edzuma, A. N., Hough, M. A., Blundell, K. L., Kagan, V. E., Kapralov, A. A., Fraser, L. A., Butt, J. N., Silkstone, G. G., Wilson, M. T., Svistunenko, D. A., and Worrall, J. A. (2013) The hydrogen-peroxide-induced radical behaviour in human cytochrome c-phospholipid complexes: implications for the enhanced pro-apoptotic activity of the G41S mutant. *Biochem. J. 456*, 441−452.

(28) Josephs, T. M., Morison, I. M., Day, C. L., Wilbanks, S. M., and Ledgerwood, E. C. (2014) Enhancing the peroxidase activity of cytochrome c by mutation of residue 41: implications for the peroxidase mechanism and cytochrome c release. *Biochem. J. 458*, 259−265.

(29) Mason, J. M., Bendall, D. S., Howe, C. J., and Worrall, J. A. (2012) The role of a disulfide bridge in the stability and folding kinetics of Arabidopsis thaliana cytochrome c(6A). *Biochim. Biophys. Acta, Proteins Proteomics 1824*, 311−318.

(30) Kabsch, W. (2010) XDS. *Acta Crystallogr., Sect. D: Biol. Crystallogr. 66*, 125−132.

DOI: 10.1021/acs.biochem.7b00890
Biochemistry XXXX, XXX, XXX−XXX

(31) Evans, P. R., and Murshudov, G. N. (2013) How good are my data and what is the resolution? *Acta Crystallogr., Sect. D: Biol. Crystallogr. 69*, 1204−1214.
(32) McCoy, A. J., Grosse-Kunstleve, R. W., Adams, P. D., Winn, M. D., Storoni, L. C., and Read, R. J. (2007) Phaser crystallographic software. *J. Appl. Crystallogr. 40*, 658−674.
(33) Murshudov, G. N., Vagin, A. A., and Dodson, E. J. (1997) Refinement of macromolecular structures by the maximum-likelihood method. *Acta Crystallogr., Sect. D: Biol. Crystallogr. 53*, 240−255.
(34) Emsley, P., and Cowtan, K. (2004) Coot: model-building tools for molecular graphics. *Acta Crystallogr., Sect. D: Biol. Crystallogr. 60*, 2126−2132.
(35) Davis, I. W., Leaver-Fay, A., Chen, V. B., Block, J. N., Kapral, G. J., Wang, X., Murray, L. W., Arendall, W. B., 3rd, Snoeyink, J., Richardson, J. S., and Richardson, D. C. (2007) MolProbity: all-atom contacts and structure validation for proteins and nucleic acids. *Nucleic Acids Res. 35*, W375−383.
(36) Krissinel, E. (2012) Enhanced fold recognition using efficient short fragment clustering. *J. Mol. Biochem. 1*, 76−85.
(37) Karsisiotis, A. I., Deacon, O. M., Rajagopal, B. S., Macdonald, C., Blumenschein, T. M., Moore, G. R., and Worrall, J. A. (2015) Backbone resonance assignments of ferric human cytochrome c and the pro-apoptotic G41S mutant in the ferric and ferrous states. *Biomol. NMR Assignments 9*, 415−419.
(38) Vranken, W. F., Boucher, W., Stevens, T. J., Fogh, R. H., Pajon, A., Llinas, M., Ulrich, E. L., Markley, J. L., Ionides, J., and Laue, E. D. (2005) The CCPN data model for NMR spectroscopy: development of a software pipeline. *Proteins: Struct., Funct., Genet. 59*, 687−696.
(39) Goddard, T. D., and Kneller, D. G. (2008) *SPARKY 3*, University of California, San Francisco.
(40) Bai, Y., Milne, J. S., Mayne, L., and Englander, S. W. (1993) Primary structure effects on peptide group hydrogen exchange. *Proteins: Struct., Funct., Genet. 17*, 75−86.
(41) Hoshino, M., Katou, H., Yamaguchi, K.-I., and Goto, Y. (2007) Dimethylsulfoxide-quenched hydrogen/deuterium exchange method to study amyloid fibril structure. *Biochim. Biophys. Acta, Biomembr. 1768*, 1886−1899.
(42) Palmer, A. G., Rance, M., and Wright, P. E. (1991) Intramolecular Motions of a Zinc Finger DNA-Binding Domain from Xfin Characterized by Proton-Detected Natural Abundance C-12 Heteronuclear Nmr-Spectroscopy. *J. Am. Chem. Soc. 113*, 4371−4380.
(43) Delaglio, F., Grzesiek, S., Vuister, G. W., Zhu, G., Pfeifer, J., and Bax, A. (1995) NMRPipe: a multidimensional spectral processing system based on UNIX pipes. *J. Biomol. NMR 6*, 277−293.
(44) Liptak, M. D., Fagerlund, R. D., Ledgerwood, E. C., Wilbanks, S. M., and Bren, K. L. (2011) The Proapoptotic G41S Mutation to Human Cytochrome c Alters the Heme Electronic Structure and Increases the Electron Self-Exchange Rate. *J. Am. Chem. Soc. 133*, 1153−1155.
(45) Zeldin, O. B., Gerstel, M., and Garman, E. F. (2013) RADDOSE-3D: time- and space-resolved modelling of dose in macromolecular crystallography. *J. Appl. Crystallogr. 46*, 1225−1230.
(46) Beitlich, T., Kuhnel, K., Schulze-Briese, C., Shoeman, R. L., and Schlichting, I. (2007) Cryoradiolytic reduction of crystalline heme proteins: analysis by UV-Vis spectroscopy and X-ray crystallography. *J. Synchrotron Radiat. 14*, 11−23.
(47) Kekilli, D., Moreno-Chicano, T., Chaplin, A. K., Horrell, S., Dworkowski, F. S. N., Worrall, J. A. R., Strange, R. W., and Hough, M. A. (2017) Photoreduction and validation of haem-ligand intermediate states in protein crystals by in situ single-crystal spectroscopy and diffraction. *IUCrJ 4*, 263−270.
(48) Takano, T., and Dickerson, R. E. (1981) Conformation change of cytochrome c. II. Ferricytochrome c refinement at 1.8 A and comparison with the ferrocytochrome structure. *J. Mol. Biol. 153*, 95−115.
(49) Brayer, G. D., and Murphy, M. P. (1996) Structural studies of eukaryotic cytochromes c. In *Cytochrome c: A multidisciplinary approach* (Scott, R. A., and Mauk, A. G., Eds.) 1st ed., pp 103−166, University Science Books, Sausalito, CA.
(50) Shortle, D. (1995) Staphylococcal nuclease: a showcase of m-value effects. *Advances in protein chemistry 46*, 217−247.
(51) Hammack, B. N., Smith, C. R., and Bowler, B. E. (2001) Denatured state thermodynamics: residual structure, chain stiffness and scaling factors. *J. Mol. Biol. 311*, 1091−1104.
(52) Godbole, S., Dong, A., Garbin, K., and Bowler, B. E. (1997) A lysine 73−>histidine variant of yeast iso-1-cytochrome c: evidence for a native-like intermediate in the unfolding pathway and implications for m value effects. *Biochemistry 36*, 119−126.
(53) Rosell, F. I., Ferrer, J. C., and Mauk, A. G. (1998) Proton-linked protein conformational switching: Definition of the alkaline conformational transition of yeast iso-1-ferricytochrome c. *J. Am. Chem. Soc. 120*, 11234−11245.
(54) Wuthrich, K. (1969) High-resolution proton nuclear magnetic resonance spectroscopy of cytochrome. *Proc. Natl. Acad. Sci. U. S. A. 63*, 1071−1078.
(55) Ubbink, M., Worrall, J. A., Canters, G. W., Groenen, E. J., and Huber, M. (2002) Paramagnetic resonance of biological metal centers. *Annu. Rev. Biophys. Biomol. Struct. 31*, 393−422.
(56) Santos, H., and Turner, D. L. (1987) Proton NMR studies of horse ferricytochrome c. Completion of the assignment of the well resolved hyperfine shifted resonances. *FEBS Lett. 226*, 179−185.
(57) Feng, Y. Q., Roder, H., and Englander, S. W. (1990) Assignment of paramagnetically shifted resonances in the ^{1}H NMR spectrum of horse ferricytochrome c. *Biophys. J. 57*, 15−22.
(58) Senn, H., and Wuthrich, K. (1985) Amino acid sequence, haem-iron co-ordination geometry and functional properties of mitochondrial and bacterial c-type cytochromes. *Q. Rev. Biophys. 18*, 111−134.
(59) Burns, P. D., and Lamar, G. N. (1979) Detection of Localized Conformational Flexibility in Horse Heart Cytochrome-C by Proton Nuclear Magnetic-Resonance. *J. Am. Chem. Soc. 101*, 5844−5846.
(60) Burns, P. D., and La Mar, G. N. (1981) Characterization of conformational heterogeneity in the heme pocket of ferricytochrome c using high field proton nuclear magnetic resonance spectroscopy. *J. Biol. Chem. 256*, 4934−4939.
(61) Zhong, L., Wen, X., Rabinowitz, T. M., Russell, B. S., Karan, E. F., and Bren, K. L. (2004) Heme axial methionine fluxionality in Hydrogenobacter thermophilus cytochrome c552. *Proc. Natl. Acad. Sci. U. S. A. 101*, 8637−8642.
(62) Angstrom, J., Moore, G. R., and Williams, R. J. P. (1982) The Magnetic-Susceptibility of Ferricytochrome-C. *Biochim. Biophys. Acta, Protein Struct. Mol. Enzymol. 703*, 87−94.
(63) Englander, S. W., and Kallenbach, N. R. (1983) Hydrogen-Exchange and Structural Dynamics of Proteins and Nucleic-Acids. *Q. Rev. Biophys. 16*, 521−655.
(64) Hannibal, L., Tomasina, F., Capdevila, D. A., Demicheli, V., Tortora, V., Alvarez-Paggi, D., Jemmerson, R., Murgida, D. H., and Radi, R. (2016) Alternative Conformations of Cytochrome c: Structure, Function, and Detection. *Biochemistry 55*, 407−428.
(65) Bayir, H., Fadeel, B., Palladino, M. J., Witasp, E., Kurnikov, I. V., Tyurina, Y. Y., Tyurin, V. A., Amoscato, A. A., Jiang, J., Kochanek, P. M., DeKosky, S. T., Greenberger, J. S., Shvedova, A. A., and Kagan, V. E. (2006) Apoptotic interactions of cytochrome c: redox flirting with anionic phospholipids within and outside of mitochondria. *Biochim. Biophys. Acta, Bioenerg. 1757*, 648−659.
(66) Krishna, M. M., Lin, Y., Rumbley, J. N., and Englander, S. W. (2003) Cooperative omega loops in cytochrome c: role in folding and function. *J. Mol. Biol. 331*, 29−36.
(67) Krishna, M. M., Maity, H., Rumbley, J. N., Lin, Y., and Englander, S. W. (2006) Order of steps in the cytochrome c folding pathway: evidence for a sequential stabilization mechanism. *J. Mol. Biol. 359*, 1410−1419.
(68) Maity, H., Maity, M., Krishna, M. M., Mayne, L., and Englander, S. W. (2005) Protein folding: the stepwise assembly of foldon units. *Proc. Natl. Acad. Sci. U. S. A. 102*, 4741−4746.
(69) Kroll, T., Hadt, R. G., Wilson, S. A., Lundberg, M., Yan, J. J., Weng, T. C., Sokaras, D., Alonso-Mori, R., Casa, D., Upton, M. H., Hedman, B., Hodgson, K. O., and Solomon, E. I. (2014) Resonant inelastic X-ray scattering on ferrous and ferric bis-imidazole porphyrin

DOI: 10.1021/acs.biochem.7b00890
Biochemistry XXXX, XXX, XXX−XXX

and cytochrome c: nature and role of the axial methionine-Fe bond. *J. Am. Chem. Soc. 136*, 18087−18099.
(70) Mara, M. W., Hadt, R. G., Reinhard, M. E., Kroll, T., Lim, H., Hartsock, R. W., Alonso-Mori, R., Chollet, M., Glownia, J. M., Nelson, S., Sokaras, D., Kunnus, K., Hodgson, K. O., Hedman, B., Bergmann, U., Gaffney, K. J., and Solomon, E. I. (2017) Metalloprotein entatic control of ligand-metal bonds quantified by ultrafast x-ray spectroscopy. *Science 356*, 1276−1280.
(71) Vallee, B. L., and Williams, R. J. (1968) Metalloenzymes: the entatic nature of their active sites. *Proc. Natl. Acad. Sci. U. S. A. 59*, 498−505.
(72) McClelland, L. J., Mou, T. C., Jeakins-Cooley, M. E., Sprang, S. R., and Bowler, B. E. (2014) Structure of a mitochondrial cytochrome c conformer competent for peroxidase activity. *Proc. Natl. Acad. Sci. U. S. A. 111*, 6648−6653.
(73) Robinson, M. N., Boswell, A. P., Huang, Z. X., Eley, C. G., and Moore, G. R. (1983) The conformation of eukaryotic cytochrome c around residues 39, 57, 59 and 74. *Biochem. J. 213*, 687−700.
(74) Schejter, A., Koshy, T. I., Luntz, T. L., Sanishvili, R., Vig, I., and Margoliash, E. (1994) Effects of mutating Asn-52 to isoleucine on the haem-linked properties of cytochrome c. *Biochem. J. 302* (Part 1), 95−101.
(75) Maity, H., Rumbley, J. N., and Englander, S. W. (2006) Functional role of a protein foldon–an Ω-loop foldon controls the alkaline transition in ferricytochrome c. *Proteins: Struct., Funct., Genet. 63*, 349−355.
(76) Assfalg, M., Bertini, I., Dolfi, A., Turano, P., Mauk, A. G., Rosell, F. I., and Gray, H. B. (2003) Structural model for an alkaline form of ferricytochrome C. *J. Am. Chem. Soc. 125*, 2913−2922.
(77) Huttemann, M., Lee, I., Pecinova, A., Pecina, P., Przyklenk, K., and Doan, J. W. (2008) Regulation of oxidative phosphorylation, the mitochondrial membrane potential, and their role in human disease. *J. Bioenerg. Biomembr. 40*, 445−456.
(78) Huttemann, M., Lee, I., Grossman, L. I., Doan, J. W., and Sanderson, T. H. (2012) Phosphorylation of mammalian cytochrome c and cytochrome c oxidase in the regulation of cell destiny: respiration, apoptosis, and human disease. *Advs Expt Med. Biol. 748*, 237−264.
(79) Lee, I., Salomon, A. R., Yu, K., Doan, J. W., Grossman, L. I., and Huttemann, M. (2006) New prospects for an old enzyme: mammalian cytochrome c is tyrosine-phosphorylated in vivo. *Biochemistry 45*, 9121−9128.
(80) Yu, H., Lee, I., Salomon, A. R., Yu, K., and Huttemann, M. (2008) Mammalian liver cytochrome c is tyrosine-48 phosphorylated in vivo, inhibiting mitochondrial respiration. *Biochim. Biophys. Acta, Bioenerg. 1777*, 1066−1071.
(81) Mahapatra, G., Varughese, A., Ji, Q., Lee, I., Liu, J., Vaishnav, A., Sinkler, C., Kapralov, A. A., Moraes, C. T., Sanderson, T. H., Stemmler, T. L., Grossman, L. I., Kagan, V. E., Brunzelle, J. S., Salomon, A. R., Edwards, B. F., and Huttemann, M. (2017) Phosphorylation of Cytochrome c Threonine 28 Regulates Electron Transport Chain Activity in Kidney: IMPLICATIONS FOR AMP KINASE. *J. Biol. Chem. 292*, 64−79.
(82) Pecina, P., Borisenko, G. G., Belikova, N. A., Tyurina, Y. Y., Pecinova, A., Lee, I., Samhan-Arias, A. K., Przyklenk, K., Kagan, V. E., and Huttemann, M. (2010) Phosphomimetic substitution of cytochrome C tyrosine 48 decreases respiration and binding to cardiolipin and abolishes ability to trigger downstream caspase activation. *Biochemistry 49*, 6705−6714.
(83) Garcia-Heredia, J. M., Diaz-Moreno, I., Diaz-Quintana, A., Orzáez, M., Navarro, J. A., Hervas, M., and De la Rosa, M. A. (2012) Specific nitration of tyrosines 46 and 48 makes cytochrome c assemble a non-functional apoptosome. *FEBS Lett. 586*, 154−158.
(84) Moreno-Beltran, B., Guerra-Castellano, A., Diaz-Quintana, A., Del Conte, R., Garcia-Maurino, S. M., Diaz-Moreno, S., Gonzalez-Arzola, K., Santos-Ocana, C., Velazquez-Campoy, A., De la Rosa, M. A., Turano, P., and Diaz-Moreno, I. (2017) Structural basis of mitochondrial dysfunction in response to cytochrome c phosphorylation at tyrosine 48. *Proc. Natl. Acad. Sci. U. S. A. 114*, E3041−E3050.
(85) Moore, G. R., and Pettigrew, G. W. (1990) *Cytochrome c: Evolutionary, Structural and Physicochemical Aspects*, Springer-Verlag, London.

DOI: 10.1021/acs.biochem.7b00890
Biochemistry XXXX, XXX, XXX−XXX